Fall 2021

Dynamic behavior and interactions of ferrofluid droplets under magnetic fields in low Reynolds number flows

Md Rifat Hassan

Department: Mechanical and Aerospace Engineering

DYNAMIC BEHAVIOR AND INTERACTIONS OF FERROFLUID DROPLETS UNDER MAGNETIC FIELDS IN LOW REYNOLDS NUMBER FLOWS

by

MD RIFAT HASSAN

A DISSERTATION

Presented to the Graduate Faculty of the

MISSOURI UNIVERSITY OF SCIENCE AND TECHNOLOGY

In Partial Fulfillment of the Requirements for the Degree

DOCTOR OF PHILOSOPHY

in

MECHANICAL ENGINEERING

2021

Approved by:

Cheng Wang, Advisor
K. M. Isaac
K. Chandrashekhara
Kelly Homan
Yanzhi Zhang

PUBLICATION DISSERTATION OPTION

This dissertation consists of the following six articles, which have been published/submitted for publication as follows:

Paper I, found on pages 11-44, has been published in Physics of Fluids.

Paper II, found on pages 45-80, has been published in Physics of Fluids.

Paper III, found on pages 81-120, has been published in Colloids and Surfaces A: Physicochemical and Engineering Aspects.

Paper IV, found on pages 121-160, has been published in Langmuir.

Paper V, found on pages 161-199, has been published in Colloid and Interface Science Communications.

Paper VI, found on pages 200-240, has been submitted for publication in Colloids and Surfaces A: Physicochemical and Engineering Aspects.

ABSTRACT

Digital microfluidics in combination with emulsion microfluidics are crucial building blocks of droplet-based microfluidics, which are prevalent in a wide variety of industrial and biomedical applications, including polymer processing, food production, drug delivery, inkjet printing, and cell-based assays. Therefore, understanding the dynamics and interactions of droplets as well as the interactions between the droplets and solid surfaces are of great importance in order to improve the performance or product in these applications.

Recently, several studies in the literature have demonstrated the potential of magnetic fields in controlling the behavior of droplets in microscale; however, the fundamental mechanism behind the interesting dynamics of droplets and the full potential has not been fully understood. To advance both fundamental knowledge as well as demonstrate practical applications, this research combines both numerical and experimental approaches to investigate novel manipulations of ferrofluid droplets using magnetic fields.

The first part of this research focuses on the numerical and experimental investigations on deformation and lateral migration of microscale ferrofluid droplets in shear flows, while the second and third parts, utilizing a numerical approach, explore the breakup and interactions of droplets under uniform magnetic fields, respectively. Next, the fourth part demonstrates the potential of permanent magnetic fields in the control of coalescence of sessile droplets on hydrophobic surfaces, while the fifth part studies the freely falling droplets under the influence of gravity and a uniform magnetic field. Finally, both numerical and experimental approaches are adopted to investigate the wetting and bouncing dynamics of ferrofluid droplets upon impact onto a solid flat surface under permanent magnetic fields. The results demonstrate several simple, versatile and powerful methods for the manipulation of droplet dynamics using magnetic fields, which can play a crucial role in droplet-based applications.

ACKNOWLEDGMENTS

At first, I would like to express my sincere gratitude to my advisor, Dr. Cheng Wang, for his insightful guidance and immense support over the entire duration of my graduate studies at Missouri S&T. He was always open to my ideas and made himself available whenever I needed to have a discussion with him about personal/research issues. Most importantly, I am truly indebted to him for giving me all the freedom in the world, which I believe, got the best out of me during the last four and half years. Moreover, his research passion, vast knowledge, collaboration, teaching methods, and empathetic nature not only made me a better researcher but also made me a better person. Furthermore, I gratefully acknowledge the Department of Mechanical and Aerospace Engineering at Missouri S&T for providing financial support during my graduate study.

I would also like to extend my deepest gratitude to my dissertation committee members, Dr. K. M. Isaac, Dr. K. Chandrashekhara, Dr. Kelly Homan, and Dr. Yanzhi Zhang for their valuable suggestions and comments, which was very helpful in the completion of my dissertation.

Additionally, I am very thankful to my research group members Dr. Jie Zhang and Dr. Christopher A. Sobecki for the insightful discussions on life and research. I would also like to thank my friends, Mr. Chinmoy Kumar Podder, Mr. Md Al-Amin, Mr. Tousif Mahmood, Mr. Rupack Ranjan Haldar, and Dr. Monirul Islam Russel for their support and help during my stay in Rolla.

Finally, I would like to express my sincere thanks and gratitude to my parents and family members for their unconditional support, love, and sacrifice during my study in the United States. Also, I am extremely grateful to my lifelong friends Mr. Monjur Rizvi, Mr. Sanid Abdullah, and Mr. Tanvir Hasan Piash (I call them brothers from another mother), who always had my back during the good and bad times.

TABLE OF CONTENTS

Page

LIST OF ILLUSTRATIONS

PAPER V

LIST OF TABLES

1. INTRODUCTION

Droplets dispersed in another immiscible liquid are frequently encountered in a number of industrial applications that involve liquid-liquid extraction [Abeynaike et al., 2012, Lifton, 2016, Nilsson et al., 2013], emulsification [Jafari et al., 2008, Lobo and Svereika, 2003], and in particular, polymer blending [Ionescu-Zanetti et al., 2004, Shum et al., 2008], which is one of the fastest and most commercial means of producing materials with improved properties. The microscale structure of a polymer blend, developed during the processing, is dependent on the droplet distribution and plays a pivotal role in the determination of the mechanical strength and permeability of the polymer blends.

A single droplet in simple shear flow serves as an excellent model problem to understand droplet dynamics and can provide fundamental insights to more complex emulsion systems [Rallison, 1984, Stone, 1994]. Following the pioneering work of Taylor [Taylor, 1932, 1934], numerous experimental [Guido and Villone, 1998, Rumscheidt and Mason, 1961, Sibillo et al., 2006], theoretical [Barthes-Biesel and Acrivos, 1973], and numerical studies [Feigl et al., 2007, Griggs et al., 2007, Li et al., 2000, Xi and Duncan, 1999] have been carried out to investigate the deformation and breakup of a Newtonian droplet suspended in shear flow of another viscous Newtonian fluid. Three-dimensional single-droplet deformation and breakup under simple shear flow using numerical simulation has been investigated by Xi [Xi and Duncan, 1999]. Debruijn [Debruijn, 1991] developed a Couette device to study the breakup of non-Newtonian droplets in a quasi-steady simple shear flow. Li [Li et al., 2000] performed a numerical simulation using the volume of fluid (VOF) method to observe the breakup of a single droplet into daughter droplets via an end-pinching mechanism. Feigl [Feigl et al., 2007] conducted both a simulation and experiments to study the deformation and orientation of the droplet in a simple shear flow. These investigations find that the droplet deformation depends on several dimensionless parameters, including the Capillary number, Reynolds number, viscosity ratio between the

dispersed and continuous phases, and the confinement ratio. For a comprehensive review of this topic, readers are referred to a number of excellent review articles [Rallison, 1984, Stone, 1994].

It is a well known fact that when polymer processing involves complex flow fields, the droplet size and distribution are mainly affected by two key phenomena: droplet coalescence and breakup, which can also simultaneously occur in polymer blends. In general, coalescence is a more complex phenomenon than breakup since coalescence involves droplet-droplet interactions, while breakup requires a single drop and is not greatly influenced by the presence of neighboring drops in polymer blends [Loewenberg and Hinch, 1997]. The coalescence phenomenon mainly consists of three distinct phases: approach leading to collision, film drainage between liquid phases due to the flattening of the interfaces, and rupture leading to confluence. Sometimes, droplet collision does not inevitably result in coalescence, due to increased droplet deformation, which eventually decreases the probability of coalescence [Chesters, 1991].

In recent years, small scale mixing devices are getting more attention in the development stage of the polymer blends and composites [Cassagnau and Fenouillot, 2004, Son, 2009], and due to their small size, the wall effects on the droplets can not be neglected. The flow in these types of mixing devices is a combination of both shear and extensional flow; however, shear flow is often considered as the main flow component. As a result, most of the studies in the literature are devoted to the structural organization of droplets in a confined shear flow [De Bruyn et al., 2014], and in order to obtain a precise control on the size and shape of the droplets in a confined shear flow, a comprehensive understanding of the underlying hydrodynamics behind the interaction behavior between droplets is required.

Following the pioneering works of Taylor [Taylor, 1932, 1934], several authors investigated the collision between two droplets in a shear flow [Edwards et al., 2009, Rother et al., 1997]. Guido and Simeone [Guido and Villone, 1998] used an optical microscopy to analyze droplet collision in a simple shear flow; however, the coalescence conditions were

not mentioned in their work. Baldessari and Leal [Baldessari and Leal, 2006] performed a theoretical investigation on the interaction between a pair of droplets in a linear flow at a low capillary number and found that overall droplet deformation plays a crucial role on the drainage of the film during coalescence, while Jaeger et al. [Jaeger et al., 1994] found that coalescence depends on the mobility of the interfaces. Burkhart et al. [Burkhart et al., 2001] theoretically predicted the final size distribution of non-deformable drops in a dispersion based on the degree of droplet deformation. Moreover, a review on the potential of more classical forces, such as, dispersion and supramolecular forces on film rupture is provided by Bergeron [Bergeron, 1999].

Experimental investigations are mainly focused on the evolution of the final shape of the droplet or size distribution in a dispersion of droplets exposed to steady or transient flows [Lyu et al., 2002, Marić and Macosko, 2002]. Chen et al. [Chen et al., 2009] analyzed the confinement effect on droplet coalescence in a pure shear flow and found that coalescence is promoted by confinement. De Bruyn et al. [De Bruyn et al., 2013] studied the effect of initial offset in the velocity gradient direction on the coalescence proficiency of two droplets in a confined shear flow and found that confinement initiates reversal droplet trajectories at small initial offsets. Yang et al. [Yang et al., 2001] and Ha et al. [Ha et al., 2003] analyzed the individual flow-induced coalescence events under confined conditions, and their results suggest that droplet interactions involve a richer phenomena, which is dependent on the droplet deformation and corresponding hydrodynamic interactions among themselves. Furthermore, splitting and coalescence of droplets under confined conditions in microfluidic devices have been explored by Christopher et al. [Christopher et al., 2009] and Chen et al. [Chen et al., 2007].

Numerical simulations are useful in the study of droplet interactions, in situations with initial conditions that are difficult to implement in experiments. Additionally, the flexibility of numerical models provides a greater advantage in predicting the performance of coalescence in complex systems [Farhat and Lee, 2011, Yue et al., 2005]. Chen and Wang

[Chen and Wang, 2014] investigated droplets interaction in a shear flow under confinement using VOF method and found that an increase in confinement leads to a reversing motion instead of a passing-over motion. Shardt et al. [Shardt et al., 2013] implemented a lattice Boltzmann method to study droplet coalescence in a simple shear flow and observed that with an increase in the droplet sizes, the critical capillary number decreases. In another work, a lattice Boltzmann method was implemented by Sun et al. [Sun et al., 2013] to analyze head-on droplet collision, while Dupuy et al. [Dupuy et al., 2010] used the Cahn-Hillard free energy method to examine coalescence for non-uniform systems.

Moreover, in contrast to emulsion microfluidics, digital microfluidics deals with the behavior of sessile droplets on an open surface and in combination with emulsion microfluidics are crucial building blocks of droplet-based microfluidics, which has been prevalent as a well established research field in the literature for over a decade now. One of the main advantages of digital microfluidics over emulsion microfluidics (also known as continuous-flow droplet based microfluidics) is that emulsion microfluidics requires an external pumping mechanism to attain continuous generation of droplets through a closed microfluidic channel, whereas in digital microfluidics, manipulation of droplets takes place on an open plain surface without any confinement, which in turn enables droplets to act as independent virtual reactors that are often utilized in point-of-care diagnostics, which require synthesis of hazardous materials [Javed et al., 2014, Keng et al., 2012] or preparation of complex samples [Choi et al., 2013, Ng et al., 2015, Pipper et al., 2007, 2008] and cell-based assays [Choi et al., 2012].

Droplet manipulation in microfluidics applications is usually accomplished either by controlling the behavior of magnetic particles by a permanent magnet or an array of electromagnets that consists of micro coils. Okochi et al. [Okochi et al., 2010] controlled droplets with magnetic particles by placing a permanent magnet below the channel surface and achieved coalescence with a lysis buffer droplet, while a simple configuration of total RNA extraction droplet array is presented by Shi et al. [Shi et al., 2015a], which facilitates

the transportation of magnetic beads through buffer solutions. In contrast, several other analytical and numerical studies [Beyzavi and Nguyen, 2008a,b, Lehmann et al., 2006a,b, Rida et al., 2003] implemented micro coils as electromagnets in order to achieve controlled transportation of magnetic droplets; however, one of the major issues arises as a result of using electromagnets, which is known as Joule heating, and in turn requires a cooling mechanism to mitigate the heating effect [Chiou et al., 2013].

Furthermore, droplet on demand (DOD) is one of the most prominent processes involved in inkjet printing — a prospective material-conserving and cost-effective localized additive deposition technique for large area manufacturing where the ejection of a desired volume of ink droplet is substantially achieved via a nozzle, followed by an abrupt piezo-electric actuated quasi-adiabatic reduction in the chamber volume [Liu et al., 2013, Pabst et al., 2013, Tekin et al., 2008]. Subsequently, the ejected droplet encounters air resistance while falling under the influence of gravity, until impinging and spreading on the substrate, which is again aided by the momentum gained by the droplet during the free fall and surface tension flow along the surface [He et al., 2017, Pesach and Marmur, 1987]. Interestingly, the spreading and final shape of the droplet are also strongly dependent on the printing height and viscosity of the medium, which eventually are crucial in the determination of ultimate resolution in printing techniques [Jung et al., 2013, Perelaer et al., 2009a,b].

When the size of droplets is smaller than the capillary length, the impact process is typically governed by the inertial, capillary, and viscous forces, which is accomplished in five consecutive stages i.e., kinematic, spreading, relaxation, wetting, and equilibrium phases. Moreover, during the spreading phase, the spreading diameter of the impinging droplet undergoes continuous changes, which in turn affects the heat transfer in spray cooling process [Lin and Ponnappan, 2003]. Several analytical [Chandra and Avedisian, 1991, Madejski, 1976, Yonemoto and Kunugi, 2017] and experimental [Kim and Chun, 2001, Pasandideh-Fard et al., 1996, Scheller and Bousfield, 1995] works on the spreading dynamics of droplets are reported in the literature, which discuss the relationship between

the maximum droplet spreading and several dimensionless groups that affect the droplet dynamics. These dimensionless groups include but are not limited to Reynolds number (ratio between inertial and viscous forces), Weber number (ratio between inertial and surface tension forces), and Ohnesorge number (ratio between viscous, inertial, and surface tension forces). Moreover, the interaction between the bottom solid substrate and the droplet is crucial to the overall dynamics of droplet spreading, which again can be described by the contact angle — an equilibrium parameter among solid, liquid, and vapor interfaces.

In addition to hydrodynamic, gravitational, and surface tension forces, droplet rheology can also be manipulated by using external forces through an electric [Bararnia and Ganji, 2013, Supeene et al., 2008], acoustic [Pangu and Feke, 2004, Wixforth et al., 2004], and magnetic field [Sherwood, 1988, Zakinyan et al., 2012]. Salipante and Vlahovska [Salipante and Vlahovska, 2010] experimentally studied the electrohydrodynamics of drops under uniform DC electric fields and came to a conclusion that the threshold field strength of high viscous drops can be estimated using Quincke rotation criterion. Chen et al. [Chen et al., 2015] performed both theoretical and numerical analyses on the alternating current induced double droplets interaction in a microchannel to speculate the relationship between droplet separation and critical electric intensity. An experimental work on droplet coalescence in a polymer blend under the impact of electric fields was done by Aida et al. [Aida et al., 2010].

However, in order to use magnetic fields as an additional means of manipulating the shape of a droplet, the droplet or continuous phase needs to be a ferrofluid — stable colloidal suspensions of nanoscale magnetic particles suspended in a non-magnetic carrier liquid and having a coating of surfactants to inhibit clumping. Also, due to the uniform distribution of magnetic nanoparticles, ferrofluids can be transported to different locations for liquid phase reactions [Bitar et al., 2014] and are conventionally used as sealant [Raj and Moskowitz, 1990] in hard drives and coolant in loudspeakers [Mary et al., 2010]. Nguyen et al. [Nguyen et al., 2010] conducted experiments on the motion of a droplet un-

der a moving permanent magnetic field and derived a critical velocity, above which the droplet fails move with the same velocity as the moving magnet. Moreover, Beyzavi and Nguyen demonstrated one-dimensional [Beyzavi and Nguyen, 2008b] and two-dimensional [Beyzavi and Nguyen, 2009] manipulation of ferrofluid droplet using micro coil arrays and found that a small magnetic field gradient is enough to induce movement in a ferrofluid droplet, while Egatz-Gómez et al. [Egatz-Gómez et al., 2006] observed coalescence between two water drops under a moving permanent magnetic field. Since the fluids exhibit different magnetic properties, Maxwell stresses appear in the computational domain, which give rise to interfacial instabilities in ferrofluids [Cowley and Rosensweig, 1967]. An experimental study on the use of an alternating magnetic field on forced convective heat transfer using aqueous ferrofluids in a copper tube revealed a significant heat transfer enhancement [Ghofrani et al., 2013]. Ray et al. [Ray et al., 2017] performed both numerical and experimental investigations on the manipulation of ferrofluid droplets by a permanent magnet and observed coalescence and mixing of ferrofluid droplets under magnetic fields, while Rowghanian et al. [Rowghanian et al., 2016] implemented a computational scheme to study the dynamics of a ferrofluid droplet under spatially uniform magnetic fields.

The objective of this doctoral research is to systematically explore the dynamic behavior and interactions of droplets under the presence of magnetic fields at low Reynolds number flows, which involves developing accurate numerical models and experimental setups in order to systematically analyze the deformation, orientation, breakup, coalescence, wetting, and bouncing of droplets in shear and gravity induced flows and on open surfaces. This approach will be advantageous over the existing traditional hydrodynamic and external force-based techniques in biomedical, lab-on-a-chip, and inkjet printing applications terms of simple implementation in resource limited point-of-care applications, feasibility of scaling up, and higher tolerance to liquid properties.

2. ORGANIZATION OF DISSERTATION

In this research, many technical developments have been achieved; however, only six major developments are presented in this dissertation. The first and sixth paper are focused on both numerical and experimental approaches to investigate the dynamic behavior of droplets, while a numerical investigation is carried out in the rest of the papers to analyze the dynamic behavior of droplets in shear and gravity induced flows and open surfaces. Specifically, Paper I focuses on deformation and orientation of a ferrofluid droplet in a simple shear flow under uniform magnetic fields. Paper II studies the breakup mechanism of a single droplet, while Paper III investigates the interaction behavior between two droplets in a simple shear flow under uniform magnetic fields. Paper IV analyzes the magnetic field induced transportation and coalescence behavior of sessile droplets under a permanent magnetic field. Paper V studies the dynamic interaction behavior between two uneven sized freely falling ferrofluid droplets under uniform magnetic fields, while Paper VI proposes a novel method to manipulate the wetting and bouncing dynamics of droplets after impact using non-uniform magnetic fields.

All six papers share a similar research topic: manipulation of droplet dynamics by using uniform and permanent magnetic fields, while each of them has a different focus.

Paper I presents direct numerical simulation and experimental approaches to investigate the deformation, orientation, and lateral migration behavior of a ferrofluid droplet in a simple shear flow under uniform magnetic fields. Here, the effects of shear rates, magnetic field directions, and strengths are numerically investigated, and the results demonstrate a novel method to control the behavior of dispersed droplets in another immiscible fluid, which is important is emulsion-based applications.

Paper II analyzes the breakup mechanism of a ferrofluid droplet in high shear flow conditions under the presence of a uniform magnetic field. Here, the effects of magnetic field strengths, directions, and viscosity ratios on the breakup event are demonstrated in low

Reynolds number flows. The findings indicate the enormous potential of magnetic fields in controlling the breakup of ferrofluid droplets and emulsion rheology, which are relevant to a variety of applications in the fields of microfluidics and polymer processing.

In order to have a comprehensive understanding on the complex interaction behavior between a pair of droplets, Paper III proposes a level set algorithm that can track the free interface of droplets and correctly capture the coalescence and separation behavior where the application of an uniform magnetic field provides the users an external control to manually manipulate the interaction behavior of droplets in low Reynolds number flows. This paper discusses the effects of shear flows, magnetic field strengths, directions, and initial vertical separation on the interaction phenomenon between droplets, which is critical in order to achieve a better control on the behavior of droplets in microfluidics-based applications.

To demonstrate the potential of non-uniform magnetic fields in the actuation and flexibility of implementation in resource limited point-of-care applications, a phase field method based numerical approach is proposed in Paper IV to analyze the dynamic behavior of sessile droplets on hydrophobic surfaces under a permanent magnetic field. Here, an in-detailed discussion on the effects of magnetic field strengths, contact angles, and viscosity ratios on the coalescence pattern between sessile droplets are presented, which are again considered as integral processes in digital microfluidics, including the synthesis of hazardous materials or preparation of complex samples and cell based assays.

The continuous production of satellite droplets in addition to main droplets is considered as a common and troublesome feature in inkjet printing processes, which again greatly affects the resolution of the final quality of the product. In order to address this issue, Paper V demonstrates a novel method to manipulate the dynamic interaction behavior of freely falling droplets under gravity using uniform magnetic fields. The results suggest that it is possible to manually delaying and expediting the coalescence event between uneven-sized droplets before the impact by the application of magnetic fields along different directions.

Finally, Paper VI investigates the complex post-impact wetting and bouncing dynamics of droplets on a wide range of hydrophobic surfaces under a non-uniform magnetic field. Here, both numerical and experimental approaches are adopted to analyze the effects of magnetic field strengths, magnet sizes, and viscosity ratios on the droplet impact process, and the results signify the potential of non-uniform magnetic fields in the active control of wetting and bouncing dynamics of an impinging droplet on hydrophobic surfaces, which is critical to spray cooling and advanced 3D printing of metals.

PAPER

I. DEFORMATION OF A FERROFLUID DROPLET IN SIMPLE SHEAR FLOWS UNDER UNIFORM MAGNETIC FIELDS

Md Rifat Hassan, Jie Zhang, and Cheng Wang
Department of Mechanical & Aerospace Engineering
Missouri University of Science and Technology
Rolla, Missouri 65409
Tel: 573–341–4636, Fax: 573–341–4607
Email: wancheng@mst.edu

ABSTRACT

We numerically investigate deformation and orientation of a ferrofluid droplet in a simple shear flow under a uniform magnetic field. The numerical simulation is based on the finite element method and couples the magnetic and flow fields. A level set method is used to model the dynamic motion of the droplet interface. Systematic numerical simulations are used to assess the effects of direction and the strength of the magnetic field. Focusing on low Reynolds number flows (Re $\lesssim 0.02$), the numerical results indicate that at a small capillary number (Ca ≈ 0.02), the magnetic field dominates over the shear flow above a certain magnetic bond number ($\mathrm{Bo}_m \approx 3$). The orientation of the droplet is aligned with the direction of the magnetic field, while the deformation of the droplet varies slightly when the direction of the magnetic field is varied. On the other hand, for large capillary numbers (Ca ≈ 0.23), the deformation and orientation of the droplet is influenced by both the shear flow and the magnetic field, except for a small magnetic bond number ($\mathrm{Bo}_m \lesssim 0.2$). In both the small and large capillary number cases, the droplet deformation is found to be maximum at $\alpha = 45^\circ$ (direction of magnetic field) and minimum at $\alpha = 135^\circ$. In addition, the effect

of the magnetic field on the flow field inside and outside the droplet at different conditions is examined. We demonstrate active control of lateral migration of ferrofluid droplets in wall-bounded simple shear flows. The direction of the lateral migration depends on the orientation of the deformed droplets due to uniform magnetic fields at different directions.

Keywords: Microdroplets, Magnetic fields, Two-phase systems, Deformation, Microfluidics, Magnetic fluids, Ferrohydrodynamics

1. INTRODUCTION

Emulsions are liquid droplets dispersed in another immiscible liquid phase. When subjected to shear flows, the droplets deform and may break up. Understanding the dynamics of droplets in shear flows is of great importance to a variety of technological and industrial applications that utilize emulsions, including cosmetics, food production, and polymer processing [Lamura *et al.*, 1999, Mosbach and Andersson, 1977]. For example, in blending of molten polymers, the distribution of droplet size and shape is critical to the rheology and physical properties of the polymer system [Van der Sman and Van der Graaf, 2006, 2008, Yue *et al.*, 2004].

A single droplet in simple shear flow serves as an excellent model problem to understand droplet dynamics and can provide fundamental insights to more complex emulsion systems [Rallison, 1984, Stone, 1994]. Following the pioneering work of Taylor [Taylor, 1932, 1934], numerous experimental [Guido and Villone, 1998, Rumscheidt and Mason, 1961, Sibillo *et al.*, 2006], theoretical [Barthes-Biesel and Acrivos, 1973], and numerical studies [Feigl *et al.*, 2007, Griggs *et al.*, 2007, Li *et al.*, 2000, Xi and Duncan, 1999] have been carried out to investigate the deformation and breakup of a Newtonian droplet suspended in shear flow of another viscous Newtonian fluid. Three-dimensional single-droplet deformation and breakup under simple shear flow using numerical simulation has been investigated by Xi [Xi and Duncan, 1999]. Debruijn [Debruijn, 1991] developed a Couette device to study the breakup of non-Newtonian droplets in a quasi-steady simple

shear flow. Li [Li *et al.*, 2000] performed a numerical simulation using the volume of fluid (VOF) method to observe the breakup of a single droplet into daughter droplets via an end-pinching mechanism. Feigl [Feigl *et al.*, 2007] conducted both a simulation and experiments to study the deformation and orientation of the droplet in a simple shear flow. These investigations find that the droplet deformation depends on several dimensionless parameters, including the Capillary number, Reynolds number, viscosity ratio between the dispersed and continuous phases, and the confinement ratio. For a comprehensive review of this topic, readers are referred to a number of excellent review articles [Rallison, 1984, Stone, 1994].

In addition to using viscous shear, external force fields such as electric or magnetic fields provide an additional means of controlling the deformation of droplets [Stone *et al.*, 1999]. When the droplets and suspending fluid have different electrical properties, an electric field will result in additional Maxwell stresses on the fluid interface to affect the droplet deformation [Maehlmann and Papageorgiou, 2009, Vlahovska, 2011]. Vlahovska [Vlahovska, 2011] developed an analysis to describe the effect of a uniform electric field on the deformation and orientation of dielectric droplets in a simple shear flow. Mahlmann et al. [Maehlmann and Papageorgiou, 2009] investigated the electric field effects on two dimensional drops in simple shear flow at arbitrary Reynolds numbers. Mandal [Mandal *et al.*, 2016] analytically studied the effect of a uniform electric field on the motion of droplet in an unbounded poiseuille flow and also in a simple shear flow [Mandal and Chakraborty, 2017].

Magnetic fields have been demonstrated to control the dynamics of single ferrofluid droplets [Afkhami *et al.*, 2010, Bacri *et al.*, 1982] or emulsion systems [Dikansky *et al.*, 2011, Zakinyan and Dikansky, 2011, Zakinyan *et al.*, 2014]. To use magnetic manipulation, either the droplet or suspending fluid needs to be a ferrofluid [Rosensweig, 1985] – a dispersion of magnetic nanoparticles (typical diameter around 10 nm, and typical volume fraction 5%). Multiphase ferrofluid droplets have promising biomedical applications due

to their ability to be delivered at a specific site with the help of proper manipulation of a magnetic field. A notable biomedical application is the treatment of retinal detachment [Mefford *et al.*, 2007] by guiding a ferrofluid droplet inside the retinae. The magnetic field has also been extensively used in microfluidics to control the various manipulation of microdroplets. Varma et al. studied the magnetic field experimentally inducing the merging of droplets on a lab-on-a-chip application [Varma *et al.*, 2016]. Liu et al. and Wu et al. studied the ferrofluid droplet formation under a uniform magnetic field [Liu *et al.*, 2011, Wu *et al.*, 2013]. Tan et al. reported the manipulation of a ferrofluid droplet at a microfluidic T-junction by using magnetic fields induced by permanent magnets [Tan *et al.*, 2010]. Recently, Zhang et al. studied the flow regimes of ferrofluid droplets under a nonuniform magnetic field [Zhang *et al.*, 2018].

To understand the role of the magnetic field, researchers have numerically and experimentally investigated motion and deformation of a ferrofluid droplet suspended in a viscous medium under different flow conditions. Ghaffari [Ghaffari *et al.*, 2015] performed numerical simulations to study the equilibrium shape and coalescence behavior of suspended ferrofluid droplets under a uniform magnetic field. Bacri [Bacri *et al.*, 1982] studied the deformation of large magnetic agglomerates of ferrofluid that are sandwiched in a Hele-Shaw cell in a weak magnetic field. Afkhami et al. [Afkhami *et al.*, 2008, 2010] numerically investigated the deformation of a neutrally buoyant hydrophobic ferrofluid droplet in a viscous medium under a uniform magnetic field. Afkhami et al. also investigated the motion of a ferrofluid droplet in an axisymmetric geometry under a uniform magnetic field. Shi [Shi *et al.*, 2014] numerically investigated the dynamics of a ferrofluid droplet falling in a non-magnetic fluid under a uniform magnetic field. Korlie [Korlie *et al.*, 2008] studied the rising of a bubble and sinking of a droplet in a ferrofluid by considering the gravity effect, while Zhu et al. [Zhu *et al.*, 2011] studied the nonlinear deformation of large ferrofluid droplets under the influence of a uniform magnetic field and gravity.

However, till now, few have studied the deformation of ferrofluid droplets in a simple shear flow under the influence of a uniform magnetic field. Recently, Jesus et al. [Jesus *et al.*, 2017] performed a three-dimensional numerical analysis on the droplet dynamics and field induced deformation of a ferrofluid droplet in another Newtonian fluid. They investigated the influence of the magnetic field on the time evolution of the droplet deformation for low shear rate and found that the presence of the magnetic field causes the deformation a longer time to reach a steady state. Their results suggest that at a fixed low shear rate, the magnetic field takes control of the deformation and orientation of the droplet at a higher magnetic bond number, Bo_m. Further, they found that for $\mathrm{Bo}_m \approx O(1)$ and small Ca, the droplet deformation in the vorticity direction can be of the same order as that occurring in the shear plane. One advantage of using magnetic fields, when compared to electric fields, is that magnetic fields can be applied at arbitrary directions with ease. However, the existing investigations on magnetic control have primarily focused either on the field direction perpendicular and/or parallel to the flow direction [Jesus *et al.*, 2017, Liu *et al.*, 2011] or a droplet in a quiescent flow [Afkhami *et al.*, 2010, Bacri *et al.*, 1982, Ghaffari *et al.*, 2015, Korlie *et al.*, 2008]. A thorough understanding of the deformation dynamics of a ferrofluid droplet under both shear flows and magnetic fields is missing.

By using two-dimensional (2D) direct numerical simulations, this paper investigates the dynamics and deformation of a ferrofluid droplet in a simple shear flow under a uniform magnetic field that is focused in an arbitrary direction. For computational efficiency, we have chosen to use 2D simulations in order to study a wide range of parameters (i.e., capillary number, magnetic bond number, and field direction). Prior studies have shown that 2D numerical simulations are able to qualitatively and correctly capture the characteristics of droplet deformations in simple shear flows and droplet deformation under uniform magnetic fields [Ansari *et al.*, 2012, Shi *et al.*, 2014, Van der Sman and Van der Graaf, 2008, Van

Der Sman *et al.*, 2003]. Our numerical simulation, built with a commercial FEM solver, models the dynamic deformation of droplet interface by using the level set method and couples the magnetic and flow fields.

The remainder of this paper is organized as follows: in Section 2, the mathematical model and numerical method are described. In Section 3, we first present numerical results obtained from droplet deformation in a simple shear flow only and droplet deformation under a uniform magnetic field, and we validate our numerical model against existing theories. We then examine the effect of the magnetic field on the droplet deformation and orientation by varying the field direction, magnetic bond number, and capillary number. Furthermore, by combining wall-bound simple shear flows and uniform magnetic fields, we demonstrate a versatile control of lateral migration motions of the ferrofluid droplets by adjusting the direction of the magnetic field. Finally, major findings are summarized in Section 4.

2. NUMERICAL SIMULATION METHOD

2.1. LEVEL SET METHOD

In our model, we have used the conservative level set method to track the dynamic evolution of the interface between the droplet and suspending medium [Ansari *et al.*, 2012, Osher and Fedkiw, 2001]. The level set function ϕ is an auxiliary scalar function used to represent the phases of the two fluids: In the droplet phase as $\phi = 1$, and in the continuous phase as $\phi = 0$. The value of ϕ smoothly transits from 0 to 1 over the interface, and here $\phi = 0.5$ is used to define the position of the interface. The level set function ϕ is advected by the velocity field by [COMSOL, 2018, Olsson and Kreiss, 2005]:

$$\frac{d\phi}{dt} + \mathbf{u} \cdot \nabla\phi = \gamma \nabla \cdot \left(\epsilon \nabla\phi - \phi(1-\phi) \frac{\nabla\phi}{|\nabla\phi|} \right), \tag{1}$$

where $\mathbf{u}$, γ, and ϵ denote the velocity field, the amount of reinitialization, and the thickness of the interface, respectively. The terms on the left-hand side of the equation represent the motion of the interface, while the terms on the right-hand side are required for numerical stability. The parameter ϵ defines the thickness of the interface and is set to equal the largest size of the mesh in the domain. The amount of stabilization is defined by the parameter γ, which needs to be carefully controlled for maintaining the thickness of the interface, and the appropriate value of γ is the maximum magnitude of the velocity field. The level set function ϕ can be used to find the unit normal to the interface $\mathbf{n}$:

$$\mathbf{n} = \frac{\nabla\phi}{|\nabla\phi|}. \tag{2}$$

With the level set method, the two immiscible fluids are treated as a single phase flow, with material properties that vary according to the level set value. Here, a linear average is used, and the density (ρ), dynamic viscosity (η), magnetic permeability (μ), and magnetic susceptibility (χ) are related to ϕ via the following equations:

$$\rho = \rho_c + (\rho_d - \rho_c)\phi, \qquad \eta = \eta_c + (\eta_d - \eta_c)\phi, \tag{3}$$

$$\mu = \mu_c + (\mu_d - \mu_c)\phi, \qquad \chi = \chi_c + (\chi_d - \chi_c)\phi, \tag{4}$$

where the subscripts c and d represent the continuous and droplet phase, respectively.

2.2. GOVERNING EQUATIONS

The motion of an incompressible, immiscible ferrofluid droplet in another incompressible, immiscible medium under the effect of a uniform magnetic field is governed by the continuity and momentum equations:

$$\nabla \cdot \mathbf{u} = 0, \tag{5}$$

and

$$\rho\left(\frac{\partial \mathbf{u}}{\partial t} + \mathbf{u}\cdot\nabla\mathbf{u}\right) = -\nabla p + \nabla\cdot\boldsymbol{\tau} + \mathbf{F}_\sigma + \mathbf{F}_m, \tag{6}$$

where p denotes pressure, $\boldsymbol{\tau} = [\eta(\nabla\mathbf{u} + (\nabla\mathbf{u})^T)]$ denotes viscous stress, $\mathbf{F}_\sigma$ represents force due to surface tension, and $\mathbf{F}_m$ represents force due to the magnetic field.

The surface tension force $\mathbf{F}_\sigma$ is defined:

$$\mathbf{F}_\sigma = \nabla\cdot[\sigma\{\mathbf{I} + (-\mathbf{n}\mathbf{n}^T)\}\delta], \tag{7}$$

where σ is the coefficient of surface tension, $\mathbf{I}$ is the second-order identity tensor, δ is the Dirac delta function, and $\mathbf{n}$ is the unit normal to the interface that can be calculated using equation (2). The Dirac delta function δ is approximated using the level set function as

$$\delta = 6|\phi(1-\phi)||\nabla\phi|. \tag{8}$$

The magnetic force can be calculated as [Rosensweig, 1985]:

$$\mathbf{F}_m = \nabla\cdot\boldsymbol{\tau}_m = \nabla\cdot(\mu\mathbf{H}\mathbf{H} - \frac{\mu}{2}H^2\mathbf{I}), \tag{9}$$

where $\boldsymbol{\tau}_m$ is the magnetic stress tensor for the applied magnetic field, and $H^2 = \mathbf{H}\cdot\mathbf{H} = |\mathbf{H}|^2$. To calculate the magnetic stress tensor, the magneto-statics equations, including magnetic induction $\mathbf{B}$, magnetization $\mathbf{M}$, and magnetic field $\mathbf{H}$, are solved. Assuming linear and homogeneous material properties, the magneto-static Maxwell equation relates $\mathbf{B}$, $\mathbf{H}$, and $\mathbf{M}$ via the following relationships [Stratton, 2007]:

$$\nabla\cdot\mathbf{B} = 0, \qquad \nabla\times\mathbf{H} = 0, \qquad \mathbf{M} = \chi\mathbf{H} \quad \text{and} \quad \mathbf{B} = \mu_0(\mathbf{H}+\mathbf{M}) = \mu_0(1+\chi)\mathbf{H}, \tag{10}$$

where $\mu_0 = 4\pi \times 10^{-7}$ N/A^2 is the permeability of vacuum, and μ and χ depend on the phase function ϕ according to Equation (4). A scalar potential ψ can be defined, and its gradient represents curl-free $\mathbf{H}$ (i.e., $\mathbf{H} = -\nabla\psi$). We can now write

$$\nabla \cdot (\mu \nabla \psi) = 0. \tag{11}$$

2.3. GOVERNING EQUATIONS IN NON-DIMENSIONAL FORM

We rewrite the governing equations to understand the main effects (in terms of dimensionless groups) that control the droplet dynamics. We scale the length by the radius of the initially undeformed droplet (R_0), and time by the inverse of shear rate $\frac{1}{\dot{\gamma}}$, respectively. The other dimensionless variables are defined as follows:

$$p^* = \frac{p}{\eta\dot{\gamma}}, \quad \rho^* = \frac{\rho}{\rho_c}, \quad \eta^* = \frac{\eta}{\eta_c}, \quad \mu^* = \frac{\mu}{\mu_0}, \quad \mathbf{H}^* = \frac{\mathbf{H}}{H_0},$$

where H_0 is the magnitude of the externally applied magnetic field $\mathbf{H}_0$. Therefore, the governing equations (5) and (6) can be written as

$$\nabla^* \cdot \mathbf{u}^* = 0, \tag{12}$$

$$\mathrm{Re}\left(\rho^* \frac{D\mathbf{u}^*}{Dt^*}\right) = -\nabla^* p^* + \nabla^* \cdot \tau^* + 2\frac{\mathrm{Bo}_m}{\mathrm{Ca}} \nabla^* \cdot \boldsymbol{\tau}_m^* + \frac{1}{\mathrm{Ca}} \mathbf{F}_\sigma^*. \tag{13}$$

In the above equation, the superscript $(*)$ represents the nondimensional variables and Re, Ca, and Bo_m represent the Reynolds number, capillary number, and magnetic bond number respectively, which are defined as follows:

$$\mathrm{Re} = \frac{\rho_c {R_0}^2 \dot{\gamma}}{\eta_c}, \tag{14}$$

$$\mathrm{Ca} = \frac{\eta_c R_0 \dot{\gamma}}{\sigma}, \tag{15}$$

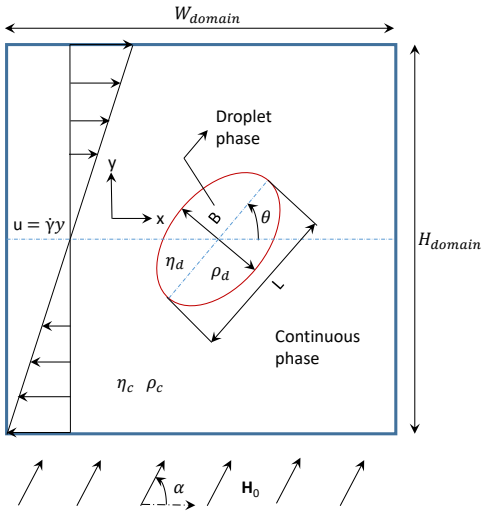

Figure 1. Schematic illustration of a ferrofluid droplet suspended in another viscous fluid in a simple shear flow under a uniform magnetic field, $\mathbf{H}_0$.

and

$$\mathrm{Bo}_m = \frac{R_0 \mu_0 {H_0}^2}{2\sigma}. \tag{16}$$

Other nondimensional groups, including the viscosity ratio λ and permeability ratio ζ are defined as follows:

$$\lambda = \frac{\eta_d}{\eta_c}, \quad \text{and} \quad \zeta = \frac{\mu_d}{\mu_0}. \tag{17}$$

Note that the ratio between Bo_m and Ca is known as the Mason number, Mn. By restricting to low Reynolds number flows ($\mathrm{Re} \lesssim 0.02$), we will mainly concentrate on the effects of Ca, Bo_m, and the direction of the magnetic field on the deformation and orientation of the droplet.

2.4. NUMERICAL MODEL

Figure 1 schematically depicts a ferrofluid droplet (with magnetic susceptibility $\chi_d = 1$) suspended in another nonmagnetic ($\chi_c = 0$) viscous fluid medium in a simple shear flow under the application of a uniform magnetic field, $\mathbf{H}_0$. The height and width of the

computational domain are $H_{domain} = W_{domain} = 10R_0$, where $R_0 = 50\ \mu$m is the radius of the initially undeformed droplet. The viscosity and density of both the phases are considered equal to each other (i.e., $\eta_c = \eta_d$) where the value of the viscosity was equal to 0.105 Pa· s. The coefficient of surface tension is considered as $\sigma = 0.0135$ N/m.

Initially, the ferrofluid droplet was placed at the center of the computational domain. The top wall moves with a velocity $\mathbf{u}_t = \frac{1}{2}\dot{\gamma}H_{domain}\mathbf{e}_x$, and the bottom wall moves with a velocity $\mathbf{u}_b = -\frac{1}{2}\dot{\gamma}H_{domain}\mathbf{e}_x$, thus resulting in a simple shear flow with the constant shear rate $\dot{\gamma}$. Periodic flow condition was applied to both the left and right walls in the x-direction. A uniform magnetic field, $\mathbf{H}_0$, was applied to the flow domain along an arbitrary direction, which is denoted by angle α. The deformed droplet is characterized by the largest and smallest dimensions, L and B, along the major-axis and minor-axis respectively. The orientation angle of the deformed droplet θ is defined as the angle measured in the counterclockwise direction from the positive x-direction to the major axis of the droplet.

2.5. GRID INDEPENDENCE TEST

We carried out a grid independence test to determine optimal mesh sizes that give accurate results while using less computational time. For this validation, the simulation used different mesh sizes and compared the deformation of the ferrofluid droplet for each case. The magnetic field was applied at 45° to the flow domain ($\alpha = 45°$). Table 1 gives different mesh sizes for the grid independence test, and Figure 2 illustrates the deformation parameter $D = \frac{L-B}{L+B}$ of the ferrofluid droplet against time for these respective mesh sizes. We used free triangular elements for creating the mesh in the domain. It can be seen that when there are greater than 26,536 elements in the flow field domain, then the results for the ferrofluid droplet deformation tend to superimpose on each other. In the remainder of this paper, we have used 42,616 elements for the flow field domain to perform numerical simulations.

Table 1. Different mesh sizes for grid independence test.

	Mesh 1	Mesh 2	Mesh 3	Mesh 4	Mesh 5	Mesh 6
Flow Field Domain	16000	19888	26536	29008	33392	42616

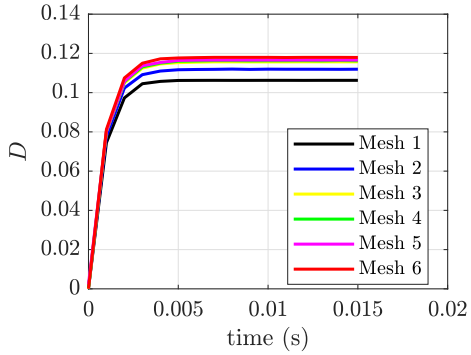

Figure 2. Grid independence test: the time evolution of deformation parameter, D of a ferrofluid droplet with different mesh settings.

3. RESULTS AND DISCUSSIONS

3.1. VALIDATION OF NUMERICAL METHOD

3.1.1. Droplet in a Simple Shear Flow. We first validated our model by simulating droplet deformation in a simple shear flow only, and compared the numerical results with existing theories in terms of deformation parameter D and orientation angle θ. According to Taylor [Taylor, 1932, 1934], the deformation parameter of a neutrally buoyant droplet suspended in another viscous fluid under simple shear at Stokes flow limit can be calculated as

$$D = \frac{L - B}{L + B} = \frac{19\eta_d + 16\eta_c}{16\eta_d + 16\eta_c}\mathrm{Ca}, \tag{18}$$

where the capillary number Ca is defined in Equation (15). Equation (18) is based on the assumption of an unbounded simple shear flow and vanishing Reynolds number. In numerical studies, however, the simple shear flow is achieved by moving two confining walls, thus giving rise to the so-called confinement effect, which is characterized by confinement

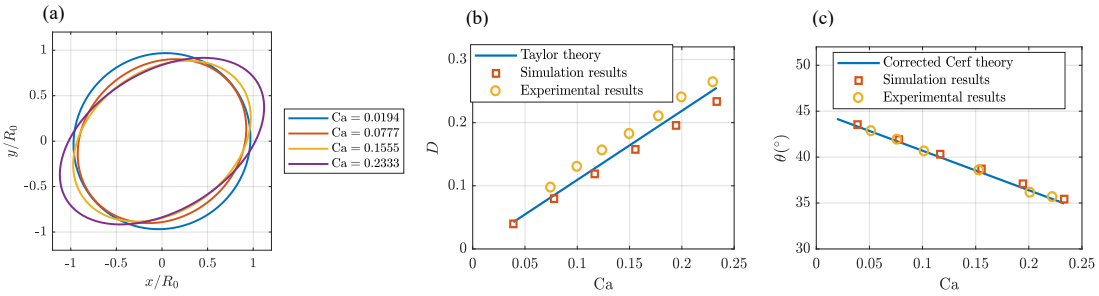

Figure 3. Droplet deformation in simple shear. (a) Outline of the droplet; (b) Comparison of simulation results against Taylor's theory [Taylor, 1932, 1934] and experimental results of Vananroye et al. [Vananroye *et al.*, 2007] , D vs Ca; and (c) Comparison of simulation results against the corrected Cerf's theory [Cerf, 1951, Roscoe, 1967] and experimental results of Vananroye et al. [Vananroye *et al.*, 2007], θ vs Ca for $\lambda = 0.3$.

ratio $\frac{2R_0}{H}$. Kennedy [Kennedy *et al.*, 1994] and Guido Guido and Villone [1998] reported that the confinement effect is negligible on the deformation of the droplet when $\frac{2R_0}{H} < 0.4$. In our model, $\frac{2R_0}{H} = 0.2$, and thus the confinement effect can be neglected.

Figure 3(a) shows the equilibrium droplet shapes under different capillary numbers. The deformation of the droplet increases with increasing Ca. Figure 3(b) represents the comparison of the simulation results with Taylor's theory and experimental results of Vananroye et al. [Vananroye *et al.*, 2007]. When Ca < 0.15, the simulation results and Taylor's theory agree very well with each other, although the experimental results slightly overestimate the values at all capillary numbers compared to the theoretical results. But, when the capillary number is large (Ca > 0.15), the difference between the numerical simulations and the theoretical prediction increases. This discrepancy could be attributed to the nature of two-dimensional simulation [Van der Sman and Van der Graaf, 2008]. Nevertheless, the numerical results are considered satisfactory since the errors are within a few percent. For example, when the capillary number was equal to 0.233, the error between the deformation of the ferrofluid droplet of the simulation results with respect to Taylor's theory was approximately 8%.

We also evaluated the orientation angle of the droplet θ for the different cases and compared our results with the corrected Cerf [Cerf, 1951, Roscoe, 1967] theory and the experiments done by Vananroye et al. [Vananroye *et al.*, 2007]. According to the theory, the orientation angle in a simple shear flow is:

$$\theta = \frac{\pi}{4} - D\frac{3+2\lambda}{5}. \tag{19}$$

In our numerical results, the orientation angle θ was found to be 43.537° and 35.424° when the capillary number was equal to 0.0388 and 0.2333, respectively. Figure 3(c) shows the comparison of orientation angle θ for different capillary numbers, Ca between simulation results, the corrected Cerf theory, and the experimental results, illustrating very good agreement with each other.

3.1.2. Droplet Deformation under a Uniform Magnetic Field in a Quiescent Flow. We further validated our model for the deformation of the ferrofluid droplet in a quiescent fluid under a uniform magnetic field. For this purpose, we used the theory provided by Afkhami et al. [Afkhami *et al.*, 2010]. According to them, the magnetic bond number Bo_m is related to the deformation of a ferrofluid droplet by the following relationship:

$$\mathrm{Bo}_m = \left(\frac{1}{\chi} + k\right)^2 \left(\frac{b}{a}\right)^{\frac{1}{3}} \left[2\frac{b}{a} - \left(\frac{b}{a}\right)^{-2} - 1\right], \tag{20}$$

where $\frac{b}{a}$ is the aspect ratio of the droplet by assuming an ellipsoidal droplet (i.e., $\frac{b}{a} = \frac{L}{B}$), and k is the demagnetizing factor:

$$k = \left(\frac{1-E^2}{2E^3}\right)\left(\ln\frac{1+E}{1-E} - 2E\right), \tag{21}$$

with E being the eccentricity of the ferrofluid droplet, which is given by

$$E = \sqrt{1 - \frac{a^2}{b^2}}. \tag{22}$$

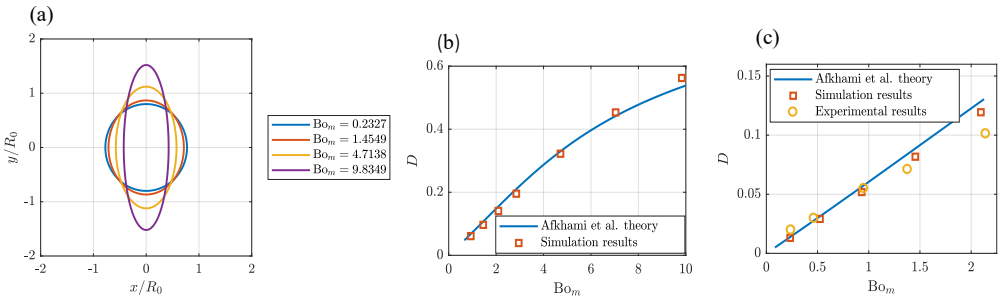

Figure 4. Deformation of a ferrofluid droplet in a uniform magnetic field. (a) Equilibrium shape of the droplet; and (b) comparison of deformation parameter, D vs Bo_m between the numerical simulation and the Afkhami et al. theory [Afkhami *et al.*, 2010]; and (c) Comparison of simulation results against the Afkhami et al. theory [Afkhami *et al.*, 2010] and experimental results[Afkhami *et al.*, 2010] for low magnetic field data with $\chi = 0.89$.

We determined the deformation of the droplet for different magnetic bond numbers from the numerical simulations. For this case, we applied the magnetic field along the y-axis (i.e., $\alpha = 90°$). Figure 4(a) indicates that with the increase in magnetic field strengths, the droplet is elongated more along the direction of magnetic field, and its steady-state shapes are approximately elliptical for Bo_m up to 10. Moreover, it can be seen from the Figure 4(b) that the simulation results agree well with the theory of Afkhami et al. for $\mathrm{Bo}_m \leq 7$. As the magnetic bond number Bo_m increases (i.e., $\mathrm{Bo}_m \approx 10$), the deformation of the droplet from our numerical simulation deviates more from the theoretical prediction. Even so, the difference between the numerical results and the theoretical prediction is within a few percent. For example, when the magnetic bond number Bo_m was equal to 9.83, the error for the ferrofluid droplet deformation parameter D between the simulation results and theory derived by Afkhami et al. was approximately 5%. One of the reasons behind this discrepancy could be that the theory is based on an axis-symmetric droplet, while we consider a two-dimensional droplet in the numerical simulation. We also compared our numerical results against the theory and experiments done by Afkhami et al. [Afkhami *et al.*, 2010] for low magnetic field data. Figure 4(c) shows that our simulation results are consistent with both theoretical results and the experimental results, except at a magnetic bond number

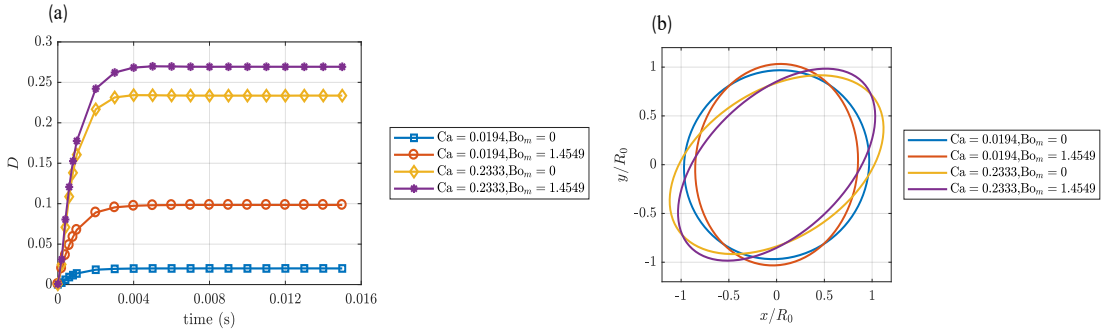

Figure 5. Effect of a perpendicular magnetic field on the deformation of a ferrofluid droplet in a simple shear flow. (a) Deformation parameter D as a function of time; (b) Outline of the droplet shape at a steady state.

$\mathrm{Bo}_m > 2$. The difference in the theoretical and simulation results with the experimental results at a magnetic bond number $\mathrm{Bo}_m > 2$ could be due to the three dimensional nature of the experiments. Nevertheless, the results show that our two-dimensional model is capable of quantitatively predicting the behavior of three-dimensional droplets and will substantially reduce computational time and allow us to investigate a wide range of parameter space.

3.2. DROPLET IN SIMPLE SHEAR FLOW WITH MAGNETIC FIELD PERPENDICULAR TO THE FLOW

When a magnetic field is applied to a ferrofluid droplet suspended in a simple shear flow, the droplet deforms due to the combined effects of the magnetic and flow fields. In this section, we first investigate the case where the magnetic field is perpendicular to the flow direction (i.e., $\alpha = 90°$) and has a field strength of $H = 2.5 \times 10^4$ A/m. Two different shear rates, $\dot{\gamma} = 50s^{-1}$ and $600s^{-1}$, are used in order to assess the effect of the magnetic field for different capillary numbers.

Figure 5 represents the effect of the magnetic field in a simple shear flow on the deformation of the ferrofluid droplet. First, the droplet takes a longer time to reach equilibrium shapes, consistent with previous findings [Jesus *et al.*, 2017]. Second, the

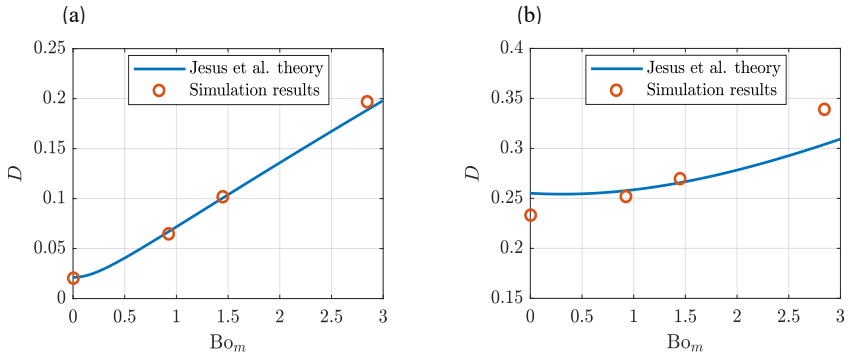

Figure 6. Comparison of simulation results against the theory given by Jesus et al. [Jesus *et al.*, 2017] of droplet deformation when $\alpha = 90°$. (a) D vs Bo_m at $\mathrm{Ca} = 0.0194$; and (b) D vs Bo_m at $\mathrm{Ca} = 0.2333$.

presence of the magnetic field tends to increase the droplet deformation, as seen in Figure 5(b). When $\mathrm{Ca} = 0.0194$, the deformation parameter of the ferrofluid droplet D under the magnetic field was found to be equal to 0.0988, which was approximately 5 times that of the deformation without a magnetic field. On the other hand, when $\mathrm{Ca} = 0.2333$, the deformation D was found to be 0.2690, which was approximately 1.2 times greater than the shear flow without the magnetic field. The reason behind this comparatively small increase in deformation at a large capillary number is the decrease in the Mason number, $\mathrm{Mn} = \mathrm{Bo}_m/\mathrm{Ca}$. The magnetic field is more dominant than the shear flow for small capillary numbers.

We also compared the deformation of the droplet with an asymptotic theory derived by Jesus et al. [Jesus *et al.*, 2017]. According to them, the deformation parameter of a ferrofluid droplet in a shear flow in the presence of a perpendicular magnetic field is given by

$$D = \frac{\sqrt{[\alpha(\lambda)\mathrm{Ca}]^2 + [\beta(\chi_d)\mathrm{Bo}_m]^2}}{2 + \frac{1}{3}\beta(\chi_d)\mathrm{Bo}_m}, \tag{23}$$

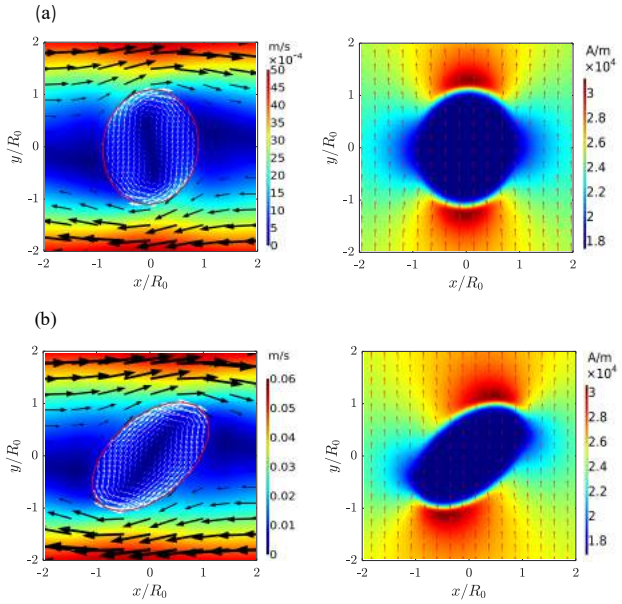

Figure 7. Velocity field and magnetic field at a steady state. (a) Ca = 0.0194, Re = 0.0015, Bo_m = 1.4549, $\alpha = 90°$; and (b) Ca = 0.2333, Re = 0.018, Bo_m = 1.4549, $\alpha = 90°$.

where $\alpha(\lambda)$ and $\beta(\chi_d)$ are functions of the viscosity ratio (λ), and the magnetic susceptibility (χ_d) of the droplet which can be written as follows:

$$\alpha(\lambda) = \frac{19\lambda + 16}{8(\lambda + 1)}, \tag{24}$$

$$\beta(\chi_d) = \frac{3\chi_d(2\chi_d + 1)}{4(\chi_d + 3)^2}. \tag{25}$$

Figure 6 shows a comparison of the droplet deformation between our numerical simulations and the asymptotic theory. It can be seen from Figure 6(a) that for a small capillary number (Ca = 0.0194), the simulation results and the theory given by Jesus et al. agree very well with each other. For the large capillary number (Ca = 0.2333), the two results show a large discrepancy with each other. This is because the theory derived by Jesus et al. is valid for small capillary numbers and low magnetic field strengths [Jesus *et al.*, 2017].

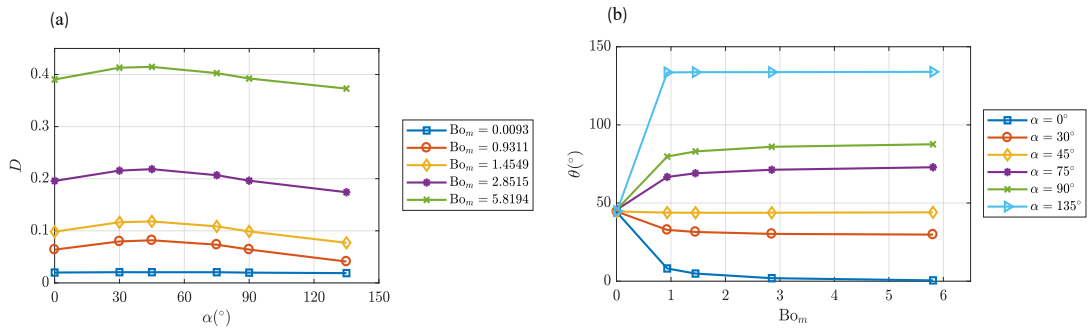

Figure 8. Effect of the magnetic field at arbitrary directions on the deformation and orientation of the droplet for Ca = 0.0194, Re = 0.0015. (a) Deformation parameter D versus α; (b) Orientation angle θ versus Bo_m.

Figure 7 presents the velocity field and magnetic field at a steady state for Ca = 0.0194, Re = 0.0015 and Ca = 0.2333, Re = 0.018 at Bo_m = 1.4549. There is circulation inside the droplet due to the surrounding flow on the outside of the ferrofluid droplet. The arrow in the velocity field plot denotes the direction of the velocity in the flow domain. The droplet experiences maximum shear stress and vorticity on the poles of the droplet. From the magnetic field plots, it is clear that the magnetic field is uniform both inside and outside of the droplet. The magnetic field lines are parallel to each other outside the droplet, while these lines are slightly deflected along the interface of the droplet. The droplet experiences maximum magnetic field strength at the interface along the poles of the droplet, while the magnetic field strength is least in magnitude along the equator of the droplet. These characteristics occur because the magnetic field is applied perpendicular to the flow domain (α = 90°), which further causes the largest ferrofluid droplet deformation along the poles of the droplet. Also, when the capillary number is low (Ca = 0.0194), the magnetic field takes control of the deformation of the droplet. As a result, the droplet tends to orient itself along the direction of the applied magnetic field.

3.3. EFFECT OF THE MAGNETIC FIELD AT ARBITRARY DIRECTIONS AT A LOW SHEAR RATE (Ca ≈ 0.02)

We now apply the magnetic field at different directions relative to the flow direction (varying $\alpha = 0°$ to $\alpha = 180°$) and examine its effects on the deformation and orientation angle of the droplet under a small shear condition (Ca = 0.0194). In the simulation, α is varied from 0 to 180° at an increment of 15°. However, for better illustration, we chose to present representative α to discuss the effect of the magnetic field on the droplet deformation and orientation. In Figure 8(a), we can see that at a lower magnetic field strength ($\mathrm{Bo}_m = 0.0093$), the deformation of the droplet seems the same no matter which direction we apply the magnetic field to the flow domain, since in this case the shear flow is dominant and it alone determines the deformation of the droplet. As we start increasing the magnetic field strength, the deformation profile of the droplet starts to change. In each case, the deformation goes on increasing and attains the maximum value when $\alpha = 45°$. This happens since the shear flow also tends to deform the droplet along 45°, and in this case, the magnetic field additionally aids the droplet to deform more along the same direction. The droplet deformation then starts decreasing as α goes on increasing and attains the minimum value at $\alpha = 135°$. This happens because we are trying to apply the magnetic field along the direction opposite to the favorable direction of the shear flow and at $\alpha = 135°$, the magnetic field direction becomes exactly opposite to the shear flow. This is why the deformation gains minimum value at this point. This is true for every case as we go on increasing the magnetic field strength up to $\mathrm{Bo}_m = 5.8194$. The deformation D increases with increasing magnetic field strength no matter the direction along which we apply the magnetic field which is due to the dominant nature of the magnetic field at a low shear rate (the Mason number, Mn, increases as we increase the magnetic field strength).

Figure 8(b) gives a clear illustration on the orientation of the droplet for different conditions. For a fixed α, the orientation of the droplet decreases as we go on increasing the magnetic field strength up to $\alpha = 45°$. This is because when the shear rate is low, as

the magnetic field strength goes on increasing, the droplet tends to align itself along the direction of the magnetic field direction. Therefore, the resultant between the direction of the shear flow and the direction of the magnetic field decreases (i.e., the orientation angle (θ) of the droplet decreases). At $\alpha = 45°$ the orientation angle θ reaches a saturation point, and at this point the orientation of the droplet is independent of the strength of the magnetic field. After that, as α increases up to 135°, the orientation angle θ of the droplet starts increasing with the increase of the magnetic field strength. The reason is due to the dominant nature of the magnetic field as a result of which the resultant between the shear flow direction and the magnetic field direction increases (i.e. the orientation angle (θ) of the droplet increases). At $\alpha = 135°$, the orientation angle reaches a saturation point again. Figure 9 represents the velocity field and the magnetic field strength at a steady state for Ca = 0.0194, Re = 0.0015, and $\mathrm{Bo}_m = 1.4549$ respectively for different values of α. These profiles give us a clear visualization about the deformation and orientation of the droplet. At $\alpha = 45°$, the magnetic field lines are trying to deform the droplet in the same direction as the shear flow direction (i.e., Deformation D becomes maximum), while at $\alpha = 135°$, the magnetic field lines are in the opposite direction of the shear flow direction, as a result of which the deformation of the droplet D attains a minimum value at this point.

3.4. EFFECT OF THE MAGNETIC FIELD AT ARBITRARY DIRECTIONS AT A HIGH SHEAR RATE (Ca ≈ 0.25)

Figure 10 represents the effect of the magnetic field at arbitrary directions on the deformation and orientation of the droplet when Ca = 0.2333 and Re = 0.018. In this case, α was varied from 0° and 180°. From Figure 10(a), it can be seen that at a lower magnetic field strength ($\mathrm{Bo}_m = 0.0093$), the deformation remains more or less the same regardless of the direction of the magnetic field, because in this case the shear flow alone takes control of the deformation and orientation of the droplet. The magnetic field has more significant influence on the ferrofluid droplet as the magnetic field strength increases (i.e., increasing

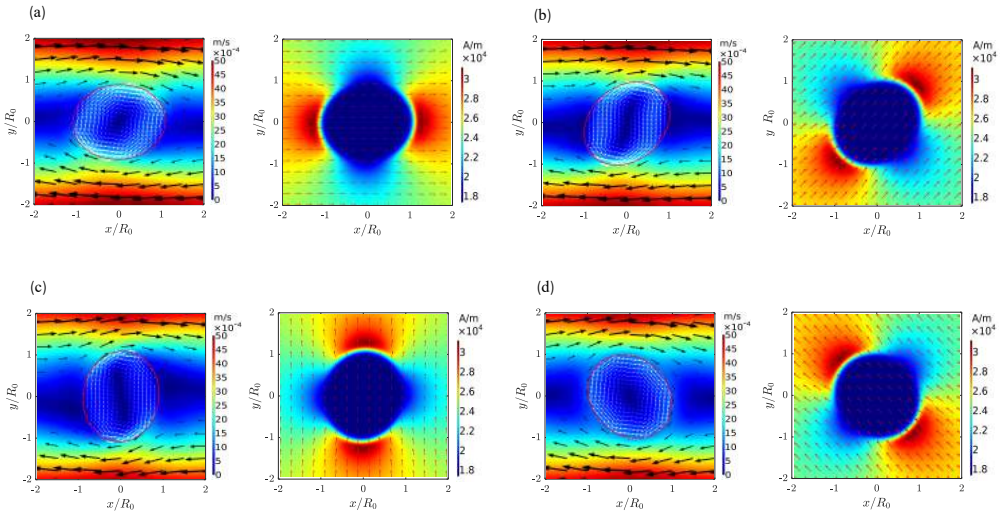

Figure 9. Velocity field and magnetic field at a steady state for Ca = 0.0194, Re = 0.0015 and Bo_m = 1.4549. (a) $\alpha = 0°$; (b) $\alpha = 45°$; (c) $\alpha = 90°$; and (d) $\alpha = 135°$.

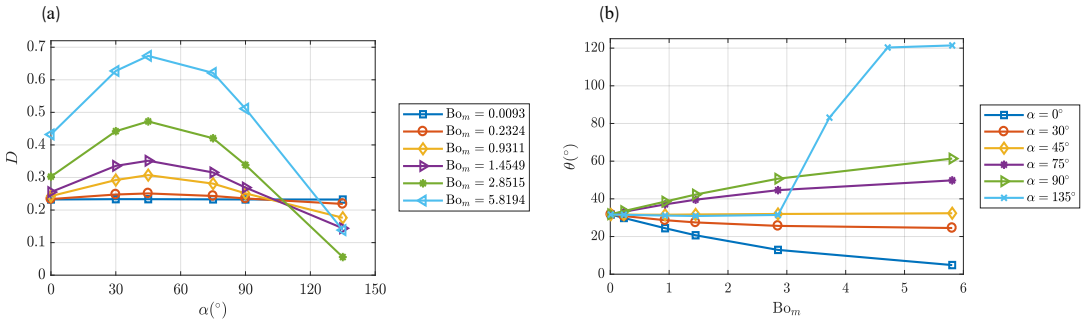

Figure 10. Effect of the magnetic field at arbitrary directions on the deformation and orientation of the droplet for Ca = 0.2333, Re = 0.018. (a) Deformation D vs α; (b) Orientation θ vs Bo_m.

Bo_m). At a fixed Bo_m, the deformation of the droplet increases and reaches a maximum value at $\alpha = 45°$, then decreases to a minimum value at $\alpha = 135°$. Such a variation could be explained by considering the “superposition" effects between the deformation due to the shear flow and deformation due to the magnetic field. Without a magnetic field, the shear flow always tends to elongate the droplet along (or nearly) 45°. On the other hand, the magnetic field always elongates the droplet along the the field direction α. As a consequence, when $\alpha = 45°$, the two effects coincide, yielding the largest deformation, while at $\alpha = 135°$, the two effects will counteract with each other, thus producing the smallest deformation.

Figure 10(b) shows the orientation of the droplet for different cases. From Figure 10(b), we can see that for $\alpha \in (5°, 45°)$ and at a fixed α, the orientation angle (θ) of the droplet decreases with an increasing magnetic bond number, Bo_m. This is because with increasing magnetic field strength, the magnetic field forces the droplet to align towards the direction of the magnetic field and therefore the resultant orientation of the droplet is decreasing due to the effect of both the magnetic field and the shear flow. Comparing these results to our low shear rate results, we can see that the orientation angle values in this case vary in a smaller range (from 10° to 50°) for the same range of magnetic bond numbers than the values at small capillary numbers (see Figure 8). This is because the shear flow has a significant effect on the orientation of the droplet at a high capillary number. At $\alpha = 45°$, the orientation angle is predominantly determined by the shear flow alone and has a value close to $\theta \approx 30°$ (similar to Figure 3(c)). As α approaches 90°, the orientation angle (θ) of the droplet increases with increasing Bo_m, which can be explained by the “superposition" effect of both the magnetic field and the shear flow. At $\alpha = 135°$, the orientation angle of the droplet seems to reach a constant value and attains similar values as $\alpha = 45°$ up to magnetic bond number, $Bo_m = 2.8515$. The slight discrepancy in the values could be due to the effect of the magnetic field strength at an opposite direction to the shear flow. But when we apply a very large magnetic field ($Bo_m > 2.8515$) at $\alpha = 135°$, a sudden jump

in the orientation angle values was observed. For example, at a magnetic bond number $\mathrm{Bo}_m = 3.7244$, the orientation angle of the droplet θ was found to be approximately 83°. The reason for this sudden change in orientation angle can be attributed to the fact that the shear flow is trying to orient the droplet along 30° (Figure 3(c)), while the magnetic field effect on the orientation of the droplet acts along 135°. As the magnetic field strength gets stronger, its effect on the orientation of the droplet becomes more dominant than the shear flow effect, resulting in a sudden jump in the orientation angle values. As a result, the orientation angle value of the droplet was found to be closer to 135° than 30° at magnetic bond number $\mathrm{Bo}_m = 5.8194$. Additionally, since the deformation of the droplet is also related to the orientation angle, the deformation of the droplet at magnetic bond number $\mathrm{Bo}_m = 5.8194$ shows different behavior than the deformation values at other magnetic bond numbers at $\alpha = 135°$, although it reaches a minimum value at that point. Figure 11 shows the corresponding velocity field and magnetic field for different values of α. It is seen that at $\alpha = 45°$, the magnetic field lines tend to deform the droplet in the same direction as the shear flow. On the other hand, at $\alpha = 135°$ the magnetic field lines are acting in an opposite direction to the shear flow, and as a result the deformation of the droplet becomes minimum at this point. Also, due to the counter-effect of the magnetic field with the flow field, the shape of the droplet becomes more rounded than elliptical in this case.

3.5. LATERAL MIGRATION OF FERROFLUID DROPLETS IN SHEAR FLOWS

In this section, we demonstrate the feasibility of controlling the lateral migration of ferrofluid droplets in the combined flow and magnetic fields. Recent studies have demonstrated a novel way to manipulate nonspherical *rigid* particles by combining a uniform magnetic field and shear flows at the microscale [Matsunaga *et al.*, 2017, Zhou *et al.*, 2017a,b]. Although uniform fields exert no forces, a nonzero magnetic torque alters the particle's rotational dynamics and influences the lateral migration of the particle via particle-wall hydrodynamic interactions. Unlike rigid particles, deformable droplets do not rotate,

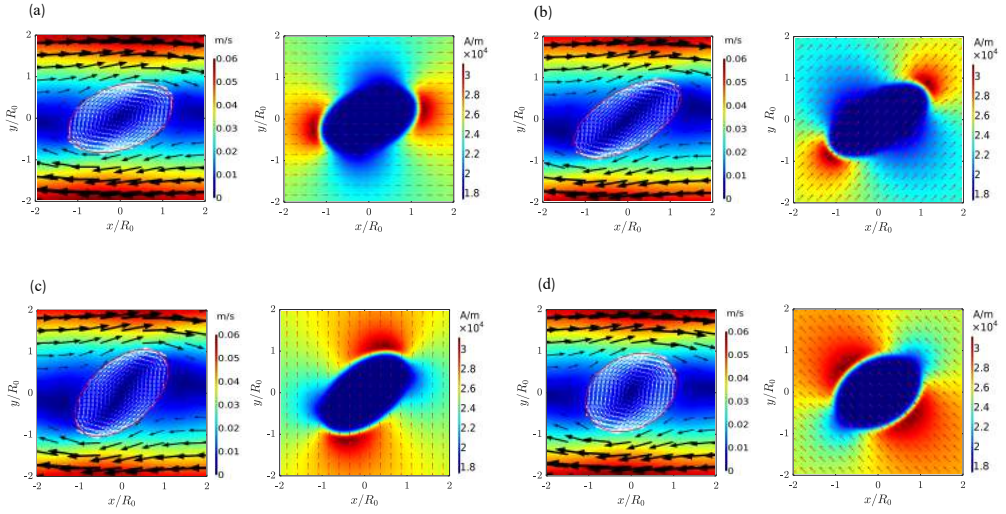

Figure 11. Velocity field and magnetic field strength at a steady state for Ca = 0.2333, Re = 0.018 and Bo_m = 1.4549. (a) $\alpha = 0°$; (b) $\alpha = 45°$; (c) $\alpha = 90°$; (d) $\alpha = 135°$.

but assume a deformed shape at an inclination angle, as seen in the previous sections. It is expected that a uniform magnetic field can effectively control the orientation angle in a similar way as for rigid particles and can influence the lateral migration.

To investigate the lateral migration behaviors, we consider the motion of the neutrally buoyant ferrofluid droplet between two plane walls with the bottom wall being fixed and the top wall moving at constant velocity, yielding a constant shear rate of 50 s^{-1}. To reduce the entrance effect, the droplet is placed far away from the left boundary, with a vertical position $y = 100\ \mu$m below the center of the flow domain. Periodic flow condition is applied to both the left and right boundaries. Keeping all other parameters and properties of the droplet and continuous phases fixed, the effect of different magnetic field strengths at two different directions, 45° and 135°, on the lateral migration of the droplet is studied.

Figure 12 shows the effect of different magnetic field strengths on the lateral migration of the droplet at a low capillary number (i.e., Ca = 0.0194). The corresponding droplet shape at different magnetic field strengths are plotted next to each case. Without a magnetic field, the droplet migrates away from the bottom wall, consistent with existing theories in

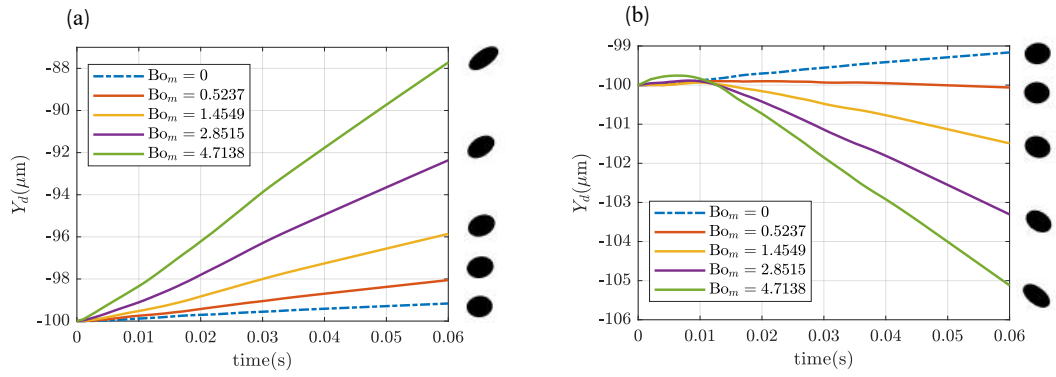

Figure 12. Effect of different magnetic field strengths on the lateral migration of the droplet at Ca = 0.0194. (a) Y_d vs time at $\alpha = 45°$; (b) Y_d vs time at $\alpha = 135°$.

the literature. With a magnetic field applied, Figure 12(a) shows that when $\alpha = 45°$, the ferrofluid droplet laterally migrates faster towards the center with increasing magnetic field strengths, while at $\alpha = 135°$ (Figure 12(b)), the droplet migrates faster towards the bottom wall. Also, at $\alpha = 45°$ the magnitude of the migration velocity of the droplet is found to be greater than at $\alpha = 135°$ for the same magnetic bond number. For example, when the magnetic bond number Bo_m was equal to 2.8515, the migration velocity of the droplet is found to be 126.92 μm/s and 74.97 μm/s at $\alpha = 45°$ and 135°, respectively. These different lateral migration behaviors of the droplet are related to the orientation and deformation of the droplet and the hydrodynamic interactions between the droplet and wall [Hiller and Kowalewski, 1986] and will be investigated in future work.

Furthermore, we experimentally demonstrate that the uniform magnetic field can control the lateral migration of ferrofluid droplets in a microchannel, which is in qualitative agreement with our numerical results. In our experiment, a microfluidic chip was fabricated with polydimethylsiloxane (PDMS) using soft-lithography method [McDonald *et al.*, 2000, Zhou and Wang, 2015]. The main microchannel had a width of 300 μm and a depth of 70 μm, and a total legth of about 14,000 μm. A uniform magnetic field was generated by a Halbach array [Raich and Blümler, 2004], which consisted of 20 cuboid permanent 0.25" ×

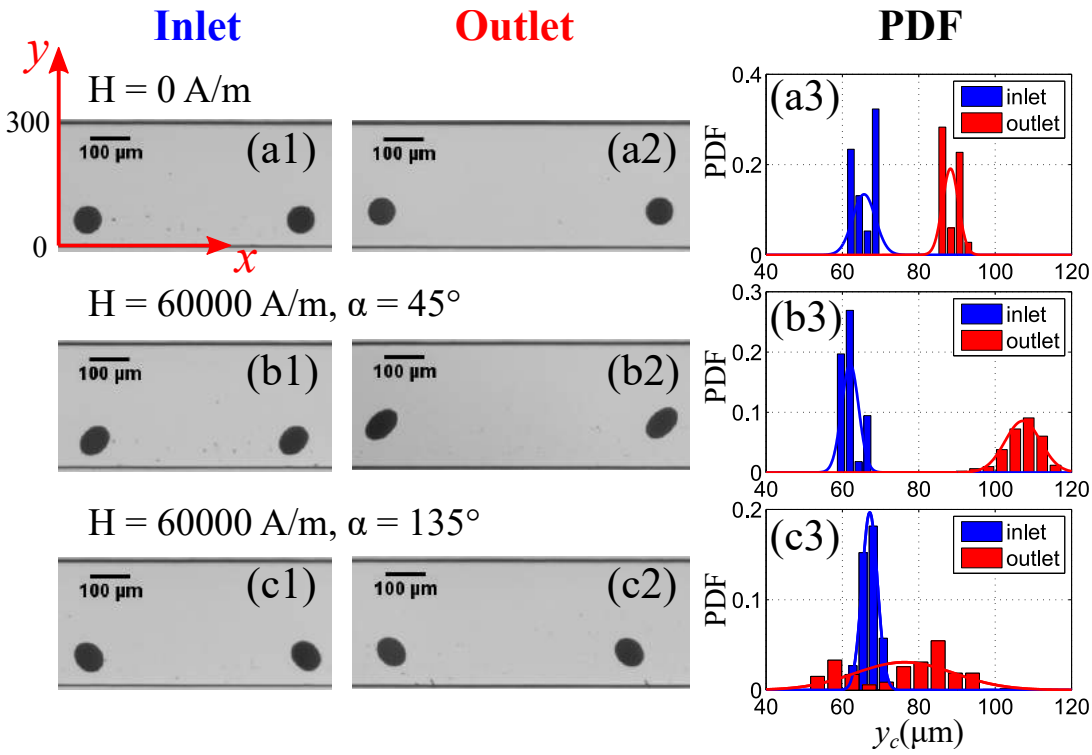

Figure 13. Images at the inlet and outlet, and the corresponding probability density function (PDF) of the ferrofluid droplet centroid in the y direction. (a1)-(a3) without applied magnetic field(H = 0 A/m); (b1)-(b3) a magnetic field (H ≈ 60,000 A/m) is applied at $\alpha = 45°$; (c1)-(c3) a magnetic field (H ≈ 60,000 A/m) is applied at $\alpha = 135°$. The total flow rate was 6 μL/min for all experiments.

0.25" × 1" magnets (K&J Magnetics, Inc.). The magnitude of the magnetic field within the central region was H ≈ 60,000 A/m measured by a gaussmeter. The EMG 304 ferrofluid (Ferrotec Corp.) work as the dispersed phase generated by a T-junction configuration and the olive oil works as the continuous phase and buffer flow. The density, viscosity and magnetic susceptibility of ferrofluids are 1.24×10^3 kg/m^3, 5×10^{-3}Pa·s and 5.03, respectively. The density, viscosity and magnetic susceptibility of olive oil are 0.92×10^3 kg/m^3, 78×10^{-3} Pa·s and 0, respectively. The total flow rate was 6 μL/min for all experiments, so the corresponding Reynolds number is 0.23. The 0.25% SPAN 80 (Sigma-Aldrich, USA) is added to olive oil to decrease interfacial tension between the olive oil and ferrofluid and

thus increase the droplet deformability. The interfacial tension after adding 0.25% SPAN 80 is measured as (10.26±0.81) mN/m using the pendant droplet method (KRUSS GmbH, USA).

Figure 13 shows the images and the probability distributions of the droplet centroid in the y direction. The average radius of droplet is 34.98 μm, so Reynolds number, capillary number and magnetic bond number of droplet is 6.18×10^{-4}, 0.0084 and 7.72, respectively. As can be seen in Figure 13(a1)-(a3), there is a little deformation of the droplet and a net lateral migration in y direction. The nonlinear velocity profile is the reason for the deformation. The inertial effect is the major reason for the net lateral migration. When the magnetic field is applied at $\alpha = 45°$ as shown in Figure 13(b1)-(b3), the droplet tend to deform in the direction of magnetic field and the degree of deformation becomes larger. The net lateral migration in y direction becomes larger compared to the result without magnetic field. When the magnetic field is applied at $\alpha = 135°$ as shown in Figure 13(c1)-(c3), the similar results for the direction and degree of droplet deformation, the net lateral migration in y direction becomes smaller compared to the result without magnetic field. The separation of magnetic droplets from non-magnetic droplets can be achieved based on this different lateral migration behaviors.

4. CONCLUSION

The influence of the magnetic field on the droplet deformation and orientation angle based on arbitrary field direction, magnetic bond number, and capillary number in a simple shear flow is systematically studied in this paper. At a small capillary number (Ca $\approx$ 0.02), the magnetic field plays a significant role and dictates the deformation and orientation of the droplet. Also, as we increase the magnetic field strength at a fixed magnetic field direction α, the deformation of the droplet increases; whereas at a fixed magnetic bond number Bo_m, the orientation angle of the droplet increases with increasing α. At a large capillary number (Ca $\approx$ 0.25), the deformation and orientation of the droplet is determined

by both the shear flow and the magnetic field. In particular, the effect of the magnetic field is substantially observed at a higher magnetic bond number, Bo_m. At a fixed α with increasing magnetic field strength, the deformation of the droplet increases up to $\alpha = 90°$ and decreases at $\alpha = 135°$, whereas the orientation angle of the droplet at a fixed Bo_m increases with increasing α up to 90°. At $\alpha = 135°$, it attains similar values as $\alpha = 45°$ except at large magnetic bond numbers (i.e., $\mathrm{Bo}_m > 2.8515$). The orientation angle values are much lower in this case compared to a low shear rate due to the dominant nature of the shear flow. In both cases, the deformation of the droplet attains a maximum value at $\alpha = 45°$ and becomes minimum at $\alpha = 135°$. Additionally, the flow field both inside and outside of the droplet are modified according to the deformation and orientation of the droplet. We also investigated the lateral migration of the ferrofluid droplet in wall-bounded shear flows in the presence of a magnetic field, both numerically and experimentally, and found that at $\alpha = 45°$, the droplet migrates towards the center of the domain, while at $\alpha = 135°$, the droplet migrates towards the wall. The magnitude of the migration velocity was also found to increase with increasing magnetic field strength. The different lateral migration behaviors of the droplet provide a simple but an effective way to separate ferrofluid droplets from nonmagnetic droplets at microscale.

ACKNOWLEDGMENTS

The authors gratefully acknowledge the financial support from the Department of Mechanical and Aerospace Engineering (MAE) and the Center for Biomedical Research (CBR) at Missouri University of Science and Technology.

REFERENCES

Afkhami, S., Renardy, Y., Renardy, M., Riffle, J. S., and Pierre, T. G. S., 'Field-induced motion of ferrofluid droplets through immiscible viscous media,' J. Fluid Mech., 2008, **610**, pp. 363–380.

Afkhami, S., Tyler, A., Renardy, Y., Renardy, M., Pierre, T. S., Woodward, R., and Riffle, J. S., 'Deformation of a hydrophobic ferrofluid droplet suspended in a viscous medium under uniform magnetic fields,' Journal of Fluid Mechanics, 2010, **663**, pp. 358–384.

Ansari, M., Hadidi, A., and Nimvari, M., 'Effect of a uniform magnetic field on dielectric two-phase bubbly flows using the level set method,' J. Magn. Magn. Mater., 2012, **324**(23), pp. 4094–4101.

Bacri, J.-C., Salin, D., and Massart, R., 'Study of the deformation of ferrofluid droplets in a magnetic field,' J. Phys. Lett-paris., 1982, **43**(6), pp. 179–184.

Barthes-Biesel, D. and Acrivos, A., 'Deformation and burst of a liquid droplet freely suspended in a linear shear field,' Journal of Fluid Mechanics, 1973, **61**(1), pp. 1–22.

Cerf, R., 'Recherches théoriques et expérimentales sur l'effet maxwell des solutions de macromolécules déformables,' Journal de Chimie Physique, 1951, **48**, pp. 59–84.

COMSOL, *CFD Module Application Library Manual*, 5.3a edition, 2018.

Debruijn, R. A., *Deformation and breakup of drops in simple shear flows*, Ph.D. thesis, AA(Technische Univ., Eindhoven (Netherlands), 1991.

Dikansky, Y. I., Tyatyushkin, A. N., and Zakinyan, A. R., 'Anisotropy of magnetic emulsions induced by magnetic and electric fields,' Phys. Rev. E, 2011, **8**(3), pp. 031402–031402.

Feigl, K., Megias-Alguacil, D., Fischer, P., and Windhab, E. J., 'Simulation and experiments of droplet deformation and orientation in simple shear flow with surfactants,' Chem. Eng. Sci., 2007, **62**(12), pp. 3242–3258.

Ghaffari, A., Hashemabadi, S. H., and Bazmi, M., 'Cfd simulation of equilibrium shape and coalescence of ferrofluid droplets subjected to uniform magnetic field,' Colloids Surf., A, 2015, **481**, pp. 186–198.

Griggs, A. J., Zinchenko, A. Z., and Davis, R. H., 'Low-Reynolds-number motion of a deformable drop between two parallel plane walls,' Int. J. Multiph. Flow, 2007, **33**(2), pp. 182–206, ISSN 0301-9322, doi: 10.1016/J.IJMULTIPHASEFLOW.2006.06.012.

Guido, S. and Villone, M., 'Three-dimensional shape of a drop under simple shear flow,' Journal of Rheology, 1998, **42**(2), pp. 395–415.

Hiller, W. and Kowalewski, T., 'An experimental study of the lateral migration of a droplet in a creeping flow,' Exp. Fluids, 1986, **5**(1), pp. 43–48.

Jesus, W. C., Roma, A. M., and Ceniceros, H. D., 'Deformation of a sheared magnetic droplet in a viscous fluid,' Commun. Comput. Phys, 2017.

Kennedy, M., Pozrikidis, C., and Skalak, R., 'Motion and deformation of liquid drops, and the rheology of dilute emulsions in simple shear flow,' Computers & fluids, 1994, **23**(2), pp. 251–278.

Korlie, M. S., Mukherjee, A., Nita, B. G., Stevens, J. G., Trubatch, A. D., and Yecko, P., 'Modeling bubbles and droplets in magnetic fluids,' J. Phys.: Condens. Matter, 2008, **20**(20), p. 204143.

Lamura, A., Gonnella, G., and Yeomans, J., 'A lattice boltzmann model of ternary fluid mixtures,' EPL (Europhysics Letters), 1999, **45**(3), p. 314.

Li, J., Renardy, Y. Y., and Renardy, M., 'Numerical simulation of breakup of a viscous drop in simple shear flow through a volume-of-fluid method,' Physics of Fluids, 2000, **12**(2), pp. 269–282.

Liu, J., Yap, Y. F., and Nguyen, N.-T., 'Numerical study of the formation process of ferrofluid droplets,' Phys. Fluids, 2011, **23**(7), p. 072008.

Maehlmann, S. and Papageorgiou, D. T., 'Numerical study of electric field effects on the deformation of two-dimensional liquid drops in simple shear flow at arbitrary reynolds number,' J. Fluid Mech., 2009, **626**, pp. 367–393.

Mandal, S., Bandopadhyay, A., and Chakraborty, S., 'The effect of uniform electric field on the cross-stream migration of a drop in plane poiseuille flow,' J. Fluid Mech., 2016, **809**, pp. 726–774.

Mandal, S. and Chakraborty, S., 'Effect of uniform electric field on the drop deformation in simple shear flow and emulsion shear rheology,' Phys. Fluids, 2017, **29**(7), p. 072109.

Matsunaga, D., Meng, F., Zöttl, A., Golestanian, R., and Yeomans, J. M., 'Focusing and sorting of ellipsoidal magnetic particles in microchannels,' Phys. Rev. Lett., 2017, **119**, p. 198002, doi:10.1103/PhysRevLett.119.198002.

McDonald, J. C., Duffy, D. C., Anderson, J. R., Chiu, D. T., Wu, H., Schueller, O. J., and Whitesides, G. M., 'Fabrication of microfluidic systems in poly (dimethylsiloxane),' ELECTROPHORESIS: An International Journal, 2000, **21**(1), pp. 27–40.

Mefford, O. T., Woodward, R. C., Goff, J. D., Vadala, T., Pierre, T. G. S., Dailey, J. P., and Riffle, J. S., 'Field-induced motion of ferrofluids through immiscible viscous media: Testbed for restorative treatment of retinal detachment,' Journal of Magnetism and Magnetic Materials, 2007, **311**(1), pp. 347–353.

Mosbach, K. and Andersson, L., 'Magnetic ferrofluids for preparation of magnetic polymers and their application in affinity chromatography,' Nature, 1977, **270**(5634), p. 259.

Olsson, E. and Kreiss, G., 'A conservative level set method for two phase flow,' Journal of computational physics, 2005, **210**(1), pp. 225–246.

Osher, S. and Fedkiw, R. P., 'Level set methods: An overview and some recent results,' J. Comput. Phys., 2001, **169**(2), pp. 463–502, ISSN 0021-9991.

Raich, H. and Blümler, P., 'Design and construction of a dipolar halbach array with a homogeneous field from identical bar magnets: Nmr mandhalas,' Concepts in Magnetic Resonance Part B: Magnetic Resonance Engineering: An Educational Journal, 2004, **23**(1), pp. 16–25.

Rallison, J., 'The deformation of small viscous drops and bubbles in shear flows,' Annual review of fluid mechanics, 1984, **16**(1), pp. 45–66.

Roscoe, R., 'On the rheology of a suspension of viscoelastic spheres in a viscous liquid,' J. Fluid Mech., 1967, **28**(2), pp. 273–293.

Rosensweig, R. E., *Ferrohydrodynamics*, Cambridge University Press, 1985.

Rumscheidt, F. and Mason, S., 'Particle motions in sheared suspensions xi. internal circulation in fluid droplets (experimental),' Journal of Colloid Science, 1961, **16**(3), pp. 210–237.

Shi, D., Bi, Q., and Zhou, R., 'Numerical simulation of a falling ferrofluid droplet in a uniform magnetic field by the voset method,' Numerical Heat Transfer, Part A: Applications, 2014, **66**(2), pp. 144–164.

Sibillo, V., Pasquariello, G., Simeone, M., Cristini, V., and Guido, S., 'Drop deformation in microconfined shear flow,' Phys. Rev. Lett., 2006, **97**(5), p. 054502.

Stone, H. A., 'Dynamics of drop deformation and breakup in viscous fluids,' Annual Review of Fluid Mechanics, 1994, **26**(1), pp. 65–102.

Stone, H. A., Lister, J. R., and Brenner, M. P., 'Drops with conical ends in electric and magnetic fields,' Proceedings of the Royal Society of London. Series A: Mathematical, Physical and Engineering Sciences, 1999, **455**(1981), pp. 329–347.

Stratton, J. A., *Electromagnetic theory*, volume 33, John Wiley & Sons, 2007.

Tan, S.-H., Nguyen, N.-T., Yobas, L., and Kang, T. G., 'Formation and manipulation of ferrofluid droplets at a microfluidic t-junction,' Journal of Micromechanics and Microengineering, 2010, **20**(4), p. 045004.

Taylor, G. I., 'The viscosity of a fluid containing small drops of another fluid,' Proceedings of the Royal Society of London. Series A, Containing Papers of a Mathematical and Physical Character, 1932, **138**(834), pp. 41–48.

Taylor, G. I., 'The formation of emulsions in definable fields of flow,' Proceedings of the Royal Society of London. Series A, containing papers of a mathematical and physical character, 1934, **146**(858), pp. 501–523.

Van der Sman, R. and Van der Graaf, S., 'Diffuse interface model of surfactant adsorption onto flat and droplet interfaces,' Rheol. Acta, 2006, **46**(1), pp. 3–11.

Van der Sman, R. and Van der Graaf, S., 'Emulsion droplet deformation and breakup with lattice boltzmann model,' Computer Physics Communications, 2008, **178**(7), pp. 492–504.

Van Der Sman, R., van Der Graaf, S., and Gijsbertsen-Abrahamse, A., '2-d droplet deformation and breakup with lattice boltzmann model,' WIT Trans. Eng. Sci., 2003, **42**.

Vananroye, A., Van Puyvelde, P., and Moldenaers, P., 'Effect of confinement on the steady-state behavior of single droplets during shear flow,' Journal of rheology, 2007, **51**(1), pp. 139–153.

Varma, V. B., Ray, A., Wang, Z. M., Wang, Z. P., and Ramanujan, R. V., 'Droplet merging on a lab-on-a-chip platform by uniform magnetic fields,' Scientific reports, 2016, **6**, p. 37671.

Vlahovska, P. M., 'On the rheology of a dilute emulsion in a uniform electric field,' J. Fluid Mech., 2011, **670**, pp. 481–503.

Wu, Y., Fu, T., Ma, Y., and Li, H. Z., 'Ferrofluid droplet formation and breakup dynamics in a microfluidic flow-focusing device,' Soft Matter, 2013, **9**(41), pp. 9792–9798.

Xi, H. and Duncan, C., 'Lattice boltzmann simulations of three-dimensional single droplet deformation and breakup under simple shear flow,' Phys. Rev. E, 1999, **59**(3), p. 3022.

Yue, P., Feng, J. J., Liu, C., and Shen, J., 'A diffuse-interface method for simulating two-phase flows of complex fluids,' J. Fluid Mech., 2004, **515**, pp. 293–317.

Zakinyan, A. and Dikansky, Y., 'Drops deformation and magnetic permeability of a ferrofluid emulsion,' Colloids Surf., A, 2011, **380**(1-3), pp. 314–318, ISSN 0927-7757.

Zakinyan, A., Dikansky, Y., and Bedzhanyan, M., 'Electrical properties of chain microstructure magnetic emulsions in magnetic field,' J. Disper. Sci. Technol., 2014, **35**(1), pp. 111–119.

Zhang, Q., Li, H., Zhu, C., Fu, T., Ma, Y., and Li, H. Z., 'Micro-magnetofluidics of ferrofluid droplet formation in a T-junction,' Colloids Surfaces A Physicochem. Eng. Asp., 2018, **537**, pp. 572–579, ISSN 18734359, doi:10.1016/j.colsurfa.2017.10.056.

Zhou, R., Bai, F., and Wang, C., 'Magnetic separation of microparticles by shape,' Lab. Chip, 2017a, **17**(3), pp. 401–406.

Zhou, R., Sobecki, C. A., Zhang, J., Zhang, Y., and Wang, C., 'Magnetic control of lateral migration of ellipsoidal microparticles in microscale flows,' Phys. Rev. Appl, 2017b, **8**(2), p. 024019.

Zhou, R. and Wang, C., 'Acoustic bubble enhanced pinched flow fractionation for microparticle separation,' Journal of Micromechanics and Microengineering, 2015, **25**(8), p. 084005.

Zhu, G.-P., Nguyen, N.-T., Ramanujan, R. V., and Huang, X.-Y., 'Nonlinear deformation of a ferrofluid droplet in a uniform magnetic field,' Langmuir, 2011, **27**(24), pp. 14834–14841.

II. MAGNETIC FIELD INDUCED FERROFLUID DROPLET BREAKUP IN A SIMPLE SHEAR FLOW AT A LOW REYNOLDS NUMBER

Md Rifat Hassan and Cheng Wang
Department of Mechanical & Aerospace Engineering
Missouri University of Science and Technology
Rolla, Missouri 65409
Tel: 573–341–4636, Fax: 573–341–4607
Email: wancheng@mst.edu

ABSTRACT

The breakup phenomenon of a ferrofluid droplet in a simple shear flow under a uniform magnetic field is numerically investigated in this paper. The numerical simulation, based on the finite element method, uses a level set method to capture the dynamic evolution of the droplet interface between the two phases. Focusing on small Reynolds numbers (i.e., $\mathrm{Re} \leq 0.03$), systematic numerical simulations are carried out to analyze the effects of magnetic field strength, direction, and viscosity ratio on the breakup phenomenon of the ferrofluid droplet. The results suggest that applying a magnetic field along $\alpha = 45^\circ$ and 90° relative to the flow direction initiates breakup in a ferrofluid droplet at a low capillary number in the Stokes flow regime, where the droplet usually does not break up in a shear flow alone. At $\alpha = 0^\circ$ and 135°, the magnetic field suppresses breakup. Also, there exists a critical magnetic bond number, Bo_{cr}, below which the droplet does not rupture, which is also dependent on the direction of the magnetic field. Additionally, the effect of the viscosity ratio on the droplet breakup is examined at variable magnetic bond numbers. The results indicate a decrease in the critical magnetic bond number Bo_{cr} values for more viscous droplets. Furthermore, more satellite droplets are observed at $\alpha = 45^\circ$ compared to $\alpha = 90^\circ$, not only at higher magnetic field strengths but also at larger viscosity ratios.

Keywords: Magnetic fields, Magnetic fluids, Drop breakup, Computer simulation

1. INTRODUCTION

Droplet dispersion in another immiscible liquid is commonly experienced in a number of industrial applications that deal with cosmetics, food processing [McClements, 2015], pharmaceutical design [Nielloud, 2000], and polymer processing [Garstecki *et al.*, 2005, Han, 2012, Larson, 1999]. Most of these applications utilize highly concentrated emulsions, where the morphology of the dispersed phase component plays a crucial role in determining the physical and rheological properties of the emulsions. Consequently, these drop sizes become a key to the design of processing equipment for a certain emulsion properties and conditions, which is often complicated by the interplay between the flow field and fluid components behavior [Loewenberg and Hinch, 1996, Vananroye *et al.*, 2006b].

When a droplet is subjected to shear flows, it deforms. Moreover, if the flow field exceeds a specific critical value, the droplet ruptures and gives rise to daughter droplets via a process called “elongative end pinching", which also reduces the mean size of the droplets [Bentley and Leal, 1986]. Smaller sized droplets, having a larger total interfacial area, produce more stable emulsions and are considered as a fundamental scaling parameter for a number of mass transfer and chemical reactions [Jansen *et al.*, 2001]. In the existing literature [Debruijn, 1991], three different droplet breakup mechanisms (i.e., binary breakup, capillary breakup, and tipstreaming) are studied, but in this study we will restrict ourselves to binary breakup in a simple shear flow.

In binary breakup, the behavior of an isolated drop is mainly governed by two dimensionless numbers: The first one is known as the Capillary number Ca, which denotes the competition between two forces: the viscous shear stress of the continuous phase $\eta_c\dot{\gamma}$, which causes deformation, and the Laplace pressure σ/R_0, which resists deformation, where η_c, $\dot{\gamma}$, σ, and R_0 represent the continuous phase viscosity, shear rate, interfacial tension, and initial radius of the droplet, respectively. The second one is the viscosity ratio $\lambda = \eta_d/\eta_c$, where η_d denotes the viscosity of the droplet phase. There exists a critical capillary number, Ca_{cr}, above which the droplet ruptures, and from the experimental analysis of Grace [Grace,

1982] it is realized that this critical capillary number is strongly dependent on the viscosity ratio (i.e., $Ca_{cr} = f(\lambda)$). The results show that an isolated droplet experiences rotational motion in a simple shear flow, which eventually prevents the droplet from breakup at a higher viscosity ratio (i.e., $\lambda = 3.8$). Rumscheidt et al. [Rumscheidt and Mason, 1961] also found that at $\lambda > 4$, the droplet initially tumbles and eventually turns into an ellipsoidal shape, aligned with the flow direction.

Following the pioneering work of Taylor [Taylor, 1932, 1934], several numerical and theoretical investigations have been conducted to analyze droplet breakup in emulsification and mixing [Feigl *et al.*, 2016, Fu *et al.*, 2017, Mason and Bibette, 1997, Scarbolo *et al.*, 2015, Stone, 1994]. Li et al. [Li *et al.*, 2000] performed a numerical simulation on the breakup mechanism of a viscous droplet in a simple shear flow and found that it is possible to induce droplet breakup at a low capillary number in Stokes flow with an increased Reynolds number. Debruijn [Debruijn, 1991] built a Couette device with an aim to investigate the breakup phenomena of non-Newtonian droplets in a quasi-steady simple shear flow. Barthes-Biesel et al. [Barthes-Biesel and Acrivos, 1973] studied the breakup conditions of a liquid droplet freely suspended in a linear shear field and observed that the droplet yields a burst criterion for λ ranging between 0.1 and 3.6. De Menech [De Menech, 2006] numerically examined droplet breakup in a three dimensional T-shaped junction and observed that the critical capillary number at which the droplet experiences breakup, is related to the viscosity ratio. Also, a two-dimensional numerical study on droplet deformation and breakup has been performed by Van der Sman and Van der Graaf [Van der Sman and Van der Graaf, 2008] using Lattice Boltzmann model.

In experimental analyses, breakup of a solitary drop is usually investigated either by direct observation of a droplet in a flow field or by observing the change in droplet size distribution. Sibilo et al. [Sibillo *et al.*, 2004] studied the effect of matrix elasticity on the breakup of an isolated Newtonian drop in a shear flow and concluded that matrix elasticity hinders breakup in a droplet. Vananroye et al. [Vananroye *et al.*, 2006a] conducted experi-

ments on droplet breakup in sheared emulsions and found that even at $\lambda > 4$, it is possible to induce breakup in droplets by applying a shear field to a larger confinement. Furthermore, an experimental study on the droplet formation and breakup in a microfluidic T-junction has been done by Garstecki et al. [Garstecki *et al.*, 2006] and Leshansky et al. [Leshansky and Pismen, 2009].

In addition to hydrodynamic forces, external force fields (i.e., electric or magnetic fields) can also manipulate the overall rheology of the droplets [Jackson *et al.*, 2017, Sherwood, 1988]. Taylor [Taylor, 1964] performed both theoretical and experimental investigation on the disintegration of water droplets in an electric field, while Collins et al. [Collins *et al.*, 2008] performed simulations and experiments to investigate the mechanisms of cone formation, jet emission, and breakup of charged drops under the presence of an electric field. Also, the deformation and breakup of aqueous drops under large electric fields have been experimentally investigated by Eow et al. [Eow and Ghadiri, 2003], which shows that initial drop sizes greatly influence the magnitude of the electric field strength for the onset of droplet stability. Interestingly, instead of using electric and magnetic fields as an external means of manipulation, an alternative algorithm approach based on logic operations has been adopted to control droplets in a parallel manner by Katsikis et al. [Katsikis *et al.*, 2015]. Moreover, an excellent experimental study on the manipulation of droplets under electric fields in microfluidic devices has been performed by Link et al. [Link *et al.*, 2006].

Magnetic field can also be used to manipulate the shape of a droplet [Ahmed *et al.*, 2018]; however, magnetic manipulation requires either the droplet or continuous phase to be a ferrofluid — a dispersion of magnetic nanoparticles (diameter typically around 10 nm and volume fraction about 5%). Due to the presence of magnetic properties, additional Maxwell stresses occur at the fluid-fluid interface in addition to the hydrodynamic stresses. Ferrofluid droplets involved in multiphase flows have notable biomedical applications in the treatment of retinal detachment [Mefford *et al.*, 2007], and the ease of both integration and flexibility of operation render a magnetic field as a popular means of droplet manipulation

in microfluidic devices. Banarjee et al. [Banerjee *et al.*, 1999] investigated the behavior of confined ferrofluid droplets under weak magnetic fields, applied in a direction parallel to the direction of the computational domain. Varma et al. [Varma *et al.*, 2016] experimentally studied the merging of ferrofluid droplets under uniform magnetic fields on a Lab-on-a-Chip platform, and also developed a micro-magnetofluidics numerical model to explain the ferrofluid droplets behavior in both uniform and hybrid magnetic fields [Varma, 2017]. Also, an investigation on the manipulation of ferrofluid droplets by a permanent magnetic field has been carried out by Ray et al. [Ray *et al.*, 2017]. Moreover, a thorough analysis on the controlled deformation and orientation of a ferrofluid droplet in a simple shear flow by means of an uniform magnetic field is presented in our recent work [Hassan *et al.*, 2018].

However, the existing studies in the literature are mainly focused on the breakup of droplets in external flow conditions [Acrivos, 1983, Grace, 1982, Rallison, 1984]. Recently, Cunha et al. [Cunha *et al.*, 2018] numerically studied magnetic field induced droplet breakup in shear flows at a higher Reynolds number (i.e., Re = 1). Their results suggest that when a magnetic field acts in a direction parallel to the direction of the flow field, it delays the breakup process and reduces the size of the satellite droplets. Instead, if the magnetic field is applied in a direction perpendicular to the flow direction, the droplet breakup can be induced, delayed or even prevented through some adjustments in magnetic field intensities. But until now, as per our knowledge, no one has ever studied the breakup mechanism of a droplet in a Stokes flow at low capillary numbers (where droplet usually does not breakup) under the effect of magnetic fields, which is more applicable to a range of different microfluidics applications [Guo *et al.*, 2012, Rosenfeld *et al.*, 2014, Squires and Quake, 2005, Stone *et al.*, 2004, Tice *et al.*, 2004]. Also, a comprehensive study on the effect of viscosity ratio on droplet breakup in shear flows under a uniform magnetic field is missing in the literature. Therefore, in this paper, we focus on investigating the effect of a uniform magnetic field on the droplet breakup phenomenon at Stokes flow limit in a simple shear flow along some specific directions. Here, a two-dimensional (2D) simulation model is

Table 1. Properties of fluid phases.

Parameter	Symbol	Value	Unit
Density of droplet phase	ρ_d	1260	kg/m^3
Viscosity of droplet phase	η_d	0.105	Pa·s
Interfacial tension	σ	0.0135	N/m

chosen in order to study a wide range of parameters, including magnetic field strength, direction, and viscosity ratio. Prior studies show that 2D numerical models are capable of qualitatively and correctly capturing the deformation of a ferrofluid droplet under a uniform magnetic field with great computational efficiency [Hassan *et al.*, 2018, Shi *et al.*, 2014]. Our numerical model, based on a commercial FEM solver, is implemented to model the droplet interface by using the level set method and coupling the magnetic and flow fields.

The rest of the paper is categorized as follows: the numerical model is described in Sec. 2. In Sec. 3, we present the numerical and mathematical methods that are required to solve our computational model. In Sec. 4, we first validate our results against the existing theories in literature and then examine the effect of magnetic field strength and viscosity ratio on the droplet breakup phenomenon at different magnetic field directions. Finally, the major findings are summed up in Sec. 5.

2. NUMERICAL MODEL

Figure 1 depicts the motion of a viscous, neutrally buoyant ferrofluid droplet dispersed in another viscous fluid medium, bounded by two plane walls translating in opposite directions and subjected to a uniform magnetic field, $\mathbf{H}_0$. Initially, the density and viscosity of both the phases are treated equal to each other (i.e., $\rho_c = \rho_d$ and $\eta_c = \eta_d$). The magnetic susceptibility of the ferrofluid droplet is considered as 1 ($\chi_d = 1$), while the continuous phase is treated as a non magnetic fluid medium ($\chi_c = 0$). The magnitude of the coefficient of the interfacial tension σ is considered equal to 0.0135 N/m.

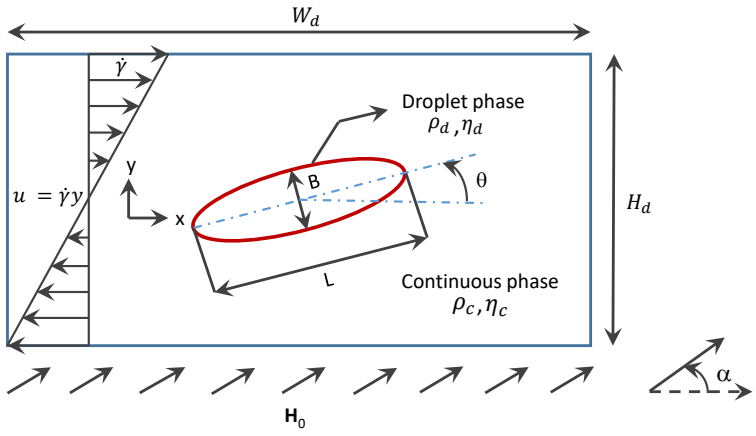

Figure 1. Schematic of the computational domain, including a ferrofluid droplet dispersed in another fluid medium in a simple shear flow subjected to a uniform magnetic field, $\mathbf{H}_0$.

Placing the ferrofluid droplet initially at the center, a simple shear flow with a constant shear $\dot{\gamma}$ is generated by moving the top wall of the computational domain with a velocity $\mathbf{u}_t = \frac{1}{2}\dot{\gamma}H_d\mathbf{e}_x$, while the bottom wall of the domain moves with a velocity of the same magnitude as the top wall, but in the opposite direction (i.e., $\mathbf{u}_b = -\frac{1}{2}\dot{\gamma}H_d\mathbf{e}_x$). The velocity is continuous at the interface of the droplet; although, the surface force experiences a discontinuity at the droplet interface due to the surface tension effect. The droplet also experiences a symmetric flow field with respect its initial position, while the velocity is zero along the center line of the flow domain. In order to simulate infinite periodicity in the x-direction, a periodic flow condition is implemented not only at the left wall, but also at the right wall of the flow domain. The application of a uniform magnetic field, $\mathbf{H}_0$, along different directions to the flow domain is denoted by angle α. When the droplet undergoes deformation, the deformation is determined using the largest major-axis and smallest minor-axis dimensions, which are denoted by L and B, respectively. The orientation angle, defined by θ, is measured as the angle between the positive x-direction and the major axis of the droplet in a counterclockwise direction.

3. NUMERICAL SIMULATION METHOD

3.1. LEVEL SET METHOD

In the study of droplet motion in a shear induced flow, most of the problems arise in tracking the free interface of the droplet, which moves to different locations following severe deformation including breakup. Therefore, in our model, an Euler approach based conservative level set method is implemented to solve the dynamically evolving droplet interface between the two fluid phases. The level set method uses a smeared Heaviside scalar function ϕ to distinguish the two fluid phases, and the value of ϕ undergoes a smooth transition between 0 and 1 across the interface. In the droplet phase, the value of ϕ is considered as 1, while it is zero in the continuous phase. The interface of the droplet is defined by the 0.5 isocontour of ϕ. The level set function ϕ moves with the velocity of fluid $\mathbf{u}$ through the following equation [COMSOL, 2018]:

$$\frac{d\phi}{dt} + \mathbf{u} \cdot \nabla\phi = \gamma \nabla \cdot \left(\epsilon \nabla\phi - \phi(1-\phi) \frac{\nabla\phi}{|\nabla\phi|} \right), \tag{1}$$

In the above equation, ϵ is a parameter used to define the droplet interface thickness, and its magnitude equals half the largest mesh size of the region passed by the droplet in the domain. However, during the pinching stage, when the value of ϵ encounters a mesh size less than half of the largest mesh size in the pinching region, it fails to resolve the interface of the droplet and eventually initiates a breakup in the middle. In our study, the magnitude of the largest mesh element size is considered equal to 4% of the diameter of the droplet, and using a mesh size lower than 4% of the droplet diameter generates a similar type of breakup phenomenon with reasonably identical shaped droplets; although, a slight increase in the breakup time is observed with the decrease in the largest mesh size. On the other hand, the re-initialization parameter γ needs a careful tuning for specific problems since too small or too high values of γ can give rise to numerical instabilities and incorrect interface, respectively. In general, the maximum magnitude of the velocity observed in the

flow domain is considered as an optimum value for the re-initialization parameter γ. Also, the unit normal to the interface $\mathbf{n}$ can be calculated using the level set function as

$$\mathbf{n} = \frac{\nabla \phi}{|\nabla \phi|}. \tag{2}$$

The level set method usually considers the multi-phase flows as a single phase flow, where the level set value ϕ smooths the jump of different parameters, such as density (ρ), magnetic permeability (μ), dynamic viscosity (η), and magnetic susceptibility (χ) across the droplet interface through the following equations:

$$\rho = \rho_c + (\rho_d - \rho_c)\phi, \qquad \mu = \mu_c + (\mu_d - \mu_c)\phi, \tag{3}$$

$$\eta = \eta_c + (\eta_d - \eta_c)\phi, \qquad \chi = \chi_c + (\chi_d - \chi_c)\phi, \tag{4}$$

where the continuous phase and droplet phase are represented by the subscripts c and d, respectively.

3.2. GOVERNING EQUATIONS

The incompressible laminar fluid flow motion, involving a viscous ferrofluid droplet suspended in another viscous fluid, can be described by the time-dependent Navier-Stokes equations, which are defined as follows:

$$\nabla \cdot \mathbf{u} = 0, \tag{5}$$

and

$$\rho \left(\frac{\partial \mathbf{u}}{\partial t} + \mathbf{u} \cdot \nabla \mathbf{u} \right) = -\nabla p + \nabla \cdot \boldsymbol{\tau} + \mathbf{F}_\sigma + \mathbf{F}_m. \tag{6}$$

Equations 5 and 6 also obey the law of conservation of mass and momentum, and the symbols p and $\boldsymbol{\tau}$ denote pressure and viscous stress, while the surface tension and magnetic forces are represented by $\mathbf{F}_\sigma$ and $\mathbf{F}_m$, respectively.

Again, the viscous stress tensor equals to $\eta\left[(\nabla\mathbf{u}) + (\nabla\mathbf{u})^T\right]$, and the surface tension force $\mathbf{F}_\sigma$ can be related to the coefficient of surface tension σ through the following equation:

$$\mathbf{F}_\sigma = \nabla \cdot [\sigma\{\mathbf{I} + (-\mathbf{n}\mathbf{n}^T)\}\delta], \tag{7}$$

where $\mathbf{I}$ is the identity operator, and δ is the Dirac delta function, which can also be approximated by the level set function ϕ as

$$\delta = 6|\phi(1-\phi)||\nabla\phi|. \tag{8}$$

Also, the additional magnetic stresses generated due to the application of a uniform magnetic field can be represented by the magnetic stress tensor $\boldsymbol{\tau}_m$, which is eventually required to calculate the applied magnetic force $\mathbf{F}_m$ in the computational domain. The calculation of the magnetic force $\mathbf{F}_m$ is as follows [Rosensweig, 1985]:

$$\mathbf{F}_m = \nabla \cdot \boldsymbol{\tau}_m = \nabla \cdot (\mu\mathbf{H}\mathbf{H} - \frac{\mu}{2}H^2\mathbf{I}), \tag{9}$$

where μ is the permeability of the fluid that varies according to the level set function ϕ, and $H^2 = |\mathbf{H}|^2$. A comprehensive understanding of the Maxwell equations and the constitutive relations among magnetic induction $\mathbf{B}$, magnetic field $\mathbf{H}$, and magnetization $\mathbf{M}$ is necessary for the calculation of magnetic stress tensor $\boldsymbol{\tau}_m$, which also maintain the following relationships [Stratton, 2007]:

$$\nabla \times \mathbf{H} = 0, \qquad \mathbf{M} = \chi\mathbf{H}, \quad \nabla \cdot \mathbf{B} = 0 \quad \text{and} \quad \mathbf{B} = \mu_0(\mathbf{H} + \mathbf{M}) = \mu_0(1+\chi)\mathbf{H}, \tag{10}$$

The symbol μ_0 denotes the permeability of vacuum, which is equal to $4\pi \times 10^{-7}$ N/A^2. A scalar magnetic potential ψ is defined under the consideration that it follows the relation $\mathbf{H} = -\nabla\psi$, which ultimately leads to the following equation:

$$\nabla \cdot (\mu \nabla \psi) = 0. \tag{11}$$

Moreover, in order to have a better understanding about the parameters that govern the overall dynamics of droplets, we rewrite the governing equations in terms of dimensionless groups. To achieve this, the droplet radius in the initial condition (R_0) is used as a scaling parameter for the length, whereas the time is scaled by the inverted shear rate $\frac{1}{\dot{\gamma}}$. The scaling for the non-dimensionalization of other parameters are as follows:

$$p^* = \frac{p}{\eta\dot{\gamma}}, \;\; \eta^* = \frac{\eta}{\eta_c}, \;\; \rho^* = \frac{\rho}{\rho_c}, \;\; \mu^* = \frac{\mu}{\mu_0}, \;\; \mathbf{H}^* = \frac{\mathbf{H}}{H_0},$$

where H_0 is a scaling parameter that denotes the magnitude of the magnetic field $\mathbf{H}_0$ applied along different directions. Now, the Navier-Stokes equations in non-dimensionalized form can be written as:

$$\nabla^* \cdot \mathbf{u}^* = 0, \tag{12}$$

$$\mathrm{Re}\left(\rho^* \frac{D\mathbf{u}^*}{Dt^*}\right) = -\nabla^* p^* + \nabla^* \cdot \tau^* + 2\frac{\mathrm{Bo}_m}{\mathrm{Ca}} \nabla^* \cdot \boldsymbol{\tau}_m^* + \frac{1}{\mathrm{Ca}} \mathbf{F}_\sigma^*. \tag{13}$$

In Equations 12 and 13, the asterisk ($*$) represents the non-dimensional variables, and Ca, Re, and Bo$_m$ represent the capillary number, Reynolds number, and magnetic Bond number, respectively, which can be elucidated as follows:

$$\mathrm{Ca} = \frac{\eta_c R_0 \dot{\gamma}}{\sigma}, \tag{14}$$

$$\mathrm{Re} = \frac{\rho_c {R_0}^2 \dot{\gamma}}{\eta_c}, \tag{15}$$

and

$$\mathrm{Bo}_m = \frac{R_0 \mu_0 {H_0}^2}{2\sigma}. \tag{16}$$

Several other important non-dimensional groups, such as the viscosity ratio λ and permeability ratio ζ can be written as follows:

$$\lambda = \frac{\eta_d}{\eta_c}, \quad \text{and} \quad \zeta = \frac{\mu_d}{\mu_0}. \tag{17}$$

Keeping the flow field restricted to the Stokes flow regime (i.e., Re $\lesssim 0.03$), in this task, the effects of different dimensionless groups Ca, Bo_m, λ, including α on the breakup phenomenon of the droplet will be investigated.

4. RESULTS AND DISCUSSIONS

4.1. DROPLET DEFORMATION IN HIGH LIMIT OF SHEAR FLOW (Ca ≥ 0.35)

At a small Reynolds number (i.e., Re ≤ 0.03), the flow is governed by Stokes flow equations. When a droplet is subjected to a simple shear flow, it deforms. According to Taylor [Taylor, 1932, 1934], the deformation of a neutrally buoyant, viscous droplet suspended in another viscous medium under a simple shear flow at Stokes flow limit can be defined as:

$$D_{taylor} = \frac{L - B}{L + B} = \frac{19\lambda + 16}{16\lambda + 16}\mathrm{Ca}. \tag{18}$$

Taylor formulated the above equation assuming that the shear flow is unbounded with a vanishing Reynolds number; however, in numerical studies, a simple shear flow is usually generated by two plane walls translating in opposite directions, which gives rise to the so-called confinement effect. This confinement effect, characterized by the confinement ratio $\frac{2R_0}{H_d}$, has a negligible effect on the deformation of the droplet when $\frac{2R_0}{H_d} < 0.4$ [Guido and Villone, 1998, Kennedy *et al.*, 1994]. In our case, the confinement ratio is equal to

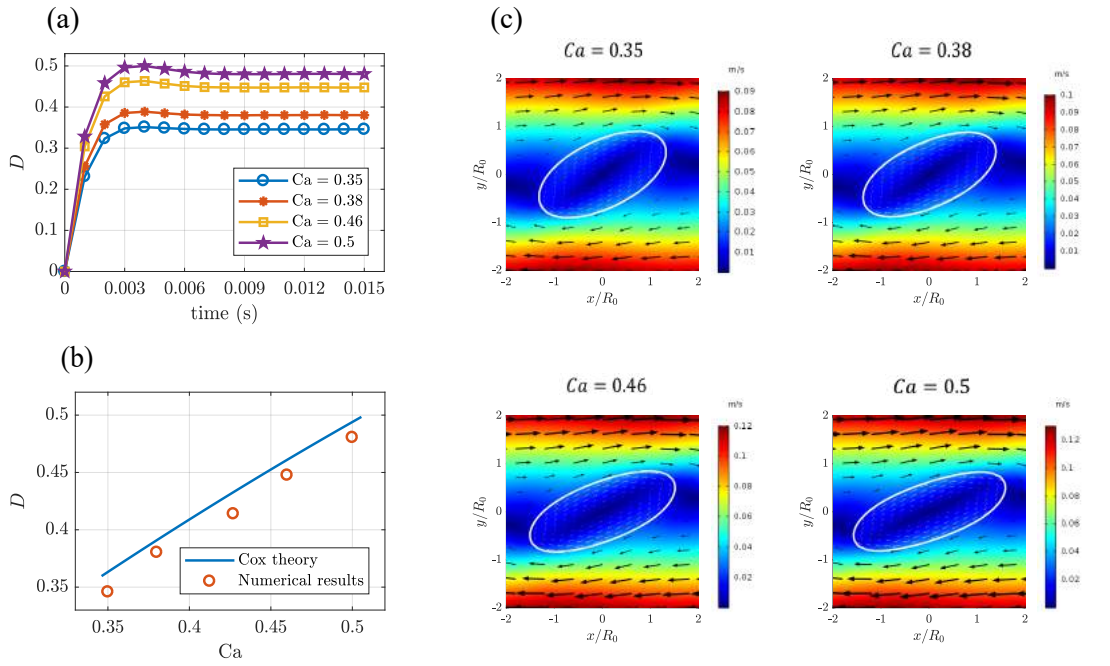

Figure 2. Droplet deformation in high limit shear flow. (a) D vs time; (b) Comparison of numerical results against Cox theory[Cox, 1969]; and (c) Equilibrium shape of the droplet.

0.1, and therefore, the confinement effect can be neglected. In this section, we study the evolution of equilibrium droplet shapes in the high limit of shear flow under the Stokes flow regime and then compare the numerical results against the existing theories in literature.

Figure 2 represents the time evolution of droplet deformation parameter D and the corresponding equilibrium droplet shapes at different Capillary numbers. From Figure 2(a), it can be seen that as the shear rate increases, the deformation increases. Also, it takes a very small amount of computational time to reach the steady state deformation. Moreover, we compared our numerical results against the asymptotic theory for small deformation given by Cox [Cox, 1969]. According to Cox, the deformation of a droplet can be approximated as:

$$D_{cox} = D_{taylor}\left[1 + \left(\frac{19\mathrm{Ca}\lambda}{20}\right)^2\right]^{-\frac{1}{2}}, \tag{19}$$

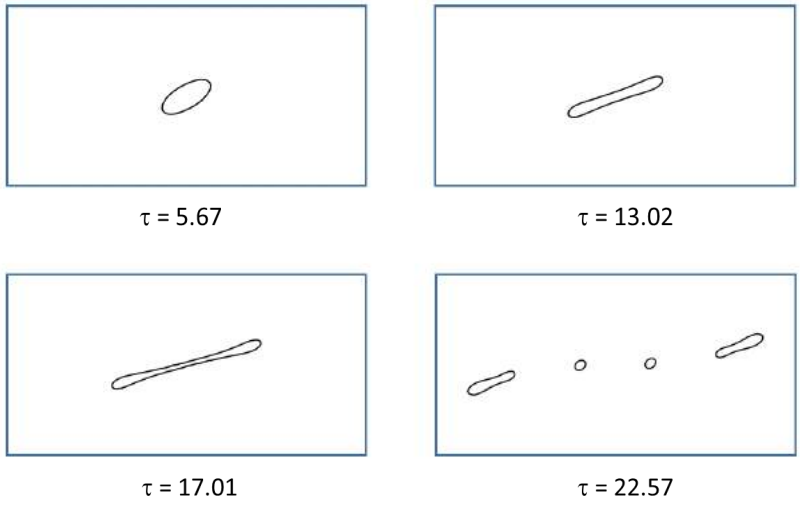

Figure 3. Droplet breakup in a simple shear flow at Re = 1, Ca = 0.5, and λ = 1.2.

where D_{taylor} is the Taylor deformation parameter defined in Equation 18. From Figure 2(b), it can be inferred that the numerical results are in very good agreement with the Cox deformation theory. Even for the maximum shear rate considered in our study (i.e., Ca = 0.5), the error between the numerical and theoretical results is found to be approximately 3.5%.

Furthermore, the corresponding equilibrium droplet shapes are shown in Figure 2(c). The droplet shapes reveal that with an increasing Capillary number, the droplet is more stretched towards the direction of the flow field, which is also consistent with our previous findings [Hassan *et al.*, 2018]. The droplet experiences maximum shear stress along the poles of the droplet. Also, the velocity field acts tangentially at the droplet interface, and near the droplet, the flow field follows the curvature of the droplet, which is also consistent with the free surface conditions. A closed circulation is observed inside the droplet due to the competition between the surface tension driven flow and the flow field outside the droplet, which is represented by the arrow in the velocity fields.

Moreover, we performed simulations at higher Reynolds numbers (i.e., Re = 1) to verify that our numerical model is capable of capturing droplet breakup at higher Reynolds numbers. Figure 3 shows the transformation of an ellipsoidal droplet into multiple droplets following a breakup at Re = 1, Ca = 0.5, and $\lambda = 1.2$. These droplet breakup results agree well with the findings of Cunha et al. [Cunha *et al.*, 2018], except the fact that in their case, one satellite droplet was observed, while in our numerical model, we observed two satellite droplets after the breakup. The primary reason behind this phenomenon can be attributed to the resolution of the interface thickness of the droplet i.e., in their numerical model the interface thickness was considered 1.5 times the largest mesh element size h ($\epsilon = 1.5h$), whereas in our study, a better interface resolution is considered ($\epsilon = 0.5h$). Additionally, the validation of the droplet deformation results under the influence of uniform magnetic fields against the findings of Afkhami et al. [Afkhami *et al.*, 2010] are presented in our previous work [Hassan *et al.*, 2018].

4.2. DROPLET BREAKUP UNDER THE EFFECT OF MAGNETIC FIELD

When applied, an external magnetic field can significantly affect the deformation and orientation of a ferrofluid droplet, which in turn offers the possibility of controlling the emulsion rheology of a droplet by inducing or suppressing the topological changes of the suspended droplet in a simple shear flow. Existing studies in the literature show that it is possible to induce breakup at a low Capillary number in a Stokes flow (where the droplet does not break) by increasing the Reynolds number [Li *et al.*, 2000]. Recently, Cunha et al. [Cunha *et al.*, 2018] have studied field induced droplet breakup in a shear flow at a higher Reynolds number where the magnetic field is applied in a perpendicular and parallel direction to the flow field. In this section, at a fixed viscosity ratio (i.e., $\lambda = 1$) and Capillary number (i.e., Ca = 0.45), we study the effect of an external uniform magnetic field on the rupture of a ferrofluid droplet in the Stokes flow regime along some specific directions.

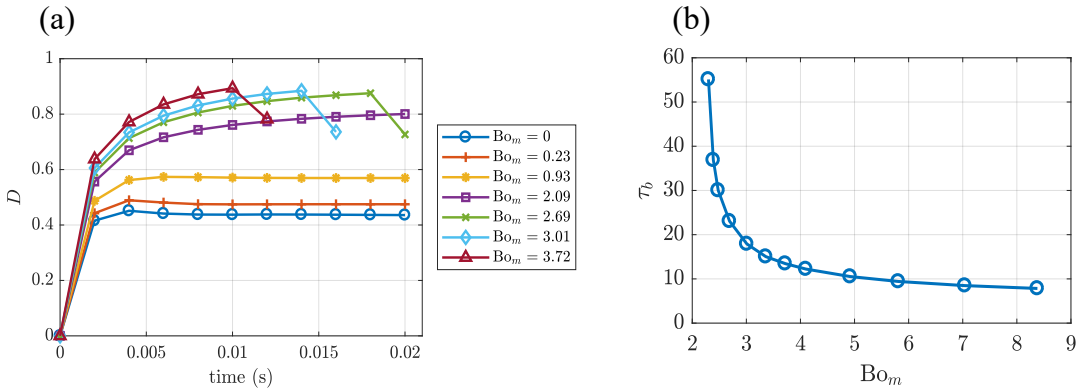

Figure 4. Droplet under the effect of a magnetic field in a simple shear flow at 45° (i.e., $\alpha = 45°$), Ca = 0.45, and $\lambda = 1$. (a) D vs time; (b) Droplet breakup time, τ_b vs Bo$_m$.

Also, note that in the absence of any external forces (i.e., Bo$_m = 0$), at Ca = 0.45 and $\lambda = 1$, the orientation angle of the droplet is found to be approximately 21.9°. In the remaining portion of the study, the Reynolds number is considered as 0.03 (i.e., Re = 0.03).

4.2.1. $\alpha = 45°$. Figure 4 represents the effect of a uniform magnetic field on the droplet rheology in a simple shear flow at $\alpha = 45°$. From Figure 4(a), it can be seen that as the magnetic field strength increases, the deformation D of the ferrofluid droplet increases. The droplet shape also attains a steady state within a very small amount of computational time; however, at a magnetic bond number equal to 2.09 (i.e., Bo$_m = 2.09$), the droplet deformation shows an unsteady behavior for a longer period of time and reaches a steady state in around 0.02 s. Furthermore, as we continue increasing the magnetic bond number beyond 2.69 (i.e., Bo$_m \geq 2.69$), the droplet deforms even more without reaching a steady state, and this unsteady behavior ultimately initiates the breakup. The sudden decline in the droplet deformation in Figure 4(a) denotes that a breakup has been initiated by the external magnetic field. Also, at $\alpha = 45°$ we found the critical deformation (deformation at which the droplet disintegrates) to be approximately 0.87 i.e., $D_{cr} \approx 0.87$. Additionally, the droplet is found to rupture earlier under a higher magnetic field strength i.e., Bo$_m = 3.72$. Figure 4(b) displays the estimated rupture time τ_b as a function of magnetic bond number Bo$_m$,

which clearly indicates that τ_b follows a nonlinear relationship with Bo_m. As the intensity of magnetic field increases, the droplet ruptures even quicker. These results also demonstrate that at $\alpha = 45°$, a critical magnetic bond number exists below which the droplet does not break up anymore, and the numerical simulations suggest this value to be approximately 2.23 (i.e, $\mathrm{Bo}_{cr} \approx 2.23$).

Figure 5 shows the evolution of droplet breakup over time at different magnetic bond numbers, Bo_m. From Figure 5(b), it can be seen that as time proceeds, the droplet transforms into a dumbbell shape from an ellipsoidal shape along with the bulbs at the ends of the droplet with a fixed diameter. As the droplet stretches itself towards the direction of the flow field, a neck is developed at the center of the droplet that continuously thins over time. In this case, the magnetic field aids the droplet more in stretching towards the flow field direction. Moreover, due to the presence of circulation inside the bulbous ends of the droplet, the surface tension driven flow acts stronger near the bulbous end while the flow is much weaker near the neck. As a result, this unstable neck eventually leads to ends pinching off ($\tau_b = 9.41$) and gives rise to satellite droplets with the remaining liquid thread in the middle; however, at $\mathrm{Bo}_m = 3.72$ (Figure 5(a)), we observed an eventual breakup of the mother droplet into two daughter droplets. Now, as we go on increasing the magnetic field strength (i.e., $\mathrm{Bo}_m = 8.38$), multiple satellite droplets appear in the computational domain. Interestingly, from Figure 5(c) we can see that the size of the second pair of satellite droplets seems smaller compared to the first pair of satellite droplets. According to Marks,Marks [1998] if the original volume fraction is not totally used by the breakup process for a large droplet, the ends of the remaining volume fraction will go through a similar breakup process as before and give rise to another pair of smaller satellite droplets, and our results agree very well with the experimental observations of Marks [Marks, 1998].

4.2.2. $\alpha = 90°$. Now, we apply the magnetic field at an angle $\alpha = 90°$ to observe its effect on the breakup phenomenon of the droplet suspended in a shear flow. Figure 6(a) displays the evolution of deformation parameter D over time when the magnetic field is

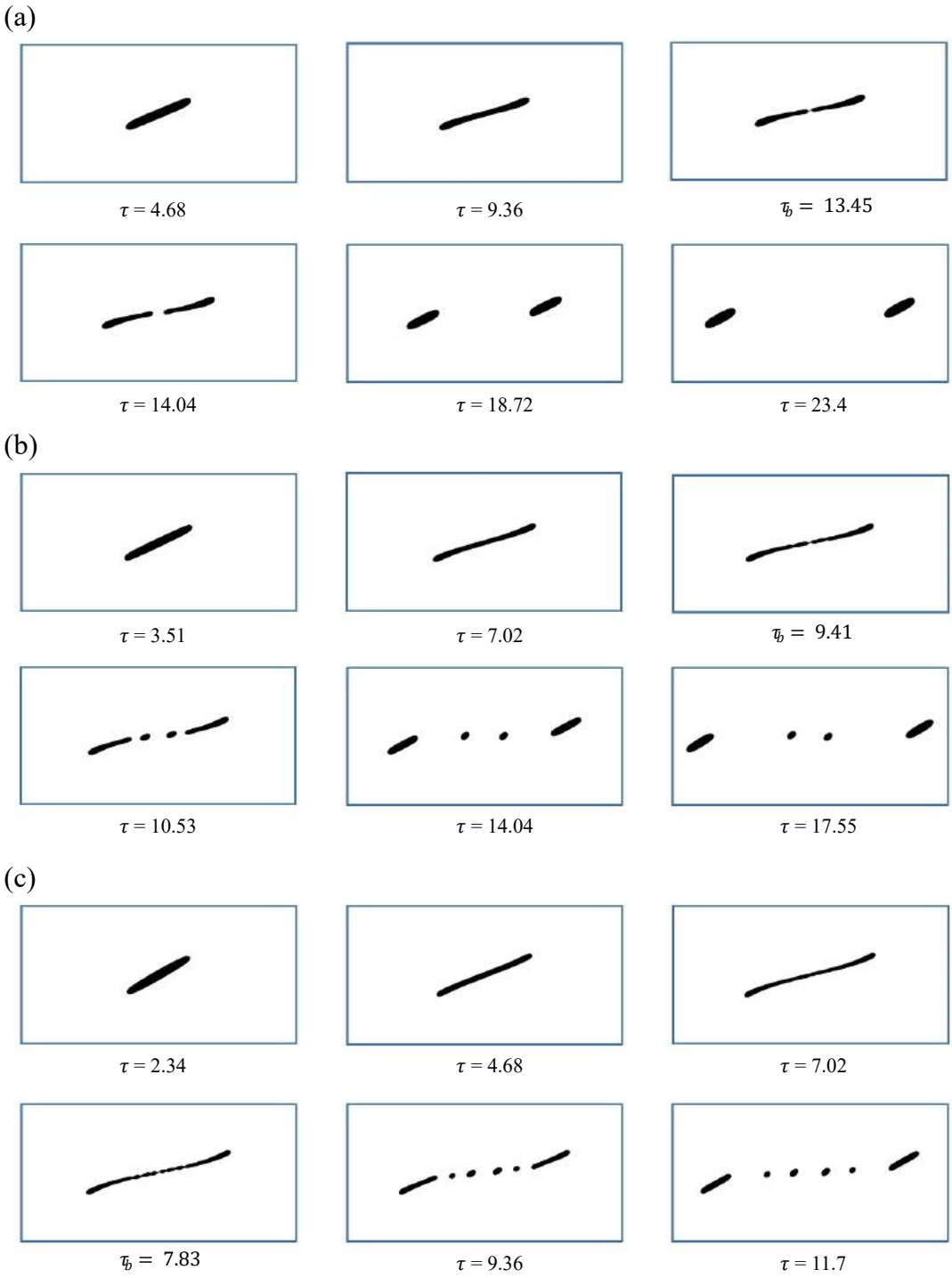

Figure 5. Evolution of droplet breakup under the magnetic field effect in a simple shear flow at 45° (i.e., $\alpha = 45°$), Ca = 0.45, and $\lambda = 1$. (a) $Bo_m = 3.72$; (b) $Bo_m = 5.81$; and (c) $Bo_m = 8.38$.

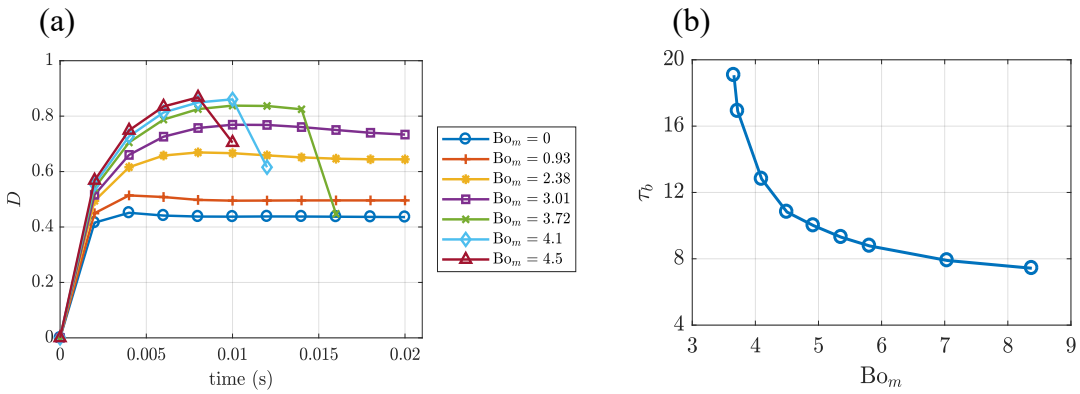

Figure 6. Droplet under the effect of a magnetic field in a simple shear flow at 90° (i.e., $\alpha = 90°$), Ca = 0.45, and $\lambda = 1$. (a) D vs time; (b) Droplet breakup time, τ_b vs Bo_m.

applied at an angle $\alpha = 90°$. It can be seen that with the increase in magnetic field strength, deformation D increases and reaches a steady state around 0.008 s; although at $\mathrm{Bo}_m = 3.01$, the droplet starts to show unsteady behavior. Moreover, as we continuously increase the magnetic field strength to $\mathrm{Bo}_m = 3.72$, similar to the case mentioned above, we observe the first breakup where the mother droplet breaks into two daughter droplets. In this case, the critical deformation is found to be approximately 0.85 (i.e., $D_{cr} \approx 0.85$). Also, at $\alpha = 90°$ the first breakup is seen at a magnetic bond number, $\mathrm{Bo}_m = 3.72$, which is slightly above the magnetic bond number that is required to initiate the first breakup at $\alpha = 45°$ (i.e., $\mathrm{Bo}_m = 2.69$). The primary reason behind this fact is that at $\alpha = 45°$, the magnetic field aids the droplet in stretching in the same direction as the velocity field, which in turn initiates the droplet breakup faster. Figure 6(b) illustrates the relationship between droplet breakup time, τ_b and magnetic bond number, Bo_m, and the numerical results suggest that the critical magnetic bond number in this case lies around 3.63 (i.e., $\mathrm{Bo}_{cr} \approx 3.63$).

Figure 7 demonstrates the evolution of droplet shapes under the magnetic field effect at $\alpha = 90°$, and it shows that the droplet continuously deforms and eventually breaks up at some point; however, no satellite droplets are observed until we apply a magnetic field strength that corresponds to a magnetic bond number, $\mathrm{Bo}_m = 8.38$ (Figure 7(c)). In all

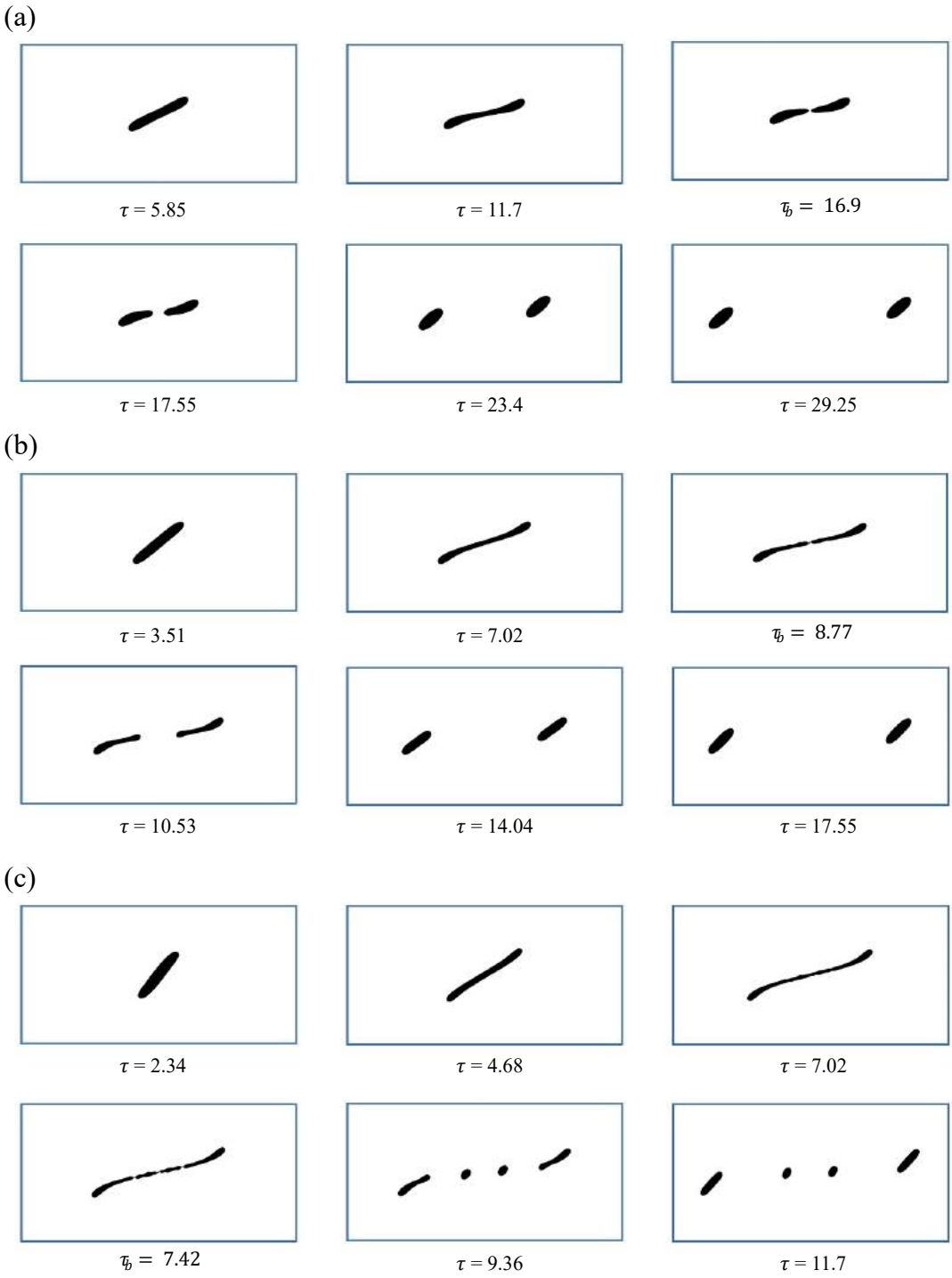

Figure 7. Evolution of droplet breakup under the magnetic field effect in a simple shear flow at 90° (i.e., $\alpha = 90°$), Ca = 0.45, and $\lambda = 1$. (a) $Bo_m = 3.72$; (b) $Bo_m = 5.81$; and (c) $Bo_m = 8.38$.

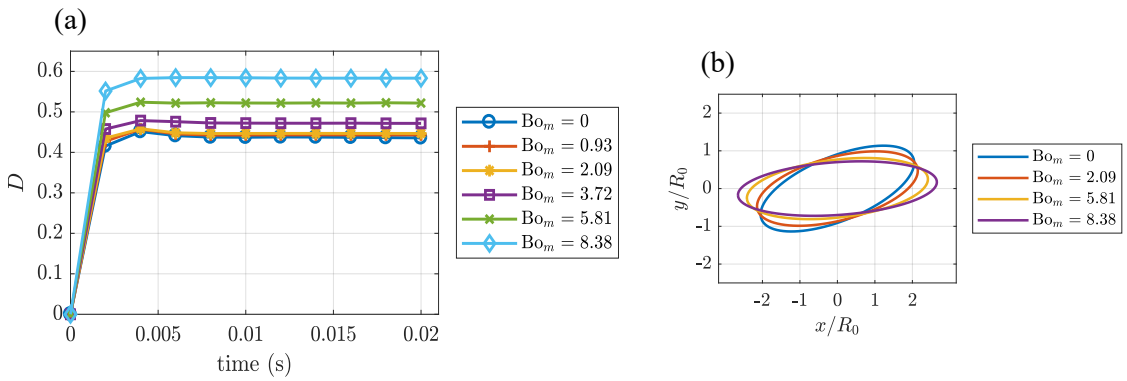

Figure 8. Droplet under the effect of a magnetic field in a simple shear flow at 0° (i.e., $\alpha = 0°$), Ca = 0.45, and $\lambda = 1$. (a) D vs time; (b) Outline of equilibrium shapes at different magnetic bond numbers, Bo$_m$.

these cases, the droplet follows a similar type of evolution from initial stage to breakup as described in the previous section (i.e., the droplet stretches itself from spherical to the dumbbell shape followed by an ellipsoidal shape, then the ends pinch off due to the presence of instabilities at the central portion, which in turn generate multiple droplets). Interestingly, in Figure 7(c) fewer satellite droplets appear compared to the number of satellite droplets that we observed at $\alpha = 45°$ (Figure 5(c)) for the same magnitude of magnetic field strength (i.e., Bo$_m$ = 8.38). The reason behind this could be attributed to the fact that in this case, the magnetic stress acts in a direction perpendicular to the flow field while the hydrodynamic stress acts along 45°, and the competition between hydrodynamic and magnetic stresses along two different directions results in a few number necks along the droplet interface, which in turn produces fewer satellite droplets.

4.2.3. $\alpha = 0°$. Figure 8 represents the effect of magnetic field on the droplet shape in a simple shear flow at $\alpha = 0°$. From Figure 8(a), it can be seen that initially as the magnetic field strength increases up to Bo$_m$ = 2.09, the magnetic field has negligible effect on the deformation of the droplet since upto this point the shear flow is dominant and controls the deformation of the droplet. But as the magnetic field strength starts to increase beyond Bo$_m \geq 3.72$, the magnetic field tends to become dominant, and as a result

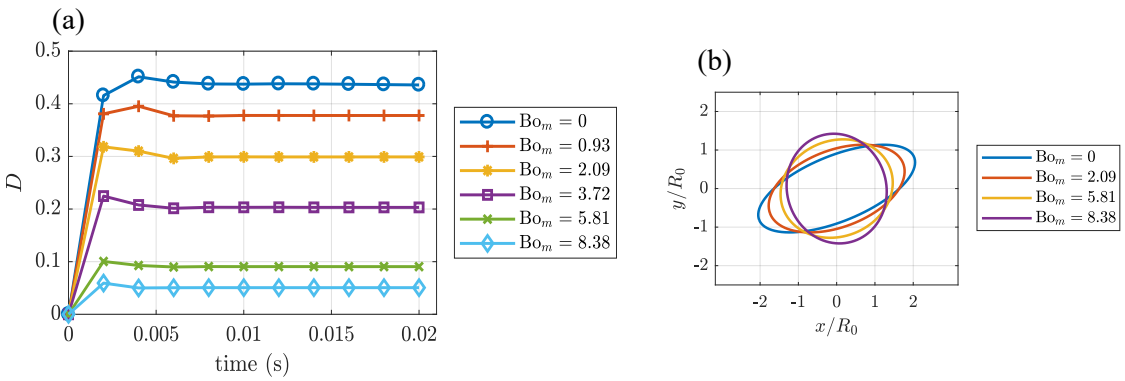

Figure 9. Droplet under the effect of a magnetic field in a simple shear flow at 135° (i.e., $\alpha = 135°$), Ca = 0.45, and $\lambda = 1$. (a) D vs time; (b) Outline of equilibrium shapes at different magnetic bond numbers, Bo$_m$.

the deformation of the droplet D increases and reaches a steady state within a very small amount of computational time. Figure 8(b) portrays the outline of the equilibrium droplet shapes at different magnetic bond numbers, Bo$_m$. The droplet shapes reveal that with the increase in magnetic field strength, the droplet aligns itself more towards the direction of the magnetic field with greater deformation. Even at a higher magnetic bond number i.e., Bo$_m$ = 8.38, we did not observe any breakup. The primary reason behind this phenomenon is that with the increase in magnetic field strength, the magnetic field rotates the droplet from the extensional quadrant to the compressional quadrant of shear, and as a result the droplet is now so aligned with the flow direction that the shear stress is not strong enough to induce rupture, which also acts as a restorative mechanism of the droplet shape.

4.2.4. $\alpha = 135°$. Finally, we apply the magnetic field along 135° (i.e., $\alpha = 135°$) to understand its effect on the droplet deformation in a significantly strong shear flow. Figure 9 represents the droplet deformation behavior under a uniform magnetic field in a shear flow at $\alpha = 135°$. From Figure 9(a), we can see that as the magnetic field strength gradually increases, the droplet deformation D decreases. This happens because, on the one hand, the shear flow is trying to deform the droplet along 45°, while, on the other hand, the magnetic field is acting along 135°, which is also the exact opposite direction to the

favorable direction of the shear flow, thus resulting in a smaller deformation. Also, the outline of equilibrium droplet shapes is illustrated in Figure 9(b), which confirms that with the increase in magnetic field strength, the droplet changes from an ellipsoidal shape to a spherical shape followed by a smaller deformation. Moreover, at $\mathrm{Bo}_m = 8.38$ the magnetic field strength starts to orient the droplet along 135°, while for the other cases, the shear flow takes control of the orientation of the droplet.

Moreover, further simulations have been carried out at very high magnetic bond numbers (i.e., $\mathrm{Bo}_m = 33.5$) along both $\alpha = 0°$ and 135° to investigate if the droplet breaks under extreme conditions, and interestingly, no breakup is observed in the computational domain even in these situations; instead, droplets with nearly pointed ends are generated, which also shows good agreement with the findings of Afkhami et al. [Afkhami *et al.*, 2010]. Overall, the results for different arbitrary directions suggest that it is possible to initiate droplet breakup in the Stokes flow regime by proper manipulation of a uniform magnetic field along 45° and 90°, while breakup can be suppressed by applying the magnetic field along both 0° and 135°.

4.3. EFFECT OF VISCOSITY RATIO

In external flow conditions, viscosity ratio plays an important role on the dynamics of isolated drops in a shear flow, and from the experimental analyses of Grace [Grace, 1982] and Debruijn [Debruijn, 1991] it is found that the droplet reaches a steady state deformation upto a certain critical Capillary number, Ca_{cr}, and above Ca_{cr} the droplet keeps deforming until rupture occurs, which is also dependent on the viscosity ratio. Conversely, in particular, a detailed study of the critical droplet deformation D_{cr} at a low Reynolds number is missing in the literature. Here, in this section, we analyze the effect of the viscosity ratio on the droplet breakup phenomenon in the Stokes flow regime under a uniform magnetic field. Keeping the droplet size and capillary number fixed (i.e., $\mathrm{Ca} = 0.45$), the magnetic field is applied along different directions for different viscosity ratios.

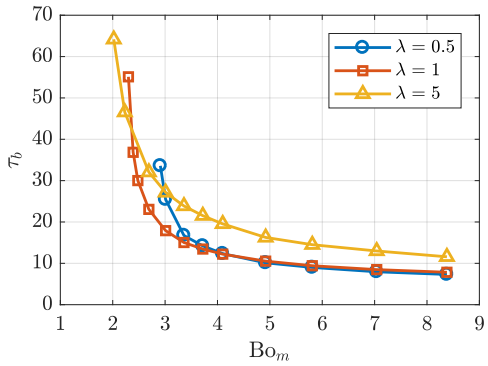

Figure 10. Effect of viscosity ratio on droplet breakup under a uniform magnetic field at $\alpha = 45°$ and Ca = 0.45. Droplet breakup time, τ_b vs Bo_m.

4.3.1. $\alpha = 45°$. Figure 10 shows the effect of the viscosity ratio on the droplet breakup time under a uniform magnetic field at $\alpha = 45°$. It can be seen that at a fixed viscosity ratio, as the magnetic bond number Bo_m increases, the droplet rupture time decreases. Also, there exists a critical magnetic bond number, Bo_{cr}, for all viscosity ratios below which the droplet does not breakup anymore. Moreover, at a fixed magnetic bond number Bo_m, as the viscosity ratio increases, the breakup time increases, except when the magnetic bond number is near the critical magnetic bond number Bo_{cr}. This is because with the increase in viscosity ratios, the droplet shows more resistance to droplet deformation. As a result, it takes more time for a particular magnetic field strength to induce rupture to a more viscous droplet compared to a less viscous droplet. Interestingly, the critical magnetic bond number Bo_{cr} also decreases for more viscous droplets.

Figure 11 shows the evolution of droplet breakup under a magnetic field at $\alpha = 45°$ for different viscosity ratios. It can be seen that at a magnetic bond number $\mathrm{Bo}_m = 8.38$ for all viscosity ratios, the droplet goes through a similar kind of evolution from the initial stage to the point where it ruptures, as discussed in the previous sections; however, more necks appear near the center of the droplet due to the increased resistance towards droplet deformation with the increase in the viscosity ratios, which in turn give rise to more number of satellite

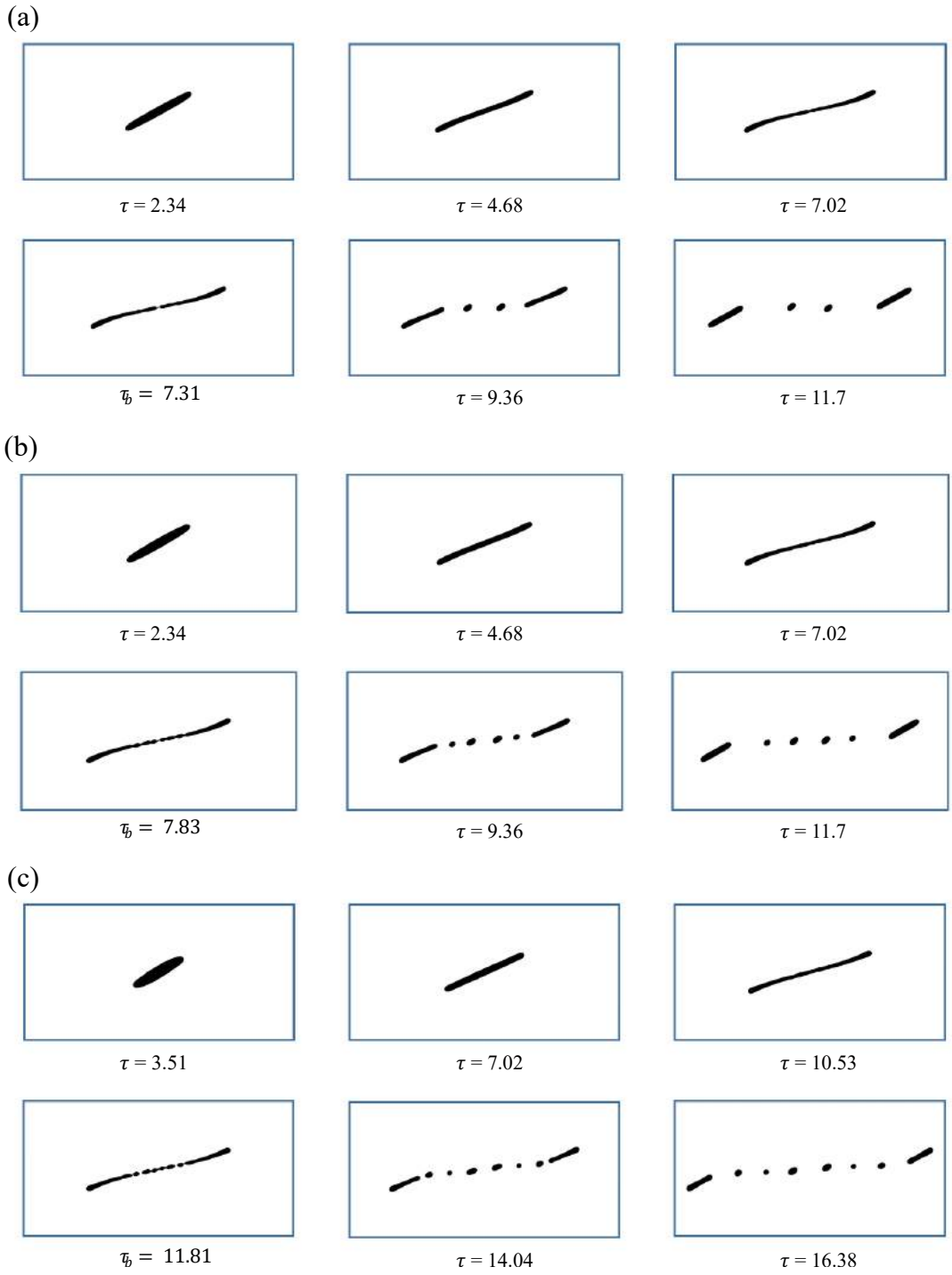

Figure 11. Evolution of droplet breakup under a uniform magnetic field in a simple shear flow at 45° (i.e., $\alpha = 45°$), Ca = 0.45, and $\mathrm{Bo}_m = 8.38$. (a) $\lambda = 0.5$; (b) $\lambda = 1$; and (c) $\lambda = 5$.

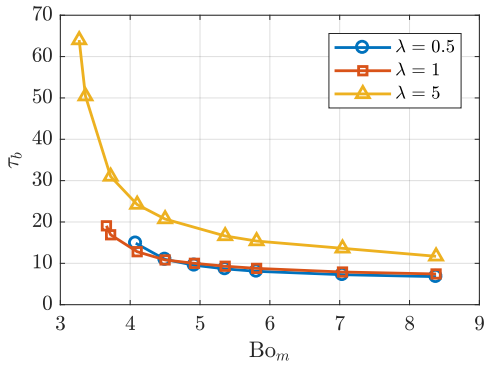

Figure 12. Effect of viscosity ratio on droplet breakup under a uniform magnetic field at $\alpha = 90°$ and Ca = 0.45. Droplet breakup time, τ_b vs Bo_m.

droplets after the droplet disintegrates. Also, we observed the subsequent production of smaller and larger satellite droplets (Figure 11(b) and (c)) followed by the formation of the largest daughter droplets by the first elongative end pinching during the droplet breakup process, which also agrees with the experimental findings of Marks. Furthermore, the size of the daughter droplets decreases with the increase in the viscosity ratio, due to the increased resistance to droplet deformation.

4.3.2. $\alpha = 90°$. Now, we apply the magnetic field in a direction perpendicular to the flow field (i.e., $\alpha = 90°$) to investigate its effect on the droplet breakup phenomenon for different viscosity ratios. Figure 12 displays the relationship between the breakup time τ_b and the magnetic bond number Bo_m at three different viscosity ratios. Similar to the $\alpha = 45°$ case mentioned above, in this case at a fixed viscosity ratio, the droplet rupture time decreases with increasing the magnetic field strength. Also, a critical magnetic bond number, Bo_{cr}, exists for all viscosity ratios, which gradually decreases for more viscous droplets. Figure 13 shows the evolution of the droplet shape from the initial stage to the breakup stage under a uniform magnetic field at $\alpha = 90°$, and it can be seen that for all the cases, the droplet initially tends to orient itself along the direction of the magnetic field over time, followed by the transformation of the spherical droplet into a dumbbell shape with

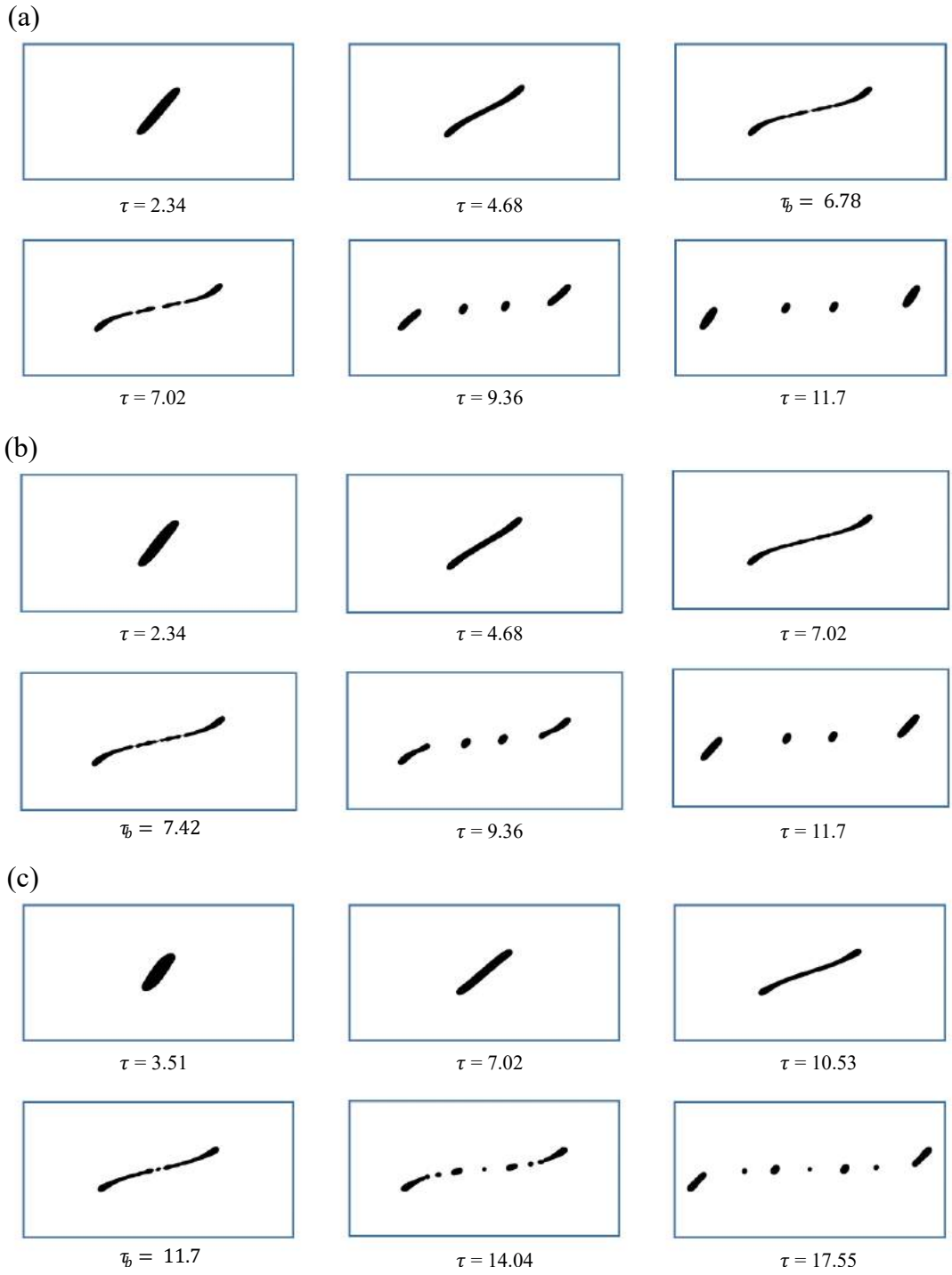

Figure 13. Evolution of droplet breakup under a uniform magnetic field in a simple shear flow at 90° (i.e., $\alpha = 90°$), Ca = 0.45, and $\mathrm{Bo}_m = 8.38$. (a) $\lambda = 0.5$; (b) $\lambda = 1$; and (c) $\lambda = 5$.

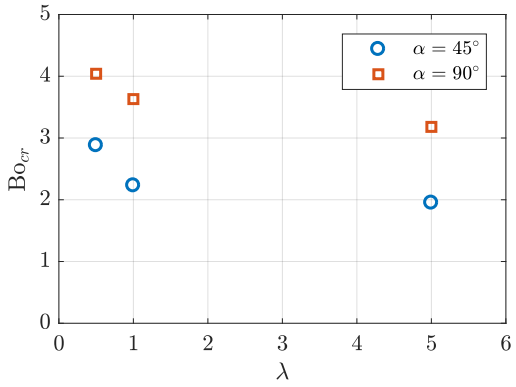

Figure 14. Relationship between critical magnetic bond number, Bo_{cr} and viscosity ratio, λ for different arbitrary magnetic field directions.

fixed diameter bulbs at both ends. Eventually, more necks are developed due to the shear and magnetic stresses acting along the interface near the center, which in turn give rise to multiple satellite droplets; however, at $\alpha = 90°$ we observed the production of smaller and larger satellite droplets only at a higher magnetic field strength (i.e., $\mathrm{Bo}_m = 8.38$). Moreover, the size of the daughter droplets appears smaller at $\alpha = 90°$ compared to $\alpha = 45°$. Furthermore, at $\alpha = 90°$ as the viscosity ratio is increased beyond $\lambda \geq 1$, fewer satellite droplets are found in the computational domain compared to the number of satellite droplets that appear at $\alpha = 45°$.

Finally, the relationship between the critical magnetic bond number, Bo_{cr}, and the viscosity ratio, λ, for different directions is demonstrated in Figure 14. It shows that at a fixed λ, the critical magnetic bond number Bo_{cr} always has a higher value at $\alpha = 90°$ than at $\alpha = 45°$. This is because the magnetic field additionally stretches the droplet along the flow direction at $\alpha = 45°$, which ultimately induces rupture in the droplet at a faster rate. As a result, the critical magnetic bond number Bo_{cr} appears earlier at $\alpha = 45°$ compared to $\alpha = 90°$, where we apply the magnetic field in a direction perpendicular to the flow domain.

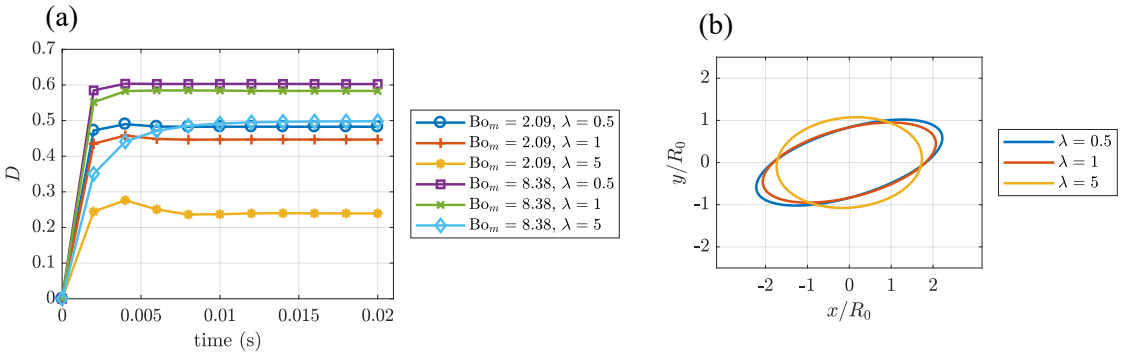

Figure 15. Effect of viscosity ratio on droplet deformation under a uniform magnetic field at $\alpha = 0°$ and Ca = 0.45. (a) D vs time; and (b) Outline of equilibrium shapes at Bo$_m$ = 2.09.

4.3.3. $\alpha = 0°$. Figure 15 illustrates the effect of the viscosity ratio on the droplet breakup under a uniform magnetic field at $\alpha = 0°$. From Figure 15(a), it can be seen that at a fixed magnetic bond number Bo$_m$, the deformation of the droplet D decreases with the increase in viscosity ratio. This is due to the fact that as the droplet becomes more viscous, it shows more resistance to deformation, which in turn results in a more spherical droplet shape. Interestingly, for a more viscous droplet (i.e., $\lambda = 5$) at a smaller magnetic field strength (i.e., Bo$_m$ = 2.09), we observed a rapid decline in deformation compared to less viscous drops (i.e., $\lambda = 0.5$ and 1). Figure 15(b) depicts the outline of the final equilibrium droplet shapes at Bo$_m$ = 2.09, which also confirms that with the increase in viscosity ratio, the droplet tends to align itself more towards the direction of magnetic field (i.e., orientation angle θ decreases).

4.3.4. $\alpha = 135°$. Finally, the magnetic field is applied along 135° to investigate its effect on droplet rheology at different viscosity ratios. From Figure 16(a), it can be seen that, similar to the case mentioned above, the droplet deformation D decreases with the increase in viscosity ratio. But in this case, at a particular magnetic field strength and viscosity ratio, the droplet deformation appears much smaller compared to the deformation at $\alpha = 0°$. The primary reason behind this could be attributed to the fact that at $\alpha = 135°$, the magnetic field induced deformation acts along the exact opposite direction of the shear

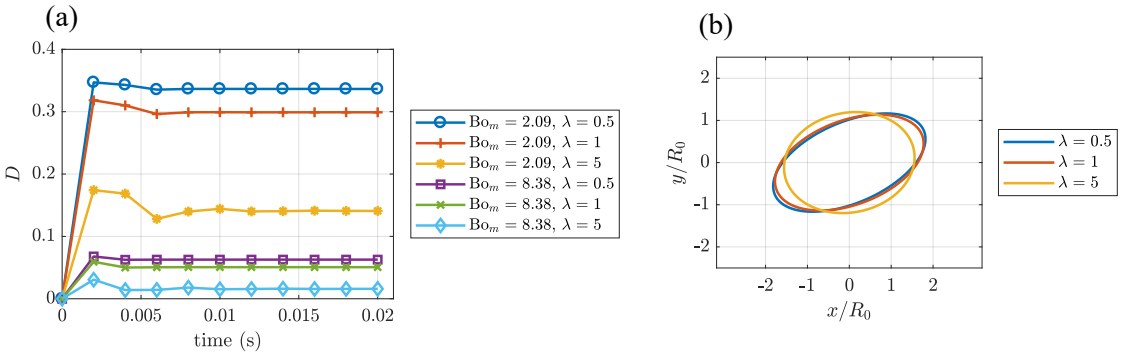

Figure 16. Effect of viscosity ratio on droplet deformation under a uniform magnetic field at $\alpha = 135°$ and Ca = 0.45. (a) D vs time; (b) Outline of equilibrium shapes at $\text{Bo}_m = 2.09$.

induced deformation i.e., deformation D decreases. Furthermore, the droplet aligns itself more towards the direction of the magnetic field with the increase in viscosity ratio (Figure 16(b)), which is also similar to the orientation trend observed at $\alpha = 0°$.

Overall, the results suggest that at Ca = 0.45, increasing the viscosity ratio along both $\alpha = 45°$ and $90°$ initiates a faster breakup. At a fixed viscosity ratio, the critical magnetic bond number Bo_{cr} always has a higher value at $\alpha = 90°$ than at $\alpha = 45°$. On the other hand, at a specific magnetic field strength (i.e., $\text{Bo}_m = 2.09$), increasing the viscosity ratio along both $\alpha = 0°$ and $135°$ results in a smaller deformation; however, the deformation of the droplet along $\alpha = 135°$ is found comparatively smaller than the deformation at $\alpha = 0°$.

5. CONCLUSION

The breakup of a ferrofluid droplet in a simple shear flow under the influence of a uniform magnetic field along different directions at a low Reynolds number (i.e., Re = 0.03) is systematically studied in this paper. The results show that at a low Capillary number (i.e., $\text{Ca} \leq 0.5$), in the absence of any external forces, the droplet reaches a steady state deformation when suspended in another viscous medium in a shear flow; however, when a magnetic field is applied along 45° and 90°, the droplet starts to show unsteady behavior with the increase in magnetic field strength and eventually ruptures. We found that there

exists a critical magnetic Bond number, Bo_{cr}, above which the droplet shows this behavior, which is also dependent on the direction of the magnetic field. For example, at $\alpha = 45°$, the magnitude of Bo_{cr} is found to be approximately 2.23 (i.e., $\mathrm{Bo}_{cr}^{45°} \approx 2.23$), while at $\alpha = 90°$, it was found to be approximately 3.63 (i.e., $\mathrm{Bo}_{cr}^{90°} \approx 3.63$). Also, as we increase the magnetic field strength beyond Bo_{cr}, for both cases, the time to induce rupture in the droplet decreases. Moreover, for the same magnetic field strength, more satellite droplets are observed at $\alpha = 45°$ compared to $\alpha = 90°$. On the other hand, applying a magnetic field along 0° and 135° suppresses droplet breakup. Even at a higher magnetic field strength, a steady state deformation was observed in both cases.

Furthermore, we investigated the effect of viscosity ratios on the droplet breakup phenomenon under a uniform magnetic field at different directions and found that for both $\alpha = 45°$ and 90°, at a fixed magnetic bond number, the breakup time increases as the viscosity ratio λ increases, except when Bo_m is near the critical magnetic bond number Bo_{cr}. Also, the critical magnetic bond number Bo_{cr} decreases for a more viscous droplet. Additionally, with the increase in viscosity ratio at a fixed magnetic bond number, more satellite droplets are observed; although, for the same Bo_m and λ, a larger number of satellite droplets are observed at $\alpha = 45°$ compared to 90°. Moreover, at a fixed λ, Bo_{cr} always has a higher value at $\alpha = 90°$ than at $\alpha = 45°$. Conversely, when the magnetic field is directed along 0° and 135°, at a particular magnetic field strength, the droplet deformation D decreases with an increase in viscosity ratio, and the droplet tends to orient itself more towards the magnetic field direction. These findings indicate the enormous potential of magnetic fields as a useful tool for controlling breakup of ferrofluid droplets and emulsion rheology, which are relevant to a variety of applications in the fields of microfluidics, polymer processing, and chemical engineering.

ACKNOWLEDGMENTS

The authors gratefully acknowledge the financial support from the Department of Mechanical and Aerospace Engineering (MAE) and the Center for Biomedical Research (CBR) at Missouri University of Science and Technology.

REFERENCES

Acrivos, A., 'The breakup of small drops and bubbles in shear flows,' Annals of the New York Academy of Sciences, 1983, **404**(1), pp. 1–11.

Afkhami, S., Tyler, A., Renardy, Y., Renardy, M., Pierre, T. S., Woodward, R., and Riffle, J. S., 'Deformation of a hydrophobic ferrofluid droplet suspended in a viscous medium under uniform magnetic fields,' Journal of Fluid Mechanics, 2010, **663**, pp. 358–384.

Ahmed, A., Fleck, B. A., and Waghmare, P. R., 'Maximum spreading of a ferrofluid droplet under the effect of magnetic field,' Physics of Fluids, 2018, **30**(7), p. 077102.

Banerjee, S., Fasnacht, M., Garoff, S., and Widom, M., 'Elongation of confined ferrofluid droplets under applied fields,' Physical Review E, 1999, **60**(4), p. 4272.

Barthes-Biesel, D. and Acrivos, A., 'Deformation and burst of a liquid droplet freely suspended in a linear shear field,' Journal of Fluid Mechanics, 1973, **61**(1), pp. 1–22.

Bentley, B. and Leal, L. G., 'An experimental investigation of drop deformation and breakup in steady, two-dimensional linear flows,' Journal of Fluid Mechanics, 1986, **167**, pp. 241–283.

Collins, R. T., Jones, J. J., Harris, M. T., and Basaran, O. A., 'Electrohydrodynamic tip streaming and emission of charged drops from liquid cones,' Nature Physics, 2008, **4**(2), p. 149.

COMSOL, *CFD Module Application Library Manual*, 5.3a edition, 2018.

Cox, R., 'The deformation of a drop in a general time-dependent fluid flow,' Journal of fluid mechanics, 1969, **37**(3), pp. 601–623.

Cunha, L. H., Siqueira, I. R., Oliveira, T. F., and Ceniceros, H. D., 'Field-induced control of ferrofluid emulsion rheology and droplet break-up in shear flows,' Physics of Fluids, 2018, **30**(12), p. 122110.

De Menech, M., 'Modeling of droplet breakup in a microfluidic t-shaped junction with a phase-field model,' Physical Review E, 2006, **73**(3), p. 031505.

Debruijn, R. A., *Deformation and breakup of drops in simple shear flows*, Ph.D. thesis, AA(Technische Univ., Eindhoven (Netherlands), 1991.

Eow, J. S. and Ghadiri, M., 'Motion, deformation and break-up of aqueous drops in oils under high electric field strengths,' Chemical Engineering and Processing: Process Intensification, 2003, **42**(4), pp. 259–272.

Feigl, K., Baniabedalruhman, A., Tanner, F. X., and Windhab, E. J., 'Numerical simulations of the breakup of emulsion droplets inside a spraying nozzle,' Physics of Fluids, 2016, **28**(12), p. 123103.

Fu, Y., Bai, L., Jin, Y., and Cheng, Y., 'Theoretical analysis and simulation of obstructed breakup of micro-droplet in t-junction under an asymmetric pressure difference,' Physics of Fluids, 2017, **29**(3), p. 032003.

Garstecki, P., Fuerstman, M. J., Stone, H. A., and Whitesides, G. M., 'Formation of droplets and bubbles in a microfluidic t-junction—scaling and mechanism of break-up,' Lab on a Chip, 2006, **6**(3), pp. 437–446.

Garstecki, P., Stone, H. A., and Whitesides, G. M., 'Mechanism for flow-rate controlled breakup in confined geometries: A route to monodisperse emulsions,' Physical review letters, 2005, **94**(16), p. 164501.

Grace, H. P., 'Dispersion phenomena in high viscosity immiscible fluid systems and application of static mixers as dispersion devices in such systems,' Chemical Engineering Communications, 1982, **14**(3-6), pp. 225–277.

Guido, S. and Villone, M., 'Three-dimensional shape of a drop under simple shear flow,' Journal of Rheology, 1998, **42**(2), pp. 395–415.

Guo, M. T., Rotem, A., Heyman, J. A., and Weitz, D. A., 'Droplet microfluidics for high-throughput biological assays,' Lab on a Chip, 2012, **12**(12), pp. 2146–2155.

Han, C., *Multiphase flow in polymer processing*, Elsevier, 2012.

Hassan, M. R., Zhang, J., and Wang, C., 'Deformation of a ferrofluid droplet in simple shear flows under uniform magnetic fields,' Physics of Fluids, 2018, **30**(9), p. 092002.

Jackson, B. A., Terhune, K. J., and King, L. B., 'Ionic liquid ferrofluid interface deformation and spray onset under electric and magnetic stresses,' Physics of Fluids, 2017, **29**(6), p. 064105.

Jansen, K., Agterof, W., and Mellema, J., 'Droplet breakup in concentrated emulsions,' Journal of rheology, 2001, **45**(1), pp. 227–236.

Katsikis, G., Cybulski, J. S., and Prakash, M., 'Synchronous universal droplet logic and control,' Nature Physics, 2015, **11**(7), p. 588.

Kennedy, M., Pozrikidis, C., and Skalak, R., 'Motion and deformation of liquid drops, and the rheology of dilute emulsions in simple shear flow,' Computers & fluids, 1994, **23**(2), pp. 251–278.

Larson, R. G., *The structure and rheology of complex fluids*, volume 150, Oxford university press New York, 1999.

Leshansky, A. M. and Pismen, L. M., 'Breakup of drops in a microfluidic t junction,' Physics of Fluids, 2009, **21**(2), p. 023303.

Li, J., Renardy, Y. Y., and Renardy, M., 'Numerical simulation of breakup of a viscous drop in simple shear flow through a volume-of-fluid method,' Physics of Fluids, 2000, **12**(2), pp. 269–282.

Link, D. R., Grasland-Mongrain, E., Duri, A., Sarrazin, F., Cheng, Z., Cristobal, G., Marquez, M., and Weitz, D. A., 'Electric control of droplets in microfluidic devices,' Angewandte Chemie International Edition, 2006, **45**(16), pp. 2556–2560.

Loewenberg, M. and Hinch, E., 'Numerical simulation of a concentrated emulsion in shear flow,' Journal of Fluid Mechanics, 1996, **321**, pp. 395–419.

Marks, C. R., 'Drop breakup and deformation in sudden onset strong flows,' 1998.

Mason, T. and Bibette, J., 'Shear rupturing of droplets in complex fluids,' Langmuir, 1997, **13**(17), pp. 4600–4613.

McClements, D. J., *Food emulsions: principles, practices, and techniques*, CRC press, 2015.

Mefford, O. T., Woodward, R. C., Goff, J. D., Vadala, T., Pierre, T. G. S., Dailey, J. P., and Riffle, J. S., 'Field-induced motion of ferrofluids through immiscible viscous media: Testbed for restorative treatment of retinal detachment,' Journal of Magnetism and Magnetic Materials, 2007, **311**(1), pp. 347–353.

Nielloud, F., *Pharmaceutical emulsions and suspensions: Revised and expanded*, CRC Press, 2000.

Rallison, J., 'The deformation of small viscous drops and bubbles in shear flows,' Annual review of fluid mechanics, 1984, **16**(1), pp. 45–66.

Ray, A., Varma, V. B., Jayaneel, P., Sudharsan, N., Wang, Z., and Ramanujan, R. V., 'On demand manipulation of ferrofluid droplets by magnetic fields,' Sensors and Actuators B: Chemical, 2017, **242**, pp. 760–768.

Rosenfeld, L., Lin, T., Derda, R., and Tang, S. K., 'Review and analysis of performance metrics of droplet microfluidics systems,' Microfluidics and nanofluidics, 2014, **16**(5), pp. 921–939.

Rosensweig, R. E., *Ferrohydrodynamics*, Cambridge University Press, 1985.

Rumscheidt, F. and Mason, S., 'Particle motions in sheared suspensions xi. internal circulation in fluid droplets (experimental),' Journal of Colloid Science, 1961, **16**(3), pp. 210–237.

Scarbolo, L., Bianco, F., and Soldati, A., 'Coalescence and breakup of large droplets in turbulent channel flow,' Physics of Fluids, 2015, **27**(7), p. 073302.

Sherwood, J., 'Breakup of fluid droplets in electric and magnetic fields,' Journal of Fluid Mechanics, 1988, **188**, pp. 133–146.

Shi, D., Bi, Q., and Zhou, R., 'Numerical simulation of a falling ferrofluid droplet in a uniform magnetic field by the voset method,' Numerical Heat Transfer, Part A: Applications, 2014, **66**(2), pp. 144–164.

Sibillo, V., Simeone, M., and Guido, S., 'Break-up of a newtonian drop in a viscoelastic matrix under simple shear flow,' Rheologica Acta, 2004, **43**(5), pp. 449–456.

Squires, T. M. and Quake, S. R., 'Microfluidics: Fluid physics at the nanoliter scale,' Reviews of modern physics, 2005, **77**(3), p. 977.

Stone, H. A., 'Dynamics of drop deformation and breakup in viscous fluids,' Annual Review of Fluid Mechanics, 1994, **26**(1), pp. 65–102.

Stone, H. A., Stroock, A. D., and Ajdari, A., 'Engineering flows in small devices: microfluidics toward a lab-on-a-chip,' Annu. Rev. Fluid Mech., 2004, **36**, pp. 381–411.

Stratton, J. A., *Electromagnetic theory*, volume 33, John Wiley & Sons, 2007.

Taylor, G. I., 'The viscosity of a fluid containing small drops of another fluid,' Proceedings of the Royal Society of London. Series A, Containing Papers of a Mathematical and Physical Character, 1932, **138**(834), pp. 41–48.

Taylor, G. I., 'The formation of emulsions in definable fields of flow,' Proceedings of the Royal Society of London. Series A, containing papers of a mathematical and physical character, 1934, **146**(858), pp. 501–523.

Taylor, G. I., 'Disintegration of water drops in an electric field,' Proceedings of the Royal Society of London. Series A. Mathematical and Physical Sciences, 1964, **280**(1382), pp. 383–397.

Tice, J. D., Lyon, A. D., and Ismagilov, R. F., 'Effects of viscosity on droplet formation and mixing in microfluidic channels,' Analytica chimica acta, 2004, **507**(1), pp. 73–77.

Van der Sman, R. and Van der Graaf, S., 'Emulsion droplet deformation and breakup with lattice boltzmann model,' Computer Physics Communications, 2008, **178**(7), pp. 492–504.

Vananroye, A., Van Puyvelde, P., and Moldenaers, P., 'Effect of confinement on droplet breakup in sheared emulsions,' Langmuir, 2006a, **22**(9), pp. 3972–3974.

Vananroye, A., Van Puyvelde, P., and Moldenaers, P., 'Structure development in confined polymer blends: steady-state shear flow and relaxation,' Langmuir, 2006b, **22**(5), pp. 2273–2280.

Varma, V. B., *Development of magnetic structures by micro-magnetofluidic techniques*, Ph.D. thesis, Nanyang Technological University, 2017.

Varma, V. B., Ray, A., Wang, Z. M., Wang, Z. P., and Ramanujan, R. V., 'Droplet merging on a lab-on-a-chip platform by uniform magnetic fields,' Scientific reports, 2016, **6**, p. 37671.

III. FERRO-HYDRODYNAMIC INTERACTIONS BETWEEN FERROFLUID DROPLET PAIRS IN SIMPLE SHEAR FLOWS

Md Rifat Hassan and Cheng Wang
Department of Mechanical & Aerospace Engineering
Missouri University of Science and Technology
Rolla, Missouri 65409
Tel: 573–341–4636, Fax: 573–341–4607
Email: wancheng@mst.edu

ABSTRACT

A numerical investigation on the interactions between a pair of equal-sized ferrofluid droplets in a simple shear flow subjected to uniform magnetic fields is carried out in this paper. Our numerical model utilizes a finite element method based level set algorithm to trace the topological changes along the droplet interface in two phase flows by coupling the flow and magnetic fields. Systematic numerical simulations with a well-resolved droplet interface are carried out in the Stokes flow limit (i.e., $\mathrm{Re} \leq 0.03$) to explore the effects of magnetic field direction, strength, and initial vertical offset on the pairwise interactions between the droplets. The findings indicate that in a solitary shear flow, a critical capillary number Ca_{cr} exists, beyond which the droplets exhibit separation through a sliding-over motion, instead of coalescence. Applying a uniform magnetic field along $\alpha = 0^\circ$ (i.e., parallel to the flow direction) results in a faster coalescence between the droplets. At $\alpha = 90^\circ$, a critical magnetic bond number Bo_{cr} appears where the droplets show a reversing motion behavior, instead of a passing-over motion leading to coalescence. In contrast, at $\alpha = 45^\circ$, the droplets separate away from each other, following a reversal motion at a capillary number where the droplets usually coalesce with each other in a solitary shear flow. Moreover, the effect of initial vertical offset on the interaction behavior of the droplets is examined, and it is found that the collision event is dependent on the initial vertical

separation distance between the droplets. Increasing the vertical separation distance along $\alpha = 0^\circ$ initiates faster coalescence, while at $\alpha = 90^\circ$, coalescence is delayed. Furthermore, at $\alpha = 45^\circ$, the droplets undergo a reversing motion and experience larger migration at increased vertical separation distances.

Keywords: Ferrofluid droplets, Magnetic field, Droplet pair, Droplet coalescence, Droplet interactions

1. INTRODUCTION

Droplets dispersed in another immiscible liquid are frequently encountered in a number of industrial applications that involve liquid-liquid extraction [Abeynaike *et al.*, 2012, Lifton, 2016, Nilsson *et al.*, 2013], emulsification [Jafari *et al.*, 2008, Lobo and Svereika, 2003], and in particular, polymer blending [Ionescu-Zanetti *et al.*, 2004, Shum *et al.*, 2008], which is one of the fastest and most commercial means of producing materials with improved properties. The microscale structure of a polymer blend, developed during the processing, is dependent on the droplet distribution and plays a pivotal role in the determination of the mechanical strength and permeability of the polymer blends.

It is a well known fact that when polymer processing involves complex flow fields, the droplet size and distribution are mainly affected by two key phenomena: droplet coalescence and breakup, which can also simultaneously occur in polymer blends. In general, coalescence is a more complex phenomenon than breakup since coalescence involves droplet-droplet interactions, while breakup requires a single drop and is not greatly influenced by the presence of neighboring drops in polymer blends [Loewenberg and Hinch, 1997]. The coalescence phenomenon mainly consists of three distinct phases: approach leading to collision, film drainage between liquid phases due to the flattening of the interfaces, and rupture leading to confluence. Sometimes, droplet collision does not inevitably result in coalescence, due to increased droplet deformation, which eventually decreases the probability of coalescence [Chesters, 1991].

In recent years, small scale mixing devices are getting more attention in the development stage of the polymer blends and composites [Cassagnau and Fenouillot, 2004, Son, 2009]; and due to their small size, the wall effects on the droplets can not be neglected. The flow in these types of mixing devices is a combination of both shear and extensional flow; however, shear flow is often considered as the main flow component. As a result, most of the studies in the literature are devoted to the structural organization of droplets in a confined shear flow [De Bruyn *et al.*, 2014], and in order to obtain a precise control on the size and shape of the droplets in a confined shear flow, a comprehensive understanding of the underlying hydrodynamics behind the interaction behavior between droplets is required.

Following the pioneering works of Taylor [Taylor, 1932, 1934], several authors investigated the collision between two droplets in a shear flow [Edwards *et al.*, 2009, Rother *et al.*, 1997]. Guido and Simeone [Guido and Simeone, 1998] used an optical microscopy to analyze droplet collision in a simple shear flow; however, the coalescence conditions were not mentioned in their work. Baldessari and Leal [Baldessari and Leal, 2006] performed a theoretical investigation on the interaction between a pair of droplets in a linear flow at a low capillary number and found that overall droplet deformation plays a crucial role on the drainage of the film during coalescence, while Jaeger et al. [Jaeger *et al.*, 1994] found that coalescence depends on the mobility of the interfaces. Burkhart et al. [Burkhart *et al.*, 2001] theoretically predicted the final size distribution of non-deformable drops in a dispersion based on the degree of droplet deformation. Moreover, a review on the potential of more classical forces, such as, dispersion and supramolecular forces on film rupture is provided by Bergeron [Bergeron, 1999].

Experimental investigations are mainly focused on the evolution of the final shape of the droplet or size distribution in a dispersion of droplets exposed to steady or transient flows [Lyu *et al.*, 2002, Marić and Macosko, 2002]. Chen et al. [Chen *et al.*, 2009] analyzed the confinement effect on droplet coalescence in a pure shear flow and found that coalescence is promoted by confinement. De Bruyn et al. [De Bruyn *et al.*, 2013] studied the effect

of initial offset in the velocity gradient direction on the coalescence proficiency of two droplets in a confined shear flow and found that confinement initiates reversal droplet trajectories at small initial offsets. Yang et al. [Yang *et al.*, 2001] and Ha et al. [Ha *et al.*, 2003] analyzed the individual flow-induced coalescence events under confined conditions, and their results suggest that droplet interactions involve a richer phenomena, which is dependent on the droplet deformation and corresponding hydrodynamic interactions among themselves. Furthermore, splitting and coalescence of droplets under confined conditions in microfluidic devices have been explored by Christopher et al. [Christopher *et al.*, 2009] and Chen et al. [Chen *et al.*, 2007].

Numerical simulations are useful in the study of droplet interactions, in situations with initial conditions that are difficult to implement in experiments. Additionally, the flexibility of numerical models provides a greater advantage in predicting the performance of coalescence in complex systems [Farhat and Lee, 2011, Yue *et al.*, 2005]. Chen and Wang [Chen and Wang, 2014] investigated droplets interaction in a shear flow under confinement using VOF method and found that an increase in confinement leads to a reversing motion instead of a passing-over motion. Shardt et al. [Shardt *et al.*, 2013] implemented a lattice Boltzmann method to study droplet coalescence in a simple shear flow and observed that with an increase in the droplet sizes, the critical capillary number decreases. In another work, a lattice Boltzmann method was implemented by Sun et al. [Sun *et al.*, 2013] to analyze head-on droplet collision, while Dupuy et al. [Dupuy *et al.*, 2010] used the Cahn-Hillard free energy method to examine coalescence for non-uniform systems.

Droplet rheology can also be manipulated by using external forces through an electric or magnetic field [Sherwood, 1988, Zakinyan *et al.*, 2012]. Salipante and Vlahovska [Salipante and Vlahovska, 2010] experimentally studied the electrohydrodynamics of drops under uniform DC electric fields and came to a conclusion that the threshold field strength of high viscous drops can be estimated using Quincke rotation criterion. Chen et al. [Chen *et al.*, 2015] performed both theoretical and numerical analyses on the alternating current

induced double droplets interaction in a microchannel to speculate the relationship between droplet separation and critical electric intensity. An experimental work on droplet coalescence in a polymer blend under the impact of electric fields was done by Aida et al. [Aida *et al.*, 2010].

In order to use magnetic fields as an additional means of manipulating the shape of a droplet, the droplet or continuous phase needs to be a ferrofluid — stable colloidal suspensions of nanoscale magnetic particles suspended in a non-magnetic carrier liquid and having a coating of surfactants to inhibit clumping. Since the fluids exhibit different magnetic properties, Maxwell stresses appear in the computational domain, which give rise to interfacial instabilities in ferrofluids [Cowley and Rosensweig, 1967]. An experimental study on the use of an alternating magnetic field on forced convective heat transfer using aqueous ferrofluids in a copper tube revealed a significant heat transfer enhancement [Ghofrani *et al.*, 2013]. Ray et al. [Ray *et al.*, 2017] performed both numerical and experimental investigations on the manipulation of ferrofluid droplets by a permanent magnet and observed coalescence and mixing of ferrofluid droplets under magnetic fields. Rowghanian et al. [Rowghanian *et al.*, 2016] implemented a computational scheme to study the dynamics of a ferrofluid droplet under spatially uniform magnetic fields, while a detailed investigation on a uniform magnetic field instigated ferrofluid droplet behavior in simple shear flows is shown in our recent works [Hassan and Wang, 2019, Hassan *et al.*, 2018].

However, most of the prevalent works are mainly concentrated on the hydrodynamic interactions between isolated droplet pairs in free shear flows at moderately high Reynolds numbers [Masiri *et al.*, 2019, Mazloomi Moqaddam *et al.*, 2016, Shardt *et al.*, 2013]. Recently, Santra et al. [Santra *et al.*, 2019] performed a numerical analysis on the pairwise interaction between droplets subjected to a transverse electric field in a shear flow at moderately high Reynolds number (i.e., Re = 0.2). Their results suggest that droplets undergo a reversing motion instead of a passing-over motion with an increase in the conductivity ratio. Additionally, application of an electric field results in an enhancement of emulsion stability

Table 1. Parameters and magnitudes.

Parameter	Symbol	Value	Unit
Density of droplet phase	ρ_d	1260	kg/m^3
Viscosity of droplet phase	η_d	0.105	Pa·s
Interfacial tension	σ	0.0135	N/m

in confined channels. However, until now, as per our knowledge, no one has ever studied the interaction phenomenon between a pair of droplets under the combined effect of shear flow and uniform magnetic fields in the Stokes flow limit, which is traditionally related to a diverse group of microfluidics applications [Baret *et al.*, 2009, Okushima *et al.*, 2004, Pautot *et al.*, 2003, Takeuchi *et al.*, 2005, Utada *et al.*, 2005, Xu *et al.*, 2005, Zhang and Xing, 2010, Zhang and Ozdemir, 2009, Zheng *et al.*, 2005, 2003]. Therefore, in this study, we concentrate on exploring the interaction behavior between a pair of isolated droplets in a simple shear flow under a uniform magnetic field, applied along several directions relative to the flow domain. A two-dimensional simulation (capable of correctly capturing the droplet interface with great computational efficiency) is implemented in our numerical model with an idea to investigate a broad range of variables i.e., magnetic field direction, strength, and initial vertical offset, which again couples the flow and magnetic fields by using a FEM based numerical approach (i.e., level set method).

The organization of the rest of the manuscript is as follows: We explain the computational model in Sec. 2, while the governing equations and numerical algorithms are described in Sec. 3. Then, the magnetic field strength and initial vertical offset effects on the droplet interaction behavior are illustrated in Sec. 4. Lastly, the crucial findings are summarized in Sec. 5.

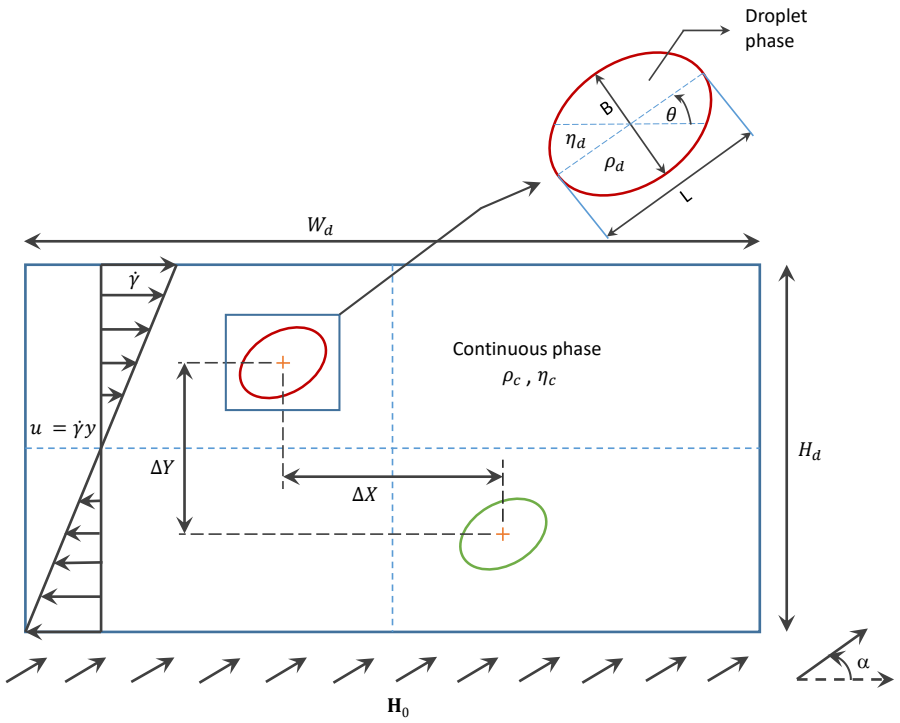

Figure 1. Graphic representation of the computational domain with a pair of suspended ferrofluid droplets in simple shear flows and uniform magnetic fields, $\mathbf{H}_0$.

2. COMPUTATIONAL MODEL

Figure 1 graphically represents a pair of buoyant ferrofluid droplets in a computational domain where the top and bottom walls translate with a velocity of the same magnitude, generated by a constant shear $\dot{\gamma}$, but in a direction opposite to each other (i.e., $\mathbf{u}_{tw} = \frac{1}{2}\dot{\gamma}H_d\mathbf{e}_x$ and $\mathbf{u}_{bw} = -\frac{1}{2}\dot{\gamma}H_d\mathbf{e}_x$). The parameter H_d represents the height of the flow domain, which equals to 10 times the initial radius of the droplet (i.e., $H_d = 10R_0$), while the width is considered twice the height of the domain (i.e., $W_d = 2H_d$). The domain size is also chosen to be large enough so that the confinement effect can be neglected.Guido and Villone [1998], Kennedy *et al.* [1994] The droplet phase is equally viscous and dense as the continuous phase (i.e., $\eta_c = \eta_d$ and $\rho_c = \rho_d$) and has a magnetic susceptibility equals to 1 (i.e., $\chi_d = 1$). On the other hand, the continuous phase is regarded as a non-magnetic medium ($\chi_c = 0$).

Initially, two ferrofluid droplets are symmetrically separated from each other with respect to the center of the computational domain by a horizontal distance ΔX along the flow direction, while a vertical distance ΔY is maintained along the velocity gradient direction. In spite of having a continuous velocity at the interface, the droplet experiences discontinuous forces along the interface due to the contribution from the effect of surface tension. The flow domain maintains a symmetric velocity field with respect to the center where the velocity diminishes to zero. Moreover, a periodic boundary condition is imposed on the left and right walls to ensure infinite periodicity in the direction of the flow. Next, the flow domain is treated with a uniform magnetic field, $\mathbf{H}_0$, along several directions α. Under combined magnetic and hydrodynamic forces, the droplet deforms and orients along different directions, which are denoted by the deformation parameter D and orientation angle θ, respectively.

3. NUMERICAL METHOD

3.1. LEVEL SET METHOD

In this study, an Eulerian strategy based conservative level-set method is enacted to track the topological changes along the droplet interface, which is considered as one of the most troublesome process in a wide range of applications that involve moving boundaries i.e., fluid-structure interactions, multi-phase flows etc. In a level set method, two fluid phases are separated by a smeared out heaviside scalar function ϕ, which assigns a value equals to 1 in the droplet phase and zero in the surrounding continuous phase, while maintaining a smooth transition over the droplet interface between 0 and 1. The exact position of the interface is defined by 0.5 isocontour of the scalar function ϕ. The level set equation, with the velocity advected scalar function ϕ, can be expressed as [Olsson and Kreiss, 2005]:

$$\frac{d\phi}{dt} + \mathbf{u} \cdot \nabla\phi = \gamma \nabla \cdot \left(\epsilon \nabla\phi - \phi(1-\phi) \frac{\nabla\phi}{|\nabla\phi|} \right). \tag{1}$$

In Equation 1, the variable **u** represents the velocity field, while the re-initialization amount and interface thickness are denoted by γ and ϵ, respectively. The right hand side terms involve higher order derivatives of ϕ, which are essential to keep the droplet interface intact in the simulation. The re-initialization parameter γ ensures that the level set function gradient remains concentrated to the droplet interface over time, and the maximum magnitude of the velocity field is considered as a suitable value of γ in the level set method. On the other hand, the parameter ϵ simply controls the thickness of the droplet interface where the variations of the level set functions are obtained, and it is set equal to half the maximum mesh size of the region passed by the droplets in the flow domain. Moreover, the level set function ϕ is used to calculate the unit normal to the interface **n** as:

$$\mathbf{n} = \frac{\nabla\phi}{|\nabla\phi|}. \tag{2}$$

Since multi-phase flows are considered as a single phase flow in the level set method, different properties of fluid, such as dynamic viscosity (η) and density (ρ) can be calculated through the following relations:

$$\eta = \eta_c + (\eta_d - \eta_c)\phi, \qquad \rho = \rho_c + (\rho_d - \rho_c)\phi. \tag{3}$$

Similarly, magnetic properties, such as, magnetic permeability (μ) and magnetic susceptibility (χ) can be approximated as:

$$\mu = \mu_c + (\mu_d - \mu_c)\phi, \qquad \chi = \chi_c + (\chi_d - \chi_c)\phi. \tag{4}$$

In Equations 3 and 4, the subscript c is used to define the properties of continuous phase, while the subscript d specifies the droplet phase properties in the computational domain.

COMSOL 5.3, a commercial finite element method (FEM) solver, is chosen in our numerical investigation to analyze pairwise interaction between droplets in shear flows under the influence of a uniform magnetic field. At first, laminar flow level set method along with transient phase initialization feature is implemented in our computational model with an aim to solving the flow domain and tracking the free interface of the droplet. The generation of a constant shear rate in the flow domain is achieved by using the moving wall feature from the laminar flow tree where the top and bottom walls move in opposite directions, but with a velocity of equal magnitude. The left and right walls are subjected to a periodic boundary condition to approximate an infinite domain in the x-direction. The flow field is then coupled with the magnetic field and simultaneously solved using the Magnetic fields, no current interface from the AC/DC module. Finally, following the creation of mesh using free triangular elements, a PARDISO solver with nested dissection multithread algorithm is employed to decipher the computation model.

3.2. GOVERNING EQUATIONS

The underlying physics of a multi-phase flow field involving two immiscible, isothermal, and viscous fluids under the presence of a magnetic field is typically governed by the incompressible Navier-Stokes equations:

$$\nabla \cdot \mathbf{u} = 0, \tag{5}$$

and

$$\rho \frac{D\mathbf{u}}{Dt} = -\nabla p + \nabla \cdot [\eta(\nabla \mathbf{u} + (\nabla \mathbf{u})^T)] + \mathbf{F}_\sigma + \mathbf{F}_m. \tag{6}$$

In Equation (6), $\frac{D\mathbf{u}}{Dt}$ represents the total derivative of the velocity field $\mathbf{u}$, which can be expanded as $\frac{\partial \mathbf{u}}{\partial t} + \mathbf{u} \cdot \nabla \mathbf{u}$. The force related to pressure is defined by p, while the interfacial tension and magnetic forces are denoted by $\mathbf{F}_\sigma$ and $\mathbf{F}_m$, respectively.

A Dirac delta function δ is used to calculate the interfacial tension force $\mathbf{F}_\sigma$:

$$\mathbf{F}_\sigma = \nabla \cdot [\sigma\{\mathbf{I} + (-\mathbf{n}\mathbf{n}^T)\}\delta], \tag{7}$$

where the level set function ϕ is utilized to approximate the Dirac delta function δ as:

$$\delta = 6|\phi(1-\phi)||\nabla\phi|. \tag{8}$$

Also, Equation (7) involves a interfacial tension coefficient σ, and $\mathbf{I}$ denotes the second-order identity tensor, while Equation (2) is used to find out the unit normal to the interface $\mathbf{n}$.

The application of a uniform magnetic field generates a magnetic stress tensor $\boldsymbol{\tau}_m$, and using $\boldsymbol{\tau}_m$, the magnetic force $\mathbf{F}_m$ can be formulated as [Rosensweig, 1985]:

$$\mathbf{F}_m = \nabla \cdot \boldsymbol{\tau}_m = \nabla \cdot (\mu\mathbf{H}\mathbf{H} - \frac{\mu}{2}H^2\mathbf{I}), \tag{9}$$

where H is the magnitude of the magnetic field $\mathbf{H}$ (i.e., $H = |\mathbf{H}|$), and μ is the permeability of the flow domain involving two fluid phases. In addition to the Maxwell equations, the calculation of the magnetic stress tensor τ_m requires a detailed understanding of the constitutive relationship between several important magnetic parameters, such as, magnetic field $\mathbf{H}$, magnetization $\mathbf{M}$, and magnetic induction $\mathbf{B}$, which are as follows [Stratton, 2007]:

$$\nabla \cdot \mathbf{B} = 0, \qquad \nabla \times \mathbf{H} = 0, \qquad \mathbf{M} = \chi\mathbf{H}, \quad \text{and} \quad \mathbf{B} = \mu_0(\mathbf{H} + \mathbf{M}) = \mu_0(1+\chi)\mathbf{H}, \tag{10}$$

where the physical constant μ_0 denotes the magnetic permeability in a classical vacuum, which equals to $4\pi \times 10^{-7}$ N/A^2. The gradient of a scalar potential ψ constitutes a curl-free magnetic field $\mathbf{H}$ (i.e., $\mathbf{H} = -\nabla\psi$), and accordingly it can be written as:

$$\nabla \cdot (\mu\nabla\psi) = 0. \tag{11}$$

Now, in order to non-dimensionalize the governing equations, the length of the flow domain is scaled by the radius of the droplet in undeformed condition R_0, whereas shear rate $\dot{\gamma}$ is used as a scaling parameter for time (i.e., $t^\star = t\dot{\gamma}$). Other dimensionless groups are as follows:

$$p^* = \frac{p}{\eta\dot{\gamma}},\ \ \eta^* = \frac{\eta}{\eta_c},\ \ \rho^* = \frac{\rho}{\rho_c},\ \ \mu^* = \frac{\mu}{\mu_0},\ \ \Delta X^* = \frac{\Delta X}{2R_0},\ \ \Delta Y^* = \frac{\Delta Y}{2R_0}, \text{and } \mathbf{H}^* = \frac{\mathbf{H}}{H_0}.$$

Accordingly, the incompressible Navier-Stokes Equations (5) and (6), in terms of dimensionless groups can be rewritten as:

$$\nabla^* \cdot \mathbf{u}^* = 0, \tag{12}$$

$$\mathrm{Re}\left(\rho^* \frac{D\mathbf{u}^*}{Dt^*}\right) = -\nabla^* p^* + \nabla^* \cdot \tau^* + 2\frac{\mathrm{Bo}_m}{\mathrm{Ca}}\nabla^* \cdot \boldsymbol{\tau}_m^* + \frac{1}{\mathrm{Ca}}\mathbf{F}_\sigma^*. \tag{13}$$

The nondimensionalization of governing Equations (5) and (6) results in the formation of three most important dimensionless groups: Reynolds number Re, magnetic bond number Bo_m, and capillary number Ca, which ultimately control the overall droplet dynamics in the computational domain and are as follows:

$$\mathrm{Re} = \frac{\rho_c {R_0}^2 \dot{\gamma}}{\eta_c}, \tag{14}$$

$$\mathrm{Ca} = \frac{\eta_c R_0 \dot{\gamma}}{\sigma}, \tag{15}$$

and

$$\mathrm{Bo}_m = \frac{R_0 \mu_0 {H_0}^2}{2\sigma}. \tag{16}$$

The other dimensionless parameters are denoted by the superscript $*$, whereas the permeability ratio ζ and viscosity ratio λ are written as:

$$\zeta = \frac{\mu_d}{\mu_0}, \quad \text{and} \quad \lambda = \frac{\eta_d}{\eta_c}. \tag{17}$$

In this task, we will focus on investigating the effects of some important dimensionless groups, i.e., Ca, Bo_m, α, and ΔY^* on the pairwise interaction between ferrofluid droplets in the Stokes flow regime (i.e., $\mathrm{Re} \lesssim 0.03$).

4. RESULTS AND DISCUSSIONS

4.1. VALIDATION OF THE NUMERICAL MODEL

In order to check the reliability of our results, we validated the numerical model against the prevalent works in the literature. Figure 2(a) represents the time evolution of the collision and coalescence of a pair of ferrofluid droplets in a simple shear flow at $\mathrm{Re} = 0.0002$ and $\mathrm{Ca} = 0.0037$. The vertical and horizontal separation distances are considered as $\Delta Y^* = 0.16$ and $\Delta X^* = 1.35$, respectively, and the results qualitatively agree well against the experimental findings of Chen et al. [Chen *et al.*, 2009]; however, the coalescence angle in our model is found to be different compared to the experimental findings. This disparity can be attributed to the the two-dimensional nature of the numerical simulation. Also, in the experiments, the magnitude of the Reynolds number was below 1×10^{-7} and the horizontal distance $\Delta X^\star$ was considered as 1.6, while it is considered as 1.35 in our numerical work to save some computational time. The deformation of the droplets at small and large capillary numbers is also validated against the theories given by Taylor [Taylor, 1932, 1934] and Cox [Cox, 1969], which is shown in Figure 2(b) and (c), respectively. Additionally, Figure 2(d) shows the comparison of the droplet trajectories in a confined simple shear flow at a moderately higher Reynolds number against the numerical findings of Chen and Wang [Chen and Wang, 2014], while droplet deformation during passing-over motion at $\mathrm{Re} \leq 0.03$ and $\mathrm{Ca} = 0.1$ is plotted against the experimental and numerical findings of Wang et al. [Wang *et al.*, 2016] in Figure 2(e), and all these results quantitatively agree very well with the existing findings in the literature.

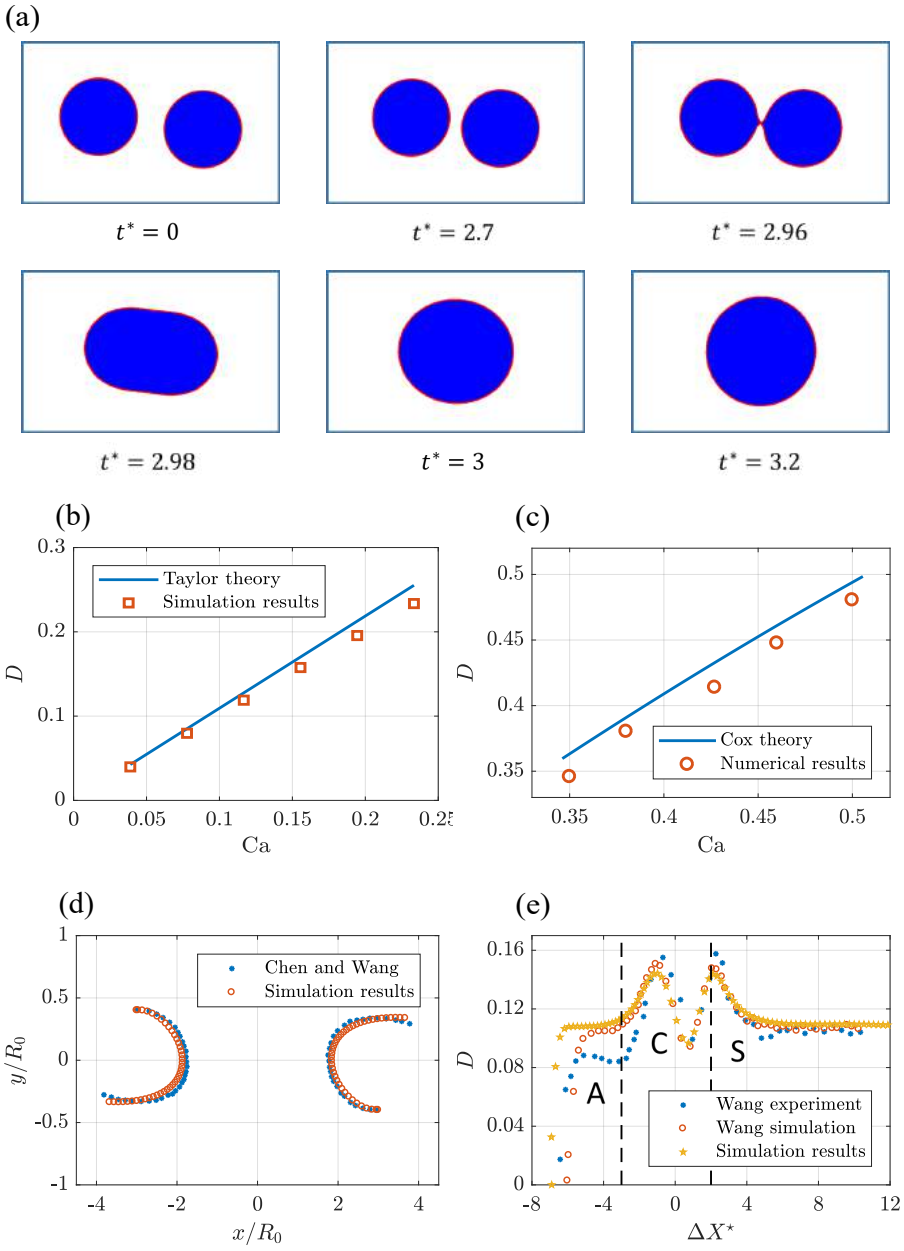

Figure 2. Validation of the numerical model. (a) Time evolution of the collision and coalescence of a pair of ferrofluid droplets in simple shear flows at Re = 0.0002, Ca = 0.0037, $\Delta Y^* = 0.16$, $\Delta X^* = 1.35$, and $\lambda = 1.1$; (b) Deformation at small Ca; (c) Deformation at large Ca; (d) Droplet trajectories in a simple shear flow at Re = 0.2, Ca = 0.2, and $R_0/H_d = 0.15$; and (e) Droplet deformation during passing-over motion at Re $\leq$ 0.03 and Ca = 0.1 where A, C, and S denote the approach, collision, and separation stages, respectively.

4.2. DROPLET PAIR INTERACTION IN SHEAR FLOWS

Taylor [Taylor, 1932, 1934] found out that under a simple shear flow droplets deform, and the droplet deformation in the limit of Stokes flow can be elucidated as:

$$D = \frac{L - B}{L + B} = \frac{19\eta_d + 16\eta_c}{16\eta_d + 16\eta_c}\text{Ca}, \tag{18}$$

where Ca denotes the capillary number (Equation 15). Moreover, existing works in the literature [Baldessari and Leal, 2006, Chen *et al.*, 2009] show that when two droplets are suspended in a simple shear flow, they either coalesce or slide over each other, and the outcome of the collision between the pair of droplets is determined by the capillary number, which also has a positive correlation with droplet deformation. In this section, first, the interaction between a pair of droplets is investigated at small capillary numbers (i.e., Ca ≤ 0.24).

Figure 3 shows the time evolution of collision and coalescence of a pair of droplets in a simple shear flow at low capillary numbers. The other parameters in this study are considered as $\Delta Y^* = 0.8$, $\Delta X^* = 4$, and $\lambda = 1$. From Figure 3, it can be seen that with the increase in the capillary number, the deformation of the droplet increases, which in turn aids the droplets to approach each other in a shear flow and form a rotating droplet pair. Concurrently, as the droplets proceed into close contact with each other, their interfaces flatten, and the fluid film between the droplets starts to drain. Eventually, when the fluid film becomes thin enough, the van der Waals intermolecular forces dominate and cause the fluid film to rupture, which ultimately contributes to droplet coalescence. In both cases, a coalescence is observed between the droplets, although the orientation angle of the droplets before the coalescence appears to be significantly different from each other as the shear rate increases. In order to have a better understanding of the orientation of the droplets during coalescence, a coalescence angle θ_c can be quantified as the angle in the clockwise direction from the negative x-axis to the the axis connecting the centroids of the droplets just before

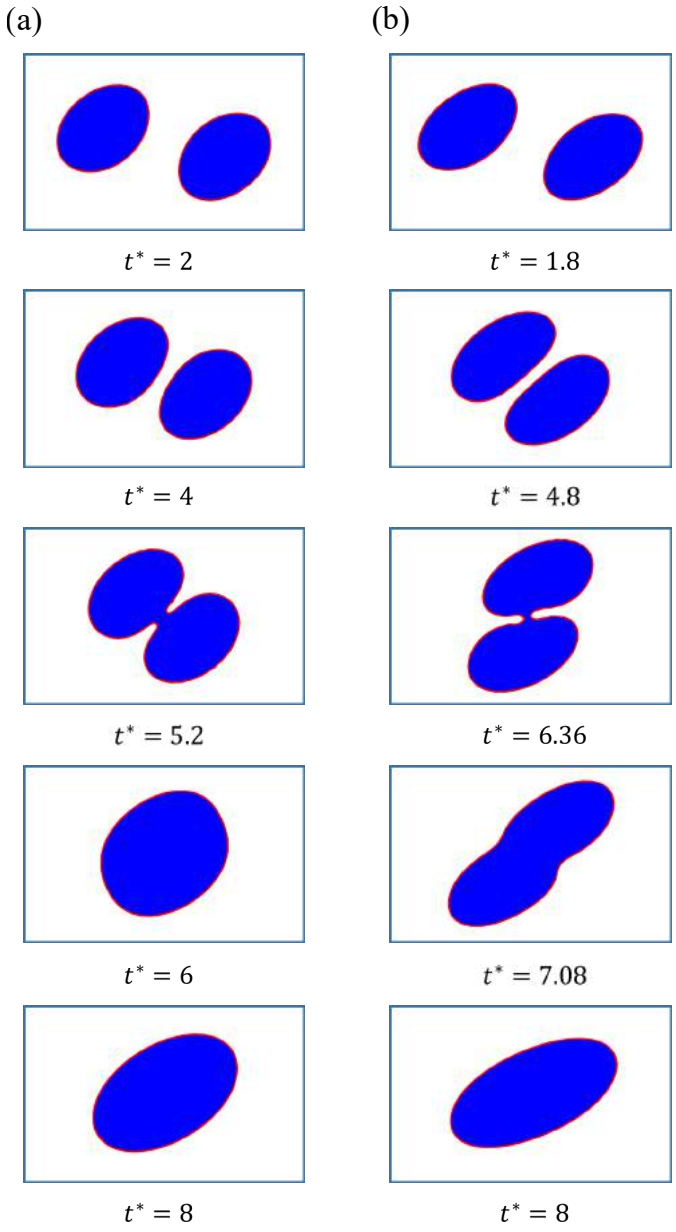

Figure 3. Time evolution of collision and coalescence of droplets under low shear rates at Re $\leq$ 0.03, $\Delta Y^* = 0.8$, $\Delta X^* = 4$, and $\lambda = 1$. (a) Ca = 0.15; and (b) Ca = 0.23.

the coalescence. Also, the steady state shape of the droplet after coalescence increases with the increase of the capillary number due to the enhanced deformation of the individual droplets at increasing shear rates, while the equilibrium orientation angle decreases.

The collision and coalescence phenomena between two droplets at small capillary numbers can be better explained by the velocity contours in the computational domain. Figure 4(a) depicts the velocity contours at Ca = 0.15, which shows that as time progresses, the deformed droplets start to approach each other and give rise to a vortex in between the two droplets. Eventually, when the droplets come close enough, the vortex between the droplets combines with the small vortices at the lower ends of the droplets, resulting in a larger vortex, which is then shared between the two droplets. Subsequently, the circulation inside the larger vortex contributes in bringing the droplet interfaces even closer, which then activates the van der Waals interaction forces to promote coalescence.

Figure 4(b) represents the trajectory of the droplets at small capillary numbers before coalescence, while the coalescence angles at different capillary numbers are plotted in Figure 4(c). From Figure 4(b), it can be seen that the droplets follow a similar kind of trajectory at all capillary numbers; however, with an increase in the shear rate, the vertical distance between the droplets increases during the approaching stage. Also, at higher shear rates, the droplets migrate further before coalescence, compared to the droplets at smaller shear rates, which increases the coalescence angle in bulk conditions (Figure 4(c)). These results are also similar to the results observed in the existing literature for pure extensional flow [Borrell *et al.*, 2004, Yoon *et al.*, 2005]. The major reason behind these phenomena can be attributed to the dependence of the drainage rate on the interaction force. Higher shear rates contribute to an increased droplet deformation due to the presence of greater hydrodynamic forces, which enlarges the the extent of contact area between the two droplets and minimizes the film thinning rate.

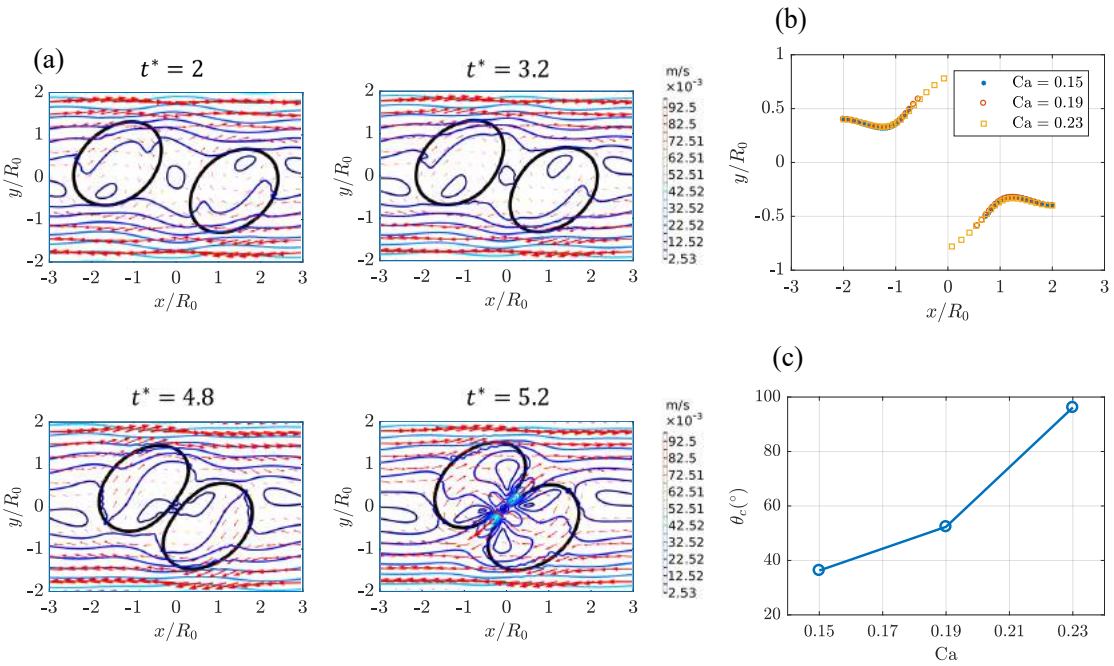

Figure 4. Interaction between a pair of droplets in shear flows at Re $\leq$ 0.03, $\Delta Y^* = 0.8$, $\Delta X^* = 4$, and $\lambda = 1$. (a) Velocity contours at Ca = 0.15; (b) Trajectory of droplets at small capillary numbers Ca; and (c) Coalescence angle θ_c vs Ca.

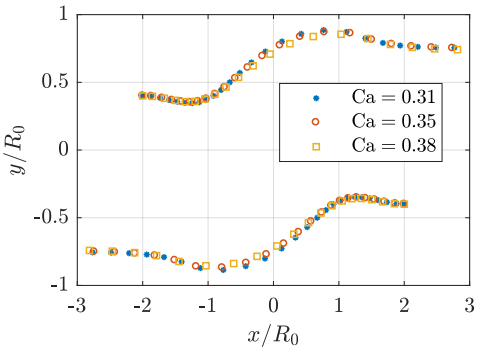

Figure 5. Trajectory of droplets under high shear rates at Re $\leq$ 0.03, $\Delta Y^* = 0.8$, $\Delta X^* = 4$, and $\lambda = 1$.

Now, we investigate the interaction phenomena between the droplet pair at moderately large capillary numbers (i.e., Ca $>$ 0.3) . Figure 5 shows the trajectory of droplets under high shear rates at Re $\leq$ 0.03 and $\lambda = 1$. Here, the same initial vertical and horizontal separation distance between the droplets are maintained as small capillary number cases. From Figure 5, it can be seen that the droplets slide over each other at all representative capillary numbers, since under these shear rates the droplets undergo greater deformation, and their interfaces flatten even more during approach, which makes the thinning of the fluid film difficult over the time of the collision. Also, at a specific capillary number, the vertical separation between the droplets decreases during the approach stage, and as soon as the droplets come into clear contact, they start to rotate over each other, which results in a sharp increase in the vertical offset between them. Subsequently, this vertical offset reaches a maximum point during the rotation and reaches an equilibrium position after the separation, which is clearly higher than the initial position before collision. These results are also in good agreement with the experimental [Chen *et al.*, 2009] and numerical [Chen and Wang, 2014] findings in the literature. Furthermore, these different trajectories of the droplets at variable shear rates suggest that there exists a critical capillary number where the droplets exhibit sliding-over motion, instead of coalescing, and from numerical simulations, the critical capillary number is found to be approximately 0.25 (i.e., $\mathrm{Ca}_{cr} \approx 0.25$).

The velocity and pressure fields are useful in providing deep insights into the hydrodynamic pairwise interaction between two droplets in a simple shear flow. Figure 6 shows the transient velocity and pressure contours of the passing over motion of a pair of ferrofluid droplets at Re $\leq$ 0.03, Ca = 0.38, and $\lambda = 1$. From Figure 6(a), it can be seen that two distinct types of velocity streamlines exist in the flow domain. One is called the passing-over streamlines, which are present throughout the major portion of the flow domain, i.e., top and bottom region of the flow domain. Another one is called the reversing streamlines, which is left behind the deformed droplets during the approach stage around the center of the flow domain. Moreover, during the approach stage, major portions of the

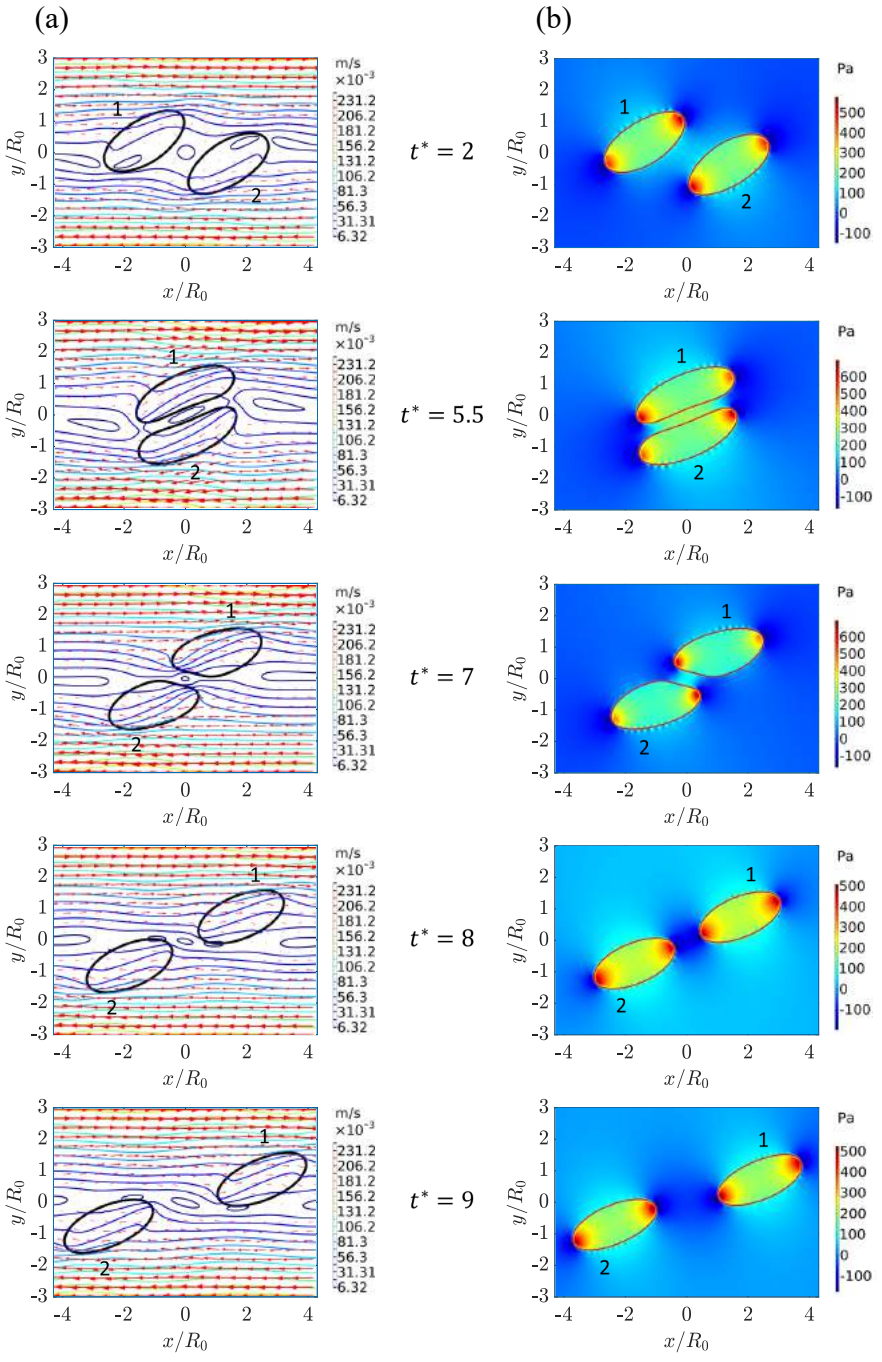

Figure 6. Time evolution of the passing-over motion of a pair of ferrofluid droplets in simple shear flows at Re $\leq$ 0.03, Ca = 0.38, and $\lambda = 1$. (a) Local velocity contours; and (b) Local pressure contours.

droplets on the upper and bottom region of the flow domain are exposed to the passing-over streamlines, which in turn generates a drag force that aids the droplets in going through a passing-over motion during the pairwise interaction of the droplets. Additionally, from Figure 6(b), it can be seen that due to the presence of shear, the droplets start to transform into ellipsoidal shapes, which consequently give rise to high pressure regions on the ends of the droplets along the major axis due to the surface tension effect that tends to keep the droplets spherical in shape ($t^* = 2$). As the droplets approach each other, the pressure in the matrix liquid between the droplets rises and navigates the matrix liquid towards the low pressure regions, which in turn contributes to the thinning of the lubrication film between the droplets. Eventually, the interfaces of the droplets flatten more due to the presence of the high pressure gradient along the interfaces of the droplets ($t^* = 5.5$). Afterwards, during the separation stage, the droplets start recoiling again into ellipsoidal shapes, followed by a thicker lubrication film, which drastically reduces the pressure in the fluid film between the droplets ($t^* = 8$). Moreover, this large pressure gradient in the fluid film is responsible for generating high curvature tips at the ends of the droplets. Also, no change in the pressure field is observed after the complete separation of the droplets, where the hydrodynamic interaction between the droplets becomes negligible. These results are also in good qualitative agreement with the numerical findings of Chen et al. [Chen and Wang, 2014].

Finally, the evolution of droplet deformation parameter D at different capillary numbers are plotted in Figure 7. From Figure 7(a), it can be seen that during coalescence, the droplet deformation continues to increase during the approach stage and then reaches a minimum during the merging stage. Subsequently, after coalescence, the droplet reaches a steady state deformation, which also increases with the increase of the capillary number. Also, in the passing-over region (Fig. 7(b)), the droplet follows an analogous deformation trend, except in this case a second maximum appears during the separation stage, which is

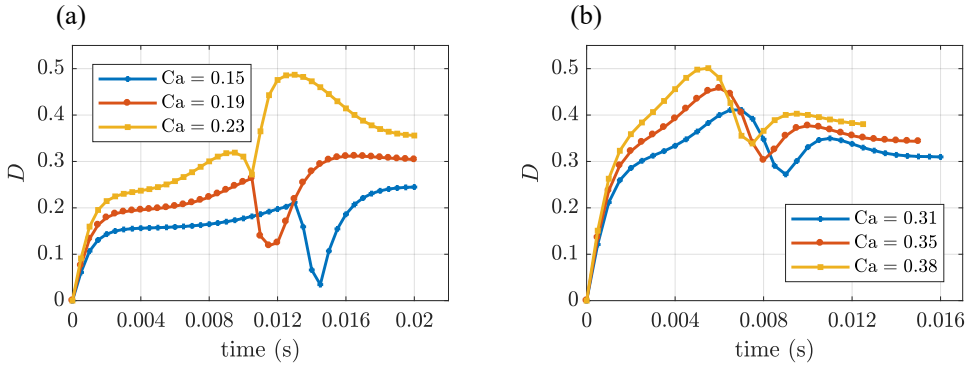

Figure 7. Deformation D vs time. (a) Coalescence region; and (b) Passing-over region.

also in qualitative agreement with experimental findings of Guido and Simeone [Guido and Simeone, 1998]. Nevertheless, the different results show that the capillary number plays a crucial role in the pairwise interaction of the droplets in a simple shear flow.

4.3. TRAJECTORY OF DROPLET PAIRS UNDER THE EFFECT OF MAGNETIC FIELD

Electric and magnetic fields introduce a mismatch in the normal stress distributions along the interface of the droplets due to the additional Maxwell stresses, which in turn offers the possibility of inducing topological changes on the interface of the droplets. Recently, Santra et al. [Santra *et al.*, 2019] investigated the electro-hydrodynamic interactions between two droplets in a shear flow under confinement and observed two varieties of motions, i.e., reversing motions and passing-over motions in the flow domain. In this section, we investigate the effect of uniform magnetic fields on the trajectory of the droplet pairs in a simple shear flow along several specific directions. The capillary number is kept constant (i.e., Ca = 0.15) throughout the rest of the study, while the initial horizontal and vertical separation distance are considered as $\Delta X^* = 4$ and $\Delta Y^* = 0.8$, respectively, unless mentioned otherwise.

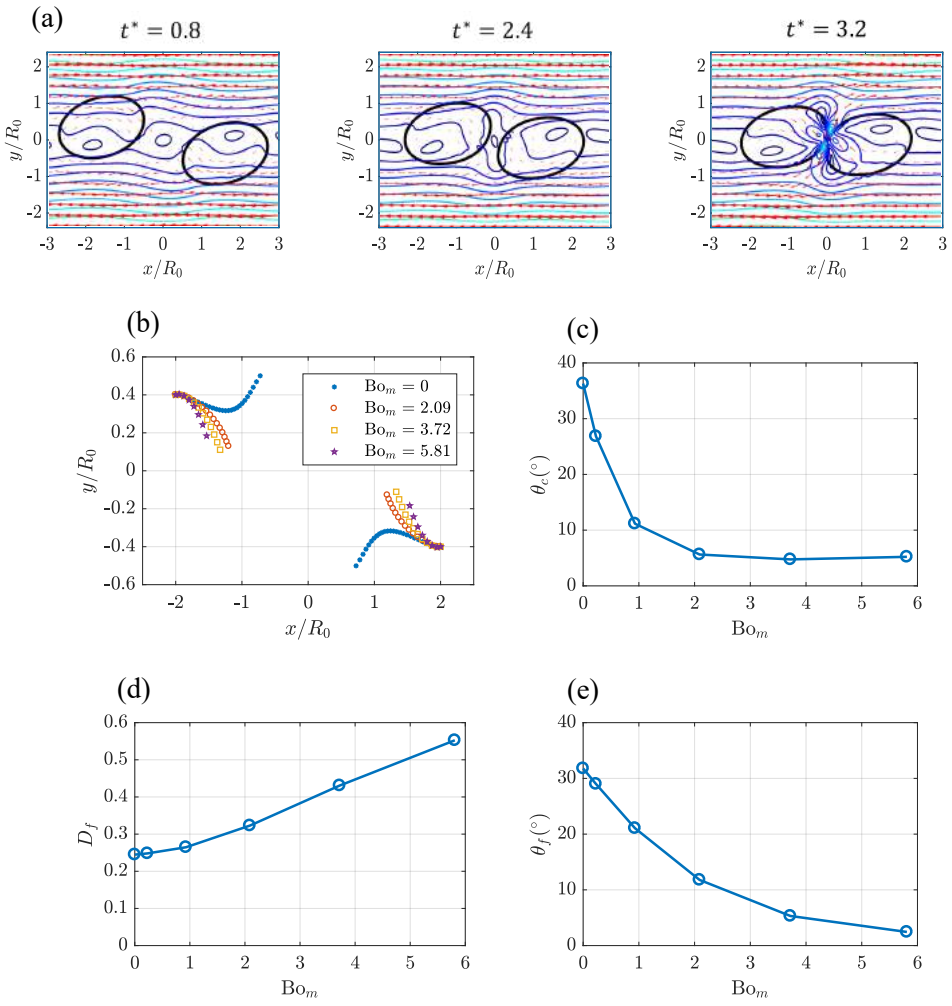

Figure 8. Effect of magnetic field strengths at $\alpha = 0°$, Re ≤ 0.03, Ca $= 0.15$, and $\lambda = 1$. (a) Time evolution of velocity contours at $\mathrm{Bo}_m = 2.09$; (b) Trajectory of droplets; (c) Coalescence angle θ_c vs Bo_m; (d) Steady state deformation D_f vs Bo_m; and (e) Steady state orientation angle θ_f vs Bo_m.

4.3.1. $\alpha = 0°$. Figure 8 shows the effect of magnetic field strengths applied along the flow direction (i.e., $\alpha = 0°$) at Re ≤ 0.03, Ca $= 0.15$, and $\lambda = 1$. Figure 8(a) shows that as soon as the magnetic field is applied (i.e., $\mathrm{Bo}_m = 2.09$), the droplets start to align themselves along the direction of the magnetic field with increased deformation, compared to the deformation in a simple shear flow alone. Also, as the orientation angle of the droplets reaches closer to 0°, the droplets follow the streamlines of the flow field more, which in turn generates a smaller vortex between the droplets. Additionally, with increased deformation the droplets approach each other faster, except in this case they do not undergo any rotational motion before coalescence. This is due to the droplets being more aligned with the flow field, which ultimately induces a reduction in the coalescence angle.

Figure 8(b) represents the trajectory of the droplets before coalescence, which further shows that an increase in magnetic field strength results in a decrease in the vertical separation distance between the droplets during the approach stage. Also, due to the increased deformation at higher magnetic field strengths, the droplets coalesce faster with a decreasing magnitude in coalescence angles (Figure 8(c)). Moreover, the coalescence angle reaches a saturation point around $\mathrm{Bo}_m = 4$. Furthermore, after the droplets coalesce, the steady state deformation of the droplet increases with an increase in the magnetic field strength (Figure 8(d)), while the orientation angle decreases (Figure 8(e)), which are also consistent with our previous findings [Hassan *et al.*, 2018].

4.3.2. $\alpha = 45°$. Now, the magnetic field is applied along 45° (i.e., $\alpha = 45°$) to investigate its effect on the interaction between two droplets, suspended in a shear flow. Figure 9 illustrates the trajectory of the droplets at Re ≤ 0.03, Ca $= 0.15$, and $\lambda = 1$. It can be seen that irrespective of the magnetic field strength, the droplets exhibit a reversing motion. Also, with the increase in magnetic field strength, the horizontal separation distance between the droplets increases due to the increased size of the width of the vortices between the droplets at higher magnetic field strengths. Moreover, after the separation stage

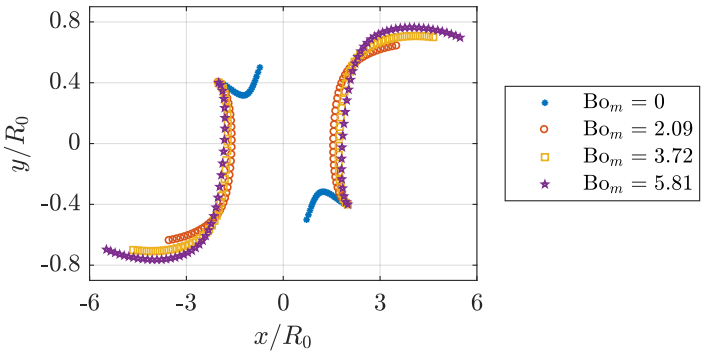

Figure 9. Trajectory of droplets under the effect of magnetic field strengths at $\alpha = 45°$, Re ≤ 0.03, Ca $= 0.15$, and $\lambda = 1$.

the droplets migrate further in the flow domain as the magnetic field strength increases, resulting in an increased vertical separation distance between the droplets at higher magnetic field strengths.

The reversing motion of the droplets can be better explained by the local velocity and pressure contours at $\mathrm{Bo}_m = 2.09$, illustrated in Figure 10. Similar to the passing-over motion described in the previous section (Figure 6), in Figure 10(a) as soon as the magnetic field is applied, the droplets turn into an ellipsoidal shape and align themselves along the direction of the magnetic field. Eventually, during the deformation process along the magnetic field direction, most of the volume of the drop is trapped into the reversing flow streamlines of the matrix liquid, which is left behind by the droplets in the approach stage along the center of the computational domain. This droplet entrainment into the reversing flow streamlines plays a crucial role in the reversing motion of the droplets. Furthermore, from Figure 10(b), it can be seen that as the droplets approach each other, the pressure in the matrix liquid between the droplets builds up; however, the pressure difference during the collision stage in the reversing motion appears smaller than the pressure difference in the passing over motion, resulting in a less flattened droplet interfaces. Also, during the separation stage the droplets are highly stretched at the ends along the major axis with larger

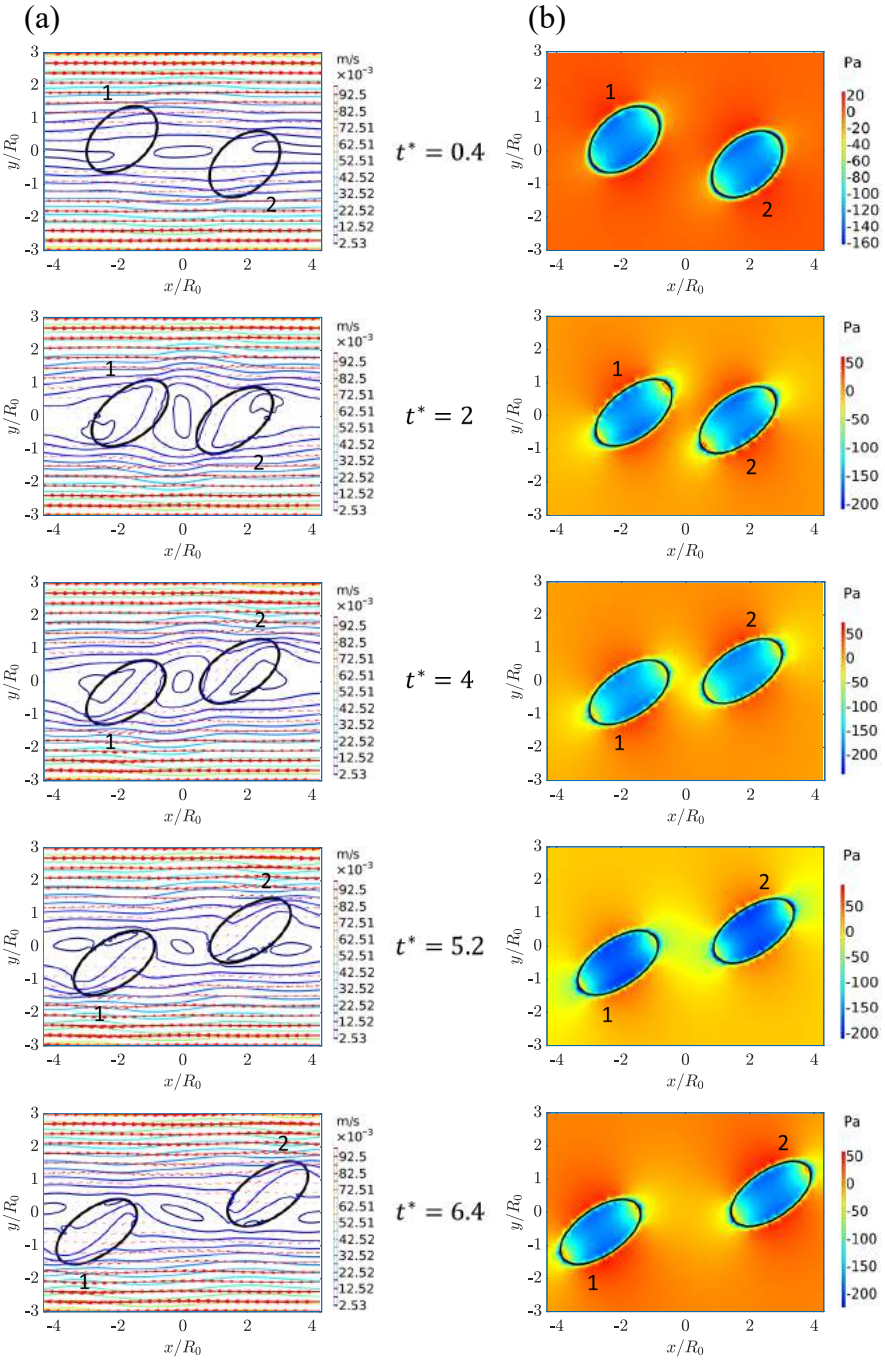

Figure 10. Time evolution of the reversing motion of a pair of ferrofluid droplets under the effect of magnetic field strengths at $\alpha = 45°$, $\mathrm{Bo}_m = 2.09$, $\mathrm{Re} \leq 0.03$, $\mathrm{Ca} = 0.15$, and $\lambda = 1$. (a) Local velocity contours; and (b) Local pressure contours.

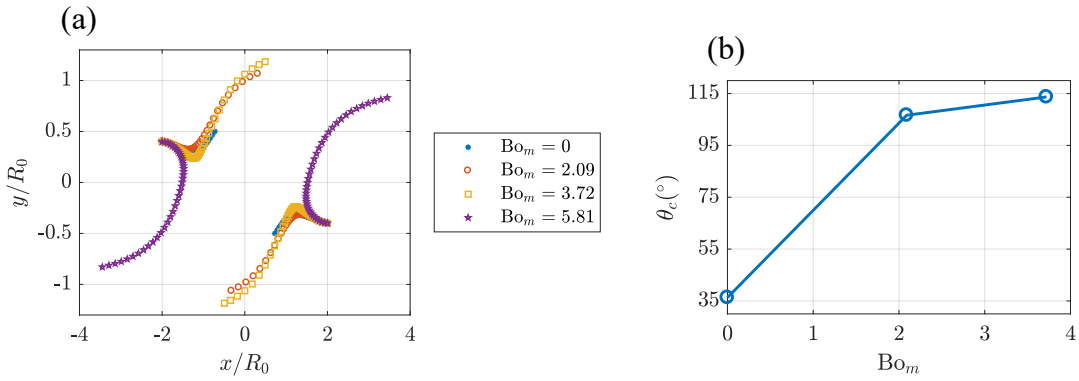

Figure 11. Interaction phenomena between a pair of droplets under uniform magnetic field strengths at $\alpha = 90°$, Re ≤ 0.03, Ca $= 0.15$, and $\lambda = 1$. (a) Trajectory of droplets; and (b) Coalescence angle θ_c vs Bo_m.

curvature, compared to the droplet interface curvature in the passing-over motion, which is also consistent with the inverse relationship of the pressure gradient at the droplet interface with the radius of interface curvature, according to Young-Laplace equation.

4.3.3. $\alpha = 90°$. Finally, we apply the magnetic field perpendicularly to the direction of flow field (i.e., $\alpha = 90°$). Figure 11 shows the interaction phenomena between a pair of droplets under uniform magnetic field strengths at Re ≤ 0.03, Ca $= 0.15$, and $\lambda = 1$. Figure 11(a) suggests that with the increase in the magnetic field strength up to $\mathrm{Bo}_m = 3.72$, the droplets undergo a passing-over motion and eventually coalesce with one another; however, at a higher magnetic field strength (i.e., $\mathrm{Bo}_m = 5.81$), the droplets exhibit reversing motion. Also, during the approach stage in the passing-over motion, the vertical separation distance between the droplets decreases with the increase in the magnetic field strength, while it increases during the collision stage before coalescence, which consequently increases the magnitude of the coalescence angle, illustrated in Figure 11(b). Moreover, the results suggest that at $\alpha = 90°$, a critical magnetic bond number exists where the droplets experience reversing motion instead of coalescence, which is considered to be approximately 3.9 (i.e., $\mathrm{Bo}_{cr} \approx 3.9$).

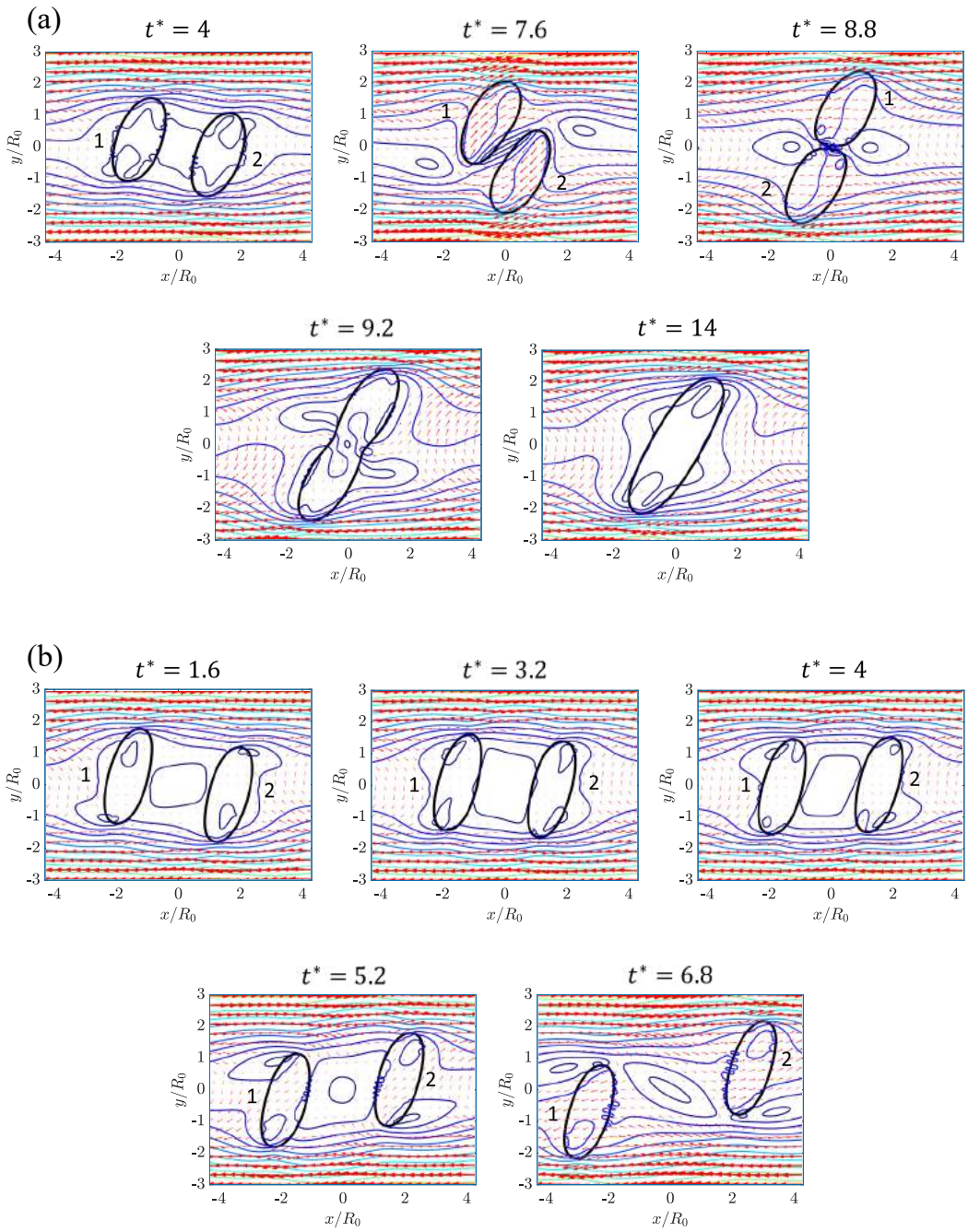

Figure 12. Local velocity contours under the effect of magnetic field strengths at $\alpha = 90°$, Re ≤ 0.03, Ca $= 0.15$, and $\lambda = 1$. (a) $\mathrm{Bo}_m = 3.72$; and (b) $\mathrm{Bo}_m = 5.81$.

Figure 12(a) represents the local velocity contours for one of the scenarios when the droplets undergo coalescence at $\mathrm{Bo}_m = 3.72$, while Figure 12(b) shows the velocity contours for the reversing motion at $\mathrm{Bo}_m = 5.81$. From Figure 12(a), it can be seen that with the application of the magnetic field, the droplets tend to align themselves along the direction of the magnetic field with increased deformation, resulting in a vortex between the droplets. Moreover, as the droplets approach each other, most of the volume of the droplet is exposed to the passing over streamlines ($t^\star = 7.6$), which in turn generates a rotational motion between the pair of droplets. Eventually, when the droplet interfaces get closer, it activates the van der Waals molecular attraction forces, which ultimately leads to coalescence. On the other hand, Figure 12(b) shows that as the droplets undergo greater deformation with increased magnetic field strength, a larger volume of fluid is trapped between them during the approach stage, generating a larger vortex between the droplets ($t^\star = 1.6$). As a result, most of the parts of the droplets are entrained into the reversing streamlines, which leads to the reversing motion. Overall, the different results along the mentioned arbitrary directions indicate that it is possible to induce either passing-over motion or reversing motion between a pair of droplets in a simple shear flow even at a capillary number where only coalescence is observed.

4.4. EFFECT OF VERTICAL SEPARATION ON THE TRAJECTORY OF DROPLET PAIRS

In addition to the hydrodynamic effects, the event of a collision between two droplets is dependent on several other factors at which the intermolecular forces play an important role in destabilizing the film between two colliding droplets, resulting in a coalescence. The reliance of these parameters on the critical capillary number can be demonstrated as [Shardt *et al.*, 2013]:

$$\mathrm{Ca}_{cr} = \mathrm{Ca}_{cr}\left(\mathrm{Re}, \Delta Y^\star, \Delta X^\star, \frac{2R}{H_d}\right). \tag{19}$$

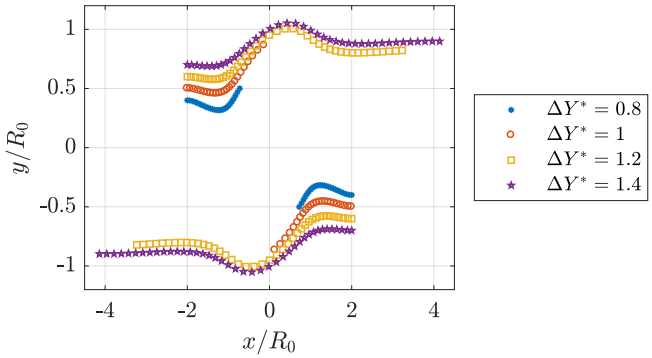

Figure 13. Initial vertical separation effect on the trajectory of the droplets at Re $\leq$ 0.03, Ca = 0.15, and λ = 1.

Keeping the Reynolds number and viscosity ratio fixed (i.e., Re $\leq$ 0.03 and λ = 1), in this section, first, we investigate the effect of vertical separation distance on the interaction behavior of two droplets in a simple shear flow and then apply a magnetic field along some specific directions.

Figure 13 shows the effect of vertical separation on the trajectory of droplets at Re $\leq$ 0.03, Ca = 0.15, and λ = 1. It can be seen that the droplets exhibit two distinct types of interaction behavior at different vertical separation distances, i.e., coalescence occurs when the magnitude of vertical separation distance is less than or equal to 1 ($\Delta Y^\star \leq 1$), while they experience a passing-over motion at $\Delta Y^\star > 1$. Also, with the increase in the vertical separation distance, in the coalescence region, the coalescence angle increases, while the droplets migrate further in the flow domain in the passing-over region and eventually find an equilibrium position after the separation stage at $\Delta Y^\star > 1$.

Figure 14 depicts the time evolution of local velocity contours for two distinct types of interactions. At $\Delta Y^\star = 1$ (Figure 14(a)), as the droplets approach each other with increased deformation, a portion of the matrix liquid gets trapped between them, resulting in a smaller vortex, which with the passage of time ultimately combines with the vortices at the lower ends of the deformed droplets to cause coalescence. On the other hand, at $\Delta Y^\star = 1.4$ (Figure 14(b)), with increased vertical separation, a larger portion of fluid

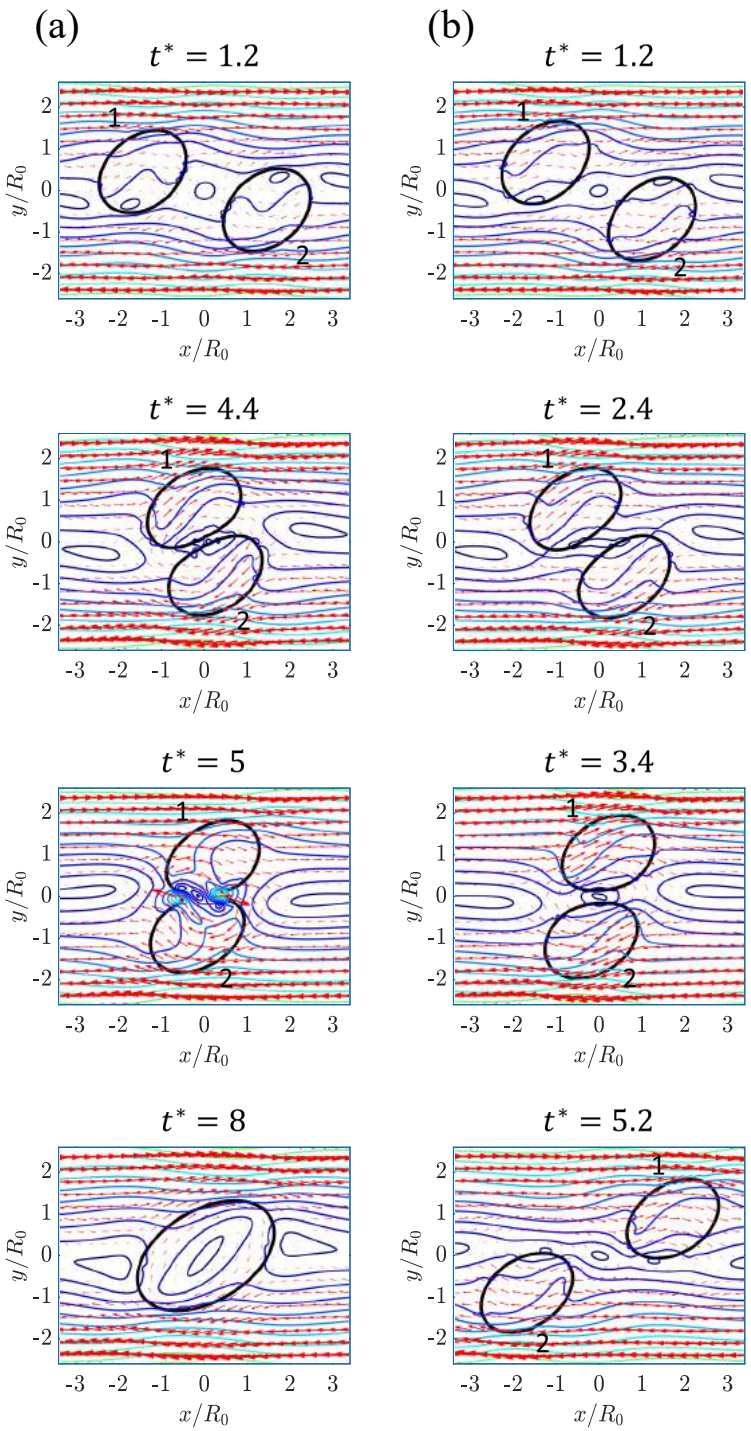

Figure 14. Local velocity contours at Re $\leq$ 0.03 and Ca = 0.15. (a) $\Delta Y^* = 1$; and (b) $\Delta Y^* = 1.4$.

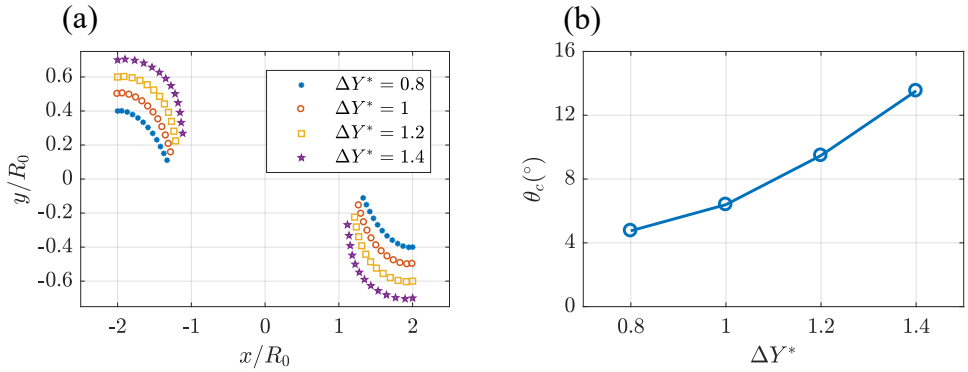

Figure 15. Effect of initial vertical separation under applied magnetic field strengths at $\alpha = 0^\circ$, $\mathrm{Bo}_m = 3.72$, and $\mathrm{Ca} = 0.15$. (a) Trajectory of droplets; and (b) Coalescence angle θ_c vs ΔY^*.

is trapped between the droplets, resulting in a bigger vortex, which eventually prevents the droplet interfaces from draining the matrix liquid during the collision stage, i.e., the droplets separate from each other. Also, with the increase in the vertical offset, the ends of the droplets get more exposed to increased shear rates, creating a greater drag force, which consequently helps the droplets to migrate further away from each other.

4.4.1. $\alpha = 0^\circ$. Now, the magnetic field is applied in a direction parallel to the direction of the flow (i.e., $\alpha = 0^\circ$) to analyze the magnetic field effect on the droplet interaction behavior at variable vertical separation distances. Figure 15(a) shows that at a certain magnetic field strength (i.e., $\mathrm{Bo}_m = 3.72$) along $\alpha = 0^\circ$, the horizontal separation distance between the droplets decreases during the approach stage with the increase in $\Delta Y^\star$; however, the droplets show similar kind of trajectories at all $\Delta Y^\star$. This happens because as the vertical separation increases, the ends of the droplets are exposed to greater shear rates, resulting in a greater drag force, which pushes the droplets closer to each other during the approach stage. Also, more fluid in the matrix phase is trapped into the space between the two droplets, resulting in a stronger vortex. Subsequently, during the approach stage, this stronger vortex aids in the faster drainage of the film between the two droplet interfaces, and

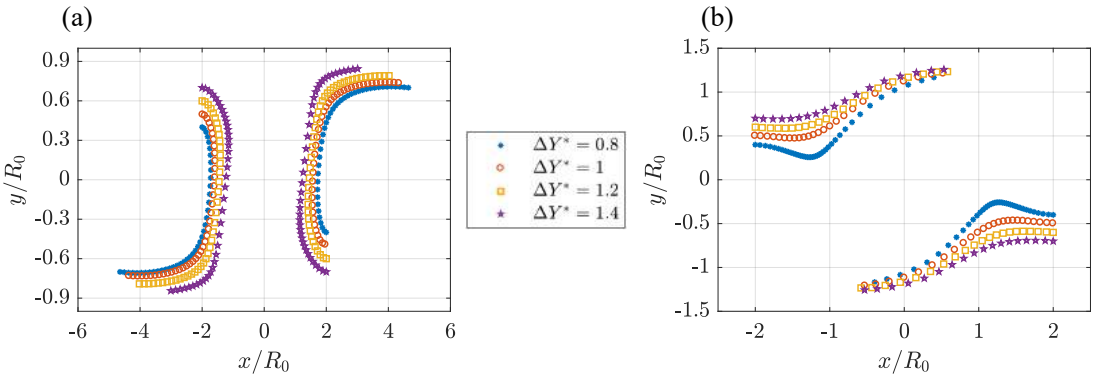

Figure 16. Effect of initial vertical separation on the trajectory of droplets under magnetic field strengths at $\mathrm{Bo}_m = 3.72$, and $\mathrm{Ca} = 0.15$. (a) $\alpha = 45°$; and (b) $\alpha = 90°$.

eventually, due to the faster drainage of the film between the droplet interfaces, an increase in the magnitude of the coalescence angle is also observed with the increase in the vertical separation distance $\Delta Y^\star$, which is illustrated in Figure 15(b).

4.4.2. $\alpha = 45°, 90°$. Figure 16(a) illustrates the effect of magnetic field strength, applied along 45°, on the droplet trajectories at variable vertical distance. It can be seen that the droplets undergo a reversing motion at every $\Delta Y^\star$; however, with increasing vertical separation distance, the droplets migrate further in the flow domain. The major reason behind this particular phenomenon can be attributed to the formation of a stronger vortex due to the entrainment of a larger portion of matrix fluid between the droplets, which ultimately creates a stronger drag force that later aids the droplet in migrating further in the flow domain. Interestingly, as the vertical separation distance $\Delta Y^\star$ increases, the horizontal separation distance $\Delta X^\star$ between the droplets decreases during the approach stage. Also, the droplets find an equilibrium position in the domain faster at an increased $\Delta Y^\star$ after going through a reversing motion.

Finally, the magnetic field is applied perpendicularly to the flow domain (i.e., $\alpha = 90°$) to analyze its effect on droplet interaction behavior at variable vertical separation distances $\Delta Y^\star$. From Figure 16(b), it can be seen that irrespective of all $\Delta Y^\star$, the droplets follow a similar kind of trajectory and experience a passing-over motion before

coalescence. Also, an increased magnitude of $\Delta Y^{\star}$ leads to a delayed coalescence due to the larger separation distance during the passing-over stage, i.e., coalescence angle increases. Nevertheless, the results show that coalescence can be either rushed or delayed by applying magnetic field strength along $\alpha = 0^{\circ}$ and 90°, respectively, at different vertical separation distances, while at $\alpha = 45^{\circ}$, increased vertical separation distance leads to a larger droplet migration in the flow domain.

5. CONCLUSION

At a low Reynolds number (i.e., $\mathrm{Re} \leq 0.03$), this paper systematically investigates the ferro-hydrodynamic interaction between two ferrofluid droplets in simple shear flows under the application of a uniform magnetic field. The findings from the results suggest that without the presence of any external force fields, at low capillary numbers (i.e., $\mathrm{Ca} \leq 0.24$), the droplets experience a passing-over motion and eventually coalesce with one another. The coalescence angle of the droplets increases with the increase in the capillary number. Contrarily, if two droplets are suspended in a shear flow at moderately high capillary numbers (i.e., $\mathrm{Ca} > 0.3$), they exhibit a passing over motion and separate away from each other. We found that there exists a critical capillary number Ca_{cr} where the droplets slide over each other instead of coalescing, and the numerical results suggest this value to be approximately 0.25 ($\mathrm{Ca}_{cr} \approx 0.25$). Additionally, applying a magnetic field in a direction parallel to the flow direction (i.e., $\alpha = 0^{\circ}$) at a low capillary number (i.e., $\mathrm{Ca} = 0.15$) results in faster coalescence of the droplets with a decrease in the magnitude of the coalescence angle, while along $\alpha = 45^{\circ}$, the droplets experience a reversing motion and separate away from each other at all magnetic bond numbers Bo_m. Moreover, when the magnetic field is applied perpendicularly to the flow direction (i.e., $\alpha = 90^{\circ}$), a passing-over motion leading to coalescence is observed at low magnetic bond numbers (i.e., $\mathrm{Bo}_m \leq 3.72$), whereas at a higher magnetic bond number (i.e., $\mathrm{Bo}_m = 5.81$), the droplets undergo a reversing motion

and separate away from each other. The critical magnetic bond number Bo_{cr} at which the droplets show this reversing motion behavior instead of a passing motion behavior along $\alpha = 90^\circ$ is found to be approximately 3.9 (i.e., $\mathrm{Bo}_{cr}^{90^\circ} \approx 3.9$).

Furthermore, we investigated the effect of initial vertical separation distance on the trajectories of the droplets in a simple shear flow at a small capillary number (i.e., Ca = 0.15) and found that the droplets coalesce when they are initially separated through a distance $\Delta Y^\star \leq 1$, whereas they separate away from each other following a passing-over motion at $\Delta Y^\star > 1$. Moreover, when a particular magnetic field strength (i.e., $\mathrm{Bo}_m = 3.72$) is applied to the flow domain along $\alpha = 0^\circ$, an increase in the vertical separation distance $\Delta Y^\star$ aids in faster coalescence of the droplets, while along $\alpha = 90^\circ$, an increase in the vertical separation distance $\Delta Y^\star$ delays coalescence. In contrast, application of a magnetic field along 45° at an increased vertical separation distance $\Delta Y^\star$ results in further migration of the droplets in the flow domain. Overall, these results indicate the usefulness of a uniform magnetic field as a potential tool for controlling the interaction behavior of the droplets in a shear flow, which is relevant to various microfluidics applications and polymer processing.

ACKNOWLEDGMENTS

The authors gratefully acknowledge the financial support from the Department of Mechanical and Aerospace Engineering (MAE) and the Center for Biomedical Research (CBR) at Missouri University of Science and Technology.

REFERENCES

Abeynaike, A., Sederman, A., Khan, Y., Johns, M., Davidson, J., and Mackley, M., 'The experimental measurement and modelling of sedimentation and creaming for glycerol/biodiesel droplet dispersions,' Chemical engineering science, 2012, **79**, pp. 125–137.

Aida, K., Na, Y. H., Nagaya, T., and Orihara, H., 'Droplet coalescence process under electric fields in an immiscible polymer blend,' Physical Review E, 2010, **82**(3), p. 031805.

Baldessari, F. and Leal, L. G., 'Effect of overall drop deformation on flow-induced coalescence at low capillary numbers,' Physics of fluids, 2006, **18**(1), p. 013602.

Baret, J.-C., Miller, O. J., Taly, V., Ryckelynck, M., El-Harrak, A., Frenz, L., Rick, C., Samuels, M. L., Hutchison, J. B., Agresti, J. J., *et al.*, 'Fluorescence-activated droplet sorting (fads): efficient microfluidic cell sorting based on enzymatic activity,' Lab on a Chip, 2009, **9**(13), pp. 1850–1858.

Bergeron, V., 'Forces and structure in thin liquid soap films,' Journal of Physics: Condensed Matter, 1999, **11**(19), p. R215.

Borrell, M., Yoon, Y., and Leal, L. G., 'Experimental analysis of the coalescence process via head-on collisions in a time-dependent flow,' Physics of Fluids, 2004, **16**(11), pp. 3945–3954.

Burkhart, B. E., Gopalkrishnan, P. V., Hudson, S. D., Jamieson, A. M., Rother, M. A., and Davis, R. H., 'Droplet growth by coalescence in binary fluid mixtures,' Physical review letters, 2001, **87**(9), p. 098304.

Cassagnau, P. and Fenouillot, F., 'Rheological study of mixing in molten polymers: 1-mixing of low viscous additives,' Polymer, 2004, **45**(23), pp. 8019–8030.

Chen, D., Cardinaels, R., and Moldenaers, P., 'Effect of confinement on droplet coalescence in shear flow,' Langmuir, 2009, **25**(22), pp. 12885–12893.

Chen, D. L., Li, L., Reyes, S., Adamson, D. N., and Ismagilov, R. F., 'Using three-phase flow of immiscible liquids to prevent coalescence of droplets in microfluidic channels: criteria to identify the third liquid and validation with protein crystallization,' Langmuir, 2007, **23**(4), pp. 2255–2260.

Chen, X., Song, Y., Li, D., and Hu, G., 'Deformation and interaction of droplet pairs in a microchannel under ac electric fields,' Physical Review Applied, 2015, **4**(2), p. 024005.

Chen, Y. and Wang, C., 'Hydrodynamic interaction of two deformable drops in confined shear flow,' Physical Review E, 2014, **90**(3), p. 033010.

Chesters, A., 'Modelling of coalescence processes in fluid-liquid dispersions: a review of current understanding,' Chemical engineering research and design, 1991, **69**(A4), pp. 259–270.

Christopher, G., Bergstein, J., End, N., Poon, M., Nguyen, C., and Anna, S. L., 'Coalescence and splitting of confined droplets at microfluidic junctions,' Lab on a Chip, 2009, **9**(8), pp. 1102–1109.

Cowley, M. and Rosensweig, R. E., 'The interfacial stability of a ferromagnetic fluid,' Journal of Fluid mechanics, 1967, **30**(4), pp. 671–688.

Cox, R., 'The deformation of a drop in a general time-dependent fluid flow,' Journal of fluid mechanics, 1969, **37**(3), pp. 601–623.

De Bruyn, P., Cardinaels, R., and Moldenaers, P., 'The effect of geometrical confinement on coalescence efficiency of droplet pairs in shear flow,' Journal of colloid and interface science, 2013, **409**, pp. 183–192.

De Bruyn, P., Chen, D., Moldenaers, P., and Cardinaels, R., 'The effects of geometrical confinement and viscosity ratio on the coalescence of droplet pairs in shear flow,' Journal of Rheology, 2014, **58**(6), pp. 1955–1980.

Dupuy, P. M., Fernandino, M., Jakobsen, H. A., and Svendsen, H. F., 'Using cahn–hilliard mobility to simulate coalescence dynamics,' Computers & Mathematics with Applications, 2010, **59**(7), pp. 2246–2259.

Edwards, S. A., Carnie, S. L., Manor, O., and Chan, D. Y., 'Effects of internal flow and viscosity ratio on measurements of dynamic forces between deformable drops,' Langmuir, 2009, **25**(6), pp. 3352–3355.

Farhat, H. and Lee, J. S., 'Suppressing the coalescence in the multi-component lattice boltzmann method,' Microfluidics and nanofluidics, 2011, **11**(2), pp. 137–143.

Ghofrani, A., Dibaei, M., Sima, A. H., and Shafii, M., 'Experimental investigation on laminar forced convection heat transfer of ferrofluids under an alternating magnetic field,' Experimental Thermal and Fluid Science, 2013, **49**, pp. 193–200.

Guido, S. and Simeone, M., 'Binary collision of drops in simple shear flow by computer-assisted video optical microscopy,' Journal of Fluid Mechanics, 1998, **357**, pp. 1–20.

Guido, S. and Villone, M., 'Three-dimensional shape of a drop under simple shear flow,' Journal of Rheology, 1998, **42**(2), pp. 395–415.

Ha, J., Yoon, Y., and Leal, L., 'The effect of compatibilizer on the coalescence of two drops in flow,' Physics of Fluids, 2003, **15**(4), pp. 849–867.

Hassan, M. R. and Wang, C., 'Magnetic field induced ferrofluid droplet breakup in a simple shear flow at a low reynolds number,' Physics of Fluids, 2019, **31**(12), p. 127104.

Hassan, M. R., Zhang, J., and Wang, C., 'Deformation of a ferrofluid droplet in simple shear flows under uniform magnetic fields,' Physics of Fluids, 2018, **30**(9), p. 092002.

Ionescu-Zanetti, C., Mechler, A., Carter, S. A., and Lal, R., 'Semiconductive polymer blends: Correlating structure with transport properties at the nanoscale,' Advanced Materials, 2004, **16**(5), pp. 385–389.

Jaeger, P. T., Janssen, J., Groeneweg, F., and Agterof, W., 'Coalescence in emulsions containing inviscid drops with high interfacial mobility,' Colloids and Surfaces A: Physicochemical and Engineering Aspects, 1994, **85**(2-3), pp. 255–264.

Jafari, S. M., Assadpoor, E., He, Y., and Bhandari, B., 'Re-coalescence of emulsion droplets during high-energy emulsification,' Food hydrocolloids, 2008, **22**(7), pp. 1191–1202.

Kennedy, M., Pozrikidis, C., and Skalak, R., 'Motion and deformation of liquid drops, and the rheology of dilute emulsions in simple shear flow,' Computers & fluids, 1994, **23**(2), pp. 251–278.

Lifton, V. A., 'Microfluidics: an enabling screening technology for enhanced oil recovery (eor),' Lab on a Chip, 2016, **16**(10), pp. 1777–1796.

Lobo, L. and Svereika, A., 'Coalescence during emulsification: 2. role of small molecule surfactants,' Journal of Colloid and Interface Science, 2003, **261**(2), pp. 498–507.

Loewenberg, M. and Hinch, E., 'Collision of two deformable drops in shear flow,' Journal of Fluid Mechanics, 1997, **338**, pp. 299–315.

Lyu, S., Bates, F. S., and Macosko, C. W., 'Modeling of coalescence in polymer blends,' AIChE journal, 2002, **48**(1), pp. 7–14.

Marić, M. and Macosko, C., 'Block copolymer compatibilizers for polystyrene/poly (dimethylsiloxane) blends,' Journal of Polymer Science Part B: Polymer Physics, 2002, **40**(4), pp. 346–357.

Masiri, S. M., Bayareh, M., and Nadooshan, A. A., 'Pairwise interaction of drops in shear-thinning inelastic fluids,' Korea-Australia Rheology Journal, 2019, **31**(1), pp. 25–34.

Mazloomi Moqaddam, A., Chikatamarla, S. S., and Karlin, I. V., 'Simulation of binary droplet collisions with the entropic lattice boltzmann method,' Physics of Fluids, 2016, **28**(2), p. 022106.

Nilsson, M. A., Kulkarni, R., Gerberich, L., Hammond, R., Singh, R., Baumhoff, E., and Rothstein, J. P., 'Effect of fluid rheology on enhanced oil recovery in a microfluidic sandstone device,' Journal of Non-Newtonian Fluid Mechanics, 2013, **202**, pp. 112–119.

Okushima, S., Nisisako, T., Torii, T., and Higuchi, T., 'Controlled production of monodisperse double emulsions by two-step droplet breakup in microfluidic devices,' Langmuir, 2004, **20**(23), pp. 9905–9908.

Olsson, E. and Kreiss, G., 'A conservative level set method for two phase flow,' Journal of computational physics, 2005, **210**(1), pp. 225–246.

Pautot, S., Frisken, B. J., and Weitz, D., 'Production of unilamellar vesicles using an inverted emulsion,' Langmuir, 2003, **19**(7), pp. 2870–2879.

Ray, A., Varma, V. B., Jayaneel, P., Sudharsan, N., Wang, Z., and Ramanujan, R. V., 'On demand manipulation of ferrofluid droplets by magnetic fields,' Sensors and Actuators B: Chemical, 2017, **242**, pp. 760–768.

Rosensweig, R. E., *Ferrohydrodynamics*, Cambridge University Press, 1985.

Rother, M. A., Zinchenko, A. Z., and Davis, R. H., 'Buoyancy-driven coalescence of slightly deformable drops,' Journal of Fluid Mechanics, 1997, **346**, pp. 117–148.

Rowghanian, P., Meinhart, C., and Campàs, O., 'Dynamics of ferrofluid drop deformations under spatially uniform magnetic fields,' Journal of Fluid Mechanics, 2016, **802**, pp. 245–262.

Salipante, P. F. and Vlahovska, P. M., 'Electrohydrodynamics of drops in strong uniform dc electric fields,' Physics of Fluids, 2010, **22**(11), p. 112110.

Santra, S., Sen, D., Das, S., and Chakraborty, S., 'Electrohydrodynamic interaction between droplet pairs in a confined shear flow,' Physics of Fluids, 2019, **31**(3), p. 032005.

Shardt, O., Derksen, J., and Mitra, S. K., 'Simulations of droplet coalescence in simple shear flow,' Langmuir, 2013, **29**(21), pp. 6201–6212.

Sherwood, J., 'Breakup of fluid droplets in electric and magnetic fields,' Journal of Fluid Mechanics, 1988, **188**, pp. 133–146.

Shum, H. C., Kim, J.-W., and Weitz, D. A., 'Microfluidic fabrication of monodisperse biocompatible and biodegradable polymersomes with controlled permeability,' Journal of the American Chemical Society, 2008, **130**(29), pp. 9543–9549.

Son, Y., 'Development of a novel microcompounder for polymer blends and nanocomposite,' Journal of applied polymer science, 2009, **112**(2), pp. 609–619.

Stratton, J. A., *Electromagnetic theory*, volume 33, John Wiley & Sons, 2007.

Sun, K., Jia, M., and Wang, T., 'Numerical investigation of head-on droplet collision with lattice boltzmann method,' International Journal of Heat and Mass Transfer, 2013, **58**(1-2), pp. 260–275.

Takeuchi, S., Garstecki, P., Weibel, D. B., and Whitesides, G. M., 'An axisymmetric flow-focusing microfluidic device,' Advanced materials, 2005, **17**(8), pp. 1067–1072.

Taylor, G. I., 'The viscosity of a fluid containing small drops of another fluid,' Proceedings of the Royal Society of London. Series A, Containing Papers of a Mathematical and Physical Character, 1932, **138**(834), pp. 41–48.

Taylor, G. I., 'The formation of emulsions in definable fields of flow,' Proceedings of the Royal Society of London. Series A, containing papers of a mathematical and physical character, 1934, **146**(858), pp. 501–523.

Utada, A. S., Lorenceau, E., Link, D. R., Kaplan, P. D., Stone, H. A., and Weitz, D., 'Monodisperse double emulsions generated from a microcapillary device,' Science, 2005, **308**(5721), pp. 537–541.

Wang, C.-Y., Zhang, C.-B., Huang, X.-Y., Liu, X.-D., and Chen, Y.-P., 'Hydrodynamics of passing-over motion during binary droplet collision in shear flow,' Chinese Physics B, 2016, **25**(10), p. 108202.

Xu, S., Nie, Z., Seo, M., Lewis, P., Kumacheva, E., Stone, H. A., Garstecki, P., Weibel, D. B., Gitlin, I., and Whitesides, G. M., 'Generation of monodisperse particles by using microfluidics: control over size, shape, and composition,' Angewandte Chemie International Edition, 2005, **44**(5), pp. 724–728.

Yang, H., Park, C. C., Hu, Y. T., and Leal, L. G., 'The coalescence of two equal-sized drops in a two-dimensional linear flow,' Physics of Fluids, 2001, **13**(5), pp. 1087–1106.

Yoon, Y., Borrell, M., Park, C. C., and Leal, L. G., 'Viscosity ratio effects on the coalescence of two equal-sized drops in a two-dimensional linear flow,' Journal of Fluid Mechanics, 2005, **525**, pp. 355–379.

Yue, P., Feng, J. J., Liu, C., and Shen, J., 'Diffuse-interface simulations of drop coalescence and retraction in viscoelastic fluids,' Journal of Non-Newtonian Fluid Mechanics, 2005, **129**(3), pp. 163–176.

Zakinyan, A., Tkacheva, E., and Dikansky, Y., 'Dynamics of a dielectric droplet suspended in a magnetic fluid in electric and magnetic fields,' Journal of Electrostatics, 2012, **70**(2), pp. 225–232.

Zhang, C. and Xing, D., 'Single-molecule dna amplification and analysis using microfluidics,' Chemical reviews, 2010, **110**(8), pp. 4910–4947.

Zhang, Y. and Ozdemir, P., 'Microfluidic dna amplification—a review,' Analytica chimica acta, 2009, **638**(2), pp. 115–125.

Zheng, B., Gerdts, C. J., and Ismagilov, R. F., 'Using nanoliter plugs in microfluidics to facilitate and understand protein crystallization,' Current opinion in structural biology, 2005, **15**(5), pp. 548–555.

Zheng, B., Roach, L. S., and Ismagilov, R. F., 'Screening of protein crystallization conditions on a microfluidic chip using nanoliter-size droplets,' Journal of the American chemical society, 2003, **125**(37), pp. 11170–11171.

IV. DIGITAL MICROFLUIDICS: MAGNETIC TRANSPORTATION AND COALESCENCE OF SESSILE DROPLETS ON HYDROPHOBIC SURFACES

Md Rifat Hassan, Jie Zhang, and Cheng Wang
Department of Mechanical & Aerospace Engineering
Missouri University of Science and Technology
Rolla, Missouri 65409
Tel: 573–341–4636, Fax: 573–341–4607
Email: wancheng@mst.edu

ABSTRACT

Magnetic digital microfluidics is advantageous over other existing droplet manipulation methods, which exploits magnetic forces for actuation and offers the flexibility of implementation in resource limited point-of-care applications. This article discusses the dynamic behavior of a pair of sessile droplets on a hydrophobic surface under the presence of a permanent magnetic field. A phase field method based solver is employed in a two-dimensional (2D) computational domain to numerically capture the dynamic evolution of the droplet interfaces, which again simultaneously solves the magnetic and flow fields. On a superhydrophobic surface (i.e., $\theta_c = 150^\circ$), the non-uniform magnetic field forces the pair of sessile droplets to move towards each other, which eventually leads to a jumping off phenomenon of the merged droplet from the solid surface after coalescence. Also, there exists a critical magnetic Bond number Bo_m^{cr}, beyond which no coalescence event between droplets is observed. Moreover, on a less hydrophobic surface ($\theta_c \leq 120^\circ$), the droplets still coalesce under a magnetic field; although, the merged droplet does not experience any upward flight after coalescence. Also, the merging phenomenon at lower contact angle values (i.e., $\theta_c = 90^\circ$) appears significantly different than at higher contact angle values (i.e., $\theta_c = 120^\circ$). Additionally, if the pair of sessile droplets is dispersed to a different

surrounding medium, the viscosity ratio plays a significant role in the upward flight of the merged droplet where the coalesced droplet exhibits increased vertical migration at higher viscosity ratios.

Keywords: Magnetic properties, Hydrophobicity, Interfaces, Contact angle, Liquids

1. INTRODUCTION

Digital microfluidics deals with the behavior of sessile droplets on an open surface and in combination with emulsion microfluidics are crucial building blocks of droplet-based microfluidics, which has been prevalent as a well established research field in the literature for over a decade now. One of the main advantages of digital microfluidics over emulsion microfluidics (also known as continuous-flow droplet based microfluidics) is that emulsion microfluidics requires an external pumping mechanism to attain continuous generation of droplets through a closed microfluidic channel, whereas in digital microfluidics, manipulation of droplets takes place on an open plain surface without any confinement, which in turn enables droplets to act as independent virtual reactors that are often utilized in point-of-care diagnostics, which require synthesis of hazardous materials [Javed *et al.*, 2014, Keng *et al.*, 2012] or preparation of complex samples [Choi *et al.*, 2013, Ng *et al.*, 2015, Pipper *et al.*, 2007, 2008] and cell-based assays [Choi *et al.*, 2012].

In general, the dynamic motion of a sessile droplet on a substrate can be exploited using gravity, given the fact that the droplet volume is large enough, which further can be magnified through an increase in the tilting angle or the hydrophobicity of the substrate, whereas surface tension plays a crucial role in the dynamics of smaller volume droplets. However, since gravitational and surface tension forces pose significant limitations, droplets in digital microfluidics can be actuated through other mechanisms, such as, electrowetting on dielectric [Cho *et al.*, 2003, Fair, 2007, Nelson and Kim, 2012], magnetic [Chiou *et al.*, 2013, Lehmann *et al.*, 2006b, Zhang *et al.*, 2013, Zhang and Wang, 2013], and surface acoustic waves [Ding *et al.*, 2013, Wang and Zhe, 2011]. Among the above mentioned mechanisms,

electrowetting on dielectric (EWOD) is the most popular one, which is capable of splitting and dispensing droplets, but requires electrodes to work that in turn provides little flexibility in operations. In contrast, magnetic actuation does not require any external sources and offers manual control, which is critical in resource limited environmental applications where availability of electricity is not always guaranteed. Another great advantage of magnetic actuation is its higher tolerance to liquid properties, while electrowetting actuation is massively dependent on the permittivity, conductivity, and surface tension of the liquid, which requires higher driving voltage in manipulation operations [Choi *et al.*, 2012]. An in-detailed description on the advantages of magnetic actuation over electrowetting on dielectric (EWOD) actuation is provided by Zhang and Nguyen [Zhang and Nguyen, 2017].

Dual functionality of magnetic particles is one of the most striking features in magnetic actuation based digital microfluidics where the magnetic particles, in addition to droplet actuation, functions as solid substrate for molecule adsorption. Pipper et al. [Pipper *et al.*, 2007] found out that under the exposure to magnetic forces, droplets containing silica-functionalized superparamagnetic particles are capable of identifying pathogenic avian influenza virus (H5N1) on a throat swab sample. Moreover, Long et al. [Long *et al.*, 2009] investigated the particle extraction behavior of droplets and realized that the magnetic particles' mass and movement speed of permanent magnet play a decisive role in the manipulation of droplets, leading to breakup under certain operating conditions, while the effects of different hydrophobic surfaces on the magnetic actuated motion of droplets are analyzed by Mats et al. [Mats *et al.*, 2015] Kim et al. [Kim *et al.*, 2015] proposed a magnetic beads droplet immunoassay microfluidic platform that is extremely sensitive to the detection of oligomer Aβ for Alzheimer's disease and simultaneously simplifies the enzyme-linked immunosorbent assay (ELISA) process. Similar investigations on ELISA process are also performed by several other authors where the magnetic particles are treated with antibodies to capture the target molecules [Park *et al.*, 2016, Shikida *et al.*, 2006].

Droplet manipulation in microfluidics applications is usually accomplished either by controlling the behavior of magnetic particles by a permanent magnet or an array of electromagnets that consists of micro coils. Okochi et al. [Okochi *et al.*, 2010] controlled droplets with magnetic particles by placing a permanent magnet below the channel surface and achieved coalescence with a lysis buffer droplet, while a simple configuration of total RNA extraction droplet array is presented by Shi et al. [Shi *et al.*, 2015a], which facilitates the transportation of magnetic beads through buffer solutions. In contrast, several other analytical and numerical studies [Beyzavi and Nguyen, 2008a,b, Lehmann *et al.*, 2006a,b, Rida *et al.*, 2003] implemented micro coils as electromagnets in order to achieve controlled transportation of magnetic droplets; however, one of the major issues arises as a result of using electromagnets, which is known as Joule heating, and in turn requires a cooling mechanism to mitigate the heating effect [Chiou *et al.*, 2013].

Ferrofluids are another examples of liquid magnet, which contain colloidal suspensions of magnetic nanoparticles in a carrier fluid and experience deformation under the exposure to magnetic fields [Hassan and Wang, 2019, 2020a,b, Hassan *et al.*, 2018, 2021, Zhang *et al.*, 2019]. Also, due to the uniform distribution of magnetic nanoparticles, ferrofluids can be transported to different locations for liquid phase reactions [Bitar *et al.*, 2014] and are conventionally used as sealant [Raj and Moskowitz, 1990] in hard drives and coolant in loudspeakers [Mary *et al.*, 2010]. Nguyen et al. [Nguyen *et al.*, 2010] conducted experiments on the motion of a droplet under a moving permanent magnetic field and derived a critical velocity, above which the droplet fails move with the same velocity as the moving magnet. Moreover, Beyzavi and Nguyen demonstrated one-dimensional [Beyzavi and Nguyen, 2008b] and two-dimensional [Beyzavi and Nguyen, 2009] manipulation of ferrofluid droplet using micro coil arrays and found that a small magnetic field gradient is enough to induce movement in a ferrofluid droplet, while Egatz-Gómez et al. [Egatz-Gómez *et al.*, 2006] observed coalescence between two water drops under a moving permanent magnetic field.

Droplet coalescence is an event where two or more droplets, following large deformations and rupture of the interface separating the droplets, merge into one single droplet upon contact. Moreover, this coalescence process is critical to the understanding of a range of science and engineering applications, including raindrop formation in clouds [Kovetz and Olund, 1969, Menchaca-Rocha *et al.*, 2001], sintering in metallurgy [Bellehumeur *et al.*, 1996], and spray painting/coating [Ashgriz, 2011, Madejski, 1976]. In these applications, the coalescence rate of adjacent drops plays a vital role in the determination of the material properties of the solidified precursor. More importantly, coalescence of drops is an integral step in controllable droplet-based functions in microfluidics, such as micro-mixing [Cho *et al.*, 2003, Geng *et al.*, 2017] and micro-reaction [Bithi *et al.*, 2014, Guo *et al.*, 2012] in lab-on-a-chip devices where advective mixing during coalescence is used to control chemical and biological assays. Several numerical studies on the coalescence of sessile droplets have also been reported in the literature [Cheng *et al.*, 2016, Liu *et al.*, 2014a, Nam *et al.*, 2013]. Shi et al. [Shi *et al.*, 2015b] implemented a lattice Boltzmann method to analyze the coalescence pattern of droplets on a textured surface and found that surface roughness affects the jumping phenomenon of merged droplet. Liu et al. [Liu *et al.*, 2014b] performed an investigation on the coalescence induced self-propelled jumping behavior of droplets on a patterned hydrophobic surface, while a similar analysis is conducted by Wang et al. [Wang *et al.*, 2019]. Recently, Liu and Liu [Liu and Liu, 2019] have succeeded in transporting a sessile droplet to different locations along a hydrophobic surface through the application of an electric field. However, the current numerical studies in the literature only focused on larger sized droplets [Cheng *et al.*, 2016, Liu *et al.*, 2014a] so that gravitational forces can induce coalescence between droplets that are initially placed in contact with each other or droplets on patterned surfaces [Liu *et al.*, 2014b, Shi *et al.*, 2015b]. Moreover, as per our knowledge, till now, no one has ever performed numerical analyses on the dynamic behavior of micro-meter sized droplets (where gravitational forces are negligible in compared to viscous forces) on an open surface under the presence of magnetic fields that will

be useful to a wide range of microfluidics applications, including biological and chemical assays [Berthier, 2012, Bitar *et al.*, 2014, Du *et al.*, 2013, Garcia-Cordero and Fan, 2017, Ma *et al.*, 2016, Nguyen *et al.*, 2010, Ueda *et al.*, 2012, Zhu *et al.*, 2013, 2015]. As a result, in this article, we numerically investigate the dynamics of a pair of sessile droplets on a hydrophobic surface under the effect of a permanent magnetic field, which ultimately leads to coalescence induced jumping/ no jumping phenomenon under certain operating conditions. Here, a two-dimensional (2D) computational scheme is adopted, which is widely proven to capture the dynamic evolution of droplet interface with great precision, while minimizing the use of a considerable amount of computational resources [Hassan and Wang, 2019, 2020a,b, Hassan *et al.*, 2018, Zhang *et al.*, 2019], which further facilitates in the investigation on the effects of a wide range of parameters i.e., magnetic field strength, contact angle, and viscosity ratio on the dynamics of droplets on hydrophobic surfaces.

The paper is organized as follows: In Numerical model section, we depict the numerical setup of the computational model, while an in-detailed description of the computational algorithm and governing equations are provided in Numerical method section. Next, the effects of different parameters i.e., magnetic field strength, contact angle, and viscosity ratio on the dynamic behavior of a pair of sessile droplets are explained in Results and discussions, which is subsequently followed by the validation of numerical model and behavior of droplets under a solitary magnetic field. Finally, the critical findings are summarized in Conclusion section. Additionally, the efficacy of the phase field method in conserving the mass of droplet and grid independence check is provided in the supporting information.

2. NUMERICAL MODEL

Figure 1 depicts the graphical representation of a pair of sessile ferrofluid droplets dispersed in another fluid medium under a permanent magnetic field, $\mathbf{H}_0$. In this investigation, both fluid phases (i.e., continuous and droplet phases) are treated as immiscible, viscous, and Newtonian fluids. In the beginning, the droplet phase is considered equally

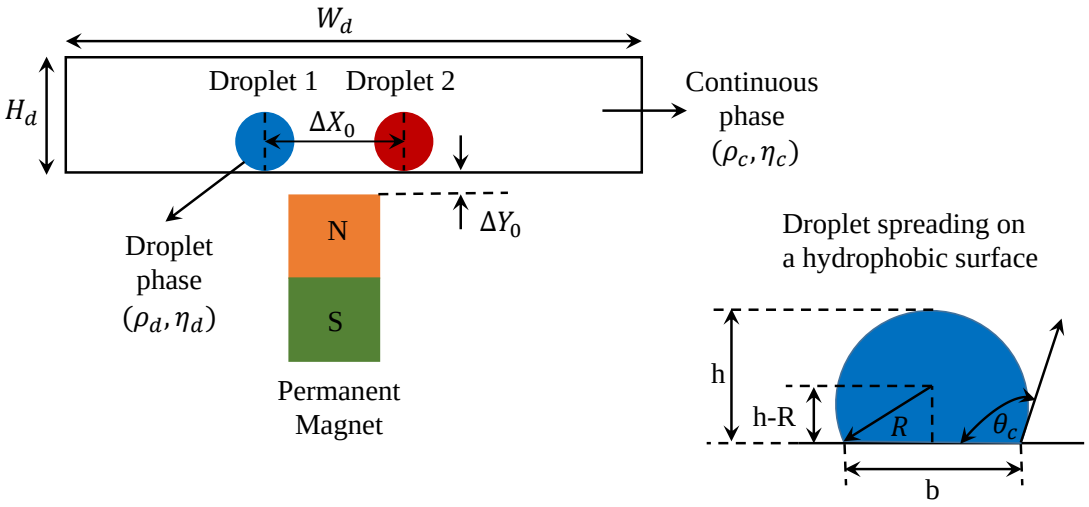

Figure 1. Graphic representation of a pair of sessile ferrofluid droplets dispersed in an immiscible and viscous continuous fluid phase under a permanent magnetic field, $\mathbf{H}_0$.

dense and viscous as the continuous phase (i.e., $\rho_d = \rho_c$ and $\eta_d = \eta_c$), where the subscripts d and c denote the droplet and continuous phases, respectively. Also, the droplet contains magnetic properties and has a magnetic permeability equal to $5\mu_0$ (i.e., $\mu_d = 5\mu_0$), while the surrounding medium is treated as a non-magnetic fluid (i.e., $\mu_c = \mu_0$). The height of the computational domain is considered five times the initial radius of the droplet R_0 (i.e., $H_d = 5R_0$), while the width equals to $5H_d$ (i.e., $W_d = 5H_d$) to ignore the effect of the side walls on the dynamic behavior of the droplets.

Initially, a pair of identical ferrofluid droplets with initial radii R_0 are separated by a distance ΔX_0 in the horizontal direction, while maintaining an initial contact with the solid surface at the bottom interface of the droplet. Next, a permanent magnetic field, $\mathbf{H}_0$, is applied at the bottom of the droplet domain, which maintains a vertical separation distance ΔY_0 between the top surface of the magnet and bottom wall of the droplet domain. Also, the distance between the center of the magnet and the centroids of droplets along the horizontal direction are set equal to each other. Under the combined effects of wetted wall condition and magnetic field, the wettability of the droplets changes, and the wettability of

Table 1. Simulation parameters and magnitudes.

Parameter	Symbol	Value	Unit
Channel width	W_d	500	μm
Channel height	H_d	100	μm
Permeability of vacuum	μ_0	$4\pi \times 10^{-7}$	H/m
Initial droplet radius	R_0	20	μm
Interfacial tension	σ	0.0135	N/m
Density of droplet phase	ρ_d	1260	kg/m^3
Viscosity of droplet phase	η_d	0.105	Pa·s
Horizontal separation distance	ΔX_0	60	μm
Vertical separation distance	ΔY_0	15	μm
Magnetic permeability of droplet phase	μ_d	$5\mu_0$	H/m
Magnetic permeability of continuous phase	μ_c	μ_0	H/m

the droplets can be characterized by the spreading diameter b and apex height h, respectively. Additionally, as the wettability of the droplets changes, the contact angle θ_c of the droplets undergoes a transition, which can be defined as the angle the droplet interface makes with the outline of the contact surface (horizontal solid surface) and is useful in determining the surface free energy of a solid material. In order to perform numerical simulations, the bottom wall of the computational domain is subjected to a wetted wall condition, while a pressure outlet boundary condition is employed to the top wall to ensure that the droplets are free from any pressure and velocity gradient effects. The phase field method uses a condition called "Wetted wall", which defines the contact angle between the droplets and bottom substrate in two-phase flows.COMSOL [2018] Additionally, a periodic boundary condition is applied to the side walls to ensure infinite periodicity in the x direction. Next, a magnetization constitutive relation is applied to the permanent magnet to generate the magnetic fields. Finally, a finite element method based commercial numerical solver (COMSOL 5.3) is implemented to capture the dynamic behavior of droplet interfaces under permanent magnetic fields, which couples both flow and magnetic fields. For the convenience of the readers, the simulation parameters and the corresponding magnitudes are listed in Table 1.

3. NUMERICAL METHOD

3.1. PHASE FIELD METHOD

Multiphase flows, in general, can occur in various forms, such as transition of liquid phase into vapor phase due to external heating and dispersed flows where one phase exists in the form of particles, droplets, or bubbles in a continuous phase i.e., liquid or gas. However, one of the most common difficulties that arises in solving multiphase flow problems involving droplets is to track the free interface of the droplet that experiences severe deformation over time under external forces and flow conditions. As a result, a phase field (PF) method, governed by a Cahn-Hilliard equation, is implemented in our model to track the diffuse interface of the droplet separating the immiscible fluid phases, which also provides a greater advantage over level set (LS) method in terms of conserving the mass of droplets. Note that, the numerical methods involving diffuse interfaces are usually constructed with an idea that they are not sharp boundaries, rather have finite width and are distinguished by smooth and rapid transitions in different physical quantities i.e., density, viscosity etc.

The phase field method involves a dimensionless variable ϕ that differentiates different phases, which has a constant value -1 in the bulk phase (i.e., $\phi_c = -1$) and 1 in the dispersed droplet phase (i.e., $\phi_d = 1$), followed by a smooth transition between -1 and 1 (i.e., -1< ϕ <1) in a hyperbolic tangent or similar manners. When $\phi = 0$, it defines the exact interface of the droplet. Since, the Cahn-Hilliard equation involves 4^{th} order derivative, our finite element method based numerical solver splits the equation into two 2^{nd} order equations:

$$\begin{aligned} &\frac{\partial \phi}{\partial t} + \mathbf{u} \cdot \nabla \phi = \nabla \gamma \nabla G, \\ &G = \lambda \left[-\nabla^2 \phi + \frac{\phi(\phi^2 - 1)}{\epsilon^2} \right] \end{aligned} \tag{1}$$

where **u** and G denote the flow velocity in the domain (m/s) and chemical potential of the system, respectively. The parameter γ represents the mobility ($m^3 \cdot s/kg$), which also determines the time scale of diffusion and is related to the thickness of the droplet interface ϵ (m) through the following equation:

$$\gamma = \chi \epsilon^2 \tag{2}$$

where χ is the mobility tuning parameter (m·s/kg). The mobility parameter γ needs a careful handling in the numerical approach so that it is large enough to retain a constant interfacial thickness but small enough to avoid the over damping of the convective terms. Moreover, the relationship among the mixing energy density λ, interface thickness ϵ, and surface tension coefficient σ can be expressed through the following equation:

$$\sigma = \frac{2\sqrt{2}}{3}\frac{\lambda}{\epsilon}. \tag{3}$$

In our model, the interface thickness ϵ is considered half the maximum mesh size h_m in the region passed by the droplet interface during its movement along the domain (i.e., $\epsilon = h_m/2$). In phase field method, the volume fractions of different fluid phases are described as:

$$V_{f1} = \frac{1-\phi}{2}, \qquad V_{f2} = \frac{1+\phi}{2}. \tag{4}$$

Moreover, since phase field method considers multiphase flow as a single phase flow, the different properties in the flow domain such as, density (ρ) and viscosity (η) can be calculated using volume fractions of fluid phases as:

$$\rho = \rho_c + (\rho_d - \rho_c)V_{f2}, \qquad \eta = \eta_c + (\eta_d - \eta_c)V_{f2}. \tag{5}$$

3.2. GOVERNING EQUATIONS

The flow dynamics of an isothermal and incompressible system involving two different Newtonian fluid phases is governed by the incompressible Navier-Stokes equations:

$$\nabla \cdot \mathbf{u} = 0 \tag{6}$$

and

$$\rho \frac{\partial \mathbf{u}}{\partial t} + \rho \left(\mathbf{u} \cdot \nabla \right) \mathbf{u} = -\nabla p + \nabla \cdot \eta \left[(\nabla \mathbf{u}) + (\nabla \mathbf{u})^T \right] + \mathbf{F}_g + \mathbf{F}_\sigma + \mathbf{F}_m. \tag{7}$$

In the above equations, p denotes the terms related to pressure, while the viscous stress tensor terms are denoted by $\eta \left[(\nabla \mathbf{u}) + (\nabla \mathbf{u})^T \right]$. On the other hand, the gravitational forces are represented by $\mathbf{F}_g$, which again equals to $\rho \mathbf{g}$, and the magnetic and surface tension forces are portrayed by the symbols $\mathbf{F}_m$ and $\mathbf{F}_\sigma$, individually. The surface tension force $\mathbf{F}_\sigma$ can be calculated using the chemical potential of the system G (mentioned in Equation 1) and phase field variable ϕ as:

$$\mathbf{F}_\sigma = G \nabla \phi. \tag{8}$$

Due to the application of magnetic field, the droplet interface experiences additional magnetic stresses, which can be expressed as $\boldsymbol{\tau}_m$ and are required to evaluate magnetic forces $\mathbf{F}_m$. The quantification of magnetic force $\mathbf{F}_m$ is as follows [Rosensweig, 1985]:

$$\mathbf{F}_m = \nabla \cdot \boldsymbol{\tau}_m = \nabla \cdot \left(\mu \mathbf{H}\mathbf{H} - \frac{\mu}{2} H^2 \mathbf{I} \right). \tag{9}$$

In Equation 9, μ represents the permeability of the flow domain, which can be evaluated using phase field variable ϕ, and $H^2 = |\mathbf{H}|^2$, whereas $\mathbf{I}$ denotes the identity operator. Additionally, the calculation of magnetic stresses requires an inclusive understanding of Maxwell equations and the constitutive relationships among magnetization $\mathbf{M}$, magnetic

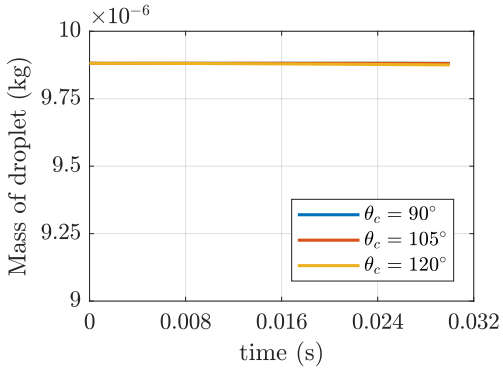

Figure 2. Mass of a sessile droplet under various wetting conditions.

field **H**, and magnetic induction **B**, which are elucidated as follows:

$$\mathbf{M} = \chi\mathbf{H}, \qquad \nabla \times \mathbf{H} = 0, \qquad \nabla \cdot \mathbf{B} = 0, \text{ and } \qquad \mathbf{B} = \mu_0(\mathbf{H} + \mathbf{M}) = \mu_0(1 + \chi)\mathbf{H} \quad (10)$$

where μ_0 denotes the permeability of vacuum, which again equals to 1.257×10^{-6} H/m. A magnetic scalar potential ψ is defined so that $\mathbf{H} = -\nabla\psi$, which eventually leads to the following relationship:

$$\nabla \cdot (\mu\nabla\psi) = 0. \quad (11)$$

In our numerical simulation, the magnetic field **H** is solved using Equation 11, which then contributes to the quantification of the magnetic forces in Equation 9.

4. RESULTS AND DISCUSSIONS

4.1. MASS CONSERVATION OF DROPLET

In order to demonstrate the clear advantage of phase field (PF) method over other numerical methods i.e., level set (LS) method, volume of fluid (VOF) method in terms of conserving the mass of a droplet in fluid domain, an investigation on the mass of a droplet is carried out under various wetted wall conditions. Figure 2 illustrates the time evolution

Table 2. Maximum mesh element size in the computational domain.

Mesh 1	Mesh 2	Mesh 3	Mesh 4	Mesh 5
$0.2R_0$	$0.1R_0$	$0.075R_0$	$0.06R_0$	$0.05R_0$

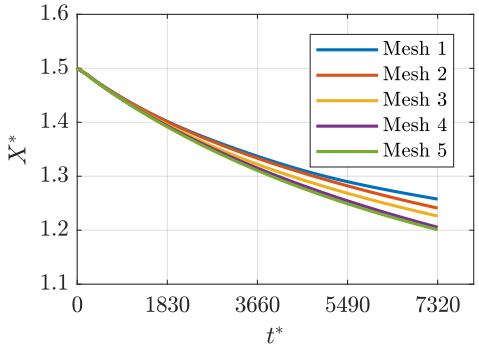

Figure 3. Grid independence test: time evolution of the magnetic field induced migration of a sessile droplet along the horizontal direction X^* for different mesh configurations at $\mathrm{Bo}_m = 0.145$ and $\theta_c = 150°$.

of the mass of a sessile droplet at different contact angles, which clearly indicates that irrespective of different boundary conditions, the droplet mass is conserved throughout the whole process in numerical simulations.

4.2. GRID INDEPENDENCE CHECK

Figure 3 represents the time evolution of the magnetic field induced migration of a sessile droplet along the horizontal direction X^* for several mesh configurations at $\mathrm{Bo}_m = 0.145$ and $\theta_c = 150°$, which are tabulated in Table 2, and it can be seen that when the maximum mesh size in the computational domain is less than $0.06R_0$, the migration results tend to overlap with each other, while traversing the same amount of distance along the horizontal direction from initial position in the time under consideration. As a result, using more refined meshes in the computational domain would only lead to minimal changes in the coalescence time, while demonstrating similar coalescence behavior under the same conditions at the expense of high computational costs. Considering the computational

cost, we have decided to use $0.05R_0$ as the magnitude of the maximum mesh element size in the domain under consideration, which eventually saves a reasonable amount of computational time, while providing accurate estimation of dynamic droplet interface during the simulations throughout the paper.

4.3. DROPLET DYNAMICS ON A SOLID SURFACE

The flow dynamics of sessile droplets is dependent on the deformation experienced by the droplets, which is predominantly influenced by the competition among viscous forces, surface tension forces, magnetic forces, and surface adhesion forces. Here, in this section, at first, we analyze the dynamic behavior of a solitary sessile droplet on a horizontal smooth surface under different wetting wall conditions. Note that, the dimensions in the x and y axes are non-dimensionalized by the initial radius of the droplet R_0, while density ρ, initial radius of droplet R_0, and surface tension coefficient σ are used as scaling parameters for dimensionless time, which are as follows:

$$X^* = \frac{x}{R_0}, \qquad Y^* = \frac{y}{R_0}, \text{ and} \qquad t^* = t\sqrt{\frac{\sigma}{\rho R_0^3}}. \tag{12}$$

Figure 4 depicts the equilibrium droplet shapes with contact angle on a solid horizontal surface, and from Figure 4(a)-(c), the equilibrium droplet shapes suggest that as the contact angle between the droplet interface and bottom wall increases (i.e., more hydrophobic), the wettability of the droplet decreases. Consequently, the base diameter of the droplet b decreases, which in turn gives rise to the magnitude of apex height h in order to conserve the total volume of the droplet. Moreover, the contact angle in each case is found to be in good agreement with the set wetted wall conditions, which again proves the accuracy of the model. Furthermore, the magnitudes of the base diameter b and height h of the droplet

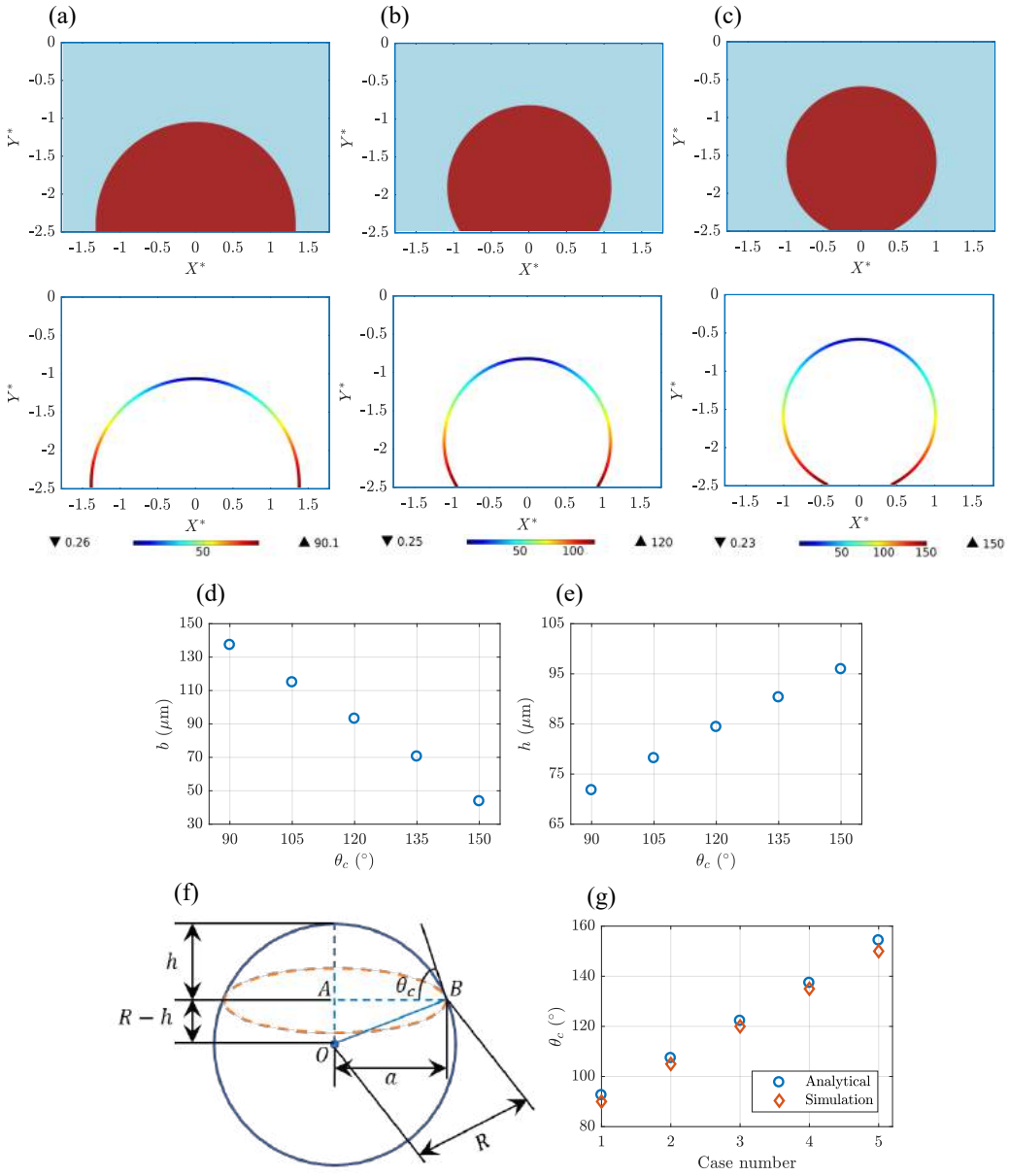

Figure 4. Equilibrium droplet shapes with contact angle on a solid horizontal surface. (a) $\theta_c = 90°$; (b) $\theta_c = 120°$; (c) $\theta_c = 150°$; (d) Base diameter b vs contact angle θ_c; (e) Height h vs contact angle θ_c; (f) Schematic for derivation of contact angle relationship in terms of base diameter and height of a droplet; and (g) Comparison of simulated contact angle θ_c results against analytical relationships.

under different wetted wall conditions are illustrated in Figure 4(d) and (e), which shows a decreasing and increasing trend in magnitudes with the increases in contact angle values, respectively.

In the absence of gravitational forces, a sessile droplet will form a perfect spherical cap on the bottom substrate. Figure 4(f) represents the schematic for derivation of contact angle relationship in terms of base diameter b and height of droplet h where R is the radius of the sphere and θ_c is the contact angle. Now, applying the Pythagorean theorem in ΔOAB, we have:

$$R^2 = (R - h)^2 + a^2. \tag{13}$$

Since, in our case, $a = b/2$, Equation 13 becomes:

$$R^2 = (R - h)^2 + \left(\frac{b}{2}\right)^2. \tag{14}$$

Simplifying Equation 14, the radius of the sphere R can be expressed in terms of b and h:

$$R = \frac{4h^2 + b^2}{8h}. \tag{15}$$

Subsequently, the radius of the droplet R is utilized in finding the contact angle θ_c, which can be approximated as follows:

$$\theta_c = \tan^{-1}\frac{b}{2(R - h)}. \tag{16}$$

Using the above geometrical relationships (Equation 15 and 16), the contact angles are calculated and compared against simulated contact angles (Figure 4(g)), which appear to agree quantitatively very well with each other. Even, for the maximum contact angle value used in the analysis ($\theta_c = 150°$), the numerical error between the analytical and simulated contact angle is found to be approximately 2.79%.

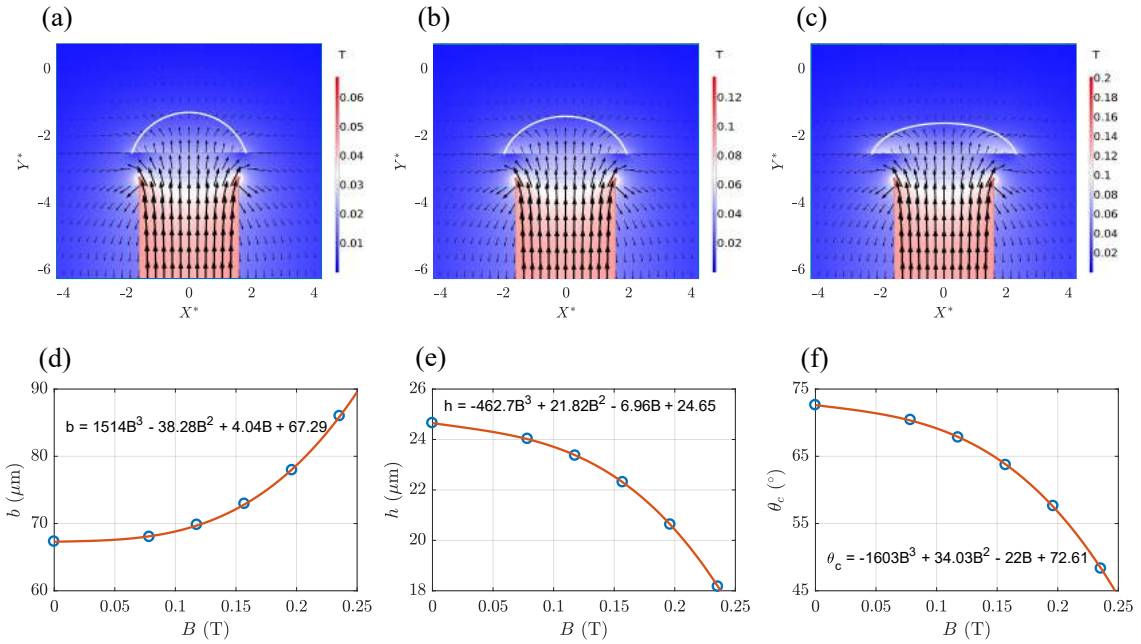

Figure 5. Steady state shapes of droplet on a hydrophillic smooth solid surface under permanent magnetic field with initial contact angle $\theta_c^0 = 72°$. (a) B = 0.078 T; (b) B = 0.157 T; and (c) B = 0.2 T. (d)-(f) Variation in spreading characteristics of a droplet on a homogeneous solid surface under a permanent magnet along the central portion of droplet. (d) Base diameter b; (e) Height h; and (f) Contact angle θ_c.

4.4. SESSILE DROPLET UNDER NON-UNIFORM MAGNETIC FIELD

Now, we investigate the effect of a permanent magnetic field on the wetting phenomenon of a sessile ferrofluid droplet (also known as magnetowetting), and the steady state shapes of a sessile ferrofluid droplet under a non-uniform magnetic field are illustrated in Figure 5(a)-(c). In the absence of a magnetic field, the droplet assumes a contact angle of 72° with the solid surface; however, as the magnetic field is applied, the shape of the droplet changes, which eventually changes the spreading dynamics of a ferrofluid droplet under magnetic fields. Figure 5(a)-(c) demonstrates that a stronger magnetic field pulls down and laterally stretch the droplet, causing an increase in the base diameter of the droplet, which in turn augments the wettability of a sessile ferrofluid droplet. Consequently, the droplet experiences a decline in its apex height and contact angle with the increase in wettability

of the droplet. Moreover, the magnetic field profiles in Figure 5(a)-(c) suggest that the magnetic field lines exit the north pole of the magnet and enters the south pole through an elliptic fashion, while being parallel to each other and maintaining a symmetric profile with respect to the y axis of the computational domain. Also, the magnetic field is strongest near the vicinity of the magnet, which is eventually encountered by the ferrofluid droplet and diminishes to zero far away from the magnet.

Furthermore, the spreading characteristics of a sessile ferrofluid droplet under a non-uniform magnetic field are shown in Figure 5(d)-(f), which indicate an increase in base diameter b (Figure 5(d)) and decrease in height h (Figure 5(e)) and contact angle θ_c (Figure 5(f)) magnitudes of the droplet with the increase in magnetic field strengths, and these results agree qualitatively well with the experimental findings of Nguyen et al. [Nguyen *et al.*, 2010]. Additionally, the spreading characteristics of the ferrofluid droplet in Figure 5(d)-(f) are found to match perfectly with a third order polynomial fitting curve under the presence of a non-uniform magnetic field.

4.5. MAGNETIC FIELD INDUCED COALESCENCE OF SESSILE DROPLETS

The results from previous sections indicate that the spreading characteristics of a solitary sessile ferrofluid droplet can be modified using different magnetic field strengths and wetted wall conditions. Now, in this section, we analyze the pairwise interaction between a pair of sessile ferrofluid droplets on a hydrophobic surface under the action of a permanent magnetic field. Here, some dimensionless groups (i.e., ζ and λ) are introduced, which respectively signify the density and viscosity ratios and are defined as:

$$\zeta = \frac{\rho_d}{\rho_c}, \quad \lambda = \frac{\eta_d}{\eta_c}, \tag{17}$$

whereas the magnetic Bond number Bo_m relates the magnetic and surface tension forces through the following relationship:

$$\mathrm{Bo}_m = \frac{\mu_0 R_0 H_0^2}{2\sigma}. \tag{18}$$

Figure 6(a) illustrates the effect of non-uniform magnetic field on the interaction phenomenon between a pair of sessile droplets on a hydrophobic surface ($\theta_c = 150°$) at $\mathrm{Bo}_m = 0.145$, $\zeta = 1$, and $\lambda = 1$, and it can be seen that with the evolution of time ($t^* = 5489.4$, 7429), as the magnetic field activates, the droplets start to approach each other along the direction of the magnet. During this sliding motion, the interface of the droplets closer to the permanent magnet experiences larger deformation due to greater magnitudes of magnetic force and tends to drag the droplet towards the magnet, while the droplet interfaces on the opposite side, being approximately circular in shape, strive to resist the movement and keep the droplet attached to the bottom surface of the domain. As a result, during the motion, a difference between the advancing contact angle θ_a and receding contact angle θ_r emerges, which ultimately gives rise to capillary force that eventually provides resistance to the droplet movement along the direction of the magnet. Moreover, the capillary force $\mathbf{F}_c$ is dependent on the base diameter b and surface tension coefficient σ, which can be expressed as:

$$\mathbf{F}_c = b\sigma(\cos\theta_r - \cos\theta_a). \tag{19}$$

Subsequently, the magnetic field brings the droplets into close proximity with each other where the drainage of the fluid film between the droplets occurs, which is ultimately followed by the flattening of the interfaces in the merging region ($t^* = 7483.9$). Eventually, the van der Waals intermolecular forces come into play and dominate the coalescence phenomenon between the droplets, and this event is similar to the coalescence phenomenon observed

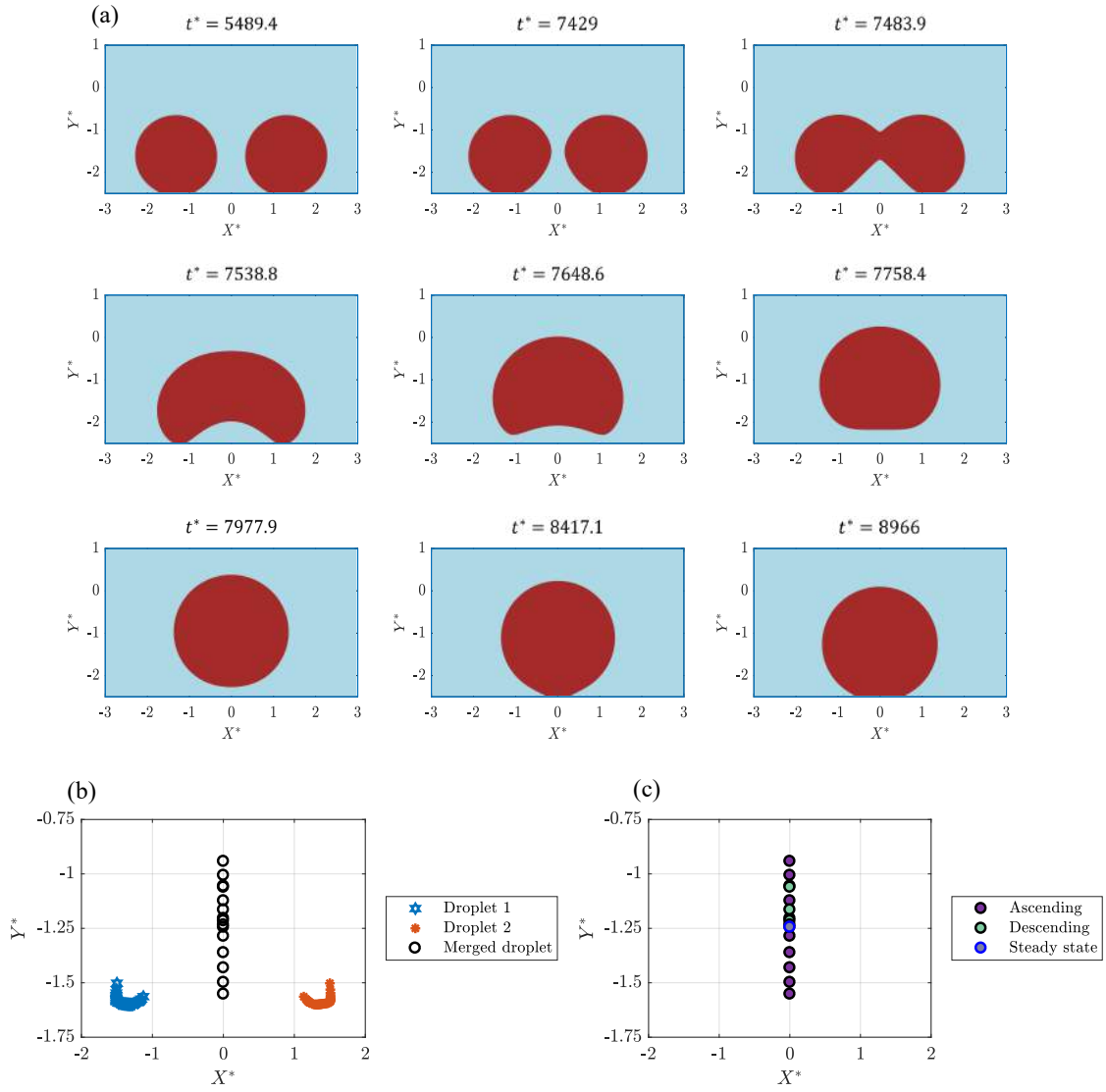

Figure 6. Dynamics of sessile droplets at $\mathrm{Bo}_m = 0.145$, $\theta_c = 150°$, $\zeta = 1$, and $\lambda = 1$. (a) Time evolution of sessile droplet movement leading to coalescence and jumping off the hydrophobic surface under permanent magnetic field at $\mathrm{Bo}_m = 0.145$, $\theta_c = 150°$, $\zeta = 1$, and $\lambda = 1$. (b)-(c) Trajectory of sessile droplets on a hydrophobic surface under permanent magnetic field at $\mathrm{Bo}_m = 0.145$, $\theta_c = 150°$, $\zeta = 1$, and $\lambda = 1$. (b) Overall trajectory; and (c) Trajectory of merged droplet.

between droplet pairs in shear flows in our previous works [Hassan and Wang, 2020a, Hassan *et al.*, 2021]. Also, the force balance along the x axis during the sliding motion leading to coalescence can be demonstrated in the following form:

$$\mathbf{F}_m = \mathbf{F}_c + \mathbf{F}_{ad} \tag{20}$$

where $\mathbf{F}_{ad}$ represents the adhesion forces during the motion and is proportional to the base diameter of the droplet (i.e., $\mathbf{F}_{ad} \propto b$). Note that, capillary force appears in a droplet due to cohesive forces where the molecules of droplet attract each other. In contrast, the adhesive force is the main reason behind the adhesion force where the molecules of droplet interact with the molecules of the bottom substrate, thereby generating a resistive force that provides resistance against the droplet motion along the substrate. Under the presence of a magnetic field, the magnetic force $\mathbf{F}_m$ dominates over $\mathbf{F}_c$ and $\mathbf{F}_{ad}$, which eventually results in the horizontal movement of the droplets along the direction of the magnet, leading to coalescence between droplets at $\mathrm{Bo}_m = 0.145$.

Moreover, during the merging process, the surface energy of the droplets converts into kinetic energy, which in turn aids the merged droplet in jumping upwards in the vertical direction from the hydrophobic surface ($t^* = 7648.6$), followed by a gradual decline in the base diameter of the merged droplet ($t^* = 7538.8$). Eventually, as the droplet takes off from the hydrophobic surface, the kinetic energy of the droplet dissipates into the surrounding viscous fluid medium, and the droplet reaches a maximum point where the velocity diminishes to zero ($t^* = 7977.9$). Consequently, as the intensity of kinetic energy diminishes, the magnetic force becomes dominant and drags the droplet back towards the bottom surface of the domain. Finally, the droplet reaches an equilibrium stage where the droplet shape, in addition to the wetted wall condition, is defined by the magnetic and surface tension forces ($t^* = 8966$). The force balance during the droplet jumping phenomenon in

the vertical direction (i.e., y axis) can be approximated in the following form:

$$\mathbf{F}_k = \mathbf{F}_m + \mathbf{F}_g + \mathbf{F}_d. \tag{21}$$

However, when the characteristic dimension of droplets decreases from the macroscopic to the micrometer scale, the effects of gravity become negligible in compared to the surface tension and viscous forces, which ultimately govern the droplet dynamics. In general, the gravitational effect can be ignored for droplets that have diameter smaller than the capillary length. In our case, the capillary length is estimated to be 1.04 mm, which is approximately 26 times larger than the droplet size (micrometer size). As a result, the contribution of gravitational force $\mathbf{F}_g$ (i.e., standard gravity) can be ignored in compared to the magnetic force $\mathbf{F}_m$, which ultimately reduces Equation 21 in the following format:

$$\mathbf{F}_k \approx \mathbf{F}_m + \mathbf{F}_d \tag{22}$$

where $\mathbf{F}_d$ denotes the drag force experienced by the droplet during the upward motion in the opposite direction.

Additionally, the overall trajectory of the droplets in Figure 6(b) indicates that during the initial stage of the sliding motion, the droplets experience a decline in the apex height and then approach each other along the horizontal direction. Next, as the droplet interfaces come in close contact with each other, the droplets experience an increase in the apex height, which ultimately leads to an upward shift of the droplet positions during the merging stage of droplets. Afterwards, following the merging phenomenon, the merged droplet continues to move upward until the kinetic energy of the droplet diminishes to zero through viscous dissipation and then reaches the steady shape under the attractive forces of the magnetic field. Note that, a MATLAB code is developed to track the centroids of droplets during the motion, which eventually defines the trajectory of the droplets in Figure 6(b)-(c). Moreover, the trajectory of the merged droplet is illustrated in Figure 6(c), which

shows that the merged droplet takes a considerable amount of time in reaching the maximum peak during ascension in the vertical direction, while descension leading to a steady state droplet position is comparatively faster under the influence of the magnetic field.

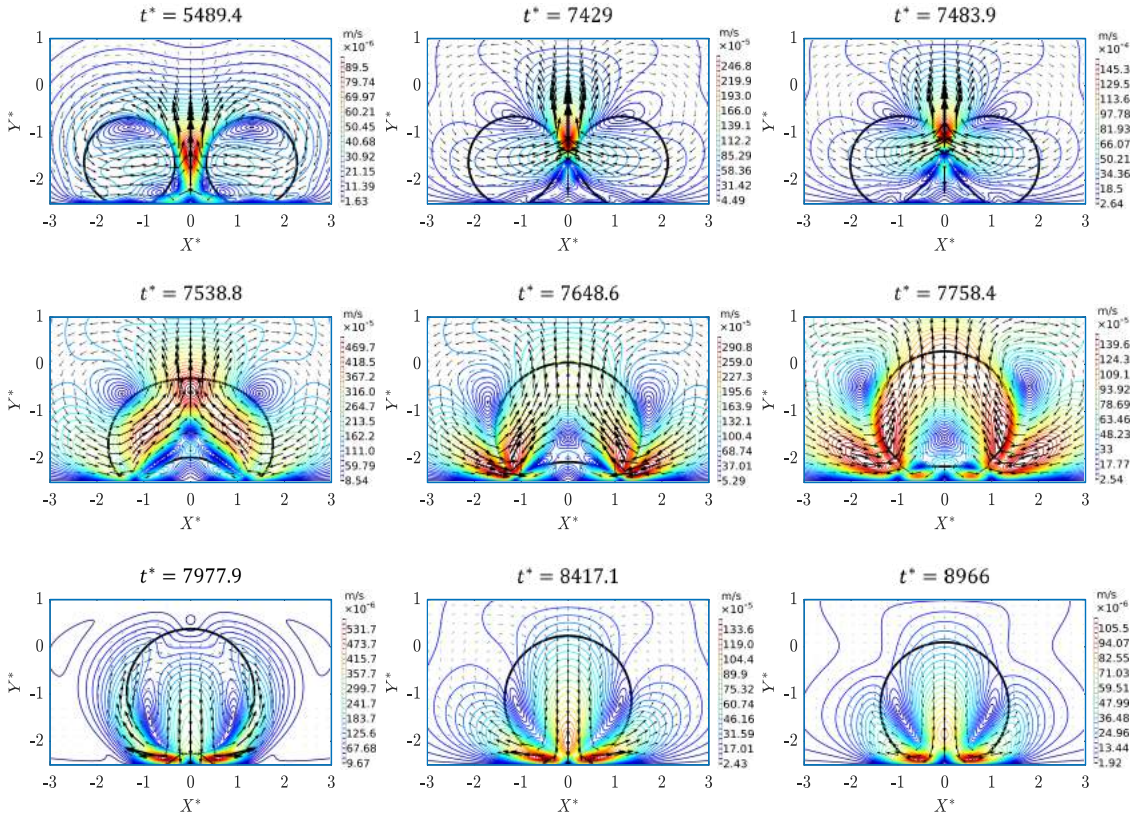

Figure 7. Time evolution of velocity contours both inside and outside of sessile droplets on a hydrophobic surface under a permanent magnetic field at $\mathrm{Bo}_m = 0.145$, $\theta_c = 150°$, $\zeta = 1$, and $\lambda = 1$.

Furthermore, the complex flow dynamics behind the interaction between a pair of sessile ferrofluid droplets under a permanent magnetic field can be better explained by the velocity contours around the droplets, and Figure 7 depicts the time evolution of velocity contours both inside and outside of sessile droplets on a hydrophobic surface under a permanent magnetic field at $\mathrm{Bo}_m = 0.145$, $\theta_c = 150°$, $\zeta = 1$, and $\lambda = 1$. It can be seen that as the magnetic field is activated, a flow field is created along the horizontal direction, which in turn starts to push the droplets towards the magnet, and as they approach each

other, the fluid region between the droplets is squeezed, which gives rise to a larger velocity gradient ($t^* = 5489.4$). Also, during the sliding motion, counter rotating vortices appear in the bottom and top region of the droplet where the size of the vortices near the top surface is much larger in compared to the vortices near the bottom interface. Consequently, the droplets come into close contact with each other and coalesce into one, which is further followed by a rapid surge in the velocity of the fluid region trapped between the droplets just before merging ($t^* = 7429$). Since the surface energy of the droplets converts into kinetic energy during merging, a larger velocity gradient appears around the merged droplet where the vortices near the bottom interface consistently attempt to adhere the droplet to the hydrophobic surface, but eventually fail due to the presence of stronger vortices near the top interface that aid the droplet in taking off from the hydrophobic surface ($t^* = 7538.8$). Eventually, the droplet reaches a maximum peak during jumping, followed by the dissipation of droplet kinetic energy in the surrounding viscous medium ($t^* = 7977.9$) and comes back rapidly on the horizontal surface under the influence of magnetic field and reaches an equilibrium shape under the prescribed wetted wall condition ($t^* = 8966$). Note that, during the coalescence phenomenon, a drainage of the fluid film between the droplets occurs, which is ultimately followed by the flattening of the interfaces in the merging region. Upon the coalescence, a large amount of interfacial energy is released near the merging point, which can be considered as a potential reason behind the increase in the size of the vortices near the top surface in compared to the bottom surface at $\mathrm{Bo}_m = 0.145$, $\theta_c = 150°$, $\zeta = 1$, and $\lambda = 1$.

Next, we expose the droplets to a comparatively larger magnetic field strength ($\mathrm{Bo}_m = 0.581$) to observe how it affects the overall dynamics of a pair of sessile ferrofluid droplets on a hydrophobic surface under similar wetted wall conditions, and Figure 8 represents the time evolution of sessile droplets on the same surface under a permanent magnetic field at $\mathrm{Bo}_m = 0.581$, $\theta_c = 150°$, $\zeta = 1$, and $\lambda = 1$. Figure 8(a) indicates that the droplets undergo greater deformation under stronger magnetic fields (a clear deformation

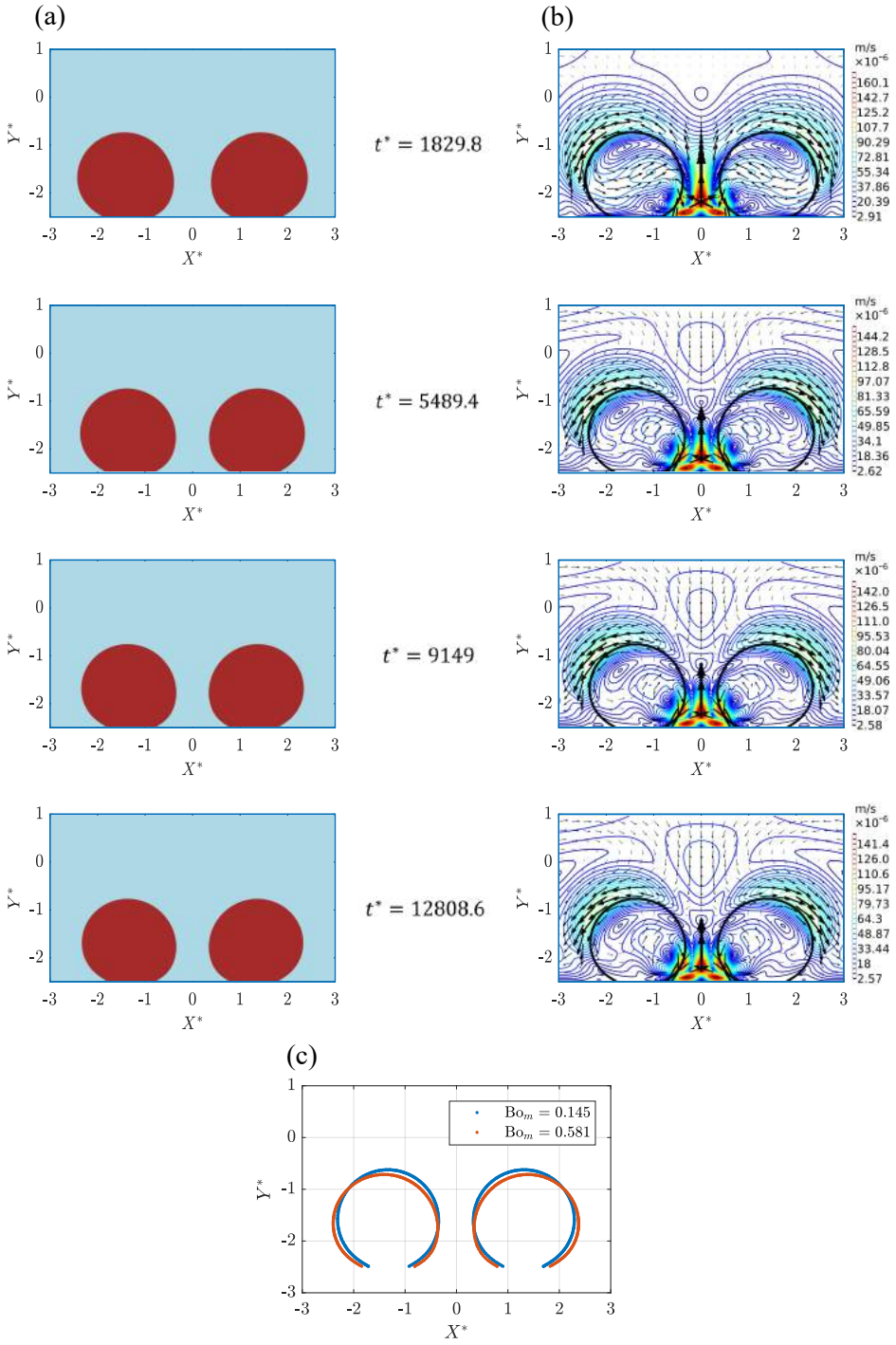

Figure 8. Time evolution of sessile droplets on a hydrophobic surface under a permanent magnetic field at $\mathrm{Bo}_m = 0.581$, $\theta_c = 150°$, $\zeta = 1$, and $\lambda = 1$. (a) Droplet shapes; (b) Velocity contours; and (c) Shapes of droplets during sliding motion under magnetic fields at $t^* = 5489.4$.

comparison is shown in Figure 8(c)), which in turn forces the droplet interfaces closer to the magnet to move towards the magnet even more, while experiencing resistance from the interfaces far away from the magnet ($t^* = 1829.8$). Eventually, as time goes on, the droplets spread more under the action of magnetic field, giving an increase to the magnitude of the base diameter of the droplets ($t^* = 5489.4$). Consequently, the adhesion energy of the droplets due to their larger spreading becomes more intense in compared to the magnetic force experienced by the droplets ($t^* = 9149$). As a result, the droplets ultimately reach a steady state without undergoing coalescence at $t^* = 12808.6$.

Moreover, the flow field profiles around the droplets in Figure 8(b) suggest that during the motion of droplets towards the magnet, a high pressure region is formed between the droplets near the hydrophobic surface due to the squeezing of the region in between droplets ($t^* = 1829.8$), while a high pressure region appeared near the top surface of the droplets under comparatively smaller magnetic field strengths at $t^* = 5489.4$ in Figure 7 . Also, a significant number of smaller vortices are found to appear near the bottom interface of the droplets, which eventually aid in the movement along the horizontal direction, whereas the larger vortices near the top interface of the droplets tend to resist the motion of droplets, which again emerges due to the movement of the deformed droplets towards the magnet in the horizontal direction ($t^* = 9149$). Finally, under the combined interaction of magnetic field and droplet adhesion, the droplets reach equilibrium positions on the hydrophobic surface at $t^* = 12808.6$.

Lastly, the dynamic behavior of sessile droplets under variable magnetic field strengths at $\theta_c = 150°$, $\zeta = 1$, and $\lambda = 1$ is summarized in Figure 9. From Figure 9(a) it can be seen that as the magnetic field strength increases upto $\mathrm{Bo}_m = 0.372$, the droplets experience faster coalescence, and the maximum peak reached by the merged droplet decreases. This decrease in maximum peak can be explained by the fact that due to the increase in magnetic Bond number, the magnetic force encountered by the merged droplet increases, which in turn provides more resistance during the upward jump from the

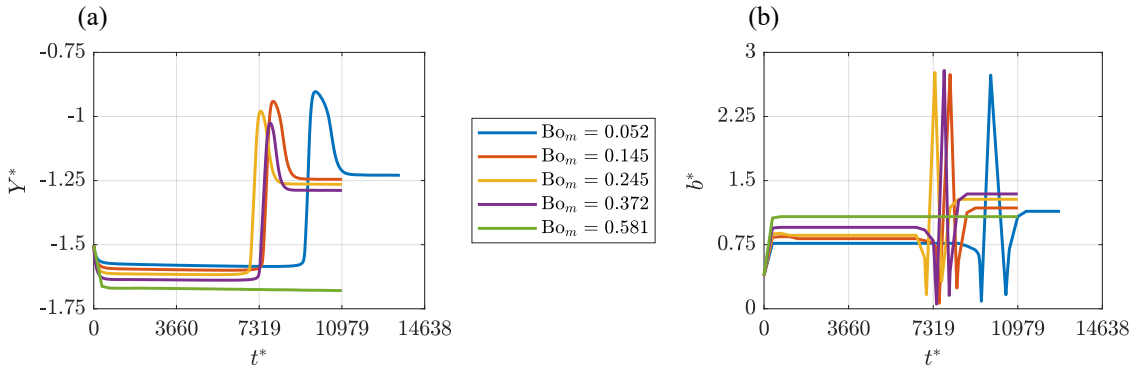

Figure 9. Dynamic behavior of sessile droplets under variable magnetic field strengths at $\theta_c = 150°$, $\zeta = 1$, and $\lambda = 1$. (a) Vertical trajectory Y^* vs t^*; and (b) Base diameter b^* vs t^* (the maximum peak represents the diameter of the merged droplet during jumping phenomenon).

surface (i.e., maximum peak decreases). Also, as the magnetic field strength starts increasing beyond $\mathrm{Bo}_m > 0.245$, the droplets still coalesce and undergo jumping phenomenon; however, a slight increase in coalescence time is observed in compared to previous lower magnetic bond number (i.e., $\mathrm{Bo}_m = 0.245$). This phenomenon emerges because as the droplets are exposed to much stronger magnetic fields, the spreading of the droplet under the action of magnetic field increases (Figure 9(b)), which ultimately increases the adhesion energy of the droplets. As a result, the magnetic field requires longer time to bring the droplets into closer contact that eventually initiates coalescence and jumping phenomenon off the surface. Moreover, if a significantly stronger magnetic field (i.e., $\mathrm{Bo}_m = 0.581$) is applied to the droplets, the droplets experience no coalescence at all and reach steady state shapes under the combined effect of magnetic field and wetted wall condition. Additionally, the effect of magnetic field strength on the spreading diameter of the droplets is depicted in Figure 9(b), which clearly shows an increase in the base diameter of the droplets at higher magnetic Bond numbers before and after the coalescence process.

Figure 9(a) provides very interesting and useful information on the conditions required to induce coalescence/no coalescence between sessile droplets during sliding motion under magnetic fields. Also, during the analysis of this critical condition, unity density and

viscosity ratios are used in order to eliminate additional complexities so that the readers have an easy understanding about the coalescence dynamics of droplets. Here, a dimensionless number (magnetic Bond number Bo_m) is used to relate the contribution of magnetic and surface tension forces, the magnitude of which again can be manually controlled through a change in the magnitude of either initial droplet radius, magnetic field strength, or surface tension values. As a result, this analysis can be very beneficial to the experimental design since it clearly provides the magnitudes of all the parameters required to replicate these phenomena during experiments under unity density and viscosity ratios at $\theta_c = 150°$.

4.6. EFFECT OF CONTACT ANGLE

Now, we investigate the effect of contact angles on the interaction phenomenon between a pair of sessile ferrofluid droplets under magnetic fields, and Figure 10(a) depicts the time evolution of spreading dynamics of sessile droplets on a hydrophobic surface under permanent magnetic field at $\mathrm{Bo}_m = 0.145$, $\theta_c = 90°$, $\zeta = 1$, and $\lambda = 1$. The shapes of droplets suggest that as they are exposed to a permanent magnetic field at $\theta_c = 90°$, the wettability of the droplets increases, and the existence of non-uniform magnetic field contributes in the generation of asymmetric droplet shapes with respect to the y axis (i.e., the interface of the droplets closer to the permanent magnet experiences greater deformation than the interface far away from the magnet) at $t^* = 548.9$. Moreover, during the spreading process, the interface of the droplets come closer to each other at $t^* = 695.3$ where a sharp flattening of the interfaces closer to the bottom wall occurs, which eventually initiates the coalescence phenomenon at $t^* = 713.6$. It is important to note that upon initiation of contact, the surface tension force drives a swift motion perpendicular to the line of centers that combines the droplets and causes a decrease in the total surface area ($t^* = 713.6$). Also, as the surface tension force drives the merging process, two large vortices appear on the sides of droplets, while a smaller sized vortex emerges near the center of the top interface

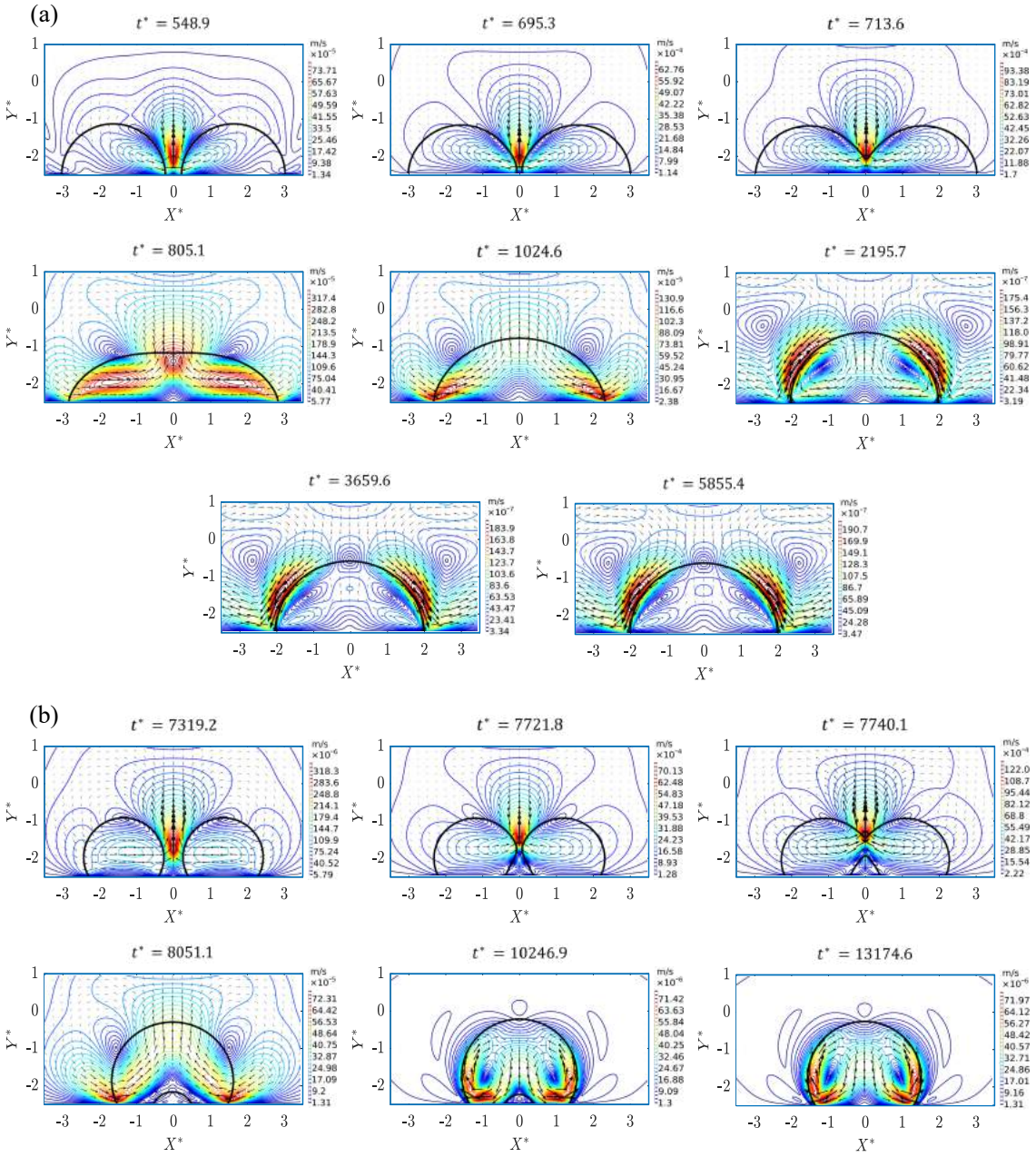

Figure 10. Time evolution of velocity contours around and inside of sessile droplets on a hydrophobic surface under permanent magnetic field at $\mathrm{Bo}_m = 0.145$, $\zeta = 1$, and $\lambda = 1$. (a) $\theta_c = 90°$; and (b) $\theta_c = 120°$.

of the merged droplet ($t^* = 805.1$). Subsequently, with the evolution of time, the two large vortices are pushed towards the bottom, while the vortex on the top interface disappears at $t^* = 1024.6$. Finally, the droplet reaches an equilibrium shape at $t^* = 5855.4$.

Next, the wetted wall condition of the droplets is changed from $\theta_c = 90°$ to $\theta_c = 120°$ under the same magnetic field strength, and Figure 10(b) represents the time evolution of velocity contours around the sessile droplets under a permanent magnetic field at $\mathrm{Bo}_m = 0.145$, $\theta_c = 120°$, $\zeta = 1$, and $\lambda = 1$. Compared to the previous case, here, under similar magnetic field strength, the base diameter of the droplets decreases ($t^* = 7319.2$), and the magnetic field forces the droplet interface closer to the magnet to approach each other ($t^* = 7721.8$), which begins the coalescence process at $t^* = 7740.1$. However, since the coalescence process starts around the center of the droplet interfaces, a void appears in the middle near the bottom interface ($t^* = 8051.1$) during merging, and the droplet tends to take off from the solid surface, which eventually fails due to the dominant nature of magnetic attraction forces and presence of high pressure regions near the bottom interface of the droplet. Lastly, the droplet settles down and assumes a steady state shape at $t^* = 13174.6$. Note that the merged droplet also takes significantly longer time in reaching a steady state shape at $\theta_c = 120°$ than at $\theta_c = 90°$.

Furthermore, the trajectory of the droplets in Figure 11(a) indicates that as the contact angle increases upto $\theta_c = 120°$, the merged droplet do not experience any jumping phenomenon, but experiences an increase in its height at steady state, followed by a decline in height during the approach stage. Also, the time required to initiate coalescence increases with the increase in contact angle values. This phenomenon can be explained by the fact that as the solid surface becomes more hydrophobic, the wettability of the droplet decreases under the same magnetic field strength, which in turn requires more time for the droplets to come into closer contact under the action of magnetic field. However, as the solid surface starts to become superhydrophobic ($\theta_c \geq 135°$), the kinetic energy of the droplets after the coalescence overcomes the adhesive energy, and the droplet ultimately jumps off the

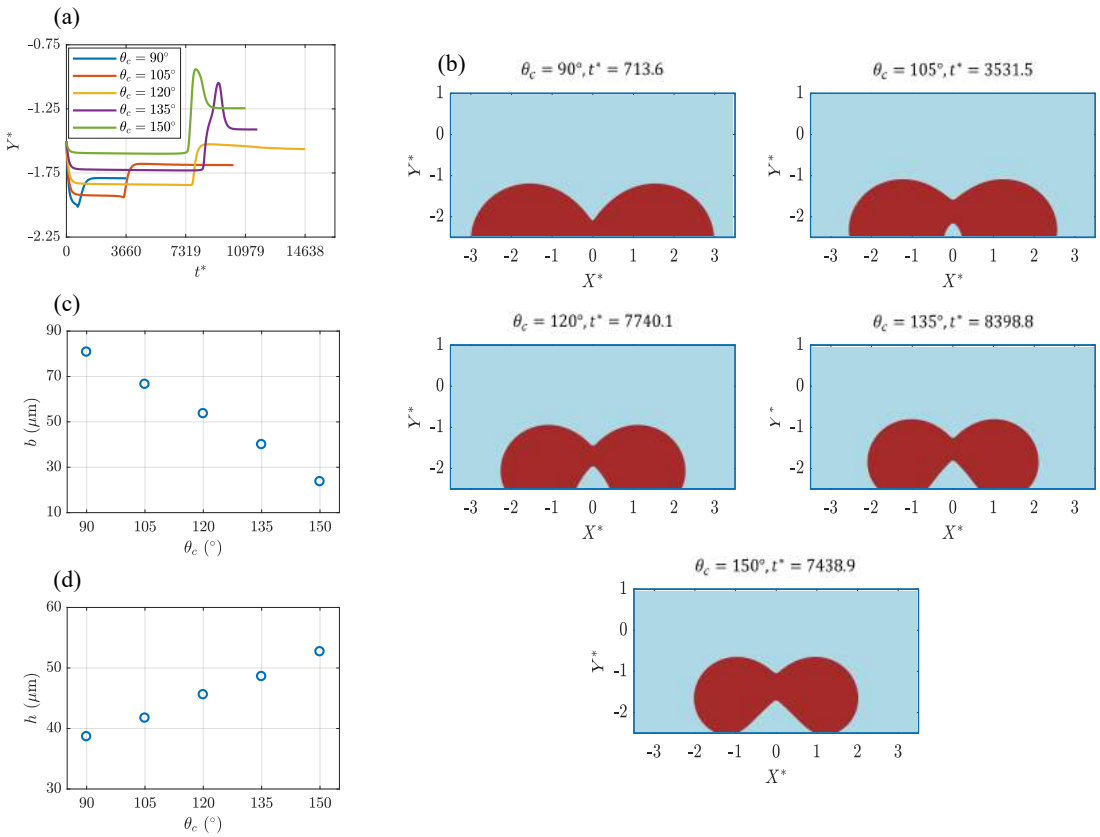

Figure 11. Contact angle effect on coalescence phenomenon between a pair of hydrophobic droplets under permanent magnetic field at $\mathrm{Bo}_m = 0.145$, $\zeta = 1$, and $\lambda = 1$. (a) Vertical trajectory of droplets; (b) Droplet shapes during merging; (c) Steady state droplet base diameter; and (d) Steady state droplet height.

surface. Moreover, the merged droplet experiences higher jumping in the vertical direction as the hydrophobicity of the bottom surface increases, which is attributed by the decrease in the adhesive energy of the droplets (i.e., reduction in base diameter) during coalescence process (Figure 11(b)).

The coalescence point between two droplets is a complex phenomenon and strongly dependent on the wettability of the surface (i.e., contact angle) and magnetic field strengths. Figure 11(b) demonstrates the droplet shapes during merging at $\mathrm{Bo}_m = 0.145$, and the shapes suggest that at $\theta_c = 90°$, the coalescence point occurs near the bottom interface of the droplets, whereas at 105°, the droplets coalesce approximately near the middle of the

droplet interfaces. However, as the hydrophobicity of the bottom substrate increases (i.e., $\theta_c \geq 120°$), the coalescence point appears near the middle of the top half of the droplet interfaces. Nevertheless, the droplet shapes indicate an interesting shift of the coalescence point between droplets from the bottom interface towards the top interface with an increase in the hydrophobicity of the bottom substrate under magnetic fields. Finally, the steady state characteristics of the merged droplet are illustrated in Figure 11(c)-(d), which shows a decrease and an increase in the base diameter and the height of the droplet, respectively under increasing contact angle values.

4.7. EFFECT OF VISCOSITY RATIO

In the final section, we focus on analyzing the effect of viscosity ratios on the coalescence phenomenon between a pair of hydrophobic sessile droplets under permanent magnetic field at $\mathrm{Bo}_m = 0.145$, $\theta_c = 150°$, and $\zeta = 1$. Here, the viscosity of the droplets are kept constant, while the viscosity of the continuous phase is varied to observe how the behavior of sessile droplets change in different surrounding medium under non-uniform magnetic field, including air where the properties of air medium gives rise to huge contrast in viscosity ratios (i.e., $\lambda \approx 5000$).

From Figure 12(a) it can be seen that irrespective of viscosity ratios, the droplets, followed by a sliding motion towards the magnet, coalesce and experience jumping phenomenon under the exposure to a permanent magnetic field; however, the maximum peak reached by the merged droplet during jumping increases with the increase in viscosity ratios. This happens because as the viscosity of the surrounding medium decreases, the kinetic energy of the droplets after merging requires longer time to get dissipated into the surroundings i.e., the droplet undergoes higher jumping in the vertical direction. Also, in addition to a decline in the coalescence time with the increase in viscosity ratios, the merged droplet requires comparatively smaller time to return to the solid surface and reach a steady state under a magnetic field. Interestingly, the trajectory of droplets at a viscosity

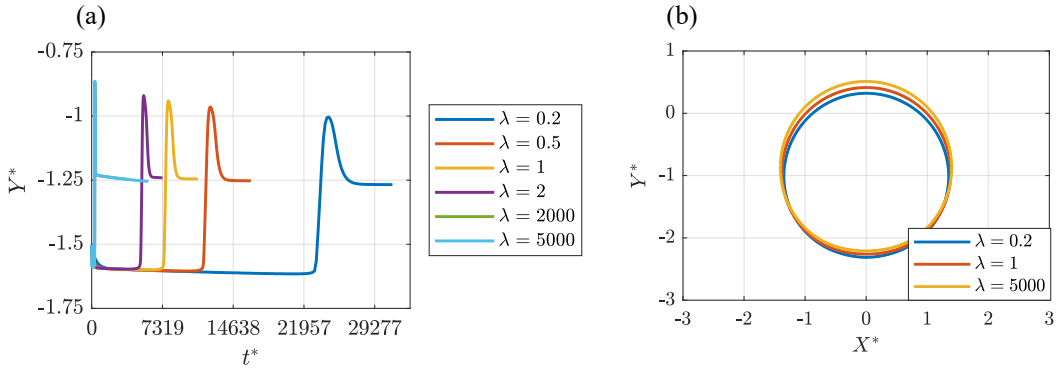

Figure 12. Viscosity ratio effect on coalescence phenomenon between a pair of hydrophobic sessile droplets under permanent magnetic field at $\mathrm{Bo}_m = 0.145$, $\theta_c = 150°$, and $\zeta = 1$. (a) Vertical trajectory of droplets; and (b) Droplet shapes at maximum peaks.

ratio beyond 2000 (i.e., $\lambda \geq 2000$) is found to overlap with each other, which also indicates the dominant behavior of magnetic field at higher viscosity ratios. Furthermore, the droplet shapes at maximum peaks for some representative viscosity ratios are depicted in Figure 12(b), which demonstrates a small increase in droplet jumping in the vertical direction in compared to the massive change in viscosity ratios.

In the research community, two-dimensional (2D) studies are extremely popular in compared to three-dimensional (3D) studies for providing flexibilities in terms of investigating the effects of a wide range of parameters on droplet dynamics, while saving a considerable amount of computational resources. Also, before moving on to the in-detailed investigation of the droplet dynamics under magnetic fields, the 2D model is systematically validated against benchmark solutions and existing experimental works in the literature to make sure that it is capable of capturing the correct droplet interface and producing accurate results. Although, a three-dimensional (3D) model would be more realistic than a 2D model, it would generate similar coalescence phenomenon under similar conditions; however, the droplet shapes could be slightly different due to the effect of surface tension in the z-direction.

5. CONCLUSION

A systematic numerical inquiry on the dynamics between a pair of sessile droplets on a smooth hydrophobic surface under a permanent magnetic field is carried out in this paper. The results indicate that a non-uniform magnetic field is capable of increasing the wettability of a hydrophobic surface, which usually has lower surface energy and interfacial tension between the droplet and solid surface. Consequently, the base diameter of the sessile droplet experiences an increase at higher magnetic field strengths, while the apex height and equilibrium contact angle decreases. Also, when a pair of sessile droplets are symmetrically separated with respect to the center of the magnet along y-axis on a superhydrophobic surface (i.e., $\theta_c = 150^\circ$), the merged droplet experiences a jumping phenomenon off the solid surface, which is eventually followed by the migration of the droplets along the horizontal direction that ultimately leads to coalescence under the action of non-uniform magnetic field. Moreover, as the magnetic field strength increases upto $\mathrm{Bo}_m = 0.372$, the droplets still experience coalescence at a faster rate; however, the maximum peak reached by the merged droplet during the upward flight decreases. Furthermore, if the magnetic field strength is allowed to increase above $\mathrm{Bo}_m > 0.372$, at $\mathrm{Bo}_m = 0.581$, the droplets do not encounter any coalescence phenomenon anymore, instead reach equilibrium shapes under the combined effects of magnetic field and wetted wall condition.

Additionally, we investigated the effect of contact angles on the dynamic interaction behavior between a pair of sessile droplets under magnetic fields, and the findings suggest the existence of a critical contact angle value, below which the droplets do not experience any jumping off phenomenon after undergoing coalescence. In our investigation, the critical contact angle value is found to be approximately 120° (i.e., $\theta_c^{cr} \approx 120^\circ$). Also, the merging pattern of droplets changes at lower contact angle values (i.e., $\theta_c = 90^\circ$). Moreover, the merged droplet sustains an attenuation in equilibrium base diameter magnitudes, while experiencing an increase in the apex height on more hydrophobic surfaces. Furthermore, on a superhydrophobic surface (i.e., $\theta_c = 150^\circ$), as the viscosity ratio increases (i.e.,

λ = 5000 in case of air as surrounding medium), the droplets encounter rapid coalescence under the attraction forces of magnetic field, and the merged droplet experiences higher jumping at higher magnitudes of viscosity ratios. Nevertheless, the findings signify the massive potential of magnetic field in the controlled transportation of sessile droplets on a hydrophobic surface that will be critical to a significant number of biological and chemical assays.

ACKNOWLEDGEMENT

The authors gratefully acknowledge the support from the Department of Mechanical and Aerospace Engineering (MAE) and the Center for Biomedical Research (CBR) at Missouri University of Science and Technology. This work is partially supported by the NSF through Grant DMS-1818642 to CW.

REFERENCES

Ashgriz, N., *Handbook of atomization and sprays: theory and applications*, Springer Science & Business Media, 2011.

Bellehumeur, C., Bisaria, M., and Vlachopoulos, J., 'An experimental study and model assessment of polymer sintering,' Polymer Engineering & Science, 1996, **36**(17), pp. 2198–2207.

Berthier, J., *Micro-drops and digital microfluidics*, William Andrew, 2012.

Beyzavi, A. and Nguyen, N.-T., 'Modeling and optimization of planar microcoils,' Journal of Micromechanics and Microengineering, 2008a, **18**(9), p. 095018.

Beyzavi, A. and Nguyen, N.-T., 'One-dimensional actuation of a ferrofluid droplet by planar microcoils,' Journal of Physics D: Applied Physics, 2008b, **42**(1), p. 015004.

Beyzavi, A. and Nguyen, N.-T., 'Programmable two-dimensional actuation of ferrofluid droplet using planar microcoils,' Journal of micromechanics and microengineering, 2009, **20**(1), p. 015018.

Bitar, A., Kaewsaneha, C., Eissa, M. M., Jamshaid, T., Tangboriboonrat, P., Polpanich, D., and Elaissari, A., 'Ferrofluids: from preparation to biomedical applications,' Journal of Colloid Science and Biotechnology, 2014, **3**(1), pp. 3–18.

Bithi, S. S., Wang, W. S., Sun, M., Blawzdziewicz, J., and Vanapalli, S. A., 'Coalescing drops in microfluidic parking networks: A multifunctional platform for drop-based microfluidics,' Biomicrofluidics, 2014, **8**(3), p. 034118.

Cheng, Y., Xu, J., and Sui, Y., 'Numerical investigation of coalescence-induced droplet jumping on superhydrophobic surfaces for efficient dropwise condensation heat transfer,' International Journal of Heat and Mass Transfer, 2016, **95**, pp. 506–516.

Chiou, C.-H., Shin, D. J., Zhang, Y., and Wang, T.-H., 'Topography-assisted electromagnetic platform for blood-to-pcr in a droplet,' Biosensors and Bioelectronics, 2013, **50**, pp. 91–99.

Cho, S. K., Moon, H., and Kim, C.-J., 'Creating, transporting, cutting, and merging liquid droplets by electrowetting-based actuation for digital microfluidic circuits,' Journal of Microelectromechanical systems, 2003, **12**(1), pp. 70–80.

Choi, K., Ng, A. H., Fobel, R., Chang-Yen, D. A., Yarnell, L. E., Pearson, E. L., Oleksak, C. M., Fischer, A. T., Luoma, R. P., Robinson, J. M., *et al.*, 'Automated digital microfluidic platform for magnetic-particle-based immunoassays with optimization by design of experiments,' Analytical chemistry, 2013, **85**(20), pp. 9638–9646.

Choi, K., Ng, A. H., Fobel, R., and Wheeler, A. R., 'Digital microfluidics,' Annual review of analytical chemistry, 2012, **5**, pp. 413–440.

COMSOL, *CFD Module Application Library Manual*, 5.3a edition, 2018.

Ding, X., Li, P., Lin, S.-C. S., Stratton, Z. S., Nama, N., Guo, F., Slotcavage, D., Mao, X., Shi, J., Costanzo, F., *et al.*, 'Surface acoustic wave microfluidics,' Lab on a Chip, 2013, **13**(18), pp. 3626–3649.

Du, G.-S., Pan, J.-Z., Zhao, S.-P., Zhu, Y., den Toonder, J. M., and Fang, Q., 'Cell-based drug combination screening with a microfluidic droplet array system,' Analytical chemistry, 2013, **85**(14), pp. 6740–6747.

Egatz-Gómez, A., Melle, S., García, A. A., Lindsay, S., Márquez, M., Domínguez-García, P., Rubio, M. A., Picraux, S., Taraci, J., Clement, T., *et al.*, 'Discrete magnetic microfluidics,' Applied Physics Letters, 2006, **89**(3), p. 034106.

Fair, R. B., 'Digital microfluidics: is a true lab-on-a-chip possible?' Microfluidics and Nanofluidics, 2007, **3**(3), pp. 245–281.

Garcia-Cordero, J. L. and Fan, Z. H., 'Sessile droplets for chemical and biological assays,' Lab on a Chip, 2017, **17**(13), pp. 2150–2166.

Geng, H., Feng, J., Stabryla, L. M., and Cho, S. K., 'Dielectrowetting manipulation for digital microfluidics: Creating, transporting, splitting, and merging of droplets,' Lab on a Chip, 2017, **17**(6), pp. 1060–1068.

Guo, M. T., Rotem, A., Heyman, J. A., and Weitz, D. A., 'Droplet microfluidics for high-throughput biological assays,' Lab on a Chip, 2012, **12**(12), pp. 2146–2155.

Hassan, M. R. and Wang, C., 'Magnetic field induced ferrofluid droplet breakup in a simple shear flow at a low reynolds number,' Physics of Fluids, 2019, **31**(12), p. 127104.

Hassan, M. R. and Wang, C., 'Ferro-hydrodynamic interactions between ferrofluid droplet pairs in simple shear flows,' Colloids and Surfaces A: Physicochemical and Engineering Aspects, 2020a, p. 124906.

Hassan, M. R. and Wang, C., 'Lateral migration of a ferrofluid droplet in a plane poiseuille flow under uniform magnetic fields,' Physical Review E, 2020b, **102**(2), p. 022611.

Hassan, M. R., Zhang, J., and Wang, C., 'Deformation of a ferrofluid droplet in simple shear flows under uniform magnetic fields,' Physics of Fluids, 2018, **30**(9), p. 092002.

Hassan, M. R., Zhang, J., and Wang, C., 'Numerical investigation of falling ferrofluid droplets under magnetic fields,' Colloid and Interface Science Communications, 2021, **40**, p. 100333.

Javed, M. R., Chen, S., Lei, J., Collins, J., Sergeev, M., Kim, H.-K., Kim, C.-J., van Dam, R. M., and Keng, P. Y., 'High yield and high specific activity synthesis of [18 f] fallypride in a batch microfluidic reactor for micro-pet imaging,' Chemical Communications, 2014, **50**(10), pp. 1192–1194.

Keng, P. Y., Chen, S., Ding, H., Sadeghi, S., Shah, G. J., Dooraghi, A., Phelps, M. E., Satyamurthy, N., Chatziioannou, A. F., van Dam, R. M., *et al.*, 'Micro-chemical synthesis of molecular probes on an electronic microfluidic device,' Proceedings of the National Academy of Sciences, 2012, **109**(3), pp. 690–695.

Kim, J. A., Kim, M., Kang, S. M., Lim, K. T., Kim, T. S., and Kang, J. Y., 'Magnetic bead droplet immunoassay of oligomer amyloid β for the diagnosis of alzheimer' s disease using micro-pillars to enhance the stability of the oil–water interface,' Biosensors and Bioelectronics, 2015, **67**, pp. 724–732.

Kovetz, A. and Olund, B., 'The effect of coalescence and condensation on rain formation in a cloud of finite vertical extent,' Journal of Atmospheric Sciences, 1969, **26**(5), pp. 1060–1065.

Lehmann, U., Hadjidj, S., Parashar, V. K., Vandevyver, C., Rida, A., and Gijs, M. A., 'Two-dimensional magnetic manipulation of microdroplets on a chip as a platform for bioanalytical applications,' Sensors and Actuators B: Chemical, 2006a, **117**(2), pp. 457–463.

Lehmann, U., Vandevyver, C., Parashar, V. K., and Gijs, M. A., 'Droplet-based dna purification in a magnetic lab-on-a-chip,' Angewandte Chemie International Edition, 2006b, **45**(19), pp. 3062–3067.

Liu, F., Ghigliotti, G., Feng, J. J., and Chen, C.-H., 'Numerical simulations of self-propelled jumping upon drop coalescence on non-wetting surfaces,' Journal of fluid mechanics, 2014a, **752**, pp. 39–65.

Liu, J. and Liu, S., 'Dynamics behaviors of droplet on hydrophobic surfaces driven by electric field,' Micromachines, 2019, **10**(11), p. 778.

Liu, X., Cheng, P., and Quan, X., 'Lattice boltzmann simulations for self-propelled jumping of droplets after coalescence on a superhydrophobic surface,' International Journal of Heat and Mass Transfer, 2014b, **73**, pp. 195–200.

Long, Z., Shetty, A. M., Solomon, M. J., and Larson, R. G., 'Fundamentals of magnet-actuated droplet manipulation on an open hydrophobic surface,' Lab on a Chip, 2009, **9**(11), pp. 1567–1575.

Ma, Y., Pan, J.-Z., Zhao, S.-P., Lou, Q., Zhu, Y., and Fang, Q., 'Microdroplet chain array for cell migration assays,' Lab on a Chip, 2016, **16**(24), pp. 4658–4665.

Madejski, J., 'Solidification of droplets on a cold surface,' International journal of heat and mass transfer, 1976, **19**(9), pp. 1009–1013.

Mary, A. R., Narayanan, T., Sunny, V., Sakthikumar, D., Yoshida, Y., Joy, P., and Anantharaman, M., 'Synthesis of bio-compatible spion–based aqueous ferrofluids and evaluation of radiofrequency power loss for magnetic hyperthermia,' Nanoscale research letters, 2010, **5**(10), pp. 1706–1711.

Mats, L., Young, R., Gibson, G. T., and Oleschuk, R. D., 'Magnetic droplet actuation on natural (colocasia leaf) and fluorinated silica nanoparticle superhydrophobic surfaces,' Sensors and Actuators B: Chemical, 2015, **220**, pp. 5–12.

Menchaca-Rocha, A., Martínez-Dávalos, A., Nunez, R., Popinet, S., and Zaleski, S., 'Coalescence of liquid drops by surface tension,' Physical Review E, 2001, **63**(4), p. 046309.

Nam, Y., Kim, H., and Shin, S., 'Energy and hydrodynamic analyses of coalescence-induced jumping droplets,' Applied Physics Letters, 2013, **103**(16), p. 161601.

Nelson, W. C. and Kim, C. J. C., 'Droplet actuation by electrowetting-on-dielectric (ewod): A review,' Journal of Adhesion Science and Technology, 2012, **26**(12-17), pp. 1747–1771.

Ng, A. H., Chamberlain, M. D., Situ, H., Lee, V., and Wheeler, A. R., 'Digital microfluidic immunocytochemistry in single cells,' Nature communications, 2015, **6**(1), pp. 1–12.

Nguyen, N.-T., Zhu, G., Chua, Y.-C., Phan, V.-N., and Tan, S.-H., 'Magnetowetting and sliding motion of a sessile ferrofluid droplet in the presence of a permanent magnet,' Langmuir, 2010, **26**(15), pp. 12553–12559.

Okochi, M., Tsuchiya, H., Kumazawa, F., Shikida, M., and Honda, H., 'Droplet-based gene expression analysis using a device with magnetic force-based-droplet-handling system,' Journal of bioscience and bioengineering, 2010, **109**(2), pp. 193–197.

Park, M. C., Kim, M., Lim, G. T., Kang, S. M., An, S. S. A., Kim, T. S., and Kang, J. Y., 'Droplet-based magnetic bead immunoassay using microchannel-connected multiwell plates (μchamps) for the detection of amyloid beta oligomers,' Lab on a Chip, 2016, **16**(12), pp. 2245–2253.

Pipper, J., Inoue, M., Ng, L. F., Neuzil, P., Zhang, Y., and Novak, L., 'Catching bird flu in a droplet,' Nature medicine, 2007, **13**(10), pp. 1259–1263.

Pipper, J., Zhang, Y., Neuzil, P., and Hsieh, T.-M., 'Clockwork pcr including sample preparation,' Angewandte Chemie, 2008, **120**(21), pp. 3964–3968.

Raj, K. and Moskowitz, R., 'Commercial applications of ferrofluids,' Journal of Magnetism and Magnetic Materials, 1990, **85**(1-3), pp. 233–245.

Rida, A., Fernandez, V., and Gijs, M., 'Long-range transport of magnetic microbeads using simple planar coils placed in a uniform magnetostatic field,' Applied Physics Letters, 2003, **83**(12), pp. 2396–2398.

Rosensweig, R. E., *Ferrohydrodynamics*, Cambridge University Press, 1985.

Shi, X., Chen, C.-H., Gao, W., Chao, S.-h., and Meldrum, D. R., 'Parallel rna extraction using magnetic beads and a droplet array,' Lab on a Chip, 2015a, **15**(4), pp. 1059–1065.

Shi, Y., Tang, G., and Xia, H., 'Investigation of coalescence-induced droplet jumping on superhydrophobic surfaces and liquid condensate adhesion on slit and plain fins,' International Journal of Heat and Mass Transfer, 2015b, **88**, pp. 445–455.

Shikida, M., Takayanagi, K., Inouchi, K., Honda, H., and Sato, K., 'Using wettability and interfacial tension to handle droplets of magnetic beads in a micro-chemical-analysis system,' Sensors and Actuators B: Chemical, 2006, **113**(1), pp. 563–569.

Ueda, E., Geyer, F. L., Nedashkivska, V., and Levkin, P. A., 'Dropletmicroarray: facile formation of arrays of microdroplets and hydrogel micropads for cell screening applications,' Lab on a Chip, 2012, **12**(24), pp. 5218–5224.

Wang, X., Chen, Z., and Xu, B., 'Coalescence-induced jumping of condensate droplets on microstructured surfaces with different gravitational fields by lattice boltzmann method,' Computers & Fluids, 2019, **188**, pp. 60–69.

Wang, Z. and Zhe, J., 'Recent advances in particle and droplet manipulation for lab-on-a-chip devices based on surface acoustic waves,' Lab on a Chip, 2011, **11**(7), pp. 1280–1285.

Zhang, J., Hassan, M. R., Rallabandi, B., and Wang, C., 'Migration of ferrofluid droplets in shear flow under a uniform magnetic field,' Soft matter, 2019, **15**(11), pp. 2439–2446.

Zhang, Y. and Nguyen, N.-T., 'Magnetic digital microfluidics–a review,' Lab on a Chip, 2017, **17**(6), pp. 994–1008.

Zhang, Y., Shin, D. J., and Wang, T.-H., 'Serial dilution via surface energy trap-assisted magnetic droplet manipulation,' Lab on a chip, 2013, **13**(24), pp. 4827–4831.

Zhang, Y. and Wang, T.-H., 'Full-range magnetic manipulation of droplets via surface energy traps enables complex bioassays,' Advanced Materials, 2013, **25**(21), pp. 2903–2908.

Zhu, Y., Zhang, Y.-X., Cai, L.-F., and Fang, Q., 'Sequential operation droplet array: an automated microfluidic platform for picoliter-scale liquid handling, analysis, and screening,' Analytical chemistry, 2013, **85**(14), pp. 6723–6731.

Zhu, Y., Zhang, Y.-X., Liu, W.-W., Ma, Y., Fang, Q., and Yao, B., 'Printing 2-dimentional droplet array for single-cell reverse transcription quantitative pcr assay with a microfluidic robot,' Scientific reports, 2015, **5**, p. 9551.

V. NUMERICAL INVESTIGATION OF FALLING FERROFLUID DROPLETS UNDER MAGNETIC FIELDS

Md Rifat Hassan, Jie Zhang, and Cheng Wang
Department of Mechanical & Aerospace Engineering
Missouri University of Science and Technology
Rolla, Missouri 65409
Tel: 573–341–4636, Fax: 573–341–4607
Email: wancheng@mst.edu

ABSTRACT

A methodical analysis on the dynamic interaction behavior between a pair of uneven sized ferrofluid droplets freely falling under gravity and exposed to a uniform magnetic field is presented in this article. Here, a conservative level set method (LSM) is adopted to precisely calculate the free interface curvature of the droplet, which again couples both magnetic and flow fields. The results indicate that at a unity viscosity ratio (i.e., $\lambda = 1$) and a fixed Galilei number (i.e., Ga = 1600), in the absence of any external forces except gravity, a critical initial vertical separation distance between the droplets prevails ($\Delta Y^{\star}_{cr} \geq 6$), which prohibits them from undergoing coalescence phenomenon before hitting the bottom wall of the computational domain. However, enacting a magnetic field along $\alpha = 0^{\circ}$ hinders coalescence, while it is expedited by the implementation of the magnetic field along $\alpha = 90^{\circ}$. On the other hand, at $\alpha = 45^{\circ}$, the droplets exhibit downward lateral migration along the secondary diagonal of the computational domain, leading to a larger separation between them at higher magnetic bond numbers Bo_m (i.e., $\mathrm{Bo}_m = 8$). Moreover, the investigation on the effects of surface tension suggests an increase in the vertical separation between droplets at higher Eötvös numbers (i.e., Eo = 9.48). Additionally, application of a magnetic field along $\alpha = 0^{\circ}$ results in the formation of round-bottom hull shaped droplets, whereas they transform into teardrop shaped droplets before coalescence at $\alpha = 90^{\circ}$. In contrast,

the magnetic field along $\alpha = 45^\circ$ greatly impedes the coalescence phenomenon, leading to migration of droplets along divergent lateral directions, whereas the droplets do not encounter any coalescence event in air before impact under gravity or gravity and magnetic fields.

Keywords: Ferrofluids, Droplets, Magnetic field, Coalescence

1. INTRODUCTION

Droplet on demand (DOD) is one of the most prominent processes involved in inkjet printing — a prospective material-conserving and cost-effective localized additive deposition technique for large area manufacturing where the ejection of a desired volume of ink droplet is substantially achieved via a nozzle, followed by an abrupt piezoelectric actuated quasi-adiabatic reduction in the chamber volume [Liu *et al.*, 2013, Pabst *et al.*, 2013, Tekin *et al.*, 2008]. Subsequently, the ejected droplet encounters air resistance while falling under the influence of gravity, until impinging and spreading on the substrate, which is again aided by the momentum gained by the droplet during the free fall and surface tension flow along the surface [He *et al.*, 2017, Pesach and Marmur, 1987]. Interestingly, the spreading and final shape of the droplet are also strongly dependent on the printing height and viscosity of the medium, which eventually are crucial in the determination of ultimate resolution in printing techniques [Jung *et al.*, 2013, Perelaer *et al.*, 2009a,b].

Moreover, size distribution and dynamic interaction between gravity induced freely falling droplets are important in flotation [Al-Shamrani *et al.*, 2002, Savino *et al.*, 2003], combustion [Kumagai *et al.*, 1971, Wang *et al.*, 1984], and atmospheric raindrop formation applications [List *et al.*, 2009, Low and List, 1982]. Magarvey et al. [Magarvey and Taylor, 1956] conducted an experimental investigation on the breakup mechanism of large water drops during free fall and concluded that breakup, being independent of turbulence flow regime, is not initiated by internal vibrations. Arecchi et al. [Arecchi *et al.*, 1989] experimentally observed the appearance of fragmentation (a dynamic instability) in droplets, freely

falling through another miscible fluid medium. Rabe et al. [Rabe *et al.*, 2010] performed experiments on the binary collision between droplets and described coalescence-separation regimes based on symmetric Weber numbers, while a experimental study on the droplet impact on a sessile droplet is conducted by Nikolopoulos et al. [Nikolopoulos *et al.*, 2010].

Several numerical investigations on gravity induced droplets have also been reported in the existing literature [Cho *et al.*, 2012, Kim *et al.*, 2014]. Bararnia et al. [Bararnia *et al.*, 2013] conducted a two-dimensional (2D) numerical analysis on the coalescence and breakup of multiple droplets during free fall, and their results suggest an increase in the droplet deformation at higher Eötvös numbers (i.e., the ratio between gravitational and surface tension forces), whereas a three-dimensional (3D) numerical simulations on binary droplet collisions is performed by Pan et al. [Pan and Suga, 2005]. Fakhari et al. [Fakhari and Rahimian, 2009] implemented a lattice Boltzmann method (LBM) to simulate the behavior of falling droplet and deduced that the droplet attains an equilibrium shape at lower Eötvös numbers, while experiencing a breakup phenomenon at higher Eötvös numbers. Strotos et al. [Strotos *et al.*, 2016] numerically quantified the heating effect on the breakup of droplets in a high temperature gaseous environment and found out the heating has minimal effects on the breakup event, except for lower Weber numbers. Furthermore, through the implementation of an inter-particle lattice Boltzmann model, a numerical analysis on the detachment behavior of droplets from solid walls under gravity is carried out by Tilehboni et al. [Tilehboni *et al.*, 2015].

Recent studies reveal that in addition to hydrodynamic forces, droplet behavior can be exploited by utilizing external force fields, such as, electric [Bararnia and Ganji, 2013, Supeene *et al.*, 2008], acoustic [Pangu and Feke, 2004, Wixforth *et al.*, 2004], and magnetic fields [Hassan and Wang, 2019, 2020a,b, Hassan *et al.*, 2018]. Jalaal et al. [Jalaal *et al.*, 2010] experimentally observed the behavior of a water droplet falling through an oil medium under DC electric fields and came to a conclusion that the droplet experiences a translational motion at higher magnitudes of electrode potential, which can also be repeated

depending on electric field strengths. Im et al. [Im *et al.*, 2011] performed an experimental investigation on the actuation of a charged droplet (suspended in a dielectric liquid) using electrophoresis and found out a positive correlation between electrolyte concentration and electrical charging limited effect, whereas a numerical investigation on droplet deformation under steady electric fields has been conducted by Hua et al. [Hua *et al.*, 2008] Additionally, Phan et al. [Phan *et al.*, 2016] used a vibrating membrane activated acoustic streaming method to control the behavior of droplets, and a review on the droplet manipulation practices in lab-on-a-chip devices using acoustic surface waves is provided in Wang and Zhe's work [Wang and Zhe, 2011].

However, the implementation of magnetic field requires a droplet to be ferrofluid — liquid containing nanoscale sized magnetite particles covered with surfactants to impede clumping [Scherer and Figueiredo Neto, 2005]. Ki [Ki, 2010] enacted a level set algorithm to study its effectiveness in two-phase incompressible flow problems i.e., rising bubble, stretching and oscillation of droplets under magnetic fields, while Tagawa [Tagawa, 2006] numerically studied the dynamics of a falling liquid metal droplet using a finite difference method dependent HSMAC algorithm. Moreover, an experimental exploration on the separation of droplets from ferrofluid jets under magnetic field effect is administered by Fabian et al. [Fabian *et al.*, 2017] where they observed a micro-thread formation before the separation of droplets. Furthermore, the recent experimental study of Zhang et al. [Zhang *et al.*, 2019] confirms controlled manipulation of droplet migration utilizing magnetic fields, which in turn depicts the potential of magnetic fields in the separation of droplets along different outlets in microchannels.

So far, to the best of our knowledge, only a few investigations are focused on the interaction phenomenon between freely falling droplets [Bararnia and Ganji, 2013, Hu *et al.*, 2017, Zhang *et al.*, 2012]. Recently, Shi et al. [Shi *et al.*, 2014] enacted a VOSET method to study the behavior of a single falling ferrofluid droplet under magnetic field, while a similar investigation based on a hybrid lattice Boltzmann method is conducted

by Ghaderi et al. [Ghaderi *et al.*, 2018] Also, in the aforementioned studies, the authors only concentrated on applying the magnetic field in a direction parallel/perpendicular to the direction of gravity. In addition to using flow focusing [Wu *et al.*, 2013, Zhang *et al.*, 2019] or T-junction [Aboutalebi *et al.*, 2018, Tan *et al.*, 2010] microfluidic channels for generating droplets required for inkjet printing, droplet production can also be achieved utilizing a nozzle, which furthermore can be manipulated efficiently using magnetic fields [Bijarchi *et al.*, 2020, Tsai and Wang, 2019]. While gravity has a negligible effect on droplet production in microfluidics, it exerts a significant effect on droplet formation from a nozzle where wettability of nozzle surface leads to variable diameter droplets, including production of satellite droplets for a range of different conditions [Fabian *et al.*, 2017, Jiang *et al.*, 2016, Tsai and Wang, 2019]. As a result, interpreting the dynamics between two uneven sized falling droplets is necessary to the understanding of inkjet printing processes. Therefore, in this article, we employ a uniform magnetic field along different directions with a view to investigating the effects of variable initial vertical separation distance, magnetic field strength, direction, surface tension, density and viscosity ratio on the dynamic interaction behavior between a pair of uneven sized ferrofluid droplets falling under the influence of gravity in a two-dimensional (2D) domain, which in addition to inkjet printing, will be useful in controlling the impact and flight of droplets in numerous applications [Castrejon-Pita *et al.*, 2013, Che and Matar, 2018, Choi *et al.*, 2008, Dhindsa *et al.*, 2020, Laan *et al.*, 2014, Saien and Bamdadi, 2012, Smith and Shin, 2012, Wanchoo *et al.*, 2003, Yudistira *et al.*, 2010]. Extensive investigations in the literature suggest that two-dimensional (2D) models have the capability to precisely track the free interface of the droplet, which additionally provides the advantage of using relatively smaller computational resources [Bararnia *et al.*, 2013, Ghaderi *et al.*, 2018, Hassan and Wang, 2020a, Hassan *et al.*, 2018, Shi *et al.*, 2014, Tilehboni *et al.*, 2015]. Here, COMSOL 5.3, a commercial simulation software, is adopted to perform the simulations where finite element method based level set algorithm couples both flow and magnetic fields.

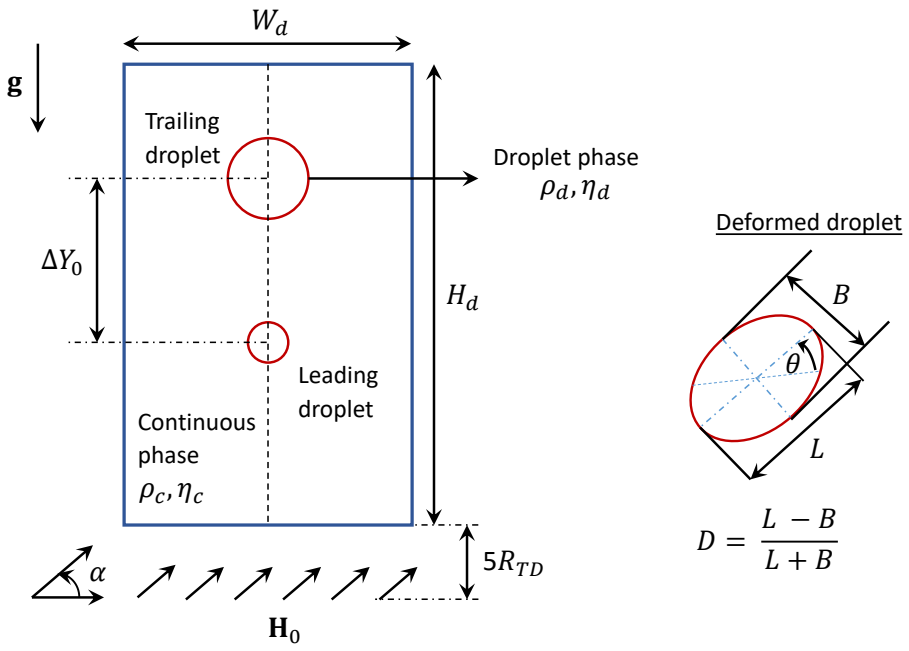

Figure 1. Schematic of a pair of ferrofluid droplets falling through another viscous fluid medium under the influence of gravity **g** and uniform magnetic fields, $\mathbf{H}_0$.

The overall organization of the article is as follows: In Section 2, we discuss the schematic of the computational model, while Section 3 depicts an in-depth understanding of the numerical schemes and governing equations required to study the dynamic interaction behavior between freely falling droplets. Next, a systematic explanation of the influence of magnetic field strength, direction, surface tension, density and viscosity ratio on droplet interactions is presented in Section 4. Finally, a grid independence test is demonstrated in Supporting information, followed by an outline of the crucial findings in Section 5.

2. COMPUTATIONAL MODEL

Figure 1 depicts the schematic of a pair of ferrofluid droplets falling through another viscous fluid medium under the combined exposure to gravity and uniform magnetic fields. Here, the bigger droplet, having a radius twice the radius of the smaller droplet, is treated as the trailing droplet, while the smaller one is considered as the leading droplet (i.e.,

$R_{TD} = 2R_{LD}$). Initially, both droplets have the same viscosity as the continuous fluid phase (i.e., $\eta_{TD} = \eta_{LD} = \eta_c$), and the density of the droplets are considered 1.2 times the density of the continuous phase (i.e., $\rho_{TD} = \rho_{LD} = 1.2\rho_c$). The subscripts TD, LD, and c symbolize the trailing droplet, leading droplet, and continuous phase, respectively. Also, the magnetic permeability of the droplet phase is considered twice as the magnetic permeability of the surrounding medium (i.e., $\mu_d = 2\mu_c$). Moreover, it is important to note that both fluid medium are assumed as incompressible fluids in our numerical model, while free triangular (unstructured) elements are utilized for meshing purposes. The dimensions of the computational model can be described as $H_d = 1.6W_d$ where H_d and W_d simultaneously signify the height and width of the computational domain. Again, the width of the domain W_d is 10 times the radius of the trailing droplet (i.e., $W_d = 10R_{TD}$). Note that, the dimensions of the domain are chosen to be large enough so that the wall effects on droplet deformation can be neglected.

In the initial stage, the droplets are separated from each other through a vertical distance ΔY_0. A no slip condition is employed on the walls of the computational domain, while initially, the velocity in the flow domain is zero (i.e., $\mathbf{u}_0 = 0$). Also, while applying the magnetic field along the mentioned directions, the other sides are kept in insulated condition (i.e., $\mathrm{n} \cdot \mathbf{B} = 0$). The droplets start to fall freely under gravity $\mathbf{g}$ with time and eventually create a flow field around themselves in the process. Next, the flow domain is exposed to a uniform magnetic field, $\mathbf{H_0}$, from different directions, which is denoted by α. Under the combined effect of gravity and magnetic fields, the droplets experience deformation, and the deformation of a droplet D can be calculated as $D = \frac{L-B}{L+B}$ where L represents the major axis droplet dimension, and B denotes the dimension along the minor axis of the droplet during the deformation process. Additionally, with deformation, the orientation angle of the droplet θ changes, which is quantified as the angle in the counter-clockwise direction from the positive x axis.

3. COMPUTATIONAL ALGORITHM SCHEME

3.1. LEVEL SET METHOD

Moving interfaces are involved in numerous applications, including breakup of surface waves [Duan *et al.*, 2003], water-air interactions [Taylor *et al.*, 2007], and solidification melt dynamics [Grabow *et al.*, 1988], which additionally involve a convoluted interaction between the free interface and the surrounding fluid phase due to a jump in the temperature and surface tension across the interface of the moving boundaries. Consequently, these interactions present a troublesome issue in tracking the interface of the moving boundaries in multi-phase flows. Therefore, a conservative level set algorithm, with an advantage of accurately calculating the curvature of the free interface, is imposed in our computational model to track the evolution of the droplet interface in two-phase flows [Olsson *et al.*, 2007].

The level set algorithm utilizes a smooth signed distance function ϕ that assigns different values on the two sides of the interface i.e., 0 in one fluid phase, and 1 in another, while preserving a smooth change across the limited thickness of the interface. Moreover, the smoothness of the level set function ϕ makes it easier to advect with the velocity field $\mathbf{u}$, which is again accomplished in two steps: In the first step, a numerical method governs the advection of ϕ, which is then used to check the preservation of the interface thickness in the second step. The level set algorithm adopts second order approximations to execute both these steps, which can be formulated as [Olsson and Kreiss, 2005]:

$$\frac{d\phi}{dt} + \mathbf{u} \cdot \nabla\phi = \gamma \nabla \cdot \left(\epsilon \nabla\phi - \phi(1-\phi) \frac{\nabla\phi}{|\nabla\phi|} \right). \tag{1}$$

In Equation 1, the velocity field is represented by $\mathbf{u}$, while ϵ and γ signify the interface thickness and the amount of re-initialization, respectively. In our model, the magnitude of ϕ is regarded as 1 in droplet phase, while it is zero in the surrounding fluid phase (i.e., $\phi_d = 1$ and $\phi_c = 0$), and the exact interface of the droplet ϕ_{int} is characterized by 0.5 iso-contour of ϕ (i.e., $\phi_{int} = \phi|_{0.5}$). The re-initialization amount γ is critical to the numerical accuracy of

the algorithm since it preserves the concentration of the gradient of ϕ across the thickness of the interface over time. A too low or too high magnitude of γ leads to the formation of unwanted liquid-gas interface and large computational times, respectively [COMSOL, 2018]. On the other hand, ϵ regulates the thickness of the free surface where the variation of ϕ will be achieved. Using a larger magnitude of ϵ results in an inaccurate representation of the droplet interface, while a smaller value leads to spurious velocity profiles. The largest mesh element size around the free interface is considered as the optimal value of ϕ in two-phase simulations [COMSOL, 2018].

The multi-phase flows are treated as a single phase flow in a level set algorithm, and as a result, the properties of the fluid phase alter accordingly with the magnitude of level set function ϕ, which further uses a linear interpolation technique to calculate the density (ρ), dynamic viscosity (η), magnetic permeability (μ), and magnetic susceptibility (χ) in the flow domain. The interpolation schemes are as follows:

$$\begin{aligned} \rho &= (1-\phi)\rho_c + \rho_d\phi, \quad \mu = (1-\phi)\mu_c + \mu_d\phi, \\ \eta &= (1-\phi)\eta_c + \eta_d\phi, \quad \chi = (1-\phi)\chi_c + \chi_d\phi, \end{aligned} \tag{2}$$

where the droplet medium and surrounding fluid medium are concurrently designated by the subscripts d and c, individually.

3.2. GOVERNING EQUATIONS

A two-phase flow consisting of an incompressible, immiscible ferrofluid droplet dispersed in another immiscible, viscous medium is typically governed by the continuity and time dependent Navier-Stokes equations, which are as follows:

$$\nabla \cdot \mathbf{u} = 0 \tag{3}$$

and

$$\rho\left(\frac{\partial \mathbf{u}}{\partial t}+\mathbf{u}\cdot\nabla\mathbf{u}\right)=-\nabla p+\eta\nabla^2\mathbf{u}+\mathbf{F}_s+\mathbf{F}_g+\mathbf{F}_m. \tag{4}$$

In Equation 4, fluid pressure is characterized by p, and the terms $\eta\nabla^2\mathbf{u}$ indicate the viscous stress. The symbol $\mathbf{F}_s$ denotes the surface tension force and can be expressed as:

$$\mathbf{F}_s=\nabla\cdot\left[\sigma\left\{\mathbf{I}+(-\mathbf{n}\mathbf{n}^T)\right\}\delta\right]. \tag{5}$$

Equation 5 involves a surface tension coefficient σ, and an identity operator $\mathbf{I}$. The unit normal to the interface $\mathbf{n}$ is related to the level set function ϕ and can be calculated as:

$$\mathbf{n}=\frac{\nabla\phi}{|\nabla\phi|}, \tag{6}$$

while ϕ is also utilized to derive the smoothed Dirac delta function δ:

$$\delta=6|\phi(1-\phi)||\nabla\phi|. \tag{7}$$

The body forces are represented by the symbols $\mathbf{F}_g$ and $\mathbf{F}_m$ where $\mathbf{F}_g$ indicates the force due to gravity and equals to $\rho\mathbf{g}$ (i.e., $\mathbf{F}_g=\rho\mathbf{g}$). On the other hand, according to Rosensweig [Rosensweig, 1985], the magnetic force $\mathbf{F}_m$ can be formulated as:

$$\mathbf{F}_m=\nabla\cdot\boldsymbol{\tau}_m=\nabla\cdot\left(\mu\mathbf{H}\mathbf{H}-\frac{\mu}{2}H^2\mathbf{I}\right) \tag{8}$$

where $\boldsymbol{\tau}_m$ represents the magnetic stress tensor, which arises due to the generation of additional stresses under the exposure to a uniform magnetic field, $\mathbf{H}_0$. Also, interpreting the Maxwell equations [Stratton, 2007] that describe the magnetic field for a nonconducting ferrofluid are indispensable to having an in-depth understanding about the magnetic stress

tensor $\boldsymbol{\tau}_m$, which can be elucidated as:

$$\nabla \times \mathbf{H} = 0 \tag{9}$$

and

$$\nabla \cdot \mathbf{B} = 0. \tag{10}$$

In Equations 9 and 10, $\mathbf{H}$ denotes the magnetic field, while magnetic induction is denoted by the symbol $\mathbf{B}$, which again requires to satisfy the following relations:

$$\mathbf{B} = \begin{cases} \mu_0(\mathbf{H} + \mathbf{M}) & \text{in } \Omega_d \\ \mu_0 \mathbf{H} & \text{in } \Omega_c \end{cases} \tag{11}$$

where Ω_d and Ω_c denote the magnetic droplet domain and nonmagnetic surrounding domain, respectively. The symbol μ_0 indicates the magnetic permeability in a classical vacuum, which has a magnitude equal to $4\pi \times 10^{-7}$ N/A^2. Moreover, the magnetization of a linearly magnetizable ferrofluid $\mathbf{M}$ can be defined as:

$$\mathbf{M} = \chi \mathbf{H}. \tag{12}$$

Furthermore, Equations 9 and 10 can be satisfied by the introduction of a scalar potential ψ as:

$$\mathbf{H} = -\nabla \psi, \tag{13}$$

which ultimately results in the following relation:

$$\nabla \cdot (\mu \nabla \psi) = 0. \tag{14}$$

3.3. GOVERNING EQUATIONS IN DIMENSIONLESS FORM

Now, due to the omnipresence of a significant number of variables in the computational domain, the governing equations are transformed into dimensionless forms, which uses the following scaling relationships:

$$\mathbf{u}^\star = \frac{\mathbf{u}}{U},\ p^\star = \frac{pD_0}{\eta U},\ t^\star = \frac{tU}{D_0},\ \rho^\star = \frac{\rho}{\rho_c},\ \eta^\star = \frac{\eta}{\eta_c},\ \mu^\star = \frac{\mu}{\mu_0},\ \mathbf{H}^\star = \frac{\mathbf{H}}{H_0}$$

where H_0 is the magnitude of the applied magnetic field $\mathbf{H}_0$. As a result, the governing equations 3 and 4 can be written as:

$$\nabla^\star \cdot \mathbf{u}^\star = 0, \tag{15}$$

$$\frac{\partial \mathbf{u}^\star}{\partial t^\star} + (\mathbf{u}^\star \cdot \nabla^\star)\mathbf{u}^\star = -\nabla^\star p^\star + \frac{1}{\mathrm{Re}}\nabla^{\star 2}\mathbf{u}^\star + \frac{1}{\mathrm{WeEo}}\mathbf{g}^\star + 2\frac{\mathrm{Bo}_m}{\mathrm{We}}\nabla^\star \cdot \boldsymbol{\tau}_m^\star + \frac{1}{\mathrm{We}}\mathbf{F}_\sigma^\star. \tag{16}$$

The conversion of dimensional equations into dimensionless forms leads to a few major dimensionless groups, which are as follows:

$$\mathrm{Re} = \frac{\rho_c U D_0}{\eta_c}, \tag{17}$$

$$\mathrm{We} = \frac{\rho_c U^2 D_0}{\sigma}, \tag{18}$$

$$\mathrm{Eo} = \frac{(\rho_d - \rho_c)\mathbf{g} D_0^2}{\sigma}, \tag{19}$$

and

$$\mathrm{Bo}_m = \frac{\mu_0 R_0 H^2}{2\sigma}, \tag{20}$$

where Re, We, Eo, and Bo_m denote the Reynolds number, Weber number, Eötvös number, and magnetic Bond number, respectively. Again, Reynolds number Re can be related to Galilei number Ga and Richardson number Ri through the following relationship:

$$\mathrm{Ga} = \mathrm{Re}^2\mathrm{Ri} \tag{21}$$

where Galilei number Ga assumes the following form:

$$\mathrm{Ga} = \frac{\rho_c^2 \mathbf{g} D_0^3}{\eta_c^2}. \tag{22}$$

In the above mentioned dimensionless groups, D_0 (diameter) and R_0 (radius) stand for the properties of the trailing droplet in undeformed condition. Other notable dimensionless groups are as follows:

$$\zeta = \frac{\rho_d}{\rho_c} \text{ and } \lambda = \frac{\eta_d}{\eta_c} \tag{23}$$

where ζ and λ signify the density and viscosity ratios, respectively. Here, in this paper, we investigate the effects of Ga, Eo, Bo_m, λ, ζ and α on the dynamics of a pair of ferrofluid droplets falling under the force of gravity **g**.

4. RESULTS AND DISCUSSIONS

4.1. VALIDATION OF COMPUTATIONAL MODEL

Here, we present the validation of our computational model against the prevalent works in the literature in terms of the dynamics of a solitary ferrofluid droplet under the force of gravity **g**. Figure 2 depicts the transformation of droplet shapes at different times under the influence of gravity at Ga = 1600, Eo = 1.24, ζ = 1.12, and λ = 0.1. From Figure 2(a), it can be seen that the droplet starts to fall under gravity, and with time the round

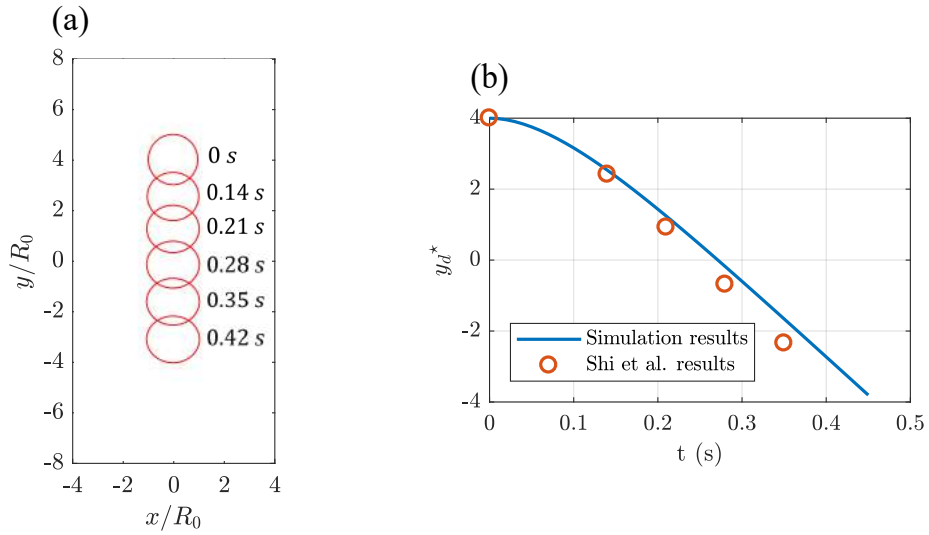

Figure 2. Freely falling droplet under the influence of gravity at Ga = 1600, Eo = 1.24, ζ = 1.12, and λ = 0.1. (a) Droplet shape transformation; and (b) Comparison of vertical droplet migration results against Shi et al. [Shi *et al.*, 2014], $y_d^\star$ vs time.

shaped droplet transforms into an oblate shaped droplet due to the effect of inertial force. Moreover, the vertical trajectory of the droplet is plotted in Figure 2(b), which apparently indicates a linear trend in the trajectory of the droplet after the droplet reaches an equilibrium shape. Furthermore, the droplet shapes and trajectories are found to agree quantitatively well with the findings of Shi et al. [Shi *et al.*, 2014], and the discrepancy between our total trajectory results and the findings of Shi et al. is perceived to be approximately 9%. The major reason behind this discrepancy can be attributed to the fact that in their paper, they mentioned rounded values of dimensionless groups, whereas the exact values would help reduce the errors in the simulation to a greater extent. Note that, here, the position of the droplet centroid $y_d^\star$ is non-dimensionalized with respect to the radius of the trailing droplet (i.e., $y_d^\star = y_d/R_0$).

Table 1. Maximum mesh element size in the computational domain.

Mesh 1	Mesh 2	Mesh 3	Mesh 4
$0.11R_0$	$0.07R_0$	$0.06R_0$	$0.04R_0$

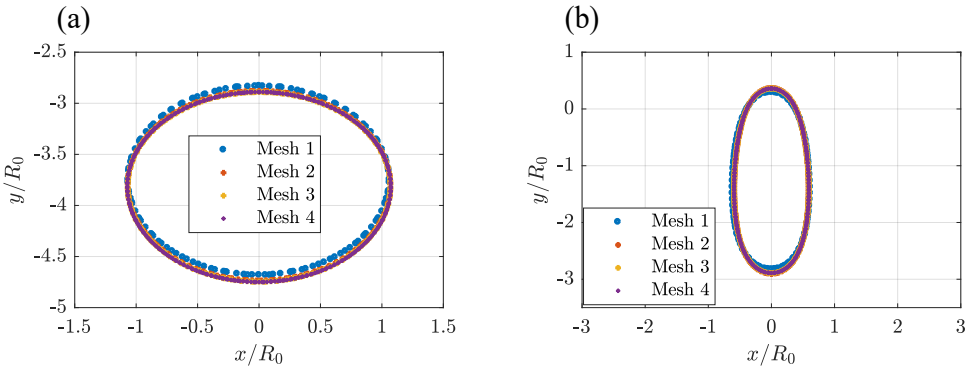

Figure 3. Grid independence test using different mesh configurations at Ga = 1600, Eo = 1.24, and $\zeta = 1.12$. (a) Steady state droplet shape at $t^\star = 22.2$ ($\mathrm{Bo}_m = 0$); and (b) Steady state droplet shape at $t^\star = 14.8$ ($\mathrm{Bo}_m = 8$, $\alpha = 90°$).

4.2. GRID INDEPENDENCE TEST

A grid independence check is also conducted to ensure that our computational model is capable of generating good results within a reasonable amount of time. Figure 3 shows the shapes of a droplet suspended in another viscous medium at Ga = 1600, Eo = 1.24, and $\zeta = 1.12$ for different mesh configurations, which are again tabulated in Table 1, and it can be seen that when the maximum mesh element size in the computational domain is less than or equal to $0.07R_0$, the droplet shapes are identical to each each other. As a result, we have decided to use $0.07R_0$ as the magnitude of maximum mesh element size in the computational domain throughout the rest of the simulations in this paper. Furthermore, the validation of the rheology of a ferrofluid droplet exposed to a uniform magnetic field is demonstrated in our previous work [Hassan *et al.*, 2018].

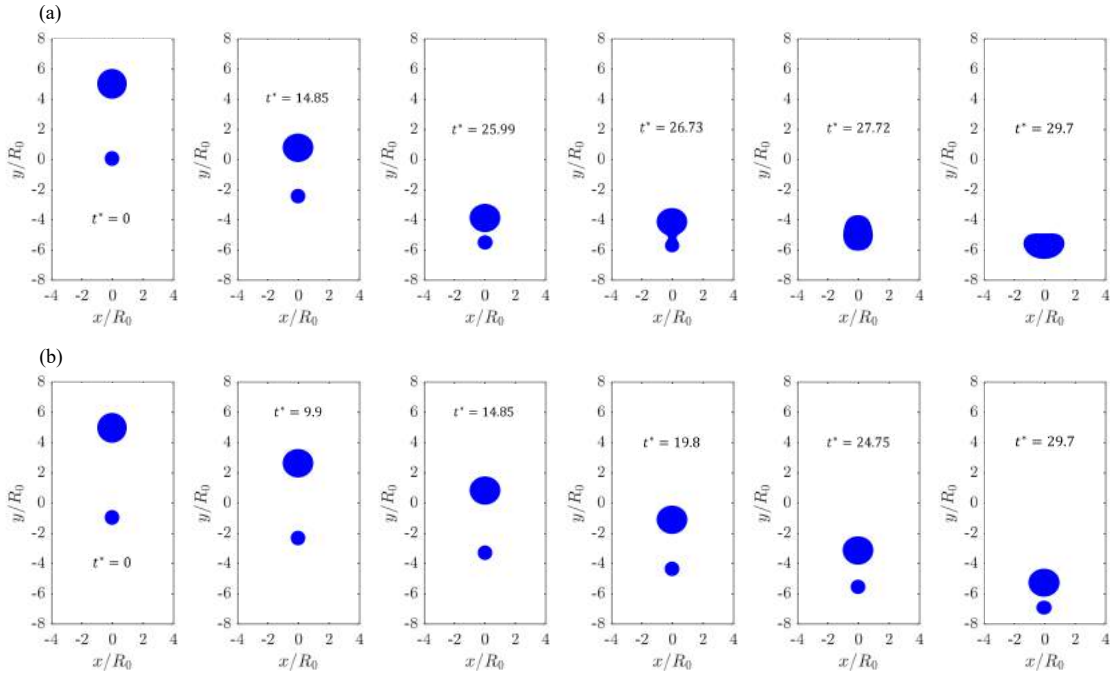

Figure 4. Transformation of droplet shapes under gravity at Ga = 1600, Eo = 1.24, and $\lambda = 1$. (a) $\Delta Y_0^\star = 5$; and (b) $\Delta Y_0^\star = 6$.

4.3. EFFECT OF INITIAL VERTICAL SEPARATION

First, we analyze the effect of initial vertical separation between droplets with an aim to understand how the separation distance affects the dynamic behavior of droplets under the influence of gravity. In the following sections, the density and viscosity ratios are considered as 1.12 and 1 ($\zeta = 1.12$, $\lambda = 1$), respectively, unless mentioned otherwise. Figure 4(a) shows the dynamics of the droplets under gravity at Ga = 1600, Eo = 1.24, $\lambda = 1$, and $\Delta Y_0^\star = 5$. Here, the symbol $\Delta Y^\star$ stands for the dimensionless vertical separation distance, which is nondimensionalized by the radius of the trailing droplet (i.e., $\Delta Y^\star = \Delta Y/R_0$), while the characteristic velocity U and trailing droplet diameter D_0 are used as scaling parameters for dimensionless times ($t^\star = tU/D_0$) where the magnitude of the characteristic velocity U equals to $\sqrt{\mathbf{g}D_0}$ (i.e., $U = \sqrt{\mathbf{g}D_0}$). Figure 4(a) indicates that as time progresses, the droplets start to fall under gravity, and the trailing droplet, owing to larger fluid volume, accelerates faster in compared to the leading smaller sized droplet. Eventually, the trailing

droplet catches up with the leading droplet ($t^\star = 25.99$), and as soon as the droplets come in close contact ($t^\star = 26.73$), their interfaces flatten and drainage of the fluid film between the droplets occurs. Eventually, as the fluid film gets thinner, the van der Waals force activates and dominates the coalescence event, which ultimately causes the droplets to coalesce into a large sized droplet ($t^\star = 27.72$). This coalescence phenomenon is similar to the coalescence event observed in our previous work [Hassan and Wang, 2020a]. Also, the shape of the droplets remain almost circular throughout the journey due to higher surface tension value, which prevents the droplets from undergoing large deformation as a result of inertial forces. Ultimately, after coalescence, the droplet tends to experience greater inertial forces, which in turn flattens the top surface of the droplet before reaching the bottom of the computational domain ($t^\star = 29.7$).

On the other hand, Figure 4(b) shows the trajectory of the droplets at Ga = 1600, Eo = 1.24, $\lambda = 1$, and $\Delta Y_0{}^\star = 6$, which confirms that when the droplets are separated by a vertical distance $6R_0$ instead of $5R_0$, the droplets do not experience any coalescence phenomenon before reaching the bottom surface of the flow domain ($t^\star = 29.7$). The shapes of the droplets also remain identical as the previous case; however, the results indicate that there exists a critical vertical separation distance (i.e., $\Delta Y^\star_{cr} \geq 6$), beyond which no coalescence is observed between the droplets in the flow domain.

4.4. EFFECT OF MAGNETIC FIELD

Magnetic fields are capable of generating additional Maxwell stresses, thus inducing a mismatch in the normal stress distribution at the fluid-fluid interface and as a result can be utilized as a potential tool in the manipulation of ferrofluids. Now, we investigate the effect of magnetic field on the dynamic behavior of gravity induced freely falling ferrofluid droplets at a fixed Galilei number. The Galilei number and vertical separation distance are kept constant throughout the rest of the article (i.e., Ga = 1600 and $\Delta Y^\star_0 = 5$), unless mentioned otherwise.

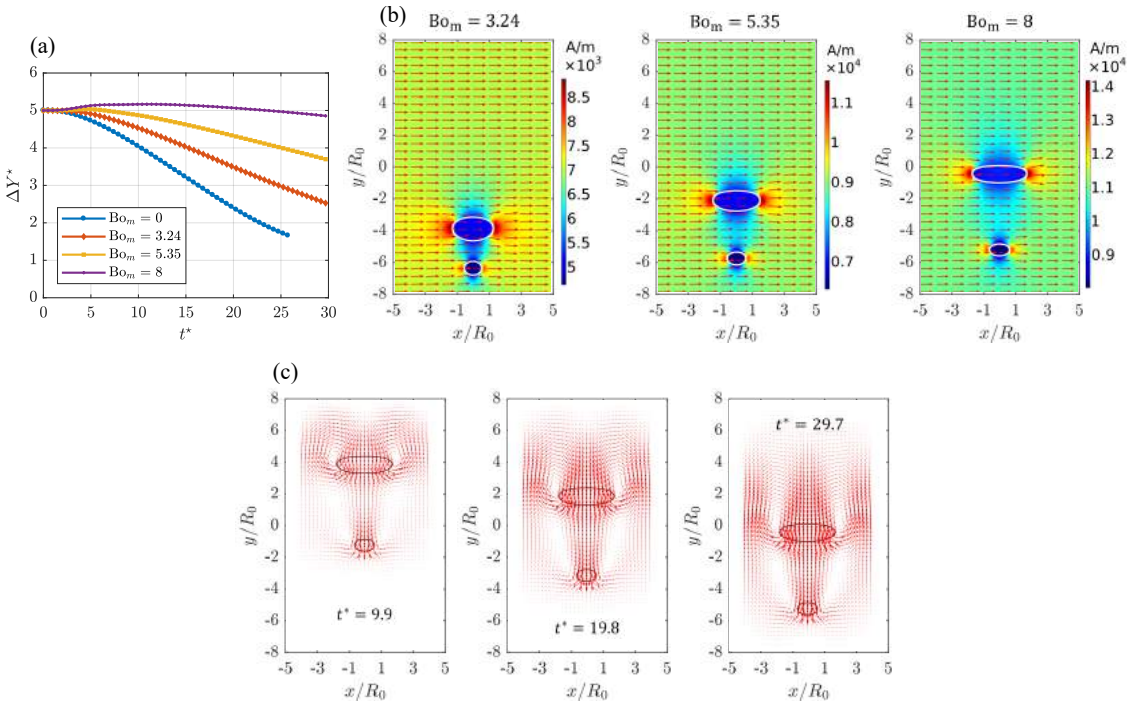

Figure 5. Dynamic behavior of freely falling droplets under gravity and magnetic fields at Ga = 1600, Eo = 1.24, $\alpha = 0°$, and $\Delta Y_0{}^\star = 5$. (a) $\Delta Y^\star$ vs $t^\star$; (b) Magnetic field, **H** profiles around droplets at $t^\star = 29.7$; and (c) Shape evolution of ferrofluid droplets at $\mathrm{Bo}_m = 8$. The flow fields in this article consist of flow fields both inside and outside of droplets where the arrow velocity inside the droplet illustrates the flow fields inside the droplet. The opposite is true for the flow fields outside the droplets.

4.4.1. $\alpha = 0°$. Figure 5 illustrates the dynamic behavior of gravity induced droplets under the exposure to a uniform magnetic field, applied in a direction perpendicular to the direction of gravity (i.e., $\alpha = 0°$) at Ga = 1600, Eo = 1.24, and $\Delta Y_0{}^\star = 5$. Figure 5(a) suggests that with the increase in magnetic field strengths, the vertical separation between the droplets increases, which in the end prevents the droplets from undergoing coalescence in a situation where coalescence phenomenon is typically observed in the absence of any external forces, except gravity (Figure 4(a)). Moreover, Figure 5(b) shows the magnetic field profiles around steady shaped droplets at $t^\star = 29.7$, which indicates an increase in the deformation of droplets at increased magnetic Bond numbers. Also, from the magnetic field profiles, it can be seen that a uniform magnetic field exists both inside and outside of the

droplets where the magnetic field lines act in a direction parallel to the direction of applied magnetic field. However, the magnetic field lines experience a small deviation along the interface of the droplets due to a sudden jump in the magnetic properties. Additionally, the magnetic field exerts a greater magnetic field strength along the equator, while it is least in magnitude along the poles of the droplets, which in turn aids the droplets in the expansion along the equator region.

The flow fields both inside and outside of the droplets provide a better explanation about the dynamics of the freely falling droplets under the exposure to a uniform magnetic field and gravity. Figure 5(c) shows the development of droplet shapes under the combined effects of gravity and magnetic fields at Ga = 1600, Eo = 1.24, Bo_m = 8, $\alpha = 0°$, and $\Delta Y_0{}^\star = 5$, which reveals that when a magnetic field is applied, the droplets start to stretch in the direction of the magnetic field and attain a steady shape around $t^\star = 19.8$, resulting in an increased drag around the droplets. Also, with increased deformation at higher magnetic Bond numbers, the droplets experience greater drag, which ultimately slows down the acceleration of the droplets in the flow domain. Moreover, the oblate shaped ellipsoids suggest the dominance of magnetic field over the surface tension force, although the top surface of the droplets are slightly flattened in compared to the bottom surface of the droplet due to the generation of higher pressure on the top surface as a result of inertial forces. Furthermore, most of the flow field lines pass through the central portion of the droplets; yet, two circulation zones are formed only along the equatorial ends of the trailing droplet due to the excessive elongation of the droplet in compared to the leading droplet along the direction of the magnetic field, which eventually leaves a larger trail as time propagates.

4.4.2. $\alpha = 90°$. Next, the magnetic field is employed in a direction parallel to the direction of flow (i.e., $\alpha = 90°$) to investigate the kinetics of droplets in a gravity induced flow field, and Figure 6(a) depicts the change in the vertical separation between the droplets upto coalescence at Ga = 1600, Eo = 1.24, $\alpha = 90°$, and $\Delta Y_0{}^\star = 5$. Figure 6(a) indicates that with the increase in the intensity of magnetic field, the droplets accelerate faster and

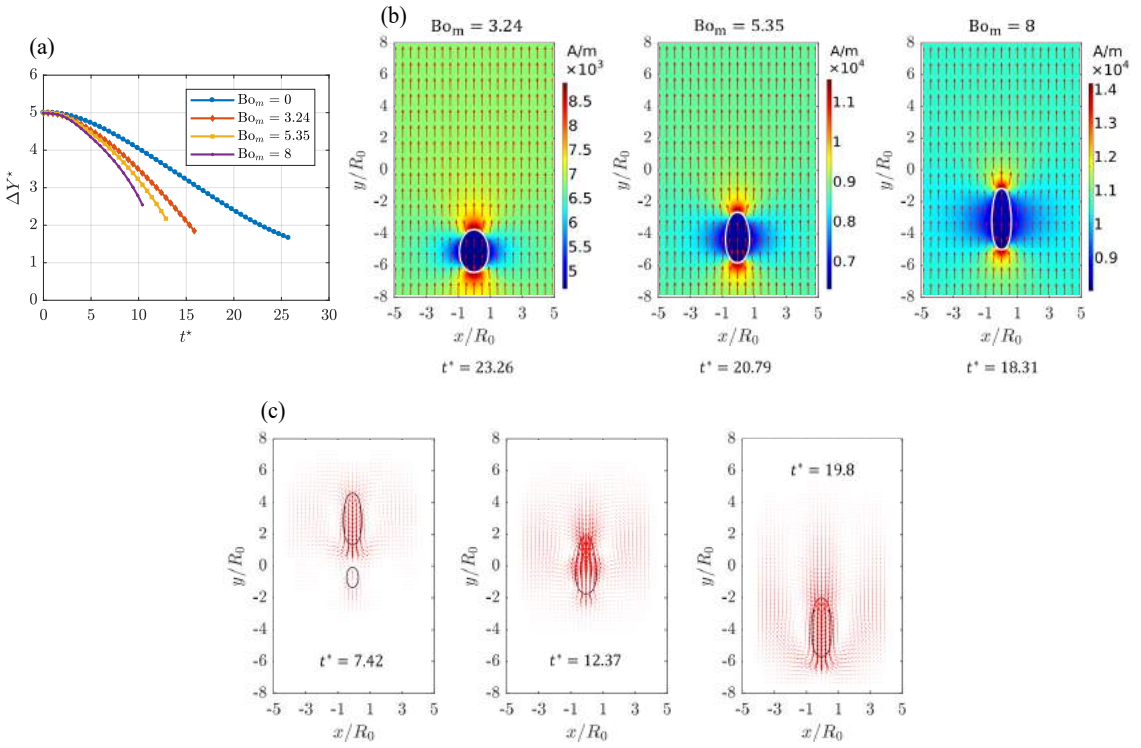

Figure 6. Dynamic behavior of freely falling droplets under gravity and magnetic fields at Ga = 1600, Eo = 1.24, $\alpha = 90°$, and $\Delta Y_0{}^\star = 5$. (a) $\Delta Y^\star$ vs $t^\star$; (b) Magnetic field, **H** profiles around droplet at representative times; and (c) Shape evolution of ferrofluid droplets at $\mathrm{Bo}_m = 8$.

coalesce with one another before reaching the bottom surface of the flow domain. Also, the coalescence phenomenon appears earlier at higher magnetic Bond numbers in compared to the droplets without the exposure to magnetic fields. Moreover, the magnetic field profiles around the merged droplets (before the droplet-wall interaction becomes dominant) are demonstrated in Fig. 6(b), which implies the highest magnetic field strength along the poles of the droplet and the lowest magnetic field strength along the equator. Also, the droplet elongates more in the direction of applied magnetic field with a rapid decrease in the droplet area perpendicular to the the direction of gravity at increased magnetic Bond numbers Bo_m.

Figure 6(c) depicts the evolution of droplet shapes under the amalgamated effect of gravity and magnetic fields at Ga = 1600, Eo = 1.24, $\mathrm{Bo}_m = 8$, $\alpha = 90°$, and $\Delta Y_0{}^\star = 5$. It shows that with the initiation of magnetic field, the droplets start to elongate along the

magnetic field direction ($t^\star$ = 7.42), resulting in prolate shaped ellipsoids, which in turn accelerate faster owing to the generation of a smaller drag around the droplets, following a decrease in the area projected perpendicular to the direction of gravity. Consequently, the droplets come into close contact with each other within a short amount of time where the van der Waals force activates and causes the droplets to merge with one another. After coalescence, the merged droplet attempts to stabilize through the combined interactions of inertial and magnetic effects ($t^\star$ = 12.37) and eventually reaches an equilibrium shape around $t^\star$ = 19.8. Additionally, the flow fields around the droplets suggest that immediately after coalescence ($t^\star$ = 12.37), the top portion of the merged droplet experiences increased inertial forces, which ultimately generates a teardrop shaped droplet in the process.

4.4.3. α = 45°. Figure 7 illustrates the migration behavior of gravity induced droplets under the exposure to the magnetic field along the secondary diagonal of the flow domain (i.e., α = 45°) at Ga = 1600, Eo = 1.24, and $\Delta Y_0{}^\star$ = 5. Figure 7(a) suggests that with the activation of magnetic field, the droplets start to line up along the direction of magnetic field and turn into prolate ellipsoidal shapes. Subsequently, the droplets begin to migrate downwards along the secondary diagonal of the computational domain under gravity; although, the trailing droplet travels faster than the leading droplet due to enhanced deformation. Besides, the droplets experience greater deformation at higher magnetic Bond numbers Bo_m. Moreover, as the trailing droplet approaches closer to the leading droplet, the leading droplet tends to move in the opposite direction. In this case, the downward diagonal movement of the droplets can be attributed to the asymmetric velocity profile around the droplets, generated due to the alignment of the droplets along the direction of the magnetic field (Figure 7(f)). Additionally, due to the intensified deformation of the trailing droplet, the flow field becomes massively disrupted and eventually diverts the trajectory of the leading droplet during close contact (Figure 7(f), $t^\star$ = 29.7).

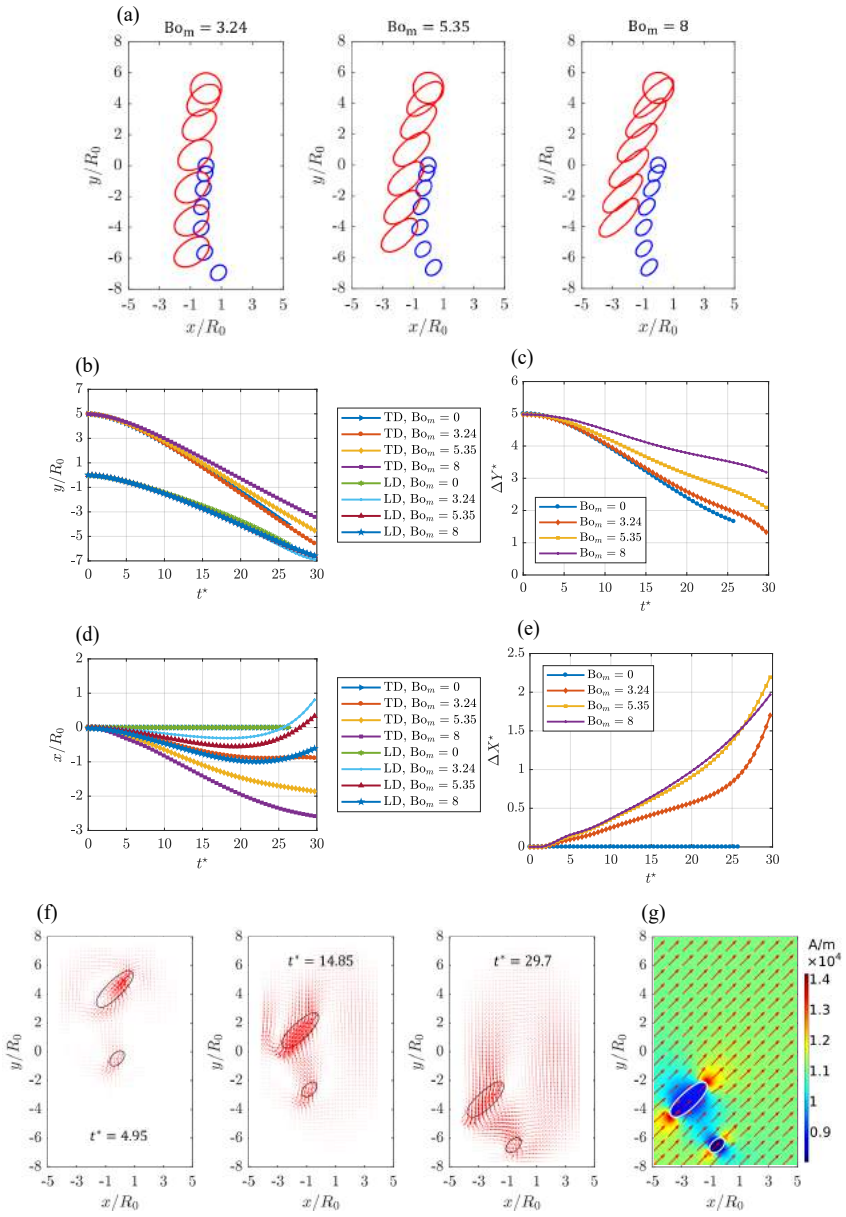

Figure 7. Migration behavior of freely falling droplets under gravity and magnetic fields at Ga = 1600, Eo = 1.24, $\alpha = 45°$, and $\Delta Y_0^\star = 5$. (a) Droplets' trajectories at various magnetic field strengths; (b) Vertical position of droplets, y/R_0 vs $t^\star$; (c) Change in vertical position between droplets, $\Delta Y^\star$ vs $t^\star$; (d) Horizontal position of droplets, x/R_0 vs $t^\star$; (e) Change in horizontal position between droplets, $\Delta X^\star$ vs $t^\star$; (f) Flow field inside and around droplets at $\mathrm{Bo}_m = 8$; and (g) Magnetic field, $\mathbf{H}$ profiles around droplets at $t^\star = 29.7$.

Figure 7(b) shows the vertical position of the droplets at different magnetic field strengths, which further indicates a decrease in the trailing droplet velocity at higher magnetic Bond numbers Bo_m. This phenomenon can be attributed to the increased drag that arises due to the greater droplet deformation at higher magnetic Bond numbers Bo_m. However, at $\mathrm{Bo}_m = 3.24$, the trailing droplet travels slightly faster than the droplet without magnetic field due to the generation of minimal drag that emerges as a result of the alignment of the droplet and reduced projection area in a direction perpendicular to the direction of gravity. Contrarily, the leading droplet, being smaller in size, is minimally affected by the change in magnetic field strengths and follows similar trajectories at all magnetic bond numbers Bo_m. Additionally, the vertical separation distance between the droplets are plotted in Figure 7(c), which also shows an increased vertical separation at higher magnetic field intensities.

Moreover, the horizontal position of the droplets at different magnetic Bond numbers are represented in Figure 7(d), which indicates that with an increase in the magnetic field intensity, both trailing and leading droplet experience larger migration in the horizontal direction; however, the trailing droplet migrates further than the leading droplet and reaches closer to the left wall of the domain. Interestingly, around $t^\star = 20$, the leading droplet changes its course of travel and starts to move in the opposite direction. Also, the migration of the leading droplet in the opposite direction decreases with the increase in the magnetic field strength. The prime rationale behind these events can be contributed to the fact that as the trailing droplet comes closer to the leading droplet, the flow field around the trailing droplet tends to push the leading droplet in the opposite direction (Figure 7(f)), and at a higher magnetic Bond number, due to the increase in the vertical separation between the droplets, the leading droplet encounters smaller interaction from the flow field of the trailing droplet i.e., the migration rate of the leading droplet in the opposite direction decreases. Finally, the horizontal separation distance between the droplets in 7(e) suggests an increase in the separation along the horizontal direction at an increased magnetic field strength.

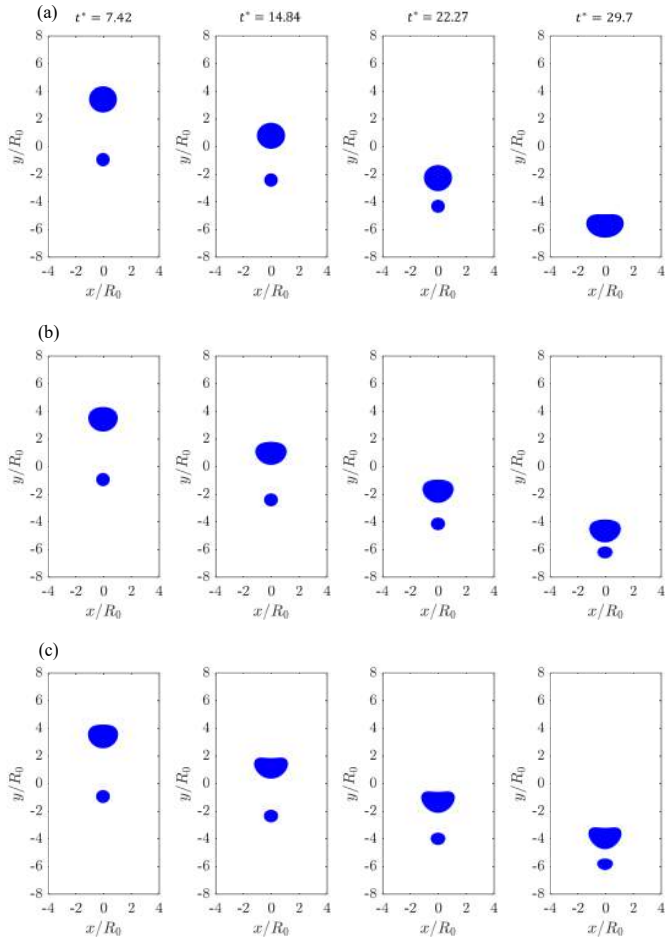

Figure 8. Shape evolution of freely falling droplets under gravity at Ga = 1600 and $\Delta Y_0^\star = 5$. (a) Eo = 1.24; (b) Eo = 4.74; and (c) Eo = 9.48.

4.5. EFFECT OF SURFACE TENSION

In multi-phase flows, surface tension force typically emerges as a result of mismatch of intermolecular forces on the interface and is dependent on the magnitude and type of intermolecular forces in the interfacial region. Moreover, it plays a fundamental role in a variety of processes, involving liquid-liquid interaction, liquid jets disintegration, and droplet/bubble formation. In particular, the importance of surface tension is imperative to the understanding of physics behind dye[Hancock *et al.*, 2011], varnish, and ink man-

ufacturing[Watanabe, 2006]. As a result, in this section, we analyze the effect of surface tension on the dynamic behavior of droplets falling under the combined effect of gravity and magnetic fields.

Figure 8 illustrates the evolution of droplet shapes falling under gravity at Ga = 1600 and $\Delta Y_0^\star = 5$. Here, Eötvös number Eo (a dimensionless group) is used to express the relationship between gravitational and surface tension forces, which again can be calculated using Equation 19. From Figure 8 it can be seen that at Eo = 1.24, the droplets retain almost circular shapes throughout their journey and eventually undergo coalescence before reaching the bottom wall of the computational domain, while experiencing minimal effects from inertial forces. However, as the Eötvös number Eo increases (i.e., Eo = 4.74), the droplets tend to transform into oblate ellipsoidal shapes, and the top surface of the trailing droplet encounters increased inertial forces, which ultimately flattens the top interface of the trailing droplet. Moreover, if we keep increasing Eo (i.e., Eo = 9.48), a wedge appears on the top surface of the trailing droplet, which subsequently progresses with time and tends to push the liquid on the top surface towards the bottom surface of the droplet. Also, no coalescence is observed at higher Eo (Figure 8(b), (c)), instead an increased vertical separation distance is noticed between the droplets. This happens because with a decline in the magnitude of surface tension values, the droplets are susceptible to enhanced deformation, thereby resulting in an increased droplet area in a direction perpendicular to the direction of gravity, which consequently magnifies the drag around the droplets (i.e., vertical separation distance increases).

4.5.1. $\alpha = 0^\circ, 90^\circ$. Now, we enforce a uniform magnetic field of constant strength (i.e., $H = 3500$ A/m) along the horizontal (i.e., $\alpha = 0^\circ$) and vertical (i.e., $\alpha = 90^\circ$) directions to investigate the dynamic behavior of droplets at variable Eötvös numbers Eo under the combined effect of gravity and magnetic fields. Figure 9(a) represents the change in the

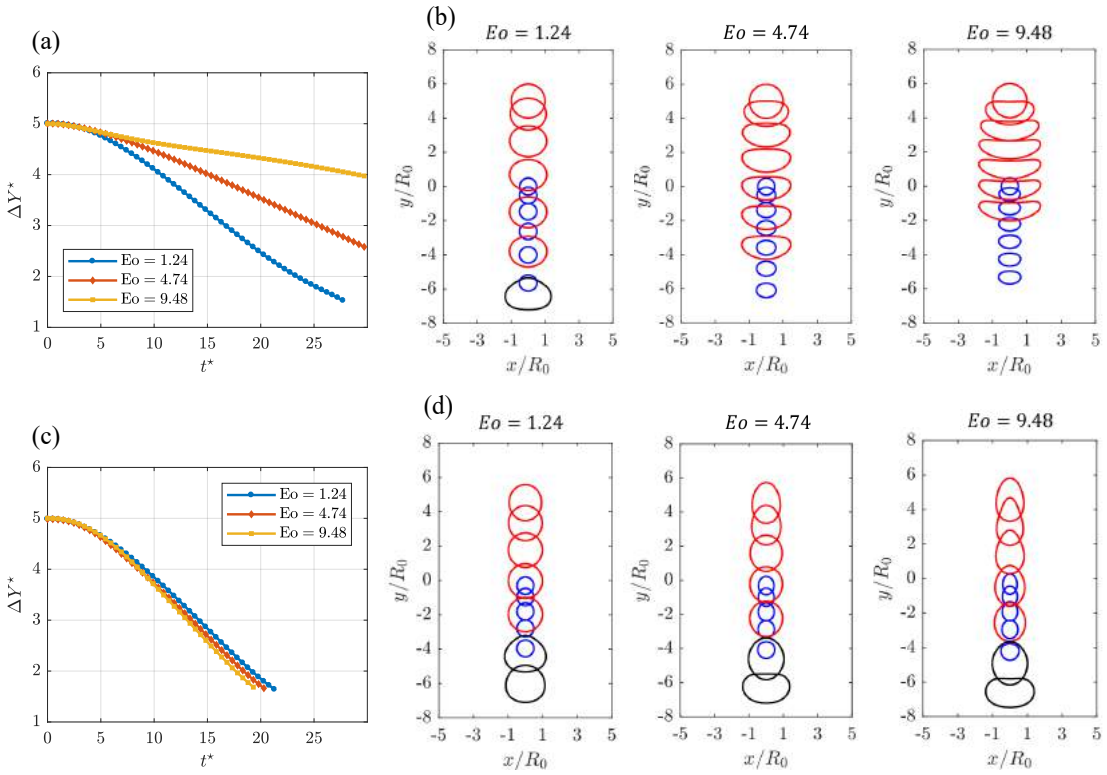

Figure 9. Dynamic behavior of freely falling droplets under gravity and magnetic fields at Ga = 1600, H = 3500 A/m, and $\Delta Y_0{}^\star = 5$. (a) $\Delta Y^\star$ vs $t^\star$ at $\alpha = 0°$; (b) Evolution of droplet shapes at different Eötvös numbers Eo along $\alpha = 0°$; (c) $\Delta Y^\star$ vs $t^\star$ at $\alpha = 90°$; and (d) Evolution of droplet shapes at different Eötvös numbers Eo along $\alpha = 90°$.

vertical separation distance between the droplets at Ga = 1600, H = 3500 A/m, $\alpha = 0°$, and $\Delta Y_0{}^\star = 5$, which indicates an increase in the vertical separation distance $\Delta Y^\star$ with an increase in the Eötvös number Eo.

The trajectory of the droplets at variable Eötvös numbers Eo can be better explained by the evolution of droplet shapes, illustrated in Figure 9(b). Previously, from Figure 8, we have realized that in the absence of any external forces except gravity, the droplets lean towards undergoing deformation in the horizontal direction. Now, as soon as the magnetic field is applied along $\alpha = 0°$, the magnetic field additionally assists the droplets in deforming along the favorable direction and thereby increases the deformation of the droplets in the process. At a lower Eo (i.e., Eo = 1.24), the magnetic field is not strong

enough to deform the droplets along the horizontal direction in compared to surface tension forces, which in general has a tendency to resist deformation and maintain circular droplet shapes. Ultimately, before reaching the bottom wall, the droplets coalesce into a larger sized droplet, which is represented by a black outline in Figure 9(b). But, as the Eo increases, the magnetic field becomes dominant and elongates the droplets along the direction of the magnetic field, thereby resulting increased drag, which eventually prevents coalescence and increases the vertical separation distance between the droplets. Also, due to the dominance of magnetic field, even at a higher Eo (i.e., Eo = 9.48), the appearance of wedge becomes less pronounced on the top interface of the trailing droplet, which subsequently contributes in generating round-bottom hull shaped droplets.

On the other hand, Figure 9(c)-(d) represents the dynamic behavior of droplets under compounded effect of gravity and magnetic fields in a direction parallel to the direction of gravity (i.e., $\alpha = 90°$) at variable Eötvös numbers Eo. From Figure 9(c), it can be seen that the vertical separation distance between the droplets $\Delta Y^{\star}$ decreases with the increase in Eo, and eventually the droplets merge with each other before reaching the bottom of the computational domain. Also, the time required to initiate coalescence between the droplets decreases with the increase in Eo, although a minimal difference in the coalescence time is observed even at higher magnitudes of Eo.

Moreover, Figure 9(d) shows the outline of the droplets, which further provides an in-depth understanding about the merging phenomenon in the flow domain at variable Eo. At a lower Eo (i.e., Eo = 1.24), the droplets exhibit greater resistance to deformation induced by the magnetic fields. Although, in the initial stage, the magnetic field tries to extend the droplet along the magnetic field direction, the pressure exerted on the top surface of the trailing droplet by the inertial forces tends to squeeze the top portion of the droplet interface towards the bottom portion of the droplet, resulting in a nearly circular shaped droplet in the process. Consequently, as time advances, the trailing droplet approaches closer to the leading droplet, which instantly activates the van der Waals interaction between the droplets

and causes coalescence. However, as Eo increases (i.e., Eo = 4.74), the droplets start to transform into prolate ellipsoidal shapes, followed by an increased deformation, which again reduces the amount of drag around the droplets to promote faster coalescence. Furthermore, at a higher Eo (i.e., Eo = 9.48), both inertial and magnetic effects become dominant, which ultimately plays a critical role in generating teardrop shaped droplets before coalescence. It is important to note that, even under the exposure to a similar magnetic field strength (i.e., H = 3500 A/m), the deformation experienced by the droplets along $\alpha = 90°$ is reasonably smaller, compared to the deformation induced by the magnetic fields along $\alpha = 0°$. The main reason behind this event can be characterized by the fact that in this case (i.e., $\alpha = 90°$), the magnetic field tries to expand the the droplet in a direction opposite to the direction of inertial force (i.e., deformation decreases), whereas along $\alpha = 0°$, since the droplets stretch in an orthogonal direction to the direction of inertial force, it enacts the magnetic field to act independently and increase the deformation of droplets at higher Weber numbers Eo.

4.5.2. $\alpha = 45°$. Figure 10(a)-(e) depicts the migration behavior of a pair of ferrofluid droplets falling under gravity at Ga = 1600, $\Delta Y_0^\star = 5$ and subjected to a uniform magnetic field of strength H = 3500 A/m along the secondary diagonal of the flow domain (i.e., $\alpha = 45°$). Figure 10(a) indicates that at a lower Eötvös number Eo (i.e., Eo = 1.24), when the magnetic field activates, the droplets tend to align themselves along the direction of the magnetic field. Moreover, the shape of the leading droplet, owing to a smaller fluid volume, is not greatly affected by the magnetic field, compared to the impact sustained by the trailing droplet. Subsequently, due to smaller deformation, the droplets experience coalescence before hitting the bottom wall of the flow domain. In contrast, at higher Eo (i.e., Eo = 4.74), the droplets demonstrate less resistance to deformation, which in turn generates ellipsoidal shaped droplets in the process. Note that, with the increase in Eo, the inertial effects become stronger and ultimately contribute in flattening the top interface of the trailing droplet, whereas the shape of the leading droplet remains approximately the same throughout its journey in the domain. Also, due to the orientation of the droplets along

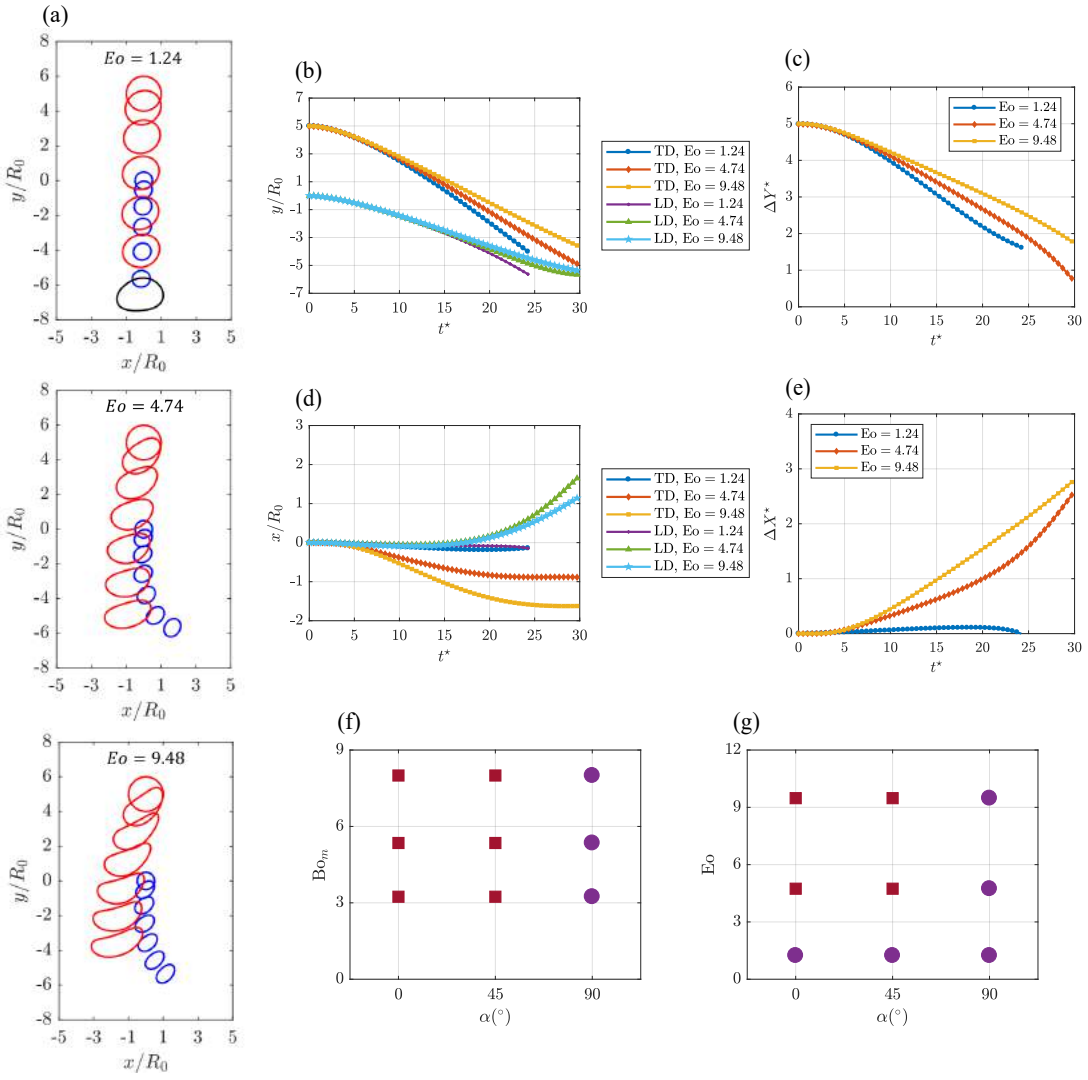

Figure 10. Droplet dynamics at Ga = 1600, H = 3500 A/m, $\alpha = 45°$, and $\Delta Y_0^\star = 5$. (a)-(e) Migration behavior of freely falling droplets under gravity and magnetic field at Ga = 1600, H = 3500 A/m, $\alpha = 45°$, and $\Delta Y_0^\star = 5$. (a) Droplets' trajectories at various magnetic field strengths; (b) Vertical position of droplets, y/R_0 vs $t^\star$; (c) Change in vertical position between droplets, $\Delta Y^\star$ vs $t^\star$; (d) Horizontal position of droplets, x/R_0 vs $t^\star$; (e) Change in horizontal position between droplets, $\Delta X^\star$ vs $t^\star$; (f)-(g) Behavior maps of falling droplets under gravity and magnetic fields at Ga = 1600, $\lambda = 1$, $\zeta = 1.12$, and $\Delta Y_0^\star = 5$ where square markers (maroon color) and circular markers (violet color) represent no coalescence region and coalescence region, respectively. (f) Droplets' behavior under various magnetic Bond numbers Bo_m at Eo = 1.24; and (g) Droplets' behavior under various Eötvös numbers Eo at H = 3500 A/m.

the magnetic field direction, the droplets experience relative motion along the direction of the magnetic field, which in turn assists the droplets in migrating towards the left wall of the domain. Furthermore, at Eo = 9.48, wedge is more pronounced on the top surface of the trailing droplet, and the droplet exhibits larger migration towards the magnetic field direction.

Additionally, at higher Eötvös numbers Eo, Figure 10(c) suggests a larger vertical separation distance between the droplets, followed by a decline in the migration rate of the droplets (Figure 10(b)), which is also similar to the phenomenon observed in Figure 7(b) and (c). However, in this case, the leading droplet demonstrates an obvious decline in migration rate at larger Eo (Figure 10(b)). On the other hand, in contrast to the vertical trajectory, the horizontal position of the trailing droplet demonstrates larger migration rate along the horizontal direction at an increased Eo (Figure 10(d)). Interestingly, irrespective of different Eo, the leading droplet remains along the central portion of the domain for a long time (upto $t^\star = 15$) until the trailing droplet nears closer to the leading droplet and pushes the leading droplet towards positive x-axis. Finally, the increasing trend of the horizontal separation distance between the droplets at higher Eo is shown in Figure 10(e). Also, the behavior of droplets at different magnetic Bond numbers (Bo_m) and Eötvös numbers (Eo) along various magnetic field directions under investigation are mapped in Figure 10(f)-(g), which depicts the coalescence and no coalescence regimes under different operating conditions.

4.6. EFFECT OF DENSITY AND VISCOSITY RATIO

In the final section, we suspend a pair of ferrofluid droplets in air to investigate the dynamic interaction between droplets under gravity and magnetic fields at Ga = 2875, Eo = 2.17, $\lambda = 49.1$, and $\zeta = 816.3$, which is also a common scenario in inkjet printing process. Here, like the previous sections, the initial separation distance $\Delta Y_0^\star$ and droplet sizes are kept constant; however, the properties of air and ferrofluid give rise to a huge contrast in density and viscosity ratios.

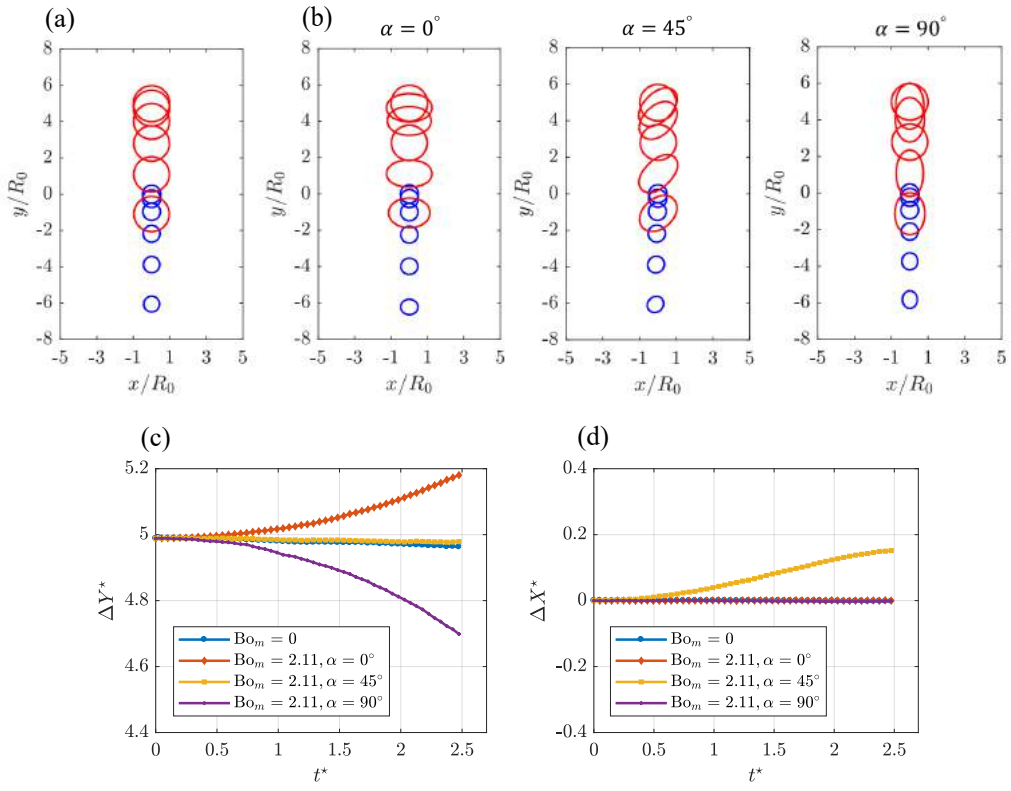

Figure 11. Migration behavior of falling ferrofluid droplets in air under gravity and magnetic fields at Ga = 2875, Eo = 2.17, $\lambda = 49.1$, $\zeta = 816.3$, and $\Delta Y_0^\star = 5$. (a) Droplets' trajectories at $\mathrm{Bo}_m = 0$; (b) Droplets' trajectories at $\mathrm{Bo}_m = 2.11$; (c) Change in vertical position between droplets, $\Delta Y^\star$ vs $t^\star$; and (d) Change in horizontal position between droplets, $\Delta X^\star$ vs $t^\star$.

Figure 11 illustrates the migration behavior of falling ferrofluid droplets in air under gravity and magnetic fields at Ga = 2875, Eo = 2.17, $\lambda = 49.1$, $\zeta = 816.3$, $\Delta Y_0^\star = 5$, and from Figure 11(a) it can be seen that the droplets experience minimal deformation and migrate downwards under the influence of gravity. However, if a magnetic field is applied along $\alpha = 0°$, the droplets turn into oblate shaped ellipsoids, while prolate shaped droplets are generated along $\alpha = 90°$. On the other hand, the implementation of magnetic field along $\alpha = 45°$ compels the droplets to deform along the magnetic field direction, which eventually contributes in the droplets' motion along the secondary diagonal of the flow domain due to asymmetry in the shapes with respect to the direction of gravity. These phenomenon are similar to the events observed in previous sections; except, due to a huge contrast in

viscosity ratio, no coalescence is observed either under the presence of gravity or gravity and magnetic fields. The droplets also do not migrate in divergent directions along $\alpha = 45°$ before the impact, in a situation where the droplets usually coalesce under gravity alone before impact at $\lambda = 1$, $\zeta = 1.12$, and $\Delta Y_0{}^{\star} = 5$. Moreover, as time evolves, the projected area of droplets perpendicular to the direction of gravity increases ($\alpha = 0°$ and $45°$) where the drag force comes into action and plays a vital role in the larger separation between droplets along the vertical direction (Figure 11(c)), while elongation of droplets along the gravity direction reduces the effect of drag force i.e., the vertical separation distance between droplets decreases ($\alpha = 90°$). Additionally, Figure 11(d) suggests an increase in the horizontal separation between droplets at $\alpha = 45°$, while the droplets maintain their positions along the center throughout the journey at $\alpha = 0°, 90°$, and $\mathrm{Bo}_m = 0$. Furthermore, it is important to note that when the droplets are dispersed in the air, the migration velocity of the droplets significantly increases, and the leading droplet reaches the bottom of the flow domain in an extremely short amount of time ($t^{\star} = 2.48$), which can be attributed to the dominant effect of inertial forces at Ga = 2875 and $\zeta = 49.1$.

Overall, the results from the effects of magnetic field, surface tension, density and viscosity ratios suggest that the freely falling droplets, followed by a transformation in dynamic shapes, can be either expedited or delayed to coalescence, which consequently contributes towards the separation and migration of droplets along different directions in a situation where the droplets usually coalesce under the effect of gravity (i.e., $\Delta Y_0^{\star} = 5$). Also, it is observed that even without the presence of magnetic field, if droplets are separated by an appropriate initial vertical distance, they experience coalescence under gravity, which further proves the independency of coalescence phenomenon on the magnetic properties of ferrofluid droplets. However, if a magnetic field is applied, the magnetic properties of ferrofluid droplets aid them in aligning themselves along the direction of magnetic field with increased deformation, which, depending on magnetic field directions, either hinders or expedites the coalescence process. In our study, we assumed standard properties of

typical ferrofluids at isothermal conditions, which are non-conducting, paramagnetic, and linearly magnetizable [Rosensweig, 1985]. Ultimately, these findings will be useful in controlling the spreading and rebounding of droplets on the bottom wall of the domain, which plays an important role in determining the resolution of printing techniques.

5. CONCLUSION

In this article, numerical simulations are implemented to investigate the dynamic interaction behavior between two uneven sized ferrofluid droplets falling under the combined exposure to gravity and uniform magnetic fields. The results suggest that at a fixed Galilei number (i.e., Ga = 1600), Eötvös number (i.e., Eo = 1.24), and viscosity ratio (i.e., $\lambda = 1$), in the absence of any external forces except gravity, there exists a critical initial vertical separation distance $\Delta Y^{\star}_{cr}$ between the droplets where they evade coalescence phenomenon before hitting the bottom wall of the domain ($\Delta Y^{\star}_{cr} \geq 6$). Also, applying a uniform magnetic field along $\alpha = 0°$ results in a larger separation distance between the droplets at increased magnetic bond numbers Bo_m, thus impeding coalescence phenomenon in a situation where the droplets usually experience coalescence (i.e., $\Delta Y^{\star}_{0} = 5$). Alternately, the coalescence event is sharply promoted through the application of the magnetic field along $\alpha = 90°$. Moreover, at $\alpha = 45°$, the ellipsoidal shaped droplets sustain a downward lateral migration along the secondary diagonal of the domain, followed by a larger horizontal and vertical separation distance at higher Bo_m (i.e., $\mathrm{Bo}_m = 8$).

Furthermore, we investigated the effect of surface tension on the dynamic behavior of droplets at a fixed Ga (i.e., Ga = 1600) and $\Delta Y^{\star}_{0}$ (i.e., $\Delta Y^{\star}_{0} = 5$). In the absence of magnetic fields, the results indicate a larger vertical separation distance between the droplets at a higher Eo (i.e., Eo = 9.48), followed by a generation of wedge on the top interface of the trailing droplet, while the leading droplet remains unaffected. Moreover, application of a magnetic field along $\alpha = 0°$ generates round-bottom hull shaped droplets, which ultimately contributes in the larger separation between the droplets at higher Eo (i.e., Eo = 9.48).

On the other hand, at $\alpha = 90°$, the droplets transform into teardrop shaped droplets and consequently coalesce with one another. Also, the coalescence time decreases with the increase in Eo. Additionally, applying the magnetic field along $\alpha = 45°$ greatly impedes the coalescence phenomenon and plays a pivotal role in the migration of the droplets along diagonal directions in the flow domain at higher Eötvös numbers Eo (i.e., Eo = 9.48). Also, an investigation on the suspension of droplets in an air medium demonstrates that the droplets do not experience any coalescence phenomenon in the presence of gravity or gravity and magnetic fields, which is eventually followed by a significantly faster migration rate in the domain. Nonetheless, the results imply the advantages of magnetic field as a prospective tool in the manipulation of interaction behavior between gravity induced uneven sized droplets, which is particularly important in inkjet printing and dropwise condensation heat transfer process.

ACKNOWLEDGMENTS

The authors greatly appreciate the financial sponsorship from the Department of Mechanical and Aerospace Engineering (MAE) and the Center for Biomedical Research (CBR) at Missouri University of Science and Technology.

REFERENCES

Aboutalebi, M., Bijarchi, M. A., Shafii, M. B., and Hannani, S. K., 'Numerical investigation on splitting of ferrofluid microdroplets in t-junctions using an asymmetric magnetic field with proposed correlation,' Journal of Magnetism and Magnetic Materials, 2018, **447**, pp. 139–149.

Al-Shamrani, A., James, A., and Xiao, H., 'Separation of oil from water by dissolved air flotation,' Colloids and Surfaces A: Physicochemical and Engineering Aspects, 2002, **209**(1), pp. 15–26.

Arecchi, F., Buah-Bassuah, P., Francini, F., Pérez-Garcia, C., and Quercioli, F., 'An experimental investigation of the break-up of a liquid drop falling in a miscible fluid,' EPL (Europhysics Letters), 1989, **9**(4), p. 333.

Bararnia, H. and Ganji, D., 'Breakup and deformation of a falling droplet under high voltage electric field,' Advanced Powder Technology, 2013, **24**(6), pp. 992–998.

Bararnia, H., Seyyedi, S., Ganji, D., and Khorshidi, B., 'Numerical investigation of the coalescence and breakup of falling multi-droplets,' Colloids and Surfaces A: Physicochemical and Engineering Aspects, 2013, **424**, pp. 40–51.

Bijarchi, M. A., Favakeh, A., and Shafii, M. B., 'The effect of a non-uniform pulse-width modulated magnetic field with different angles on the swinging ferrofluid droplet formation,' Journal of Industrial and Engineering Chemistry, 2020, **84**, pp. 106–119.

Castrejon-Pita, J. R., Baxter, W., Morgan, J., Temple, S., Martin, G., and Hutchings, I., 'Future, opportunities and challenges of inkjet technologies,' Atomization and sprays, 2013, **23**(6).

Che, Z. and Matar, O. K., 'Impact of droplets on immiscible liquid films,' Soft Matter, 2018, **14**(9), pp. 1540–1551.

Cho, S. C., Wang, Y., and Chen, K. S., 'Droplet dynamics in a polymer electrolyte fuel cell gas flow channel: Forces, deformation, and detachment. i: Theoretical and numerical analyses,' Journal of power sources, 2012, **206**, pp. 119–128.

Choi, J., Kim, Y.-J., Lee, S., Son, S. U., Ko, H. S., Nguyen, V. D., and Byun, D., 'Drop-on-demand printing of conductive ink by electrostatic field induced inkjet head,' Applied Physics Letters, 2008, **93**(19), p. 193508.

COMSOL, *CFD Module Application Library Manual*, 5.3a edition, 2018.

Dhindsa, A., Wanchoo, R. K., and Toor, A. P., 'Motion of nanofluid droplets through immiscible quiescent liquid: An experimental study,' Industrial & Engineering Chemistry Research, 2020, **59**(13), pp. 6247–6257.

Duan, R.-Q., Koshizuka, S., and Oka, Y., 'Two-dimensional simulation of drop deformation and breakup at around the critical weber number,' Nuclear engineering and design, 2003, **225**(1), pp. 37–48.

Fabian, M., Burda, P., Šviková, M., and Huňady, R., 'The influence of magnetic field on the separation of droplets from ferrofluid jet,' Journal of Magnetism and Magnetic Materials, 2017, **431**, pp. 196–200.

Fakhari, A. and Rahimian, M. H., 'Simulation of falling droplet by the lattice boltzmann method,' Communications in Nonlinear Science and Numerical Simulation, 2009, **14**(7), pp. 3046–3055.

Ghaderi, A., Kayhani, M. H., and Nazari, M., 'Numerical investigation on falling ferrofluid droplet under uniform magnetic field,' European Journal of Mechanics-B/Fluids, 2018, **72**, pp. 1–11.

Grabow, M. H., Gilmer, G. H., and Bakker, A. F., 'Molecular dynamics studies of silicon solidification and melting,' MRS Online Proceedings Library Archive, 1988, **141**.

Hancock, M. J., He, J., Mano, J. F., and Khademhosseini, A., 'Surface-tension-driven gradient generation in a fluid stripe for bench-top and microwell applications,' Small, 2011, **7**(7), pp. 892–901.

Hassan, M. R. and Wang, C., 'Magnetic field induced ferrofluid droplet breakup in a simple shear flow at a low reynolds number,' Physics of Fluids, 2019, **31**(12), p. 127104.

Hassan, M. R. and Wang, C., 'Ferro-hydrodynamic interactions between ferrofluid droplet pairs in simple shear flows,' Colloids and Surfaces A: Physicochemical and Engineering Aspects, 2020a, p. 124906.

Hassan, M. R. and Wang, C., 'Lateral migration of a ferrofluid droplet in a plane poiseuille flow under uniform magnetic fields,' Physical Review E, 2020b, **102**(2), p. 022611.

Hassan, M. R., Zhang, J., and Wang, C., 'Deformation of a ferrofluid droplet in simple shear flows under uniform magnetic fields,' Physics of Fluids, 2018, **30**(9), p. 092002.

He, B., Yang, S., Qin, Z., Wen, B., and Zhang, C., 'The roles of wettability and surface tension in droplet formation during inkjet printing,' Scientific reports, 2017, **7**(1), pp. 1–7.

Hu, C., Xia, S., Li, C., and Wu, G., 'Three-dimensional numerical investigation and modeling of binary alumina droplet collisions,' International Journal of Heat and Mass Transfer, 2017, **113**, pp. 569–588.

Hua, J., Lim, L. K., and Wang, C.-H., 'Numerical simulation of deformation/motion of a drop suspended in viscous liquids under influence of steady electric fields,' Physics of Fluids, 2008, **20**(11), p. 113302.

Im, D. J., Noh, J., Moon, D., and Kang, I. S., 'Electrophoresis of a charged droplet in a dielectric liquid for droplet actuation,' Analytical chemistry, 2011, **83**(13), pp. 5168–5174.

Jalaal, M., Khorshidi, B., and Esmaeilzadeh, E., 'An experimental study on the motion, deformation and electrical charging of water drops falling in oil in the presence of high voltage dc electric field,' Experimental thermal and fluid science, 2010, **34**(8), pp. 1498–1506.

Jiang, X. F., Wu, Y. N., Ma, Y., and Li, H. Z., 'Formation and breakup dynamics of ferrofluid drops,' Chemical Engineering Research and Design, 2016, **115**, pp. 262–269.

Jung, S., Hoath, S. D., and Hutchings, I. M., 'The role of viscoelasticity in drop impact and spreading for inkjet printing of polymer solution on a wettable surface,' Microfluidics and nanofluidics, 2013, **14**(1-2), pp. 163–169.

Ki, H., 'Level set method for two-phase incompressible flows under magnetic fields,' Computer Physics Communications, 2010, **181**(6), pp. 999–1007.

Kim, H.-Y., Jeon, S., Song, M., and Kim, K., 'Numerical simulations of water droplet dynamics in hydrogen fuel cell gas channel,' Journal of Power Sources, 2014, **246**, pp. 679–695.

Kumagai, S., Sakai, T., and Okajima, S., 'Combustion of free fuel droplets in a freely falling chamber,' in 'Symposium (International) on Combustion,' volume 13, Elsevier, 1971 pp. 779–785.

Laan, N., de Bruin, K. G., Bartolo, D., Josserand, C., and Bonn, D., 'Maximum diameter of impacting liquid droplets,' Physical Review Applied, 2014, **2**(4), p. 044018.

List, R., Nissen, R., and Fung, C., 'Effects of pressure on collision, coalescence, and breakup of raindrops. part ii: Parameterization and spectra evolution at 50 and 100 kpa,' Journal of the atmospheric sciences, 2009, **66**(8), pp. 2204–2215.

Liu, Y.-F., Tsai, M.-H., Pai, Y.-F., and Hwang, W.-S., 'Control of droplet formation by operating waveform for inks with various viscosities in piezoelectric inkjet printing,' Applied physics A, 2013, **111**(2), pp. 509–516.

Low, T. B. and List, R., 'Collision, coalescence and breakup of raindrops. part i: Experimentally established coalescence efficiencies and fragment size distributions in breakup,' Journal of the Atmospheric Sciences, 1982, **39**(7), pp. 1591–1606.

Magarvey, R. and Taylor, B., 'Free fall breakup of large drops,' Journal of Applied Physics, 1956, **27**(10), pp. 1129–1135.

Nikolopoulos, N., Strotos, G., Nikas, K.-S. P., Gavaises, M., Theodorakakos, A. P., Marengo, M., and Cossali, G. E., 'Experimental investigation of a single droplet impact onto a sessile drop,' Atomization and Sprays, 2010, **20**(10).

Olsson, E. and Kreiss, G., 'A conservative level set method for two phase flow,' Journal of computational physics, 2005, **210**(1), pp. 225–246.

Olsson, E., Kreiss, G., and Zahedi, S., 'A conservative level set method for two phase flow ii,' Journal of Computational Physics, 2007, **225**(1), pp. 785–807.

Pabst, O., Perelaer, J., Beckert, E., Schubert, U. S., Eberhardt, R., and Tünnermann, A., 'All inkjet-printed piezoelectric polymer actuators: Characterization and applications for micropumps in lab-on-a-chip systems,' Organic Electronics, 2013, **14**(12), pp. 3423–3429.

Pan, Y. and Suga, K., 'Numerical simulation of binary liquid droplet collision,' Physics of Fluids, 2005, **17**(8), p. 082105.

Pangu, G. D. and Feke, D. L., 'Acoustically aided separation of oil droplets from aqueous emulsions,' Chemical Engineering Science, 2004, **59**(15), pp. 3183–3193.

Perelaer, J., Smith, P. J., van den Bosch, E., van Grootel, S. S., Ketelaars, P. H., and Schubert, U. S., 'The spreading of inkjet-printed droplets with varying polymer molar mass on a dry solid substrate,' Macromolecular chemistry and physics, 2009a, **210**(6), pp. 495–502.

Perelaer, J., Smith, P. J., Wijnen, M. M., van den Bosch, E., Eckardt, R., Ketelaars, P. H., and Schubert, U. S., 'Droplet tailoring using evaporative inkjet printing,' Macromolecular Chemistry and Physics, 2009b, **210**(5), pp. 387–393.

Pesach, D. and Marmur, A., 'Marangoni effects in the spreading of liquid mixtures on a solid,' Langmuir, 1987, **3**(4), pp. 519–524.

Phan, H. V., Alan, T., and Neild, A., 'Droplet manipulation using acoustic streaming induced by a vibrating membrane,' Analytical chemistry, 2016, **88**(11), pp. 5696–5703.

Rabe, C., Malet, J., and Feuillebois, F., 'Experimental investigation of water droplet binary collisions and description of outcomes with a symmetric weber number,' Physics of fluids, 2010, **22**(4), p. 047101.

Rosensweig, R. E., *Ferrohydrodynamics*, Cambridge University Press, 1985.

Saien, J. and Bamdadi, H., 'Mass transfer from nanofluid single drops in liquid–liquid extraction process,' Industrial & engineering chemistry research, 2012, **51**(14), pp. 5157–5166.

Savino, R., Paterna, D., and Lappa, M., 'Marangoni flotation of liquid droplets,' Journal of Fluid Mechanics, 2003, **479**, pp. 307–326.

Scherer, C. and Figueiredo Neto, A. M., 'Ferrofluids: properties and applications,' Brazilian Journal of Physics, 2005, **35**(3A), pp. 718–727.

Shi, D., Bi, Q., and Zhou, R., 'Numerical simulation of a falling ferrofluid droplet in a uniform magnetic field by the voset method,' Numerical Heat Transfer, Part A: Applications, 2014, **66**(2), pp. 144–164.

Smith, P. J. and Shin, D. H., *Inkjet-based micromanufacturing*, John Wiley & Sons, 2012.

Stratton, J. A., *Electromagnetic theory*, volume 33, John Wiley & Sons, 2007.

Strotos, G., Malgarinos, I., Nikolopoulos, N., and Gavaises, M., 'Numerical investigation of aerodynamic droplet breakup in a high temperature gas environment,' Fuel, 2016, **181**, pp. 450–462.

Supeene, G., Koch, C. R., and Bhattacharjee, S., 'Deformation of a droplet in an electric field: nonlinear transient response in perfect and leaky dielectric media,' Journal of colloid and interface science, 2008, **318**(2), pp. 463–476.

Tagawa, T., 'Numerical simulation of two-phase flows in the presence of a magnetic field,' Mathematics and Computers in Simulation, 2006, **72**(2-6), pp. 212–219.

Tan, S.-H., Nguyen, N.-T., Yobas, L., and Kang, T. G., 'Formation and manipulation of ferrofluid droplets at a microfluidic t-junction,' Journal of Micromechanics and Microengineering, 2010, **20**(4), p. 045004.

Taylor, D., Thomas, R., and Penfold, J., 'Polymer/surfactant interactions at the air/water interface,' Advances in colloid and interface science, 2007, **132**(2), pp. 69–110.

Tekin, E., Smith, P. J., and Schubert, U. S., 'Inkjet printing as a deposition and patterning tool for polymers and inorganic particles,' Soft Matter, 2008, **4**(4), pp. 703–713.

Tilehboni, S. M., Fattahi, E., Afrouzi, H. H., and Farhadi, M., 'Numerical simulation of droplet detachment from solid walls under gravity force using lattice boltzmann method,' Journal of Molecular Liquids, 2015, **212**, pp. 544–556.

Tsai, P.-H. and Wang, A.-B., 'Classification and prediction of dripping drop size for a wide range of nozzles by wetting diameter,' Langmuir, 2019, **35**(13), pp. 4763–4775.

Wanchoo, R., Sharma, S. K., and Gupta, R., 'Shape of a newtonian liquid drop moving through an immiscible quiescent non-newtonian liquid,' Chemical Engineering and Processing: Process Intensification, 2003, **42**(5), pp. 387–393.

Wang, C., Liu, X., and Law, C. K., 'Combustion and microexplosion of freely falling multicomponent droplets,' Combustion and flame, 1984, **56**(2), pp. 175–197.

Wang, Z. and Zhe, J., 'Recent advances in particle and droplet manipulation for lab-on-a-chip devices based on surface acoustic waves,' Lab on a Chip, 2011, **11**(7), pp. 1280–1285.

Watanabe, S., 'Ink jet recording method employing inks with specific surface tensions,' 2006, uS Patent 7,121,661.

Wixforth, A., Strobl, C., Gauer, C., Toegl, A., Scriba, J., and Guttenberg, Z. v., 'Acoustic manipulation of small droplets,' Analytical and bioanalytical chemistry, 2004, **379**(7-8), pp. 982–991.

Wu, Y., Fu, T., Ma, Y., and Li, H. Z., 'Ferrofluid droplet formation and breakup dynamics in a microfluidic flow-focusing device,' Soft Matter, 2013, **9**(41), pp. 9792–9798.

Yudistira, H. T., Nguyen, V. D., Dutta, P., and Byun, D., 'Flight behavior of charged droplets in electrohydrodynamic inkjet printing,' Applied Physics Letters, 2010, **96**(2), p. 023503.

Zhang, H.-y., Wang, J., and Lu, G.-d., 'Numerical investigation of the influence of companion drops on drop-on-demand ink jetting,' Journal of Zhejiang University SCIENCE A, 2012, **13**(8), pp. 584–595.

Zhang, J., Hassan, M. R., Rallabandi, B., and Wang, C., 'Migration of ferrofluid droplets in shear flow under a uniform magnetic field,' Soft matter, 2019, **15**(11), pp. 2439–2446.

VI. IMPACT OF A FERROFLUID DROPLET ON HYDROPHOBIC SURFACES UNDER MAGNETIC FIELDS: WETTING AND BOUNCING DYNAMICS

Md Rifat Hassan, Mahdi Gharehbaygloo, Xiaoming He, and Cheng Wang
Department of Mechanical & Aerospace Engineering
Missouri University of Science and Technology
Department of Mathematics and Statistics
Missouri University of Science and Technology
Rolla, Missouri 65409
Tel: 573–341–4636, Fax: 573–341–4607
Email: mhvcp@mst.edu; wancheng@mst.edu

ABSTRACT

Hydrophobic substrates are widely used in a number of industrial and technological applications due to their extreme repellent properties where the performance of the substrate is critically dependent on understanding the relationship between the droplet impact characteristics and wetting properties. This work systematically investigates the wetting and bouncing dynamics of an impinging ferrofluid droplet on hydrophobic surfaces under the presence of both gravity and permanent magnetic fields. The numerical simulations employ a Cahn-Hilliard equation based phase field (PF) method to track the dynamic free interface of the droplet in two-phase flows. The results suggest that a non-uniform magnetic field increases the maximum droplet spreading even on hydrophobic surfaces, which usually have low surface energies and tend to repel droplets. Moreover, increased magnitudes of magnetic field strength and magnet size are found to increase the droplet spreading on a range of different hydrophobic substrates (i.e., $90^\circ \leq \theta_c \leq 150^\circ$). Furthermore, an interesting bouncing phenomenon is observed in low viscous droplets on superhydrophobic surfaces at We $\approx$ 15 where the droplet moves upward, against gravity, after impact. However, the

activation of magnetic field significantly suppresses the bouncing event and pins the droplet to the surface. Additionally, several experiments are performed on droplet impact and bouncing dynamics, which are found to be in good agreement with the numerical findings.

Keywords: Wetting, Bouncing, Ferrofluid droplet, Contact angle, Magnetic field, Hydrophobicity

1. INTRODUCTION

Spray cooling is considered as an efficient method for swift heat removal from solid surfaces, which is of immense interest in electronic cooling [Cader *et al.*, 2004, Kim, 2007] and other heat flux industrial applications [Chen *et al.*, 2002, Smakulski and Pietrowicz, 2016, Tan *et al.*, 2013]. In this process, a liquid is forced through a tiny aperture, which eventually disintegrates into a fine dispersion of small droplets that ultimately impact a heated surface. Subsequently, followed by a spreading phenomenon on the surface, the droplets either evaporate or generate a thin layer of liquid film due to latent heat of evaporation and thereby releasing a significant amount of energy at low temperatures. Moreover, the initial droplet spreading plays a substantial role on the evaporation heat transfer process [Dash and Garimella, 2014, Healy *et al.*, 2001], while the final shape of the droplet is essential in the determination of the performance of the coating of the substrate [Fauchais *et al.*, 2004]. Additionally, spray cooling is equally important in the cooling of human skin layer during dermatological laser therapy in patients with stained birthmarks [Aguilar *et al.*, 2001, Basinger *et al.*, 2004]. Therefore, it is imperative to have an intensive understanding of the complex spreading dynamics of droplets in order to achieve an efficient and controlled droplet deposition technique on target substrates.

When the size of droplets is smaller than the capillary length, the impact process is typically governed by the inertial, capillary, and viscous forces, which is accomplished in five consecutive stages i.e., kinematic, spreading, relaxation, wetting, and equilibrium phases. Moreover, during the spreading phase, the spreading diameter of the impinging

droplet undergoes continuous changes, which in turn affects the heat transfer in spray cooling process [Lin and Ponnappan, 2003]. Several analytical [Chandra and Avedisian, 1991, Madejski, 1976, Yonemoto and Kunugi, 2017] and experimental [Kim and Chun, 2001, Pasandideh-Fard *et al.*, 1996, Scheller and Bousfield, 1995] works on the spreading dynamics of droplets are reported in the literature, which discuss the relationship between the maximum droplet spreading and several dimensionless groups that affect the droplet dynamics. These dimensionless groups include but are not limited to Reynolds number (ratio between inertial and viscous forces), Weber number (ratio between inertial and surface tension forces), and Ohnesorge number (ratio between viscous, inertial, and surface tension forces). Moreover, the interaction between the bottom solid substrate and the droplet is crucial to the overall dynamics of droplet spreading, which again can be described by the contact angle — an equilibrium parameter among solid, liquid, and vapor interfaces.

Lin et al. [Lin *et al.*, 2018] conducted an experimental investigation on the impacts of droplets on different substrates and concluded that the outcome of the spreading depends not only on the physical property of the droplet but also on the wettability of the substrate. Yang et al. [Yang *et al.*, 2013] studied the recoil and oscillation of single droplets on surfaces with different wettabilities and observed that for droplets with lower Weber numbers, both inertia and capillary effects are significant in the initial spreading stages, while at higher Weber numbers, inertia dominates the spreading process. Also, Kim and Chun [Kim and Chun, 2001] performed both analytical and experimental investigations on the recoiling behavior of droplet after maximum spreading, while an experimental study on the spreading of a single water-ethanol droplet on a heated surface is conducted by Liu et al. [Liu *et al.*, 2021] Moreover, multiple authors [Clanet *et al.*, 2004, Roisman, 2009, Savva *et al.*, 2010, Vellingiri *et al.*, 2011] proposed several analytical approaches to estimate the droplet impact outcome based on the energy changes in the system and geometric assumptions of the spreading droplets. Several numerical works [Kamnis *et al.*, 2008, Lunkad *et al.*, 2007, Milacic *et al.*, 2019, Parizi *et al.*, 2007] also explored the phenomenon behind

droplet spreading on different substrates. Russo et al. [Russo *et al.*, 2020] implemented a volume of fluid (VOF) method to simulate droplet impact on spatially wettability patterned surfaces, whereas a lattice Boltzmann method (LBM) is adopted by Gupta and Kumar [Gupta and Kumar, 2010] to track the splashing behavior of droplets on a dry surface. Additionally, Zhang et al. [Zhang *et al.*, 2008] used a smoothed particle hydrodynamics algorithm to simulate the spreading, splashing, and solidification of a zirconia droplet and found that the droplet encounters a breakup when impacted at an angle less than 44° with higher Reynolds numbers. Furthermore, a review on the recent developments of droplet impact dynamics and kinematics on superhydrophobic surfaces is thoroughly presented by Khojasteh et al. [Khojasteh *et al.*, 2016], which again surveys the effects of surface characteristics on the deformation of an impinging droplet.

In addition to hydrodynamic forces, droplet manipulation can be achieved through the utilization of external forces i.e., electric [Emdadi and Pournaderi, 2020, Song *et al.*, 2013] or magnetic fields [Hassan and Wang, 2019, 2020a,b, Hassan *et al.*, 2018, 2021a,b, Zhang *et al.*, 2019]. However, in order to attain magnetic control, either the continuous phase or droplet phase needs to be a ferrofluid [Papell and Faber, 1968]— a fluid with magnetic properties, which due to its unique response to magnetic fields has gained immense popularity in numerous applications, including cancer treatment [Lübbe *et al.*, 1996], sealing rotating shafts [Raj and Moskowitz, 1990], and heat exchangers [Odenbach, 2008]. Also, since a ferrofluid offers greater flexibility in operations, it shows huge promise in 3D metal printing process where the quality of printing, followed by shape distortion of metal, is defined by the overall spreading dynamics of droplet during laser operation [Visser *et al.*, 2015]. Zhang et al. [Zhang *et al.*, 2016] developed a theoretical model to predict the spreading of liquid metal drops on a dry surface under vertical magnetic fields, while an electromagnet is utilized by Zhou and Jing [Zhou and Jing, 2019] to investigate the impact dynamics of a ferrofluid droplet on a rigid surface. Moreover, Han et al. [Han *et al.*, 2018] conducted a three-dimensional numerical study on the effects of magnetohydrodynamics

(MHD) on the spreading characteristics of a liquid metal droplet on a flat solid surface and observed an inhibition effect on the spreading dynamics under horizontal magnetic fields. Additionally, we have demonstrated versatile manipulation of droplets using magnetic fields in our previous works [Hassan and Wang, 2019, 2020a,b, Hassan *et al.*, 2018, 2021b, Zhang *et al.*, 2019].

However, the majority of numerical works on droplet impact are focused on using electromagnets on liquid metal droplets to achieve control on the spreading dynamics of droplet, while the experimental investigations are either based on water droplet [Kim and Chun, 2001]/low viscous droplet [Lin *et al.*, 2018] spreading under gravity alone or metal liquid droplets [Zhou and Jing, 2019]. Recently, Ahmed et al. [Ahmed *et al.*, 2018] performed an experimental analysis on the effects of magnetic fields on the spreading dynamics of a ferrofluid droplet (with fixed properties) and realized that magnetic fields are capable of maneuvering the droplet spreading without the need of inducing a change in surface chemistry; although, an in-depth understanding on the effects of viscosity, magnet size, and solid substrates with different wettabilities on droplet impact are missing in their work. Up to the authors' knowledge, no numerical investigations have been performed on the complex spreading phenomenon of a ferrofluid droplet under the presence of non-uniform magnetic fields at moderate Reynolds numbers (i.e., $\mathrm{Re} \leq 15$). As a result, in this article, we perform both numerical and experimental investigations to analyze the effects of a non-uniform magnetic field on the wetting and bouncing dynamics of an impinging ferrofluid droplet on hydrophobic substrates. Here, a 2D axisymmetric numerical scheme is chosen in order to investigate a wide range of variables, e.g., magnetic field strength, magnet size, and viscosity ratio. This also provides the feasibility in terms of the utilization of computational resources, while generating accurate results in a reasonable amount of time. Additionally, a phase field (PF) method [Boyer, 1999, Gurtin *et al.*, 1996, Han *et al.*, 2021, Hohenberg and Halperin, 1977, Liu and Shen, 2003, Nochetto *et al.*, 2014, Qian *et al.*, 2003] is incorporated in the numerical scheme in order to couple both flow and magnetic

Table 1. Droplet properties.

Parameter	Symbol	Value	Unit
Density of droplet phase	ρ_d	1220	kg/m^3
Viscosity of droplet phase	η_d	1-116	mPa·s
Interfacial tension	σ	63	mN/m

fields. The finite element discretization for the phase field method [Bai *et al.*, 2020, 2017, Bao *et al.*, 2012, Diegel *et al.*, 2015, Feng, 2006, Feng *et al.*, 2007, 2016, Feng and Wise, 2012, Gao *et al.*, 2018, Li *et al.*, 2020, Nochetto *et al.*, 2016, Yang *et al.*, 2019, Zhang *et al.*, 2021] is utilized in a commercial solver (COMSOL 5.3) to perform the simulations under consideration.

The paper is organized as follows: In Sec. 2, a discussion on the numerical model is presented, while an in-depth analyses on the adopted computational algorithm scheme and governing equations are provided in Sec. 3. Next, Sec. 4 discusses the effects of the magnetic field, magnet size, and viscosity ratio on the post-impact wetting dynamics of droplet on hydrophobic surfaces. Finally, followed by a short summary on the critical findings in Sec. 5, the validation of numerical model against the existing theories and experiments is provided in Appendix A.

2. NUMERICAL MODEL

Figure 1 illustrates the schematic representation of an axi-symmetric configuration of a droplet impinging on a hydrophobic substrate under gravity $\mathbf{g}$ and non-uniform magnetic fields, $\mathbf{H}_0$. Both air and droplet phases are considered as incompressible, isothermal, and viscous fluids in the numerical approach. The dimensions of the axisymmetric computational domain are denoted by W_d and H_d, which simultaneously represent the width and height of the axi-symmetric domain. Here, the width of the domain is considered large enough so that the walls exert no effect on the spreading dynamics of the impinging droplet. Also, the basic properties of the fluids are symbolized by ρ (density) and η (viscosity),

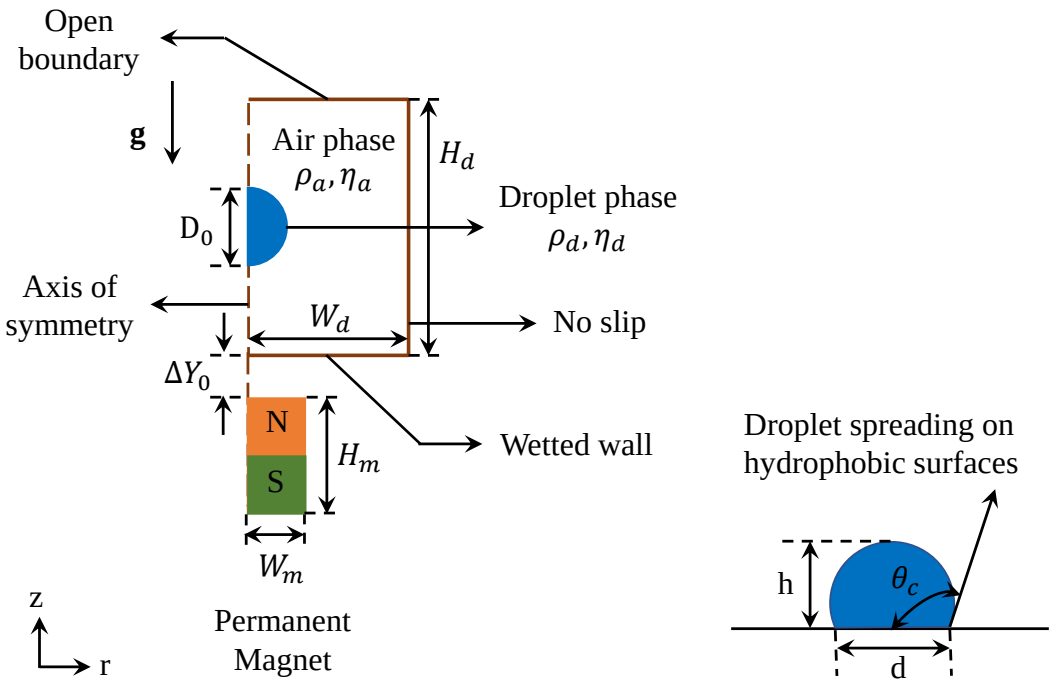

Figure 1. Schematic illustration of an axi-symmetric configuration of a droplet impinging on a hydrophobic substrate under gravity **g** and non-uniform magnetic fields, $\mathbf{H}_0$.

while the subscripts a and d signify the properties of air and droplet phases, respectively. Moreover, the droplet contains magnetic properties and has a magnetic permeability equal to $5\mu_0$ (i.e., $\mu_d = 5\mu_0$), while air is non-magnetic with a magnetic permeability equal to permeability of vacuum μ_0 (i.e., $\mu_a = \mu_0$). An open boundary condition is applied to the top boundary of the computational domain, while the bottom surface is subjected to a wetted wall condition, which again determines the wettability of the surface. Additionally, the right boundary uses a no slip boundary condition, whereas the left boundary is considered as the symmetry axis in the axi-symmetric numerical simulations.

Initially, a droplet, having an initial diameter D_0, starts to fall under gravity **g** with an initial velocity greater than zero (i.e., $U_0 > 0$). Next, the droplet is exposed to a cylindrical permanent magnet of radius W_m and thickness H_m with a non-uniform magnetic field $\mathbf{H}_0$ near the bottom substrate, which again maintains a vertical separation

ΔY_0 with the bottom hydrophobic surface. Eventually, under gravity the droplet starts to approach the bottom substrate, and when the droplet comes near the vicinity of the magnet, it experiences the interactions of the magnetic fields. Ultimately, the spreading dynamics of the impinging droplet after impact on a hydrophobic surface is influenced by the combined effects of gravity and magnetic fields and can be further characterized by the spreading diameter d and apex height h. Moreover, during the spreading phenomenon, the droplet experiences a transition in the contact angle θ_c with the bottom substrate, which in addition to determining the surface free energy of the bottom substrate, can be utilized to define the wetting properties of the droplet.

3. COMPUTATIONAL APPROACH

3.1. PHASE FIELD METHOD

Multiphase flows are one of the most common phenomena that occur both in nature and industrial processes [Gan *et al.*, 2009, Shui *et al.*, 2007, Teh *et al.*, 2008], which often involve severe topological changes on the interface during the transport mechanism, including deformation [Hassan *et al.*, 2018], migration [Hassan and Wang, 2020b, Zhang *et al.*, 2019], breakup Hassan and Wang [2019], and coalescence Hassan and Wang [2020a] of the interface. As a result, a diffuse-interface approach based phase field (PF) method is employed in the numerical simulations [Chen *et al.*, 2019, Ding *et al.*, 2007, Huang *et al.*, 2018, Kim *et al.*, 2004, Lin *et al.*, 2019, Liu and Qiao, 2019, Qin *et al.*, 2021, Shen and Yang, 2015, Wang and Wise, 2011, Xu *et al.*, 2019, Yang, 2021, Yang *et al.*, 2018, Yue *et al.*, 2004] to track the free interface of the droplet. This approach is different from the existing sharp-interface approaches (i.e., LS and VOF methods) in a way that in a diffuse-interface approach, the interface is replaced by a thin but non-zero thickness transitional region, which undergoes a smooth variation in physical properties across the interface,

while a signed distance function is utilized in a sharp-interface approach that constantly requires adjustment of the properties of the distance function during severe deformation of the interface [Wang *et al.*, 2019].

One popular governing equation of the phase field method is a fourth-order derivative based Cahn-Hilliard equation (i.e., convection-diffusion type equation), which usually has an advantage over other sharp-tracking methods in terms of the energy conservation in multiphase flows. Moreover, the phase field method consists of a phase field variable ϕ that distinguishes the fluid phases by assigning variable magnitudes of ϕ in different phases i.e., -1 in air phase ($\phi_a = -1$) and 1 in droplet phase ($\phi_d = 1$). When ϕ equals to 0, it defines the interface of the droplet (i.e., $\phi_{int} = 0$). Next, the Cahn-Hilliard equation is split up into two second-order equations in the numerical approach as follows [COMSOL, 2018]:

$$\begin{aligned} &\frac{\partial \phi}{\partial t} + \mathbf{u} \cdot \nabla \phi = \nabla \gamma \nabla G, \\ &G = \lambda \left[-\nabla^2 \phi + \frac{\phi(\phi^2 - 1)}{\epsilon^2} \right]. \end{aligned} \tag{1}$$

In Equation 1, $\mathbf{u}$ represents the flow velocity, while G denotes the chemical potential of the system. Moreover, the parameter γ that represents mobility ($m^3 \cdot s/kg$) is used to determine the time scale of diffusion, which in turn is closely associated with the thickness of the droplet interface ϵ (m) as:

$$\gamma = \chi \epsilon^2. \tag{2}$$

In the above equation, the parameter χ denotes the mobility tuning parameter (m·s/kg), which ultimately requires a very careful handling in the numerical study since a large magnitude of χ would lead to over damping of the convective terms, while a smaller magnitude leads to incorrect air-droplet interfacial thickness. On the other hand, the magnitude of ϵ is considered half of the maximum element mesh size h_m (i.e., $\epsilon = h_m/2$) in the region passed by the droplet during free fall and spreading process. Moreover, the surface tension coefficient σ is related to the mixing energy density λ and interfacial

thickness ϵ through the following relationship:

$$\sigma = \frac{2\sqrt{2}}{3}\frac{\lambda}{\epsilon}. \tag{3}$$

The phase field method treats the two-phase flow as a single phase flow where the properties in the flow domain, such as density (ρ), viscosity (η) vary according to the volume fraction of different fluid phases:

$$\rho = \rho_a + (\rho_d - \rho_a)V_{f2}, \qquad \eta = \eta_a + (\eta_d - \eta_a)V_{f2} \tag{4}$$

where V_{f1} and V_{f2} signify the volume fraction of air and droplet phases respectively, and furthermore can be related to the phase field variable ϕ as:

$$V_{f1} = \frac{1-\phi}{2}, \qquad V_{f2} = \frac{1+\phi}{2}. \tag{5}$$

3.2. GOVERNING EQUATIONS

A multiphase flow system involving a Newtonian droplet impinging under gravity and uniform magnetic fields through another viscous Newtonian fluid is predominantly governed by the time-dependent continuity and Navier-Stokes equations, which are as follows:

$$\nabla \cdot \mathbf{u} = 0 \tag{6}$$

and

$$\rho\frac{\partial \mathbf{u}}{\partial t} + \rho\left(\mathbf{u}\cdot\nabla\right)\mathbf{u} = -\nabla p + \nabla\cdot\boldsymbol{\tau} + \mathbf{F}_g + \mathbf{F}_\sigma + \mathbf{F}_m \tag{7}$$

where p denotes pressure and $\boldsymbol{\tau}$ represents the viscous stress, which again can be expanded to $\eta\left[(\nabla\mathbf{u}) + (\nabla\mathbf{u})^T\right]$. Moreover, the gravity force $\rho\mathbf{g}$ is denoted by $\mathbf{F}_g$, while $\mathbf{F}_\sigma$ and $\mathbf{F}_m$ simultaneously represent the surface tension and magnetic forces. Also, the surface tension

force $\mathbf{F}_\sigma$ is related to the chemical potential of the system G and phase field variable ϕ through the following relationship:

$$\mathbf{F}_\sigma = G\nabla\phi. \tag{8}$$

In addition to gravity forces, the implementation of a magnetic field generates additional magnetic stresses $\boldsymbol{\tau}_m$ on the interface of droplet due to a change in magnetic properties, the calculation of which requires an intensive knowledge of Maxwell equations and related constitutive correlations between magnetic induction $\mathbf{B}$, magnetic field $\mathbf{H}$, and magnetization $\mathbf{M}$. The correlations are as follows [Stratton, 2007]:

$$\nabla \times \mathbf{H} = 0, \qquad \nabla \cdot \mathbf{B} = 0, \qquad \mathbf{M} = \chi\mathbf{H}, \text{ and} \qquad \mathbf{B} = \mu_0(\mathbf{H} + \mathbf{M}) = \mu_0(1 + \chi)\mathbf{H}. \tag{9}$$

In the above equation, the parameter μ_0 expresses the permeability of vacuum, which equals to 1.257×10^{-6} H/m. A magnetic scalar potential ψ is defined so that $\mathbf{H} = -\nabla\psi$, which eventually leads to the following relationship:

$$\nabla \cdot (\mu\nabla\psi) = 0. \tag{10}$$

Finally, the formulation of the magnetic force $\mathbf{F}_m$ assumes the following form [Rosensweig, 1985]:

$$\mathbf{F}_m = \nabla \cdot \boldsymbol{\tau}_m = \nabla \cdot \left(\mu\mathbf{H}\mathbf{H} - \frac{\mu}{2}H^2\mathbf{I}\right) \tag{11}$$

where $H^2 = |\mathbf{H}|^2$, $\mathbf{I}$ is the identity operator, and μ is the permeability of the domain that can be calculated using the phase field variable ϕ.

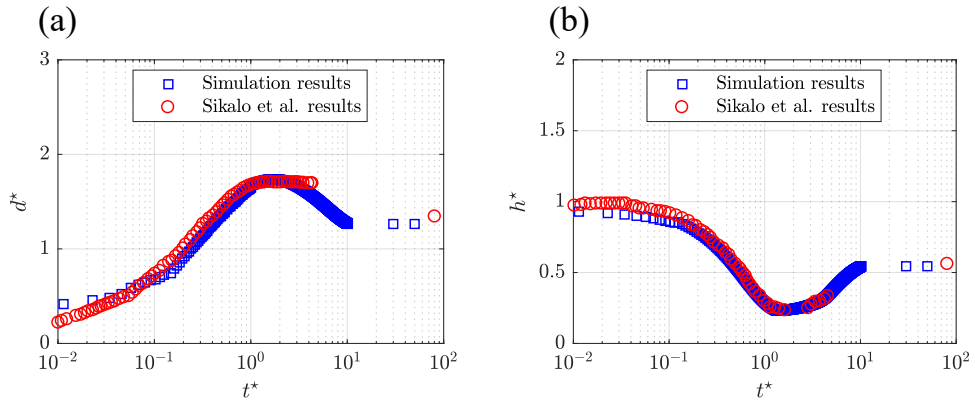

Figure 2. Comparison of spreading characteristics of a glycerin droplet on a solid surface at Oh = 0.267, Re = 36, and We = 92 against the experimental findings of Sikalo et al. [Šikalo *et al.*, 2002]. (a) Spreading and recoiling of droplet, $d^\star$ vs $t^\star$; and (b) Apex height of droplet, $h^\star$ vs $t^\star$.

4. RESULTS AND DISCUSSIONS

4.1. VALIDATION OF COMPUTATIONAL MODEL

In order to check the accuracy of the results, we also performed several validations of the numerical model against the existing experimental and theoretical findings in the literature. Figure 2 represents the spreading characteristics of a glycerin droplet on a solid surface under gravity at Oh = 0.267, Re = 36, and We = 92, and it can be observed that our simulation results (spreading and recoiling of droplet, apex height) quantitatively agree very well with the experimental findings of Sikalo et al. [Šikalo *et al.*, 2002]. Note that, in this case, the simulations mimic the exact liquid properties and magnitude of different parameters that are used in the experiments performed by Sikalo et al. [Šikalo *et al.*, 2002].

Moreover, we compared the simulated maximum spreading diameter of the droplet during spreading against the prevalent theories and experiments in the literature. According to Chandra and Avedisian [Chandra and Avedisian, 1991], for a given droplet diameter and impact velocity, the maximum spreading diameter $d^\star_{max}$ of a Newtonian droplet can be theoretically approximated as:

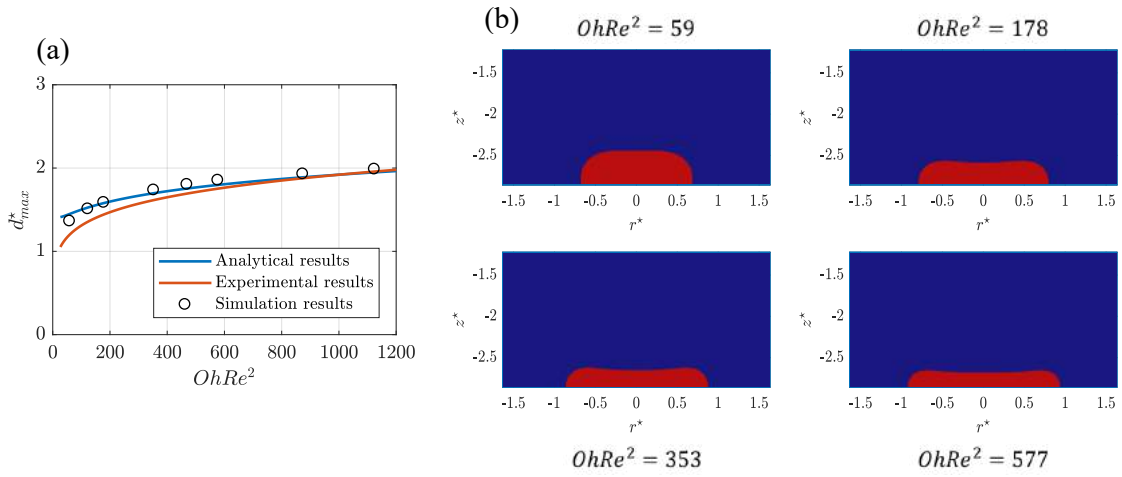

Figure 3. Comparison of simulated maximum spreading diameter $d^{\star}_{max}$ of a Newtonian droplet against analytical [Chandra and Avedisian, 1991] and experimental [Scheller and Bousfield, 1995] findings in literature. (a) $d^{\star}_{max}$ vs $OhRe^2$; and (b) Representative maximum droplet spreading diameter $d^{\star}_{max}$ under different $OhRe^2$.

$$\frac{3}{2}\mathrm{ReOh}^2 {d^{\star}_{max}}^4 + (1-\cos\theta_w){d^{\star}_{max}}^2 - \left(\frac{\mathrm{Re}^2\mathrm{Oh}^2}{3}+4\right) = 0, \tag{12}$$

whereas Schellar and Bousfield [Scheller and Bousfield, 1995] experimentally deduced an expression for the maximum spreading diameter $d^{\star}_{max}$ for a wide range of Reynolds and Ohnesorge numbers, which can be written as:

$$d^{\star}_{max} = 0.61\left(\mathrm{Re}^2\mathrm{Oh}\right)^{0.166}. \tag{13}$$

Figure 3(a) represents the comparison of simulated maximum spreading diameter $d^{\star}_{max}$ of a Newtonian droplet against the analytical (Chandra and Avedisian) and experimental (Scheller and Bousfield) findings as discussed above, and it clearly demonstrates a very good quantitative agreement among each other for a wide range of OhRe^2. Furthermore, for better visualization purposes, a few representative two-dimensional (2D) shapes of maximum spreading droplet diameter are depicted in Figure 3(b). Additionally, we have already validated the dynamics of a ferrofluid droplet under a permanent magnetic field

in our previous article [Hassan *et al.*, 2021a]. As a result, we do not feel the necessity of providing the validation of droplet dynamics under non-uniform magnetic fields in this article.

4.2. DROPLET SPREADING ON HYDROPHOBIC SURFACE

The spreading dynamics of an impinging droplet is primarily dependent on the simultaneous interactions among inertial forces, capillary forces, viscous forces, and properties of the surface. Additionally, the impact velocity of the droplet U_i is critical to the spreading phenomenon of the droplet, which further depends on the height of the droplet and initial velocity. The major dimensionless groups that ultimately play a significant role in spreading dynamics are as follows:

$$\mathrm{Re} = \frac{\rho_d U_i D_0}{\eta_d}, \tag{14}$$

$$\mathrm{We} = \frac{\rho_d U_i^2 D_0}{\sigma}, \tag{15}$$

$$\mathrm{Oh} = \frac{\eta_d}{\sqrt{D_0 \sigma \rho_d}}, \tag{16}$$

and

$$\mathrm{Bo}_m = \frac{\mu_0 R_0 H^2}{2\sigma}. \tag{17}$$

In the above equations, Reynolds number (Re) represents the relationship between inertial and viscous forces, whereas Weber number (We) denotes the competition between the inertial and surface tension forces. Additionally, the properties of a liquid can be defined by the Ohnesorge number (Oh), while the magnetic Bond number (Bo_m) relates the magnetic and surface tension forces. Also, the horizontal and vertical axes are non-dimensionalized by the initial diameter of the droplet D_0, while impact velocity U_i and D_0 are used as scaling

parameters for nondimensional times. The correlations are as follows:

$$r^* = \frac{r}{D_0}, \qquad z^* = \frac{z}{D_0}, \text{ and} \qquad t^* = \frac{tU_i}{D_0}. \tag{18}$$

Figure 4 depicts the time evolution of droplet shapes on a hydrophobic surface (i.e., $\theta_c = 90°$) under gravity at Re = 14.8, We = 15.4, and Oh = 0.267, and it suggests that as the droplet falls under gravity, the droplet assumes an oblate shape due to inertial forces ($t^\star = -0.46$). Next, as the droplet approaches near the bottom substrate ($t^\star = -0.23$), the local pressure between the bottom interface of the droplet and hydrophobic substrate increases, which in turn causes a flattening along the bottom interface of the droplet. Afterwards, the droplet impacts the surface ($t^\star = 0$) where the spreading phenomenon begins, which is usually accomplished in five consecutive stages on a hydrophobic surface i.e., kinematic, spreading, recoiling, dewetting, and equilibrium phases. Upon initial contact, the kinematic phase begins when the spreading diameter of the droplet increases upto the initial diameter of the droplet ($t^\star = 0.11$). In the following stage, the droplet enters into the spreading phase and continues spreading under inertial and capillary effects until it reaches a maximum spreading diameter i.e., primary spreading diameter ($t^\star = 0.93$) where the kinetic energy of the droplet is consumed by the viscous dissipation and conversion into surface energy. Also, at this point, the kinetic energy of the droplet diminishes to zero, and the droplet attains a minimum apex height, which marks the end of the spreading phase. However, due to inertial impact, a large amount of liquid gets squeezed near the contact line region, ultimately leading to a large curvature at the droplet-air interface that generates an increased local pressure gradient. This eventually pushes the liquid to flow inward towards the droplet center, thereby resulting in an increased apex height at $t^\star = 1.2$ (beginning of the relaxation phase). Moreover, during the relaxation stage, due to the rapid pressure increase at the droplet-air interface and viscous nature of droplet, an air-droplet interface oscillation is observed, while maintaining a fixed three phase contact line, which also agrees with the

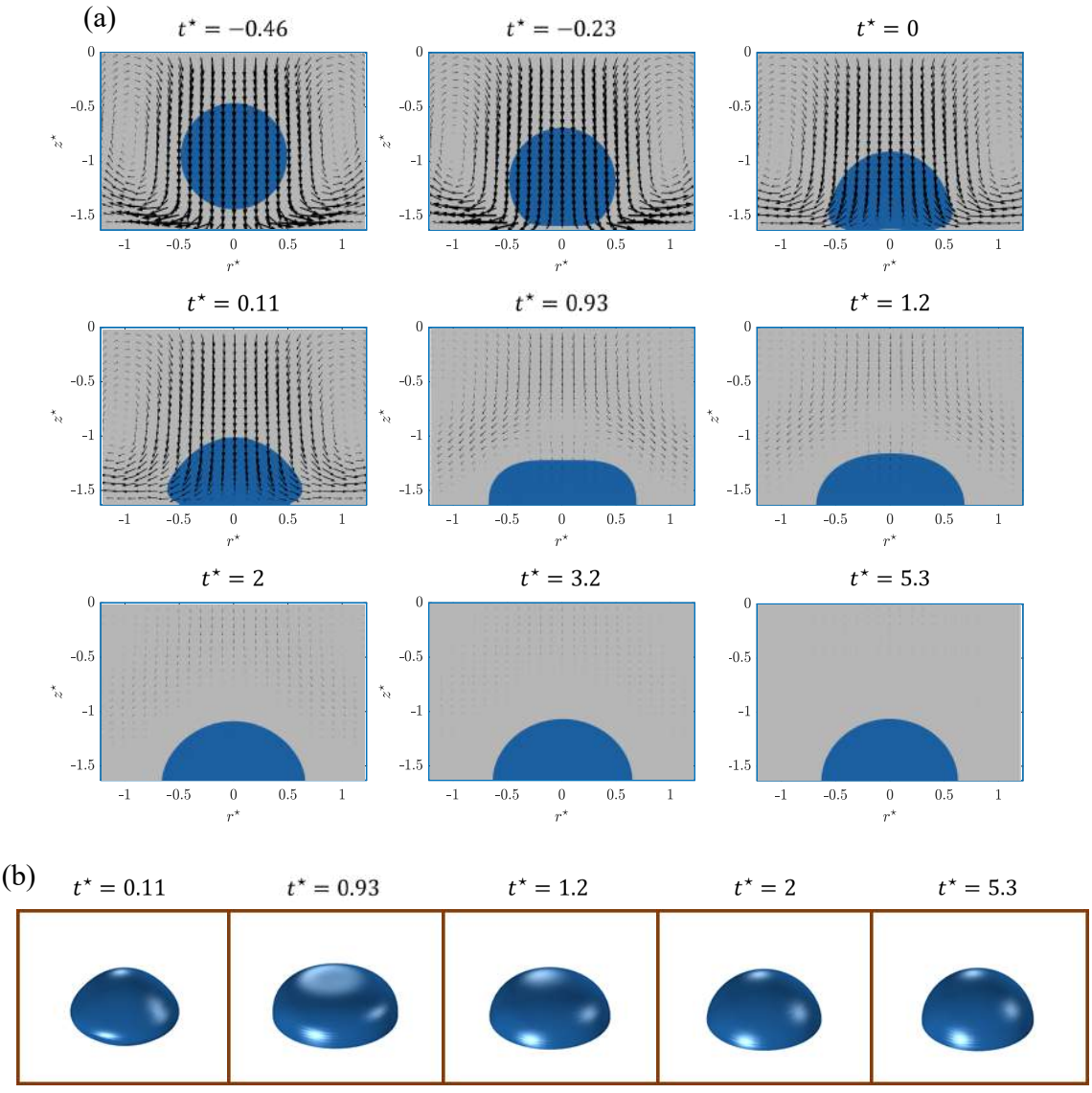

Figure 4. Time evolution of droplet shapes on a hydrophobic surface ($\theta_c = 90°$) under gravity at Re = 14.8, We = 15.4, and Oh = 0.267. (a) Wetting phenomenon of droplet (cross sectional view); and (b) Three-dimensional (3D) view of droplet shapes at representative times. The vector indicates the velocity field inside and around droplets during motion.

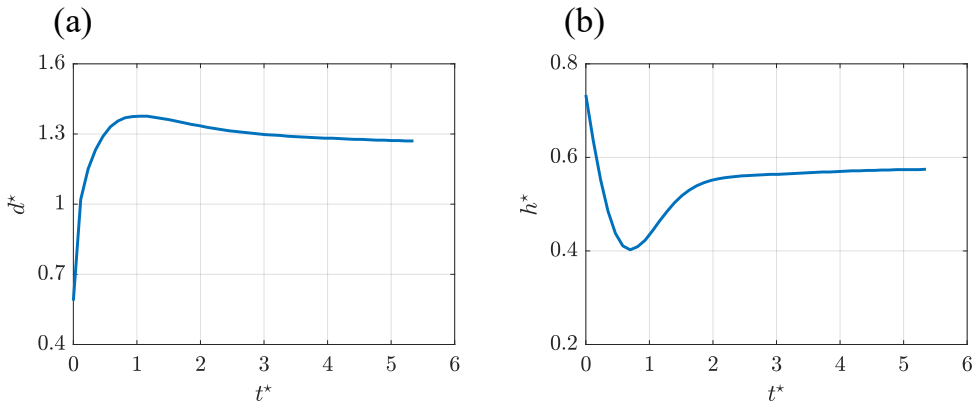

Figure 5. Wetting characteristics of an impinging droplet on a smooth hydrophobic surface (i.e., $\theta_c = 90°$) under gravity at Re = 14.8, We = 15.4, and Oh = 0.267. (a) Spreading diameter, $d^\star$ vs $t^\star$; and (b) Apex height, $h^\star$ vs $t^\star$.

existing findings in literature [Bird *et al.*, 2008, Quéré, 1997]. However, following the relaxation phase, due to the lower surface energy of the substrate, the droplet spreading behavior quickly transitions into the dewetting phase where the droplet spreading continues to decrease due to hydrophobicity of the substrate, while the magnitude of droplet apex height increases ($t^\star = 2$). After spending a significant amount of time in the dewetting phase, the droplet finally reaches a steady-state shape in the equilibrium phase ($t^\star = 5.3$), which marks the end of the spreading dynamics of droplet. Moreover, the arrow velocity in Figure 4(a) demonstrates the intensity of the flow field during different spreading stages of the droplet, which also indicates a decline in the flow field strength as the droplet transitions into successive spreading stages and completely diminishes in the equilibrium phase.

Additionally, Figure 5 shows the evolution of the spreading characteristics of an impinging droplet on a hydrophobic surface (i.e., $\theta_c = 90°$) under gravity at Re = 14.8, We = 15.4, and Oh = 0.267, which indicates a swift increase in the spreading diameter during the kinematic and spreading phases (Figure 5(a)) whereas the opposite is true for the apex height of the droplet (Figure 5(b)). However, as the droplet transitions into the

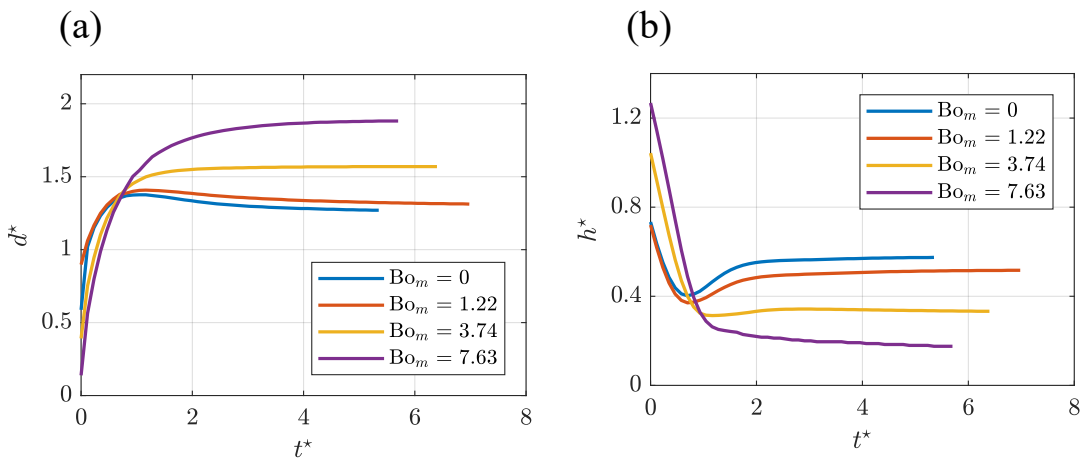

Figure 6. Wetting phenomenon of an impinging droplet on a hydrophobic substrate (i.e., $\theta_c = 90°$) under gravity and non-uniform magnetic fields at Re = 14.8, We = 15.4, and Oh = 0.267. (a) Spreading diameter, $d^\star$ vs $t^\star$; and (b) Apex height, $h^\star$ vs $t^\star$.

latter stages of spreading, the spreading diameter of the droplet continues to decrease, while giving a rise to the magnitude of the droplet apex height due to the hydrophobic nature of the bottom surface. Finally, an equilibrium stage is reached around $t^\star \approx 5.3$.

4.3. EFFECT OF NON-UNIFORM MAGNETIC FIELD

Our previous investigation on non-uniform magnetic field suggests that it is capable of inducing a significant change in the shape of a ferrofluid droplet under static situations [Hassan *et al.*, 2021a]. However, the effect of non-uniform magnetic field on droplet impact process is still unknown, as a result, now, we investigate the effect of non-uniform magnetic field on the dynamic impact phenomenon of a ferrofluid droplet to realize its contribution towards the overall impact dynamics leading to the steady state shape of a droplet.

Figure 6 represents the wetting phenomenon of an impinging droplet on a hydrophobic substrate under the combined effects of gravity and non-uniform magnetic fields at Re = 14.8, We = 15.4, and Oh = 0.267, and it can be seen that as the magnetic field intensity increases, the droplet experiences an increase in its base diameter (Fig. 6(a)), while undergoing a decrease in the apex height magnitudes at the same time (Fig. 6(b)).

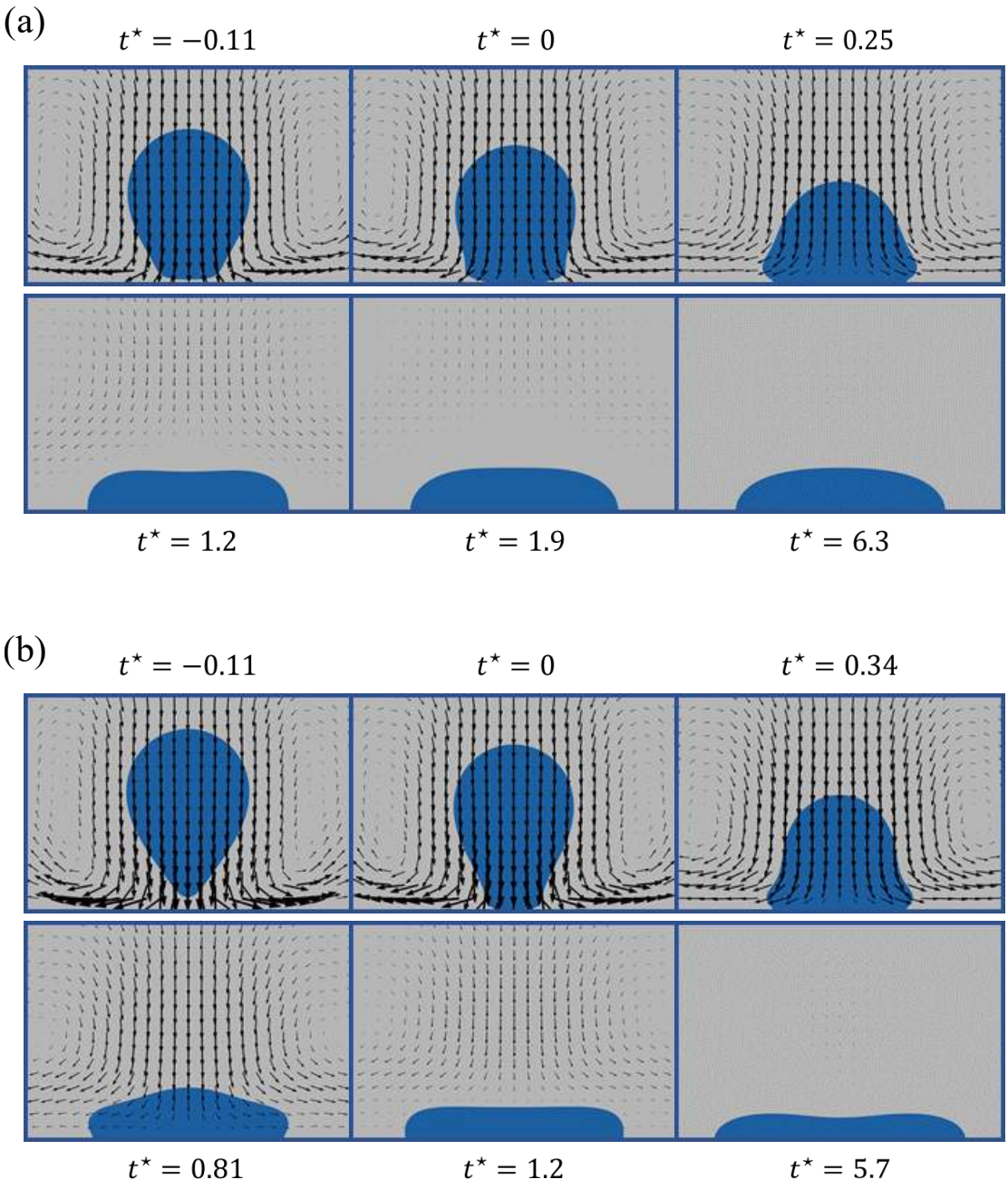

Figure 7. Time evolution of magnetic field induced droplet wetting phenomenon on a hydrophobic surface at Re = 14.8, We = 15.4, Oh = 0.267, and θ_c = 90°. (a) Bo_m = 3.74; and (b) Bo_m = 7.63. The vector indicates the velocity field inside and around droplets during motion.

Also, an increased magnetic field strength reduces the total amount of time required to reach a steady state droplet shape after impact, which also signifies the dominance of the magnetic field over the different spreading phases at higher magnetic Bond numbers Bo_m (i.e., $\mathrm{Bo}_m = 7.63$). Additionally, as the magnitude of Bo_m increases, the droplet experiences a sharp increase in its base diameter in the spreading phase, while the apex height of the droplet decreases under the attractive forces of the magnetic field.

The dynamic impact process of a ferrofluid droplet under a permanent magnetic field can be better understood by the time evolution of droplet shapes under magnetic fields at Re = 14.8, We = 15.4, Oh = 0.267, and $\theta_c = 90°$. Figure 7(a) indicates that at $\mathrm{Bo}_m = 3.74$, as the droplet approaches the bottom substrate ($t^\star = -0.11$), the spherical droplet transforms into a prolate shaped ellipsoid with greater curvature on the upper interface, while the bottom interface near the vicinity of the magnet demonstrates a huge contrast in curvature due to the attractive forces of the magnetic field. Next, as the droplet impacts onto the substrate ($t^\star = 0$), the base diameter of the droplet continually increases upto the initial droplet diameter under inertial and capillary forces, which also marks down the end of the kinematic phase at $t^\star = 0.25$. Afterwards, as the droplet enters into the spreading phase, it reaches a maximum spreading diameter at $t^\star = 1.2$, which is also known as the primary spreading diameter of the droplet. Next, followed by oscillations at the air-droplet interface, the droplet transitions into the relaxation and wetting phases on a hydrophobic surface at $t^\star = 1.9$, whereas in contrast, the droplet usually tends to enter into the dewetting phase after recoiling in the absence of magnetic fields on a hydrophobic surface (Fig. 4). Finally, the droplet attains a steady state shape at $t^\star = 6.3$. Moreover, in Figure 7(b), a similar impact phenomenon is observed at a higher magnetic Bond number (i.e., $\mathrm{Bo}_m = 7.63$). However, just before the impact ($t^\star = -0.11$), more contrast in droplet interface curvature near the vicinity of the magnet is observed, which again arises due to the stronger attraction forces of the magnet at higher Bo_m. Also, with the increase in the magnetic field strength, as the prolate shaped droplet experiences a decrease in its surface

area near the interface closer to the bottom substrate before the impact ($t^\star = -0.11$), the contact area of the droplet decreases upon initial contact at $t^\star = 0$, which also plays a significant role behind the sudden decline in the droplet base diameter and rise in apex height magnitudes at higher magnetic Bond numbers Bo_m in Figure 6. Additionally, a slight dip in the apex height is observed in the equilibrium stage ($t^\star = 5.7$) at $\mathrm{Bo}_m = 7.63$.

Furthermore, a set of experiments are conducted to analyze the impact behavior of ferrofluid droplets under the exposure to magnetic fields. For this purpose, EMG 304 (a water based ferrofluid) is chosen, which has a similar density as used in the simulations. The density, viscosity, and initial magnetic susceptibility of the ferrofluid are 1.24×10^3 kg/m^3, 5×10^{-3} Pa $\cdot$ s, and 5.03, respectively. Initially, droplets with diameter 2.4 ± 0.05 mm (similar to numerical simulations) are generated using a plastic needle, which again maintains an initial vertical separation from the bottom glass substrate. The glass surfaces, being hydrophilic in nature ($\theta_c < 40^\circ$), are treated with a water repellent spray to induce some degree of hydrophobicity, which ultimately results in a contact angle of $68.5^\circ \pm 2^\circ$ at the three phase contact line along the substrate. Next, using the pendant drop technique, the interfacial tension at the droplet-air interface is measured as 49.83 ± 2 mN/m. Afterwards, a permanent magnet (1/16″ thick and 1/4″ in diameter) is placed below the glass substrate, which again maintains a 3.51 mm vertical separation distance between the top of the magnet and bottom of the substrate. Figure 8 depicts the evolution of droplet shapes during impact, while Figure 9 represents the evolution of droplet spreading characteristics at We $\approx$ 10. These experimental results are qualitatively in good agreement with the numerical findings discussed above under the presence/absence of magnetic fields.

4.4. EFFECT OF MAGNET SIZES

Next, we analyze the effect of magnet sizes on the spreading behavior of a droplet after the impact, and Figure 10 represents the time evolution of spreading characteristics of a droplet on a hydrophobic surface ($\theta_c = 90^\circ$) at Re = 14.8, We = 15.4, and $\mathrm{Bo}_m = 3.74$.

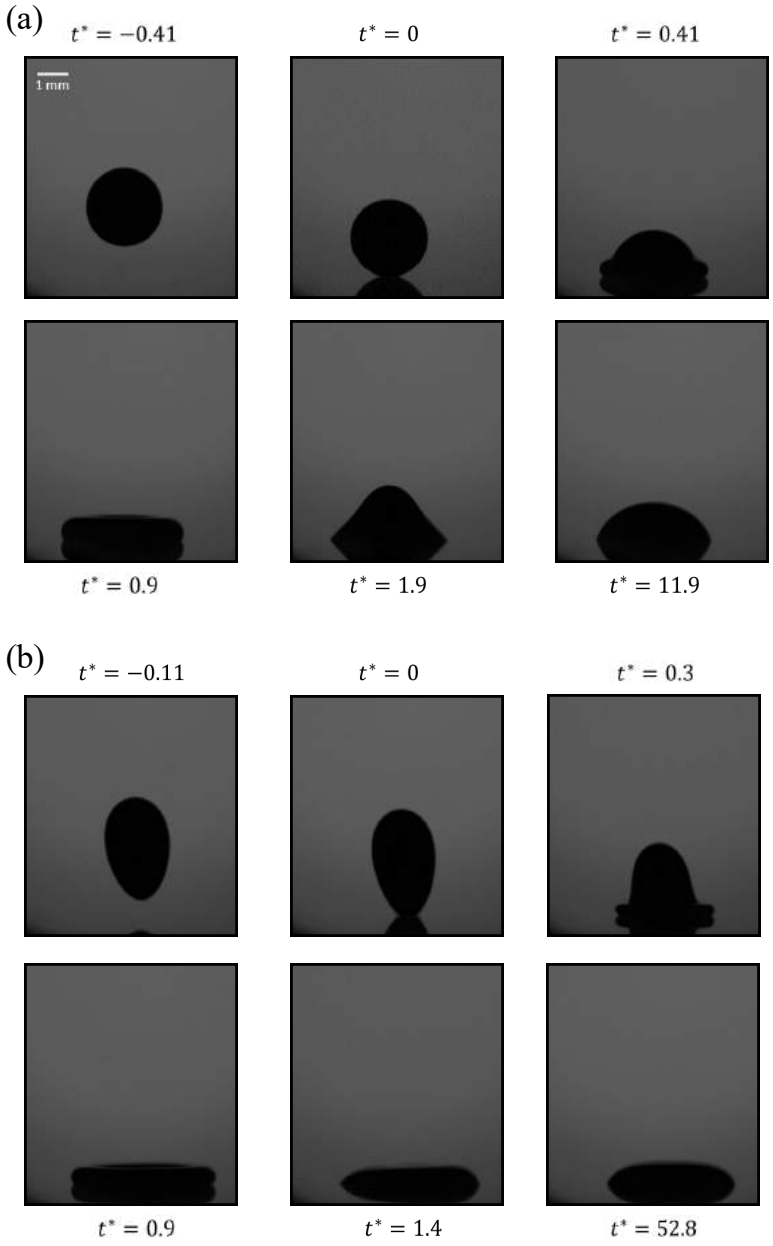

Figure 8. Experimental images for droplet impact at We ≈ 10. (a) B = 0; and (b) B = 1.32 T.

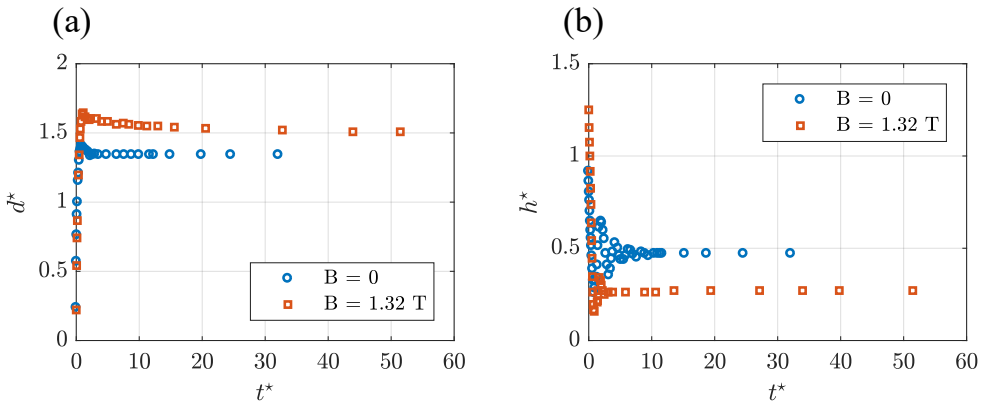

Figure 9. Evolution of droplet spreading characteristics after impact at We $\approx$ 10. (a) Spreading diameter, $d^\star$ vs $t^\star$; and (b) Apex height, $h^\star$ vs $t^\star$.

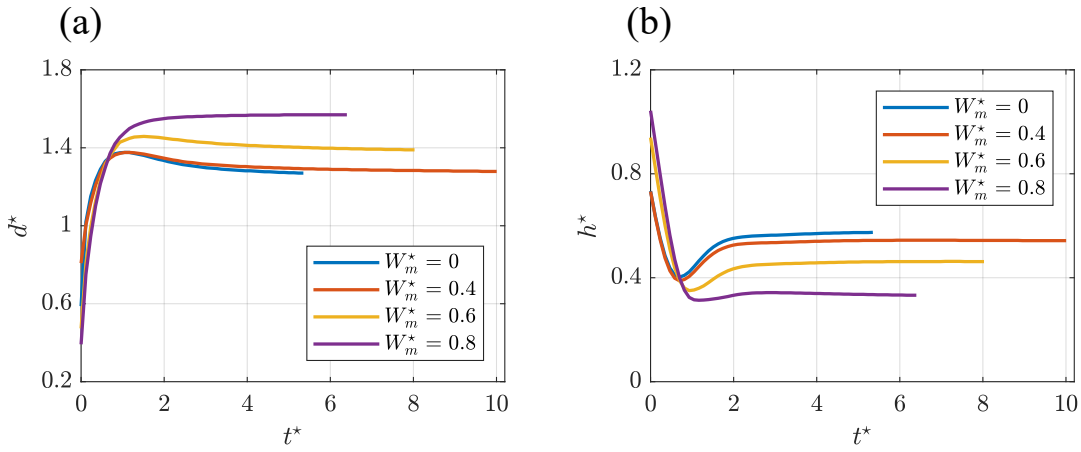

Figure 10. Effect of magnet size on droplet impact on a hydrophobic surface ($\theta_c = 90°$) at Re = 14.8, We = 15.4, and $\text{Bo}_m = 3.74$. (a) Spreading diameter, $d^\star$ vs $t^\star$; and (b) Apex height, $h^\star$ vs $t^\star$.

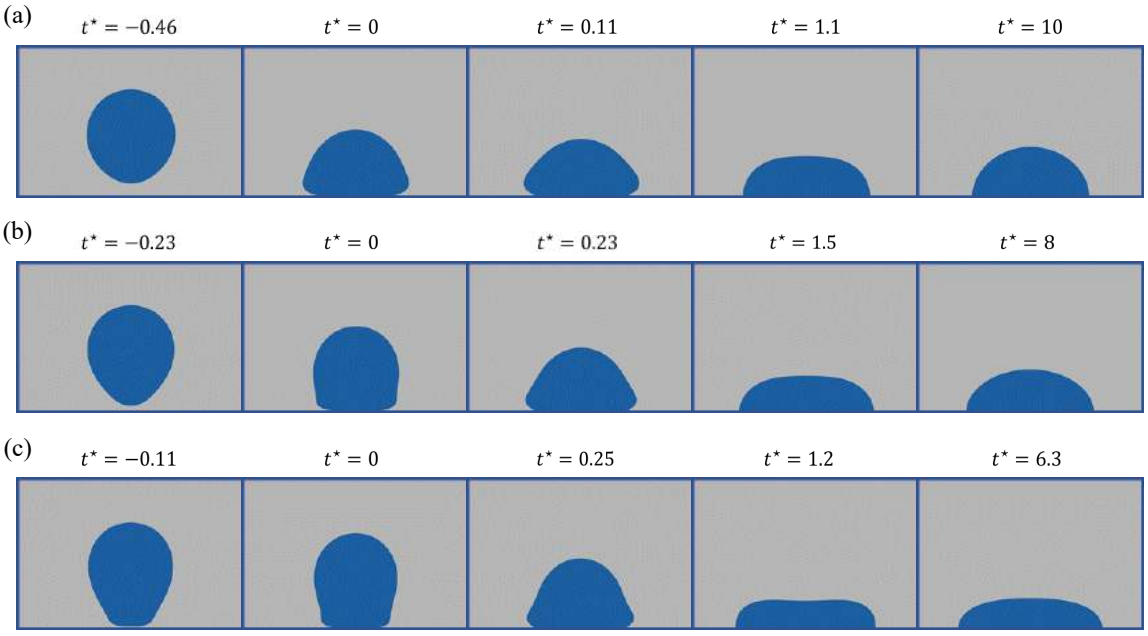

Figure 11. Two-dimensional (2D) representation of droplet shapes during spreading on a hydrophobic surface ($\theta_c = 90°$) at Re = 14.8, We = 15.4, and $\mathrm{Bo}_m = 3.74$. (a) $W_m^\star = 0.4$; (b) $W_m^\star = 0.6$; and (c) $W_m^\star = 0.8$.

In this analysis, the magnetic field strength and thickness of the magnet are kept constant, while the diameter is varied to obtain different magnet sizes, which is also considered as a common practice in industrial applications. From Figure 10(a), it can be seen that as the size of the magnet increases, the base diameter of the droplet during spreading also increases, which in turn causes a significant decrease in the apex height of the droplet during the process (Figure 10(b)). Also, as the magnet size increases upto $W_m^\star = 0.8$, the recoiling of droplet during relaxation phase of spreading diminishes, and the droplet directly transitions into the wetting phase after the completion of spreading phase, which further demonstrates the predominant effects of magnetic fields. Additionally, with the increase in the magnet sizes, the droplet interface becomes exposed to greater magnetic flux lines, which in turn aids the droplet in reaching a steady state shape faster under the influence of a magnetic field.

Moreover, the dynamic evolution of the droplet interface during the impact event at Re = 14.8, We = 15.4, and Bo_m = 3.74 is shown in Figure 11, which suggests that the droplet encounters a similar spreading phenomenon under different magnet sizes; however, as the droplet approaches closer to the bottom substrate before impact, the droplet shape becomes more distorted at increased magnet sizes, which ultimately reduces the magnitude of base diameter that makes contact with the bottom substrate at $t^\star = 0$. Eventually, followed by a kinematic phase, the droplet undergoes consecutive spreading and relaxation phases and ultimately reaches an equilibrium stage after the wetting phase. Interestingly, the droplet attains steady state shapes at a faster rate at increased magnitudes of $W_m^\star$.

Furthermore, Figure 12 illustrates the effect of magnet sizes on the droplet spreading dynamics on different hydrophobic substrates at Bo_m = 3.74 and Oh = 0.267. It can be seen that without the presence of any external forces except gravity, as the hydrophobicity of the substrate increases (i.e., increasing magnitudes of θ_c), the base diameter of the droplet decreases (Figure 12(a)), while giving rise to the magnitudes of the apex height (Figure 12(b)) at the same time to conserve the volume of the droplet. However, as the magnetic field is applied, the droplet encounters a transition in its shape. This also changes significantly under increased magnet sizes. For example, at a fixed contact angle, as the size of the magnet increases, the base diameter also increases, while the apex height decreases. This event is consistent for different hydrophobic substrates under consideration. Moreover, at a fixed magnet size, under the same magnetic field strength, the equilibrium spreading diameter experiences an increase at lower contact angles compared with more hydrophobic substrates. Interestingly, as the hydrophobicity of the bottom substrate increases, the increment rate in the base diameter and decrement rate in the apex height decreases at higher magnitudes of magnet sizes (i.e., $W_m^\star \geq 0.6$). The lower surface energy and higher surface tension of the droplet can be considered as major reasons behind the lower rate of spreading on more hydrophobic substrates. Additionally, the outline of equilibrium droplet shapes on

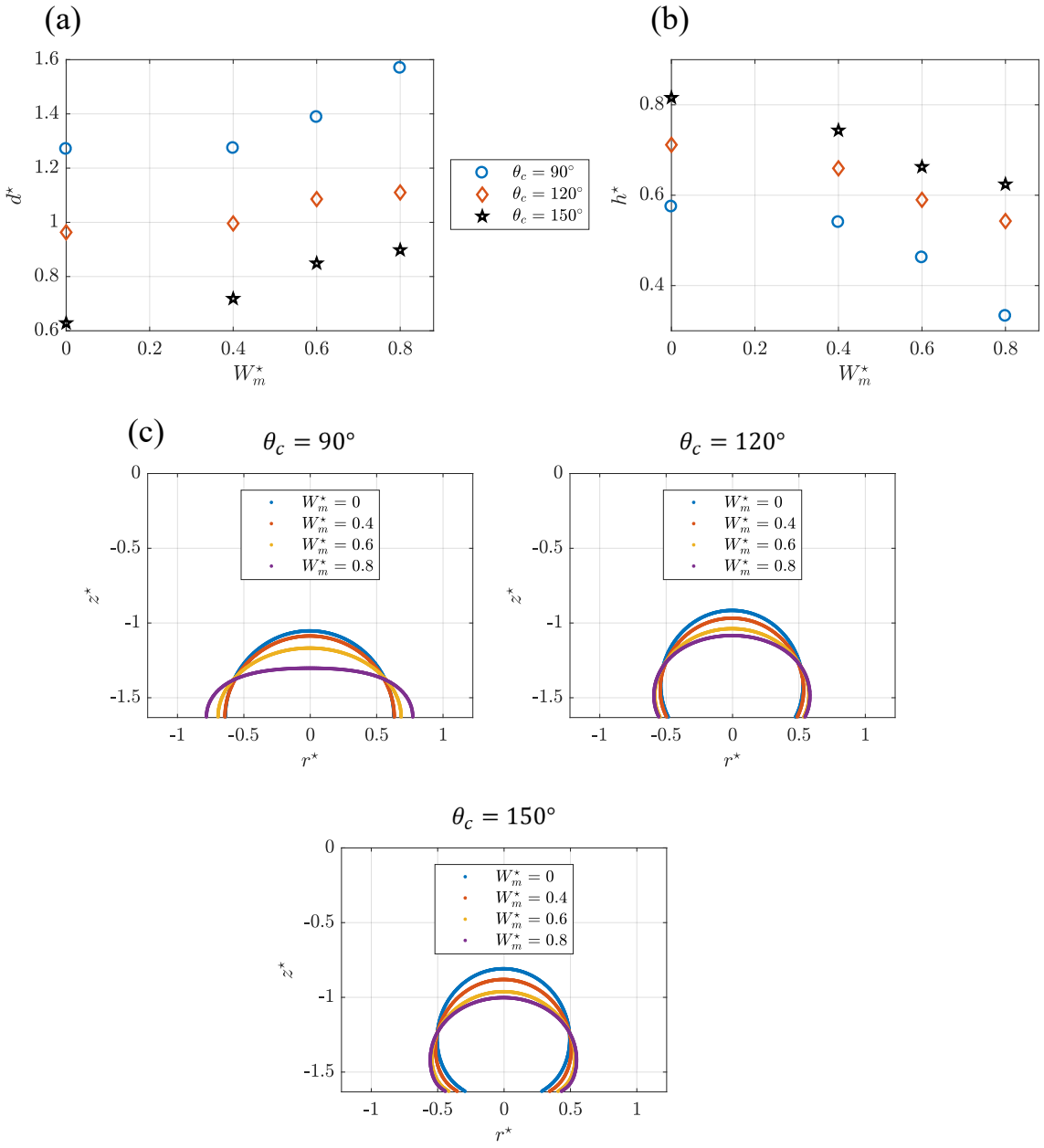

Figure 12. Magnet size effects on droplet spreading dynamics on different hydrophobic substrates at $\mathrm{Bo}_m = 3.74$ and $\mathrm{Oh} = 0.267$. (a) Equilibrium spreading diameter, $d^\star$ vs $W_m^\star$; (b) Equilibrium apex height, $h^\star$ vs $W_m^\star$; and (c) Outline of equilibrium droplet shapes on various hydrophobic surfaces under different magnet widths $W_m^\star$.

various hydrophobic surfaces under different magnet widths $W_m^\star$ are shown in Figure 12(c), which clearly demonstrates the clear contrast in steady state shapes under the influence of non-uniform magnetic fields generated by different width permanent magnets.

4.5. BOUNCING OF DROPLETS

When a droplet impacts on a substrate, depending on the wetting properties of the substrate, the droplet can either wet or stick to the surface. However, if the impact substrate is superhydrophobic in nature, it can repel impinging droplets under dynamic conditions, which is critical to a variety of purposes, including pesticide sprays and self-cleaning applications. Therefore, in the final section, we analyze the effects of superhydrophobic surfaces on the post-impact dynamic behavior of droplets with different viscosities. Here, a dimensionless group (i.e., Ohnesorge number Oh) is used to identify droplets with different viscous properties, which has been defined in previous sections (Equation 16).

Figure 13 depicts the dynamic behavior of droplets on a superhydrophobic substrate after impact under various Oh at We = 15.4 and $\theta_c = 170°$. It can be seen that at Oh = 0.057 (Figure 13(a)), as a low viscous droplet impacts the bottom substrate, it undergoes a similar spreading phenomenon in the kinematic phase as observed in previous sections. However, as the droplet transitions into the spreading phase, the inertial forces generated during the impact process push the liquid downwards, i.e., towards the bottom substrate. This results in a distorted shape at $t^\star = 1$, which in turn forces the droplet to undergo a vigorous transition in the recoiling phase. As the droplet starts recoiling ($t^\star = 1.3$), the spreading diameter of the droplet continues to decrease. During the kinematic and spreading phases, the kinetic energy of the droplet during impact is not fully consumed by the viscous dissipation. Hence, the residual kinetic energy is carried on by the droplet in the recoiling phase, which ultimately aids the droplet in bouncing off the surface ($t^\star = 3.1$). Note that, in this case, the extremely lower surface energy of the bottom substrate additionally plays an important role in generating a bouncing phenomenon in droplets on a superhydrophobic

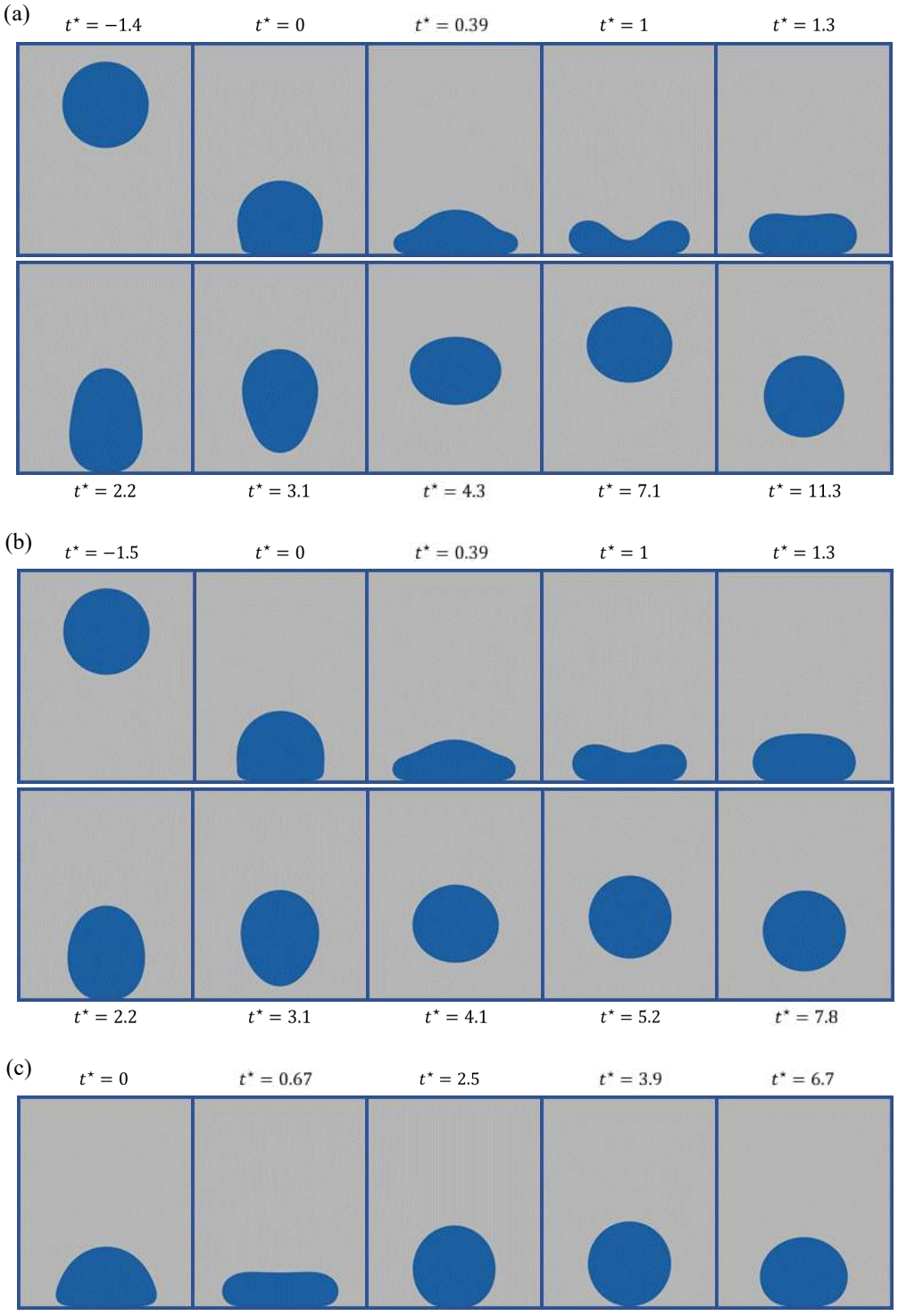

Figure 13. Bouncing of droplets on a superhydrophobic surface after impact under various Oh at We = 15.4 and $\theta_c = 170°$. (a) Oh = 0.057; (b) Oh = 0.115; and (c) Oh = 0.267.

surface. Next, as the droplet starts to migrate upward against gravity, it experiences drag forces, which eventually provide resistance against the motion of the droplet. Ultimately, the upward kinetic energy of the droplet is completely consumed by viscous dissipation and drag forces. And, the droplet reaches a maximum height during the upward motion where the velocity of the droplet diminishes to zero ($t^\star = 7.1$), which next triggers a downward motion under the action of gravity at $t^\star = 11.3$. However, as the viscosity of the droplet increases (Figure 13(b)), the distortion in droplet is less pronounced due to the inertial impact at $t^\star = 1$. If the viscosity of the droplet is increased to an even greater extent, the inertial forces engenders a minimal impact on the shape of the droplet after impact (Figure 13(c), $t^\star = 0.67$). Also, at Oh = 0.267, the greater viscous dissipation of droplet overcomes the kinetic and recoiling energies and in turn makes the bouncing phenomenon difficult even on a superhydrophobic surface. That is, the droplet barely leaves the substrate at $t^\star = 3.9$. Moreover, the maximum height attained by droplets during the upward motion decreases with the increase in droplet viscosities, and the droplet spends more time in the bouncing regime at lower Ohnesorge numbers. Furthermore, these results agree well with the recent experimental findings of Jha et al. [Jha *et al.*, 2020].

Next, we apply a non-uniform magnetic field below the bottom substrate to observe its effect on the bouncing phenomenon of droplets. Figure 14 illustrates the magnetic field effect on the bouncing of droplets on a superhydrophobic surface at Oh = 0.115, We = 15.4, and $\theta_c = 170^\circ$. Here, two different magnetic field scenarios (varying magnitudes of Bo_m and $W_m^\star$) are used to demonstrate the impact of magnetic fields under different conditions. Figure 14(a) suggests that as the magnetic field is activated ($\mathrm{Bo}_m = 1.22$, $W_m^\star = 0.6$), the droplet still tries to jump off the substrate at $t^\star = 3.7$. However, it fails due to the stronger attraction forces generated by the non-uniform magnetic field. Eventually, the droplet undergoes a transition in its shape under the combined effects of gravity and the magnetic field and reaches an equilibrium shape at $t^\star = 26.5$ after a series of oscillations. Moreover, if a stronger magnetic field is applied using a magnet of greater widths (i.e., $\mathrm{Bo}_m = 3.74$, $W_m^\star = 0.8$), the dominance

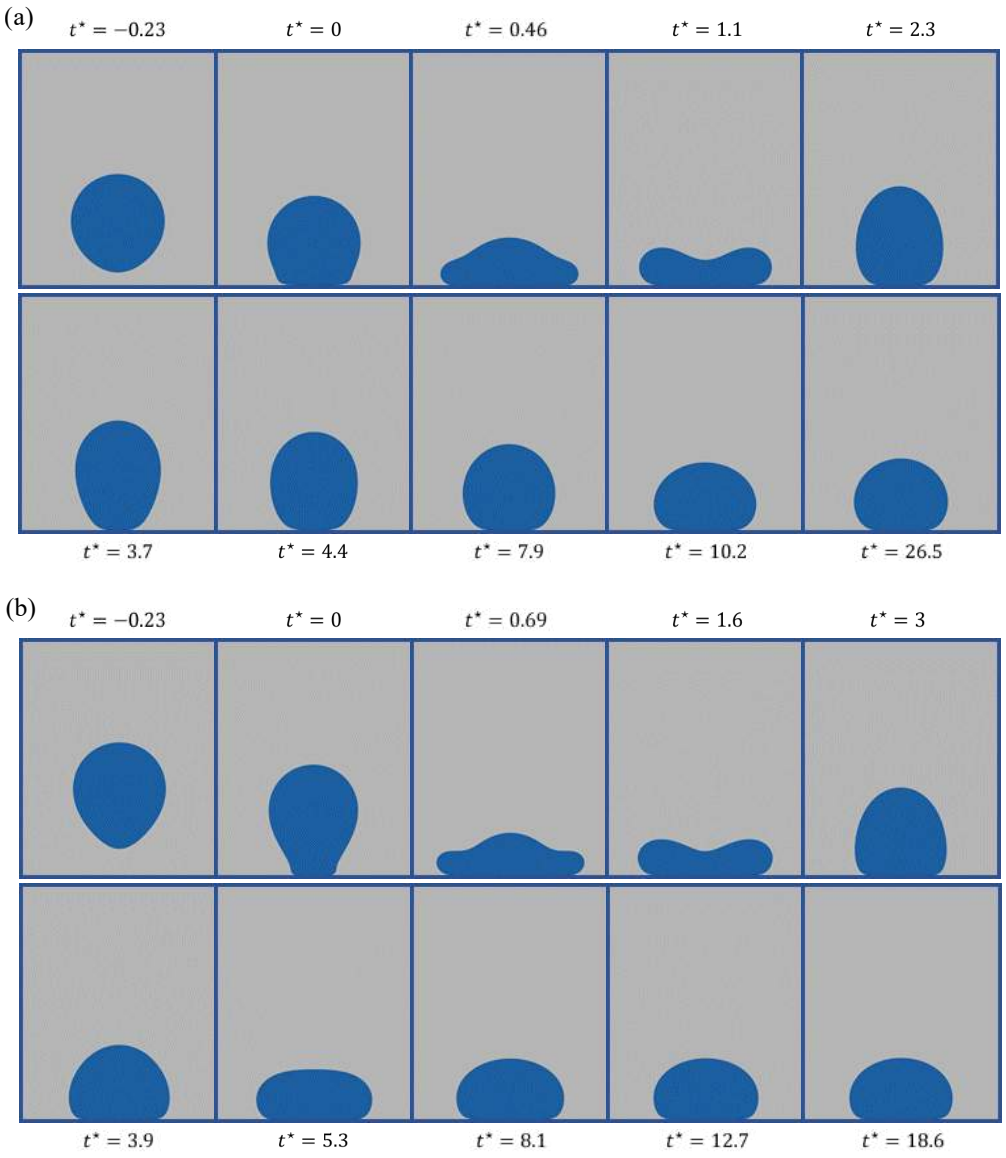

Figure 14. Magnetic field effect on the bouncing of droplets on a superhydrophobic surface at Oh = 0.115, We = 15.4, and $\theta_c = 170°$. (a) $\mathrm{Bo}_m = 1.22$, $W_m^\star = 0.6$; and (b) $\mathrm{Bo}_m = 3.74$, $W_m^\star = 0.8$.

of the magnetic field on the dynamic behavior of droplets is observed to an even greater extent, which in turn again increases the maximum spreading diameter of droplet during the spreading phase ($t^\star = 0.69$) and resists the bouncing event even more in comparison to droplet spreading at lower Bo_m and $W_m^\star$ (Figure 14(a), $t^\star = 0.46$). Furthermore, the droplet reaches a steady state shape faster under increased magnetic field strength ($t^\star = 18.6$) with an increase in base diameter and decrease in apex height magnitudes, which again agrees well with the findings in the previous sections.

In the final step, we experimentally demonstrate the bouncing phenomenon of droplets at We = 15.5 (similar to numerical simulations) on a superhydrophobic surface i.e., $\theta_c \approx 150°$. Here, in order to induce superhydrophobicity on the bottom substrate, followed by a thorough cleaning with Isopropanone (IPA) and drying, the glass slides are treated with a commercial superhydrophobic coating (Ultra-Ever Dry). This ultimately results in a contact angle around $150° \pm 3°$ for EMG 304 water-based ferrofluid droplets. Figure 15 illustrates the impact of a droplet on a superhydrophobic substrate at We = 15.5. It can be seen that in the absence of magnetic fields (Figure 15(a)), the droplet experiences an upward flight against gravity after the impact, which eventually reaches a maximum height before coming back to the surface again due to the influence of gravity, while the application of a magnetic field (Figure 15(b)) suppresses the bouncing phenomenon and provides resistance against the upward flight i.e., the droplet sticks to the surface after the impact. Moreover, these phenomena along with the evolution of droplet shapes during and after impact agree qualitatively well with the numerical findings discussed above. Furthermore, these results demonstrate the potential of magnetic fields in controlling the bouncing phenomenon of low viscous droplets on substrates with extremely low surface energies ($\theta_c \geq 150°$) after the impact under the influence of gravity.

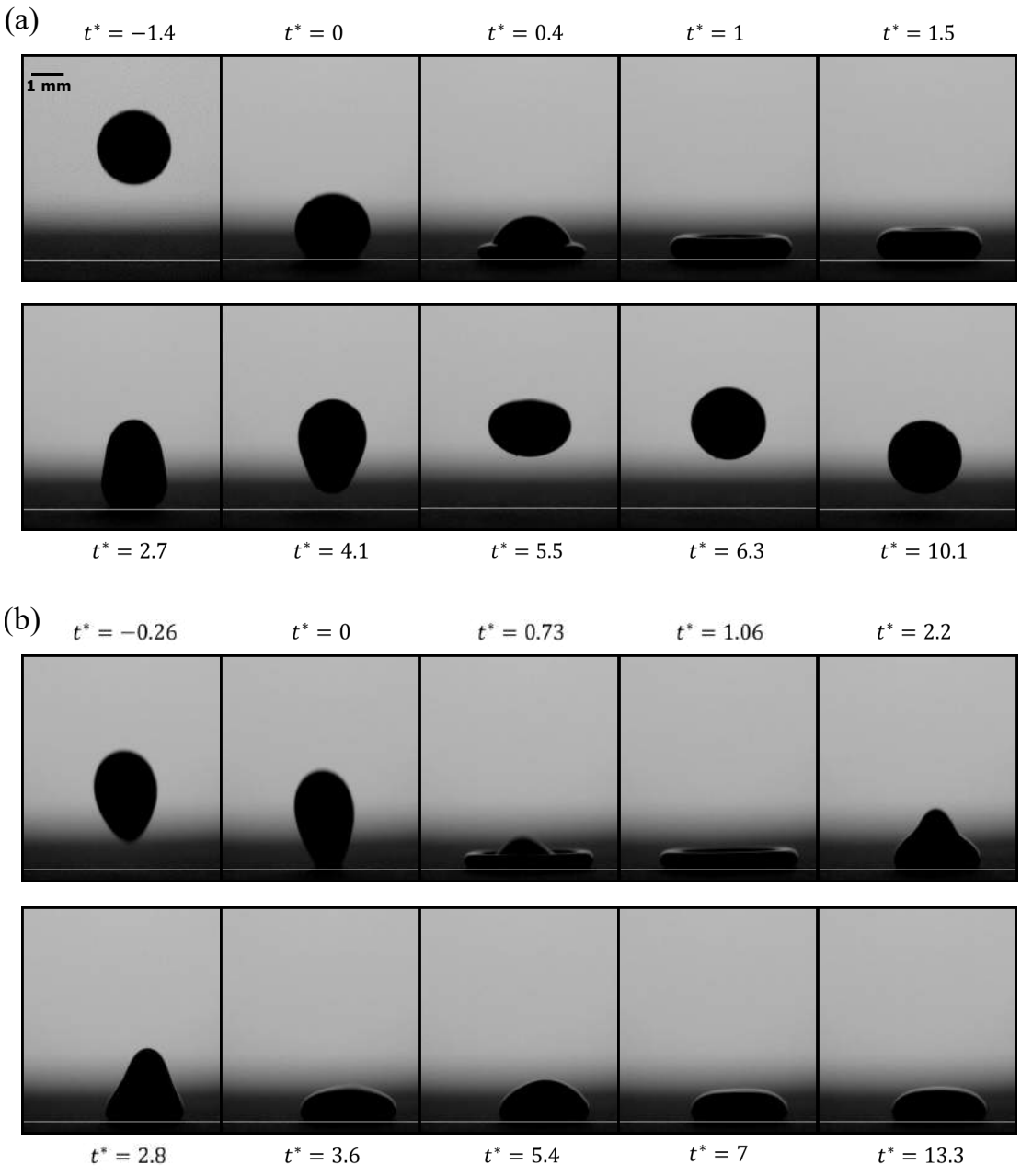

Figure 15. Bouncing of droplets at We = 15.5 and $\theta_c = 150° \pm 3°$. (a) B = 0; and (b) B = 1.32 T.

5. CONCLUSION

This work presents numerical and experimental analyses on the wetting and bouncing dynamics of a ferrofluid droplet on hydrophobic surfaces under the combined effects of gravity and permanent magnetic fields. The results indicate that when a ferrofluid droplet approaches the vicinity of non-uniform magnetic fields at Re = 14.8 and We = 15.4, it transforms into a cone shaped droplet, whereas an oblate shaped droplet is generated in the absence of any magnetic forces before impact. Also, the curvature of the droplet near the bottom substrate significantly changes before impact, with the increase in the magnetic field strengths. Moreover, the application of a non-uniform magnetic field results in an increase in the spreading diameter of the droplet during the spreading and equilibrium phases even on a hydrophobic surface (i.e., $\theta_c = 90°$), while causing a sharp decrease in the apex height magnitude after the impact. Also, an increase in both magnetic field strength and magnet width increases the spreading diameter of droplets even more on hydrophobic surfaces, which eventually changes the steady state shape of droplets in the equilibrium conditions. Additionally, these results are consistent on a range of different substrates that are either hydrophobic or superhydrophobic in nature (i.e., $90° \leq \theta_c \leq 150°$).

Furthermore, the bouncing phenomenon of droplets is investigated under the influence of magnetic fields at different Ohnesorge numbers Oh, and the results suggest that as Oh decreases to 0.115 (i.e., Oh = 0.115), the droplet encounters a bouncing event during the recoiling stage, which is even more pronounced at lower magnitudes of Oh (i.e., Oh = 0.057). Also, after bouncing off the surface, the droplet spends more time during the upward flight at lower magnitudes of Oh, which ultimately increases the maximum height reached by the droplet before the kinetic energy is totally consumed by the viscous dissipation and drag forces. However, the activation of a permanent magnetic field suppresses the bouncing event and reduces the number of oscillations between the relaxation and equilibrium phases at higher magnetic Bond numbers Bo_m. The results signify the potential of

using non-uniform magnetic fields in the active control of wetting and bouncing dynamics of an impinging droplet on hydrophobic surfaces, which is relevant to many technological applications, such as spray cooling and advanced 3D printing of metals.

ACKNOWLEDGMENTS

The authors gratefully acknowledge the support from the Department of Mechanical and Aerospace Engineering (MAE) at Missouri University of Science and Technology. This work is partially supported by the NSF through Grant DMS-1818642.

REFERENCES

Aguilar, G., Majaron, B., Pope, K., Svaasand, L. O., Lavernia, E. J., and Nelson, J. S., 'Influence of nozzle-to-skin distance in cryogen spray cooling for dermatologic laser surgery,' Lasers in Surgery and Medicine: The Official Journal of the American Society for Laser Medicine and Surgery, 2001, **28**(2), pp. 113–120.

Ahmed, A., Fleck, B. A., and Waghmare, P. R., 'Maximum spreading of a ferrofluid droplet under the effect of magnetic field,' Physics of Fluids, 2018, **30**(7), p. 077102.

Bai, F., Han, D., He, X.-M., and Yang, X., 'Deformation and coalescence of ferrodroplets in Rosensweig model using the phase field and modified level set approaches under uniform magnetic fields,' Commun. Nonlinear Sci. Numer. Simul., 2020, **85**, p. 105213.

Bai, F., He, X.-M., Zhou, R., Yang, X., and Wang, C., 'Three dimensional phase-field investigation of droplet formation in microfluidic flow focusing devices with experimental validation,' Int. J. Multiphase Flow, 2017, **93**, pp. 130–141.

Bao, K., Shi, Y., Sun, S., and Wang, X., 'A finite element method for the numerical solution of the coupled Cahn-Hilliard and Navier-Stokes system for moving contact line problems,' J. Comput. Phys., 2012, **231**(24), pp. 8083–8099.

Basinger, B., Aguilar, G., and Nelson, J. S., 'Effect of skin indentation on heat transfer during cryogen spray cooling,' Lasers in Surgery and Medicine, 2004, **34**(2), pp. 155–163.

Bird, J. C., Mandre, S., and Stone, H. A., 'Short-time dynamics of partial wetting,' Physical review letters, 2008, **100**(23), p. 234501.

Boyer, F., 'Mathematical study of multi-phase flow under shear through order parameter formulation,' Asymptot. Anal., 1999, **20**(2), pp. 175–212.

Cader, T., Westra, L. J., and Eden, R. C., 'Spray cooling thermal management for increased device reliability,' IEEE Transactions on Device and Materials Reliability, 2004, **4**(4), pp. 605–613.

Chandra, S. and Avedisian, C., 'On the collision of a droplet with a solid surface,' Proceedings of the Royal Society of London. Series A: Mathematical and Physical Sciences, 1991, **432**(1884), pp. 13–41.

Chen, M., Bollada, P. C., and Jimack, P. K., 'Dynamic load balancing for the parallel, adaptive, multigrid solution of implicit phase-field simulations,' Int. J. Numer. Anal. Model., 2019, **16**, pp. 297–318.

Chen, R.-H., Chow, L. C., and Navedo, J. E., 'Effects of spray characteristics on critical heat flux in subcooled water spray cooling,' International Journal of Heat and Mass Transfer, 2002, **45**(19), pp. 4033–4043.

Clanet, C., Béguin, C., Richard, D., and Quéré, D., 'Maximal deformation of an impacting drop,' Journal of Fluid Mechanics, 2004, **517**, p. 199.

COMSOL, *CFD Module Application Library Manual*, 5.3a edition, 2018.

Dash, S. and Garimella, S. V., 'Droplet evaporation on heated hydrophobic and superhydrophobic surfaces,' Physical Review E, 2014, **89**(4), p. 042402.

Diegel, A. E., Feng, X., and Wise, S. M., 'Analysis of a mixed finite element method for a Cahn-Hilliard-Darcy-Stokes system,' SIAM J. Numer. Anal., 2015, **53**(1), pp. 127–152.

Ding, H., Spelt, P. D. M., and Shu, C., 'Diffuse interface model for incompressible two-phase flows with large density ratios,' J. Comput. Phys., 2007, **226**(2), pp. 2078–2095.

Emdadi, M. and Pournaderi, P., 'Numerical simulation of conducting droplet impact on a surface under an electric field,' Acta Mechanica, 2020, **231**(3), pp. 1083–1103.

Fauchais, P., Vardelle, A., Vardelle, M., and Fukumoto, M., 'Knowledge concerning splat formation: an invited review,' Journal of Thermal Spray Technology, 2004, **13**(3), pp. 337–360.

Feng, X., 'Fully discrete finite element approximations of the Navier-Stokes-Cahn-Hilliard diffuse interface model for two-phase fluid flows,' SIAM J. Numer. Anal., 2006, **44**(3), pp. 1049–1072.

Feng, X., He, Y., and Liu, C., 'Analysis of finite element approximations of a phase field model for two-phase fluids,' Math. Comp., 2007, **76**(258), pp. 539–571.

Feng, X., Li, Y., and Xing, Y., 'Analysis of mixed interior penalty discontinuous Galerkin methods for the Cahn-Hilliard equation and the Hele-Shaw flow,' SIAM J. Numer. Anal., 2016, **54**(2), pp. 825–847.

Feng, X. and Wise, S., 'Analysis of a Darcy-Cahn-Hilliard diffuse interface model for the Hele-Shaw flow and its fully discrete finite element approximation,' SIAM J. Numer. Anal., 2012, **50**(3), pp. 1320–1343.

Gan, H., Shan, X., Eriksson, T., Lok, B., and Lam, Y., 'Reduction of droplet volume by controlling actuating waveforms in inkjet printing for micro-pattern formation,' Journal of micromechanics and microengineering, 2009, **19**(5), p. 055010.

Gao, Y., He, X.-M., Mei, L., and Yang, X., 'Decoupled, linear, and energy stable finite element method for the Cahn-Hilliard-Navier-Stokes-Darcy phase field model,' SIAM J. Sci. Comput., 2018, **40**(1), pp. B110–B137.

Gupta, A. and Kumar, R., 'Droplet impingement and breakup on a dry surface,' Computers & fluids, 2010, **39**(9), pp. 1696–1703.

Gurtin, M. E., Polignone, D., and nals, J. V., 'Two-phase binary fluids and immiscible fluids described by an order parameter,' Math. Models Methods Appl. Sci., 1996, **6**(6), pp. 815–831.

Han, D., He, X.-M., Wang, Q., and Wu, Y., 'Existence and weak-strong uniqueness of solutions to the Cahn-Hilliard-Navier-Stokes-Darcy system in superposed free flow and porous media,' Nonlinear Anal., 2021, **211**, p. #112411.

Han, T.-Y., Yang, J.-C., Zhang, J., and Ni, M.-J., 'Three-dimensional numerical simulation on the spreading characteristics of a liquid metal droplet in a horizontal magnetic field,' Numerical Heat Transfer, Part A: Applications, 2018, **74**(12), pp. 1786–1803.

Hassan, M. R. and Wang, C., 'Magnetic field induced ferrofluid droplet breakup in a simple shear flow at a low reynolds number,' Physics of Fluids, 2019, **31**(12), p. 127104.

Hassan, M. R. and Wang, C., 'Ferro-hydrodynamic interactions between ferrofluid droplet pairs in simple shear flows,' Colloids and Surfaces A: Physicochemical and Engineering Aspects, 2020a, p. 124906.

Hassan, M. R. and Wang, C., 'Lateral migration of a ferrofluid droplet in a plane poiseuille flow under uniform magnetic fields,' Physical Review E, 2020b, **102**(2), p. 022611.

Hassan, M. R., Zhang, J., and Wang, C., 'Deformation of a ferrofluid droplet in simple shear flows under uniform magnetic fields,' Physics of Fluids, 2018, **30**(9), p. 092002.

Hassan, M. R., Zhang, J., and Wang, C., 'Digital microfluidics: Magnetic transportation and coalescence of sessile droplets on hydrophobic surfaces,' Langmuir, 2021a, **37**(19), pp. 5823–5837.

Hassan, M. R., Zhang, J., and Wang, C., 'Numerical investigation of falling ferrofluid droplets under magnetic fields,' Colloid and Interface Science Communications, 2021b, **40**, p. 100333.

Healy, W. M., Hartley, J., and Abdel-Khalik, S., 'On the validity of the adiabatic spreading assumption in droplet impact cooling,' International Journal of Heat and Mass Transfer, 2001, **44**(20), pp. 3869–3881.

Hohenberg, P. C. and Halperin, B. I., 'Theory of dynamic critical phenomena,' Rev. Mod. Phys., 1977, **49**(3), pp. 435–479.

Huang, Q., Yang, X., and He, X.-M., 'Numerical approximations for a smectic-A liquid crystal flow model: first-order, linear, decoupled and energy stable schemes,' Discrete Contin. Dyn. Syst. Ser. B, 2018, **23**(6), pp. 2177–2192.

Jha, A., Chantelot, P., Clanet, C., and Quéré, D., 'Viscous bouncing,' Soft Matter, 2020, **16**(31), pp. 7270–7273.

Kamnis, S., Gu, S., Lu, T., and Chen, C., 'Numerical modelling of sequential droplet impingements,' Journal of Physics D: Applied Physics, 2008, **41**(16), p. 165303.

Khojasteh, D., Kazerooni, M., Salarian, S., and Kamali, R., 'Droplet impact on superhydrophobic surfaces: A review of recent developments,' Journal of Industrial and Engineering Chemistry, 2016, **42**, pp. 1–14.

Kim, H.-Y. and Chun, J.-H., 'The recoiling of liquid droplets upon collision with solid surfaces,' Physics of fluids, 2001, **13**(3), pp. 643–659.

Kim, J., 'Spray cooling heat transfer: The state of the art,' International Journal of Heat and Fluid Flow, 2007, **28**(4), pp. 753–767.

Kim, J., Kang, K., and Lowengrub, J., 'Conservative multigrid methods for Cahn-Hilliard fluids,' J. Comput. Phys., 2004, **193**(2), pp. 511–543.

Li, R., Gao, Y., Chen, J., Zhang, L., He, X.-M., and Chen, Z., 'Discontinuous finite volume element method for a coupled Navier-Stokes-Cahn-Hilliard phase field model,' Adv. Comput. Math., 2020, **46**, p. #25.

Lin, F., He, X.-M., and Wen, X., 'Fast, unconditionally energy stable large time stepping method for a new Allen-Cahn type square phase-field crystal model,' Appl. Math. Lett., 2019, **92**, pp. 248–255.

Lin, L. and Ponnappan, R., 'Heat transfer characteristics of spray cooling in a closed loop,' International Journal of Heat and Mass Transfer, 2003, **46**(20), pp. 3737–3746.

Lin, S., Zhao, B., Zou, S., Guo, J., Wei, Z., and Chen, L., 'Impact of viscous droplets on different wettable surfaces: Impact phenomena, the maximum spreading factor, spreading time and post-impact oscillation,' Journal of colloid and interface science, 2018, **516**, pp. 86–97.

Liu, C. and Shen, J., 'A phase field model for the mixture of two incompressible fluids and its approximation by a Fourier-spectral method,' Phys. D, 2003, **179**(3-4), pp. 211–228.

Liu, H., Si, C., Cai, C., Zhao, C., and Yin, H., 'Experimental investigation on impact and spreading dynamics of a single ethanol–water droplet on a heated surface,' Chemical Engineering Science, 2021, **229**, p. 116106.

Liu, Z. and Qiao, Z., 'Wong-Zakai Approximations of Stochastic Allen-Cahn Equation,' Int. J. Numer. Anal. Model., 2019, **16**, pp. 681–694.

Lübbe, A. S., Bergemann, C., Riess, H., Schriever, F., Reichardt, P., Possinger, K., Matthias, M., Dörken, B., Herrmann, F., Gürtler, R., *et al.*, 'Clinical experiences with magnetic drug targeting: a phase i study with 4'-epidoxorubicin in 14 patients with advanced solid tumors,' Cancer research, 1996, **56**(20), pp. 4686–4693.

Lunkad, S. F., Buwa, V. V., and Nigam, K., 'Numerical simulations of drop impact and spreading on horizontal and inclined surfaces,' Chemical Engineering Science, 2007, **62**(24), pp. 7214–7224.

Madejski, J., 'Solidification of droplets on a cold surface,' International journal of heat and mass transfer, 1976, **19**(9), pp. 1009–1013.

Milacic, E., Baltussen, M., and Kuipers, J., 'Direct numerical simulation study of droplet spreading on spherical particles,' Powder Technology, 2019, **354**, pp. 11–18.

Nochetto, R. H., Salgado, A. J., and Tomas, I., 'A diffuse interface model for two-phase ferrofluid flows,' Comput. Methods Appl. Mech. Engrg., 2016, **309**, pp. 497–531.

Nochetto, R. H., Salgado, A. J., and Walker, S. W., 'A diffuse interfce model for electrowetting with moving contat lines,' Math. Models Methods Appl. Sci., 2014, **24**(1), pp. 67–111.

Odenbach, S., *Ferrofluids: magnetically controllable fluids and their applications*, volume 594, Springer, 2008.

Papell, S. S. and Faber, O. C., *On the influence of nonuniform magnetic fields on ferromagnetic colloidal sols*, volume 4676, National Aeronautics and Space Administration, 1968.

Parizi, H. B., Rosenzweig, L., Mostaghimi, J., Chandra, S., Coyle, T., Salimi, H., Pershin, L., McDonald, A., and Moreau, C., 'Numerical simulation of droplet impact on patterned surfaces,' Journal of Thermal Spray Technology, 2007, **16**(5-6), pp. 713–721.

Pasandideh-Fard, M., Qiao, Y., Chandra, S., and Mostaghimi, J., 'Capillary effects during droplet impact on a solid surface,' Physics of fluids, 1996, **8**(3), pp. 650–659.

Qian, T., Wang, X., and Sheng, P., 'Molecular scale contact line hydrodynamics of immiscible flows,' Phys. Rev. E, 2003, **68**(1), p. 016306 (15 pages).

Qin, Y., Wang, C., and Zhang, Z., 'A positivity-preserving and convergent numerical scheme for the binary fluid-surfactant system,' Int. J. Numer. Anal. Model., 2021, **18**, pp. 399–425.

Quéré, D., 'Inertial capillarity,' EPL (Europhysics Letters), 1997, **39**(5), p. 533.

Raj, K. and Moskowitz, R., 'Commercial applications of ferrofluids,' Journal of Magnetism and Magnetic Materials, 1990, **85**(1-3), pp. 233–245.

Roisman, I. V., 'Inertia dominated drop collisions. ii. an analytical solution of the navier–stokes equations for a spreading viscous film,' Physics of Fluids, 2009, **21**(5), p. 052104.

Rosensweig, R. E., *Ferrohydrodynamics*, Cambridge University Press, 1985.

Russo, A., Icardi, M., Elsharkawy, M., Ceglia, D., Asinari, P., and Megaridis, C. M., 'Numerical simulation of droplet impact on wettability-patterned surfaces,' Physical Review Fluids, 2020, **5**(7), p. 074002.

Savva, N., Kalliadasis, S., and Pavliotis, G. A., 'Two-dimensional droplet spreading over random topographical substrates,' Physical review letters, 2010, **104**(8), p. 084501.

Scheller, B. L. and Bousfield, D. W., 'Newtonian drop impact with a solid surface,' AIChE Journal, 1995, **41**(6), pp. 1357–1367.

Shen, J. and Yang, X., 'Decoupled, energy stable schemes for phase-field models of two-phase incompressible flows,' SIAM J. Numer. Anal., 2015, **53**(1), pp. 279–296.

Shui, L., Eijkel, J. C., and Van den Berg, A., 'Multiphase flow in microfluidic systems–control and applications of droplets and interfaces,' Advances in colloid and interface science, 2007, **133**(1), pp. 35–49.

Šikalo, Š., Marengo, M., Tropea, C., and Ganić, E., 'Analysis of impact of droplets on horizontal surfaces,' Experimental thermal and fluid science, 2002, **25**(7), pp. 503–510.

Smakulski, P. and Pietrowicz, S., 'A review of the capabilities of high heat flux removal by porous materials, microchannels and spray cooling techniques,' Applied Thermal Engineering, 2016, **104**, pp. 636–646.

Song, F., Li, B., and Liu, C., 'Molecular dynamics simulation of nanosized water droplet spreading in an electric field,' Langmuir, 2013, **29**(13), pp. 4266–4274.

Stratton, J. A., *Electromagnetic theory*, volume 33, John Wiley & Sons, 2007.

Tan, Y., Xie, J., Duan, F., Wong, T., Toh, K., Choo, K., Chan, P., and Chua, Y., 'Multi-nozzle spray cooling for high heat flux applications in a closed loop system,' Applied thermal engineering, 2013, **54**(2), pp. 372–379.

Teh, S.-Y., Lin, R., Hung, L.-H., and Lee, A. P., 'Droplet microfluidics,' Lab on a Chip, 2008, **8**(2), pp. 198–220.

Vellingiri, R., Savva, N., and Kalliadasis, S., 'Droplet spreading on chemically heterogeneous substrates,' Physical Review E, 2011, **84**(3), p. 036305.

Visser, C. W., Pohl, R., Sun, C., Römer, G.-W., Huis in 't Veld, B., and Lohse, D., 'Toward 3d printing of pure metals by laser-induced forward transfer,' Advanced materials, 2015, **27**(27), pp. 4087–4092.

Wang, C. and Wise, S. M., 'An energy stable and convergent finite-difference scheme for the modified phase field crystal equation,' SIAM J. Numer. Anal., 2011, **49**(3), pp. 945–969.

Wang, H., Yuan, X., Liang, H., Chai, Z., and Shi, B., 'A brief review of the phase-field-based lattice boltzmann method for multiphase flows,' Capillarity, 2019, **2**(3), pp. 33–52.

Xu, C., Chen, C., Yang, X., and He, X.-M., 'Numerical approximations for the hydrodynamics coupled binary surfactant phase field model: second order, linear, unconditionally energy stable schemes,' Commun. Math. Sci., 2019, **17**(3), pp. 835–858.

Yang, J., Mao, S., He, X.-M., Yang, X., and He, Y., 'A diffuse interface model and semi-implicit energy stable finite element method for two-phase magnetohydrodynamic flows,' Comput. Meth. Appl. Mech. Eng., 2019, **356**, pp. 435–464.

Yang, X., 'On a novel fully decoupled, second-order accurate energy stable numerical scheme for a binary fluid-surfactant phase-field model,' SIAM J. Sci. Comput., 2021, **43**(2), pp. B479–B507.

Yang, X., Chhasatia, V. H., and Sun, Y., 'Oscillation and recoil of single and consecutively printed droplets,' Langmuir, 2013, **29**(7), pp. 2185–2192.

Yang, X., Zhao, J., and He, X.-M., 'Linear, second order and unconditionally energy stable schemes for the viscous Cahn-Hilliard equation with hyperbolic relaxation using the invariant energy quadratization method,' J. Comput. Appl. Math., 2018, **343**(1), pp. 80–97.

Yonemoto, Y. and Kunugi, T., 'Analytical consideration of liquid droplet impingement on solid surfaces,' Scientific reports, 2017, **7**(1), pp. 1–11.

Yue, P., Feng, J., Liu, C., and Shen, J., 'A diffuse-interface method for simulating two-phase flows of complex fluids,' J. Fluid Mech., 2004, **515**, pp. 293–317.

Zhang, G., He, X.-M., and Yang, X., 'Decoupled, linear, and unconditionally energy stable fully-discrete finite element numerical scheme for a two-phase ferrohydrodynamics model,' SIAM J. Sci. Comput., 2021, **43**(1), pp. B167–B193.

Zhang, J., Han, T.-Y., Yang, J.-C., and Ni, M.-J., 'On the spreading of impacting drops under the influence of a vertical magnetic field,' Journal of Fluid Mechanics, 2016, **809**.

Zhang, J., Hassan, M. R., Rallabandi, B., and Wang, C., 'Migration of ferrofluid droplets in shear flow under a uniform magnetic field,' Soft matter, 2019, **15**(11), pp. 2439–2446.

Zhang, M., Zhang, H., and Zheng, L., 'Simulation of droplet spreading, splashing and solidification using smoothed particle hydrodynamics method,' International Journal of Heat and Mass Transfer, 2008, **51**(13-14), pp. 3410–3419.

Zhou, J. and Jing, D., 'Effects of vertical magnetic field on impact dynamics of ferrofluid droplet onto a rigid substrate,' Physical Review Fluids, 2019, **4**(8), p. 083602.

SECTION

3. SUMMARY AND CONCLUSIONS

This dissertation, through numerical and experimental methods, has demonstrated several novel methods to manipulate a wide range of droplet behavior i.e., deformation, breakup, coalescence, wetting, and bouncing in droplet-based microfluidics applications by using magnetic fields. The magnetic approach is advantageous over the traditional electric field based methods, including manual control and flexibility of operations in resource limited environmental applications.

First, an investigation is carried out on the deformation and orientation of a ferrofluid droplet in simple shear flows under uniform magnetic fields. The results suggest that the magnetic field plays a significant role at small capillary numbers (i.e., Ca $\approx$ 0.02) and dictates the deformation and orientation of droplets. In contrast, at a large Capillary number (i.e., Ca $\approx$ 0.25), the deformation and orientation of the droplet is determined by both shear flow and magnetic fields. Also, both numerical and experimental results demonstrate the lateral migration behavior of droplets under uniform magnetic fields along $\alpha = 45°$ (migration towards the center of the flow domain) and 135° (migration towards the bottom wall of the flow domain).

Second, the breakup mechanism of a ferrofluid droplet in a simple shear flow under uniform magnetic fields is investigated at a low Reynolds number (i.e., Re = 0.03). The results show that a magnetic field, applied along 45° and 90°, is capable of inducing a breakup event in a droplet at a capillary number (i.e., Ca $\leq$ 0.5) where it usually does not undergo a breakup phenomenon. On the other hand, applying a uniform magnetic field along 0° and 135° suppresses droplet breakup. Also, an investigation on the effect of viscosity

ratios on the droplet breakup suggests a decrease in the critical magnetic Bond number Bo_{cr} values for more viscous droplets. Moreover, more satellite droplets are observed at higher magnetic field strengths and larger viscosity ratios.

Third, an investigation on the ferro-hydrodynamic interactions between two equal sized ferrofluid droplets is carried out at a low Reynolds number ($\mathrm{Re} \leq 0.03$) in simple shear flows under uniform magnetic fields. The findings suggest that there exists a critical capillary number (i.e., $\mathrm{Ca} \approx 0.25$) where the droplets slide over each other instead of coalescence. However, application of an uniform magnetic field along $\alpha = 0^\circ$ results in faster coalescence, while the droplets experience a reversing motion and separate away from each other along $\alpha = 45^\circ$. Moreover, at $\alpha = 90^\circ$, a critical magnetic Bond number (i.e., $\mathrm{Bo}_{cr} \approx 3.9$) exists where the droplets show reversing motion behavior instead of a passing over motion leading to coalescence. Furthermore, it is found that the collision event is dependent on the initial vertical separation distance between droplets where the application of uniform magnetic fields provides the users an external control on manipulating the interaction behavior between droplets in shear flows.

Fourth, an inquiry on the dynamics between a pair of sessile droplets on a smooth hydrophobic surface under a permanent magnetic field indicates that a non-uniform magnetic field is capable of increasing the wettability of a hydrophobic surface, which in general has lower surface energy and interfacial tension between the droplet and solid surface. On a superhydrophobic surface (i.e., $\theta_c = 150^\circ$), the non-uniform magnetic field forces the droplets towards each other, which followed by a coalescence phenomenon, leads to a jumping-off event of the merged droplet from the surface. Also, a critical magnetic Bond number exists, above which the droplets do not undergo any coalescence phenomenon. However, at $\theta_c \leq 120^\circ$, the droplets are still found to coalesce into a single droplet, but no jumping phenomenon is observed. Additionally, as the viscosity of the surrounding medium decreases, the merged droplet exhibits an increased vertical migration against the direction of gravity.

Fifth, a numerical analysis is carried out to investigate the dynamic interaction behavior between a pair of uneven sized ferrofluid droplets falling through air under gravity and uniform magnetic fields. The findings suggest that in the absence of any external forces except gravity, a critical initial vertical separation between droplets exists ($\Delta Y^{\star}_{cr} \geq 6$), which prevents the droplets from undergoing coalescence phenomenon before hitting the bottom wall. However, an uniform magnetic field along $\alpha = 0^{\circ}$ hinders coalescence, while it is expedited along $\alpha = 90^{\circ}$. Moreover, the application of magnetic fields along 45° greatly impedes the coalescence event where the droplets are found to migrate along divergent lateral directions.

Last, both numerical and experimental approaches are adopted to analyze the post-impact wetting and bouncing dynamics of droplets on a hydrophobic surface under gravity and permanent magnetic fields. The results indicate that a non-uniform magnetic field is capable of increasing the maximum and equilibrium spreading diameters of droplets after impact on a wide range of hydrophobic surfaces ($90^{\circ} \leq \theta_c \leq 150^{\circ}$), which usually have tendencies to repel droplets. Moreover, an interesting bouncing phenomenon is observed in low viscous droplets on a superhydrophobic surface (i.e., $\theta_c \approx 170^{\circ}$); however the activation of magnetic field significantly suppresses the bouncing event and pins the droplet to the surface. Furthermore, both numerical and experimental results are found to be in well agreement with each other. Nevertheless, these above mentioned techniques provide simple and effective mechanisms for manipulation of a wide range of behavior of micro-droplets, including deformation, breakup, coalescence, migration, wetting, and bouncing, which in turn demonstrates the great potential of magnetic fields in industrial, biological, and biomedical droplet-based applications.

REFERENCES

A Abeynaike, AJ Sederman, Y Khan, ML Johns, JF Davidson, and MR Mackley. The experimental measurement and modelling of sedimentation and creaming for glycerol/biodiesel droplet dispersions. *Chemical engineering science*, 79:125–137, 2012.

Kohei Aida, Yang Ho Na, Tomoyuki Nagaya, and Hiroshi Orihara. Droplet coalescence process under electric fields in an immiscible polymer blend. *Physical Review E*, 82(3):031805, 2010.

Fabio Baldessari and L Gary Leal. Effect of overall drop deformation on flow-induced coalescence at low capillary numbers. *Physics of fluids*, 18(1):013602, 2006.

H Bararnia and DD Ganji. Breakup and deformation of a falling droplet under high voltage electric field. *Advanced Powder Technology*, 24(6):992–998, 2013.

D Barthes-Biesel and Andreas Acrivos. Deformation and burst of a liquid droplet freely suspended in a linear shear field. *Journal of Fluid Mechanics*, 61(1):1–22, 1973.

Vance Bergeron. Forces and structure in thin liquid soap films. *Journal of Physics: Condensed Matter*, 11(19):R215, 1999.

Ali Beyzavi and Nam-Trung Nguyen. Modeling and optimization of planar microcoils. *Journal of Micromechanics and Microengineering*, 18(9):095018, 2008a.

Ali Beyzavi and Nam-Trung Nguyen. One-dimensional actuation of a ferrofluid droplet by planar microcoils. *Journal of Physics D: Applied Physics*, 42(1):015004, 2008b.

Ali Beyzavi and Nam-Trung Nguyen. Programmable two-dimensional actuation of ferrofluid droplet using planar microcoils. *Journal of micromechanics and microengineering*, 20(1):015018, 2009.

Ahmad Bitar, Chariya Kaewsaneha, Mohamed M Eissa, Talha Jamshaid, Pramuan Tangboriboonrat, Duangporn Polpanich, and Abdelhamid Elaissari. Ferrofluids: from preparation to biomedical applications. *Journal of Colloid Science and Biotechnology*, 3(1):3–18, 2014.

Brian E Burkhart, Prasad V Gopalkrishnan, Steven D Hudson, Alex M Jamieson, Michael A Rother, and Robert H Davis. Droplet growth by coalescence in binary fluid mixtures. *Physical review letters*, 87(9):098304, 2001.

Philippe Cassagnau and Françoise Fenouillot. Rheological study of mixing in molten polymers: 1-mixing of low viscous additives. *Polymer*, 45(23):8019–8030, 2004.

S Chandra and CT Avedisian. On the collision of a droplet with a solid surface. *Proceedings of the Royal Society of London. Series A: Mathematical and Physical Sciences*, 432 (1884):13–41, 1991.

Delai L Chen, Liang Li, Sebastian Reyes, David N Adamson, and Rustem F Ismagilov. Using three-phase flow of immiscible liquids to prevent coalescence of droplets in microfluidic channels: criteria to identify the third liquid and validation with protein crystallization. *Langmuir*, 23(4):2255–2260, 2007.

Dongju Chen, Ruth Cardinaels, and Paula Moldenaers. Effect of confinement on droplet coalescence in shear flow. *Langmuir*, 25(22):12885–12893, 2009.

Xiaodong Chen, Yongxin Song, Dongqing Li, and Guoqing Hu. Deformation and interaction of droplet pairs in a microchannel under ac electric fields. *Physical Review Applied*, 4(2):024005, 2015.

Yongping Chen and Chengyao Wang. Hydrodynamic interaction of two deformable drops in confined shear flow. *Physical Review E*, 90(3):033010, 2014.

A_K Chesters. Modelling of coalescence processes in fluid-liquid dispersions: a review of current understanding. *Chemical engineering research and design*, 69(A4):259–270, 1991.

Chi-Han Chiou, Dong Jin Shin, Yi Zhang, and Tza-Huei Wang. Topography-assisted electromagnetic platform for blood-to-pcr in a droplet. *Biosensors and Bioelectronics*, 50:91–99, 2013.

Kihwan Choi, Alphonsus HC Ng, Ryan Fobel, and Aaron R Wheeler. Digital microfluidics. *Annual review of analytical chemistry*, 5:413–440, 2012.

Kihwan Choi, Alphonsus HC Ng, Ryan Fobel, David A Chang-Yen, Lyle E Yarnell, Elroy L Pearson, Carl M Oleksak, Andrew T Fischer, Robert P Luoma, John M Robinson, et al. Automated digital microfluidic platform for magnetic-particle-based immunoassays with optimization by design of experiments. *Analytical chemistry*, 85(20):9638–9646, 2013.

GF Christopher, J Bergstein, NB End, M Poon, C Nguyen, and Shelley L Anna. Coalescence and splitting of confined droplets at microfluidic junctions. *Lab on a Chip*, 9(8): 1102–1109, 2009.

MD Cowley and Ronald E Rosensweig. The interfacial stability of a ferromagnetic fluid. *Journal of Fluid mechanics*, 30(4):671–688, 1967.

Pieter De Bruyn, Ruth Cardinaels, and Paula Moldenaers. The effect of geometrical confinement on coalescence efficiency of droplet pairs in shear flow. *Journal of colloid and interface science*, 409:183–192, 2013.

Pieter De Bruyn, Dongju Chen, Paula Moldenaers, and Ruth Cardinaels. The effects of geometrical confinement and viscosity ratio on the coalescence of droplet pairs in shear flow. *Journal of Rheology*, 58(6):1955–1980, 2014.

Robert Antonie Debruijn. *Deformation and breakup of drops in simple shear flows*. PhD thesis, AA(Technische Univ., Eindhoven (Netherlands), 1991.

Pablo M Dupuy, Maria Fernandino, Hugo A Jakobsen, and Hallvard F Svendsen. Using cahn–hilliard mobility to simulate coalescence dynamics. *Computers & Mathematics with Applications*, 59(7):2246–2259, 2010.

Scott A Edwards, Steven L Carnie, Ofer Manor, and Derek YC Chan. Effects of internal flow and viscosity ratio on measurements of dynamic forces between deformable drops. *Langmuir*, 25(6):3352–3355, 2009.

Ana Egatz-Gómez, Sonia Melle, Antonio A García, SA Lindsay, M Márquez, P Domínguez-García, Miguel A Rubio, ST Picraux, JL Taraci, T Clement, et al. Discrete magnetic microfluidics. *Applied Physics Letters*, 89(3):034106, 2006.

H Farhat and Joon Sang Lee. Suppressing the coalescence in the multi-component lattice boltzmann method. *Microfluidics and nanofluidics*, 11(2):137–143, 2011.

Kathleen Feigl, David Megias-Alguacil, Peter Fischer, and Erich J Windhab. Simulation and experiments of droplet deformation and orientation in simple shear flow with surfactants. *Chem. Eng. Sci.*, 62(12):3242–3258, 2007.

A Ghofrani, MH Dibaei, A Hakim Sima, and MB Shafii. Experimental investigation on laminar forced convection heat transfer of ferrofluids under an alternating magnetic field. *Experimental Thermal and Fluid Science*, 49:193–200, 2013.

Andrew J. Griggs, Alexander Z. Zinchenko, and Robert H. Davis. Low-Reynolds-number motion of a deformable drop between two parallel plane walls. *Int. J. Multiph. Flow*, 33(2):182–206, feb 2007. ISSN 0301-9322. doi: 10.1016/J.IJMULTIPHASEFLOW.2006.06.012.

Stefano Guido and Marco Villone. Three-dimensional shape of a drop under simple shear flow. *Journal of Rheology*, 42(2):395–415, 1998.

JW Ha, Yosang Yoon, and LG Leal. The effect of compatibilizer on the coalescence of two drops in flow. *Physics of Fluids*, 15(4):849–867, 2003.

Bing He, Sucui Yang, Zhangrong Qin, Binghai Wen, and Chaoying Zhang. The roles of wettability and surface tension in droplet formation during inkjet printing. *Scientific reports*, 7(1):1–7, 2017.

Cristian Ionescu-Zanetti, Adam Mechler, Sue A Carter, and Ratnesh Lal. Semiconductive polymer blends: Correlating structure with transport properties at the nanoscale. *Advanced Materials*, 16(5):385–389, 2004.

Ph T Jaeger, JJM Janssen, F Groeneweg, and WGM Agterof. Coalescence in emulsions containing inviscid drops with high interfacial mobility. *Colloids and Surfaces A: Physicochemical and Engineering Aspects*, 85(2-3):255–264, 1994.

Seid Mahdi Jafari, Elham Assadpoor, Yinghe He, and Bhesh Bhandari. Re-coalescence of emulsion droplets during high-energy emulsification. *Food hydrocolloids*, 22(7): 1191–1202, 2008.

Muhammad Rashed Javed, Supin Chen, Jack Lei, Jeffrey Collins, Maxim Sergeev, Hee-Kwon Kim, Chang-Jin Kim, R Michael van Dam, and Pei Yuin Keng. High yield and high specific activity synthesis of [18 f] fallypride in a batch microfluidic reactor for micro-pet imaging. *Chemical Communications*, 50(10):1192–1194, 2014.

Sungjune Jung, Stephen D Hoath, and Ian M Hutchings. The role of viscoelasticity in drop impact and spreading for inkjet printing of polymer solution on a wettable surface. *Microfluidics and nanofluidics*, 14(1-2):163–169, 2013.

Pei Yuin Keng, Supin Chen, Huijiang Ding, Saman Sadeghi, Gaurav J Shah, Alex Dooraghi, Michael E Phelps, Nagichettiar Satyamurthy, Arion F Chatziioannou, R Michael van Dam, et al. Micro-chemical synthesis of molecular probes on an electronic microfluidic device. *Proceedings of the National Academy of Sciences*, 109(3): 690–695, 2012.

H-Y Kim and J-H Chun. The recoiling of liquid droplets upon collision with solid surfaces. *Physics of fluids*, 13(3):643–659, 2001.

Ulrike Lehmann, Smail Hadjidj, Virendra K Parashar, Caroline Vandevyver, Amar Rida, and Martin AM Gijs. Two-dimensional magnetic manipulation of microdroplets on a chip as a platform for bioanalytical applications. *Sensors and Actuators B: Chemical*, 117(2):457–463, 2006a.

Ulrike Lehmann, Caroline Vandevyver, Virendra K Parashar, and Martin AM Gijs. Droplet-based dna purification in a magnetic lab-on-a-chip. *Angewandte Chemie International Edition*, 45(19):3062–3067, 2006b.

Jie Li, Yuriko Y Renardy, and Michael Renardy. Numerical simulation of breakup of a viscous drop in simple shear flow through a volume-of-fluid method. *Physics of Fluids*, 12(2):269–282, 2000.

Victor A Lifton. Microfluidics: an enabling screening technology for enhanced oil recovery (eor). *Lab on a Chip*, 16(10):1777–1796, 2016.

Lanchao Lin and Rengasamy Ponnappan. Heat transfer characteristics of spray cooling in a closed loop. *International Journal of Heat and Mass Transfer*, 46(20):3737–3746, 2003.

Yu-Feng Liu, Ming-Hsu Tsai, Yen-Fang Pai, and Weng-Sing Hwang. Control of droplet formation by operating waveform for inks with various viscosities in piezoelectric inkjet printing. *Applied physics A*, 111(2):509–516, 2013.

Lloyd Lobo and Aileen Svereika. Coalescence during emulsification: 2. role of small molecule surfactants. *Journal of Colloid and Interface Science*, 261(2):498–507, 2003.

M Loewenberg and EJ Hinch. Collision of two deformable drops in shear flow. *Journal of Fluid Mechanics*, 338:299–315, 1997.

SuPing Lyu, Frank S Bates, and Christopher W Macosko. Modeling of coalescence in polymer blends. *AIChE journal*, 48(1):7–14, 2002.

J Madejski. Solidification of droplets on a cold surface. *International journal of heat and mass transfer*, 19(9):1009–1013, 1976.

Milan Marić and CW Macosko. Block copolymer compatibilizers for polystyrene/poly (dimethylsiloxane) blends. *Journal of Polymer Science Part B: Polymer Physics*, 40 (4):346–357, 2002.

AP Reena Mary, TN Narayanan, Vijutha Sunny, D Sakthikumar, Yasuhiko Yoshida, PA Joy, and MR Anantharaman. Synthesis of bio-compatible spion–based aqueous ferrofluids and evaluation of radiofrequency power loss for magnetic hyperthermia. *Nanoscale research letters*, 5(10):1706–1711, 2010.

Alphonsus HC Ng, M Dean Chamberlain, Haozhong Situ, Victor Lee, and Aaron R Wheeler. Digital microfluidic immunocytochemistry in single cells. *Nature communications*, 6(1):1–12, 2015.

Nam-Trung Nguyen, Guiping Zhu, Yong-Chin Chua, Vinh-Nguyen Phan, and Say-Hwa Tan. Magnetowetting and sliding motion of a sessile ferrofluid droplet in the presence of a permanent magnet. *Langmuir*, 26(15):12553–12559, 2010.

Michael A Nilsson, Ruta Kulkarni, Lauren Gerberich, Ryan Hammond, Rohitashwa Singh, Elizabeth Baumhoff, and Jonathan P Rothstein. Effect of fluid rheology on enhanced oil recovery in a microfluidic sandstone device. *Journal of Non-Newtonian Fluid Mechanics*, 202:112–119, 2013.

Mina Okochi, Hiroyoshi Tsuchiya, Fumitaka Kumazawa, Mitsuhiro Shikida, and Hiroyuki Honda. Droplet-based gene expression analysis using a device with magnetic force-based-droplet-handling system. *Journal of bioscience and bioengineering*, 109(2): 193–197, 2010.

Oliver Pabst, Jolke Perelaer, Erik Beckert, Ulrich S Schubert, Ramona Eberhardt, and Andreas Tünnermann. All inkjet-printed piezoelectric polymer actuators: Characterization and applications for micropumps in lab-on-a-chip systems. *Organic Electronics*, 14(12):3423–3429, 2013.

Gautam D Pangu and Donald L Feke. Acoustically aided separation of oil droplets from aqueous emulsions. *Chemical Engineering Science*, 59(15):3183–3193, 2004.

M Pasandideh-Fard, YM Qiao, Sanjeev Chandra, and Javad Mostaghimi. Capillary effects during droplet impact on a solid surface. *Physics of fluids*, 8(3):650–659, 1996.

Jolke Perelaer, Patrick J Smith, Erwin van den Bosch, Stephen SC van Grootel, Peter HJM Ketelaars, and Ulrich S Schubert. The spreading of inkjet-printed droplets with varying polymer molar mass on a dry solid substrate. *Macromolecular chemistry and physics*, 210(6):495–502, 2009a.

Jolke Perelaer, Patrick J Smith, Mike MP Wijnen, Erwin van den Bosch, Rebecca Eckardt, Peter HJM Ketelaars, and Ulrich S Schubert. Droplet tailoring using evaporative inkjet printing. *Macromolecular Chemistry and Physics*, 210(5):387–393, 2009b.

Dora Pesach and Abraham Marmur. Marangoni effects in the spreading of liquid mixtures on a solid. *Langmuir*, 3(4):519–524, 1987.

Juergen Pipper, Masafumi Inoue, Lisa FP Ng, Pavel Neuzil, Yi Zhang, and Lukas Novak. Catching bird flu in a droplet. *Nature medicine*, 13(10):1259–1263, 2007.

Juergen Pipper, Yi Zhang, Pavel Neuzil, and Tseng-Ming Hsieh. Clockwork pcr including sample preparation. *Angewandte Chemie*, 120(21):3964–3968, 2008.

K Raj and R Moskowitz. Commercial applications of ferrofluids. *Journal of Magnetism and Magnetic Materials*, 85(1-3):233–245, 1990.

JM Rallison. The deformation of small viscous drops and bubbles in shear flows. *Annual review of fluid mechanics*, 16(1):45–66, 1984.

Ayan Ray, Vijaykumar Babulalji Varma, PJ Jayaneel, NM Sudharsan, ZP Wang, and Raju V Ramanujan. On demand manipulation of ferrofluid droplets by magnetic fields. *Sensors and Actuators B: Chemical*, 242:760–768, 2017.

A Rida, V Fernandez, and MAM Gijs. Long-range transport of magnetic microbeads using simple planar coils placed in a uniform magnetostatic field. *Applied Physics Letters*, 83(12):2396–2398, 2003.

Michael A Rother, Alexander Z Zinchenko, and Robert H Davis. Buoyancy-driven coalescence of slightly deformable drops. *Journal of Fluid Mechanics*, 346:117–148, 1997.

P Rowghanian, CD Meinhart, and O Campàs. Dynamics of ferrofluid drop deformations under spatially uniform magnetic fields. *Journal of Fluid Mechanics*, 802:245–262, 2016.

FD Rumscheidt and SG Mason. Particle motions in sheared suspensions xi. internal circulation in fluid droplets (experimental). *Journal of Colloid Science*, 16(3):210–237, 1961.

Paul F Salipante and Petia M Vlahovska. Electrohydrodynamics of drops in strong uniform dc electric fields. *Physics of Fluids*, 22(11):112110, 2010.

Brian L Scheller and Douglas W Bousfield. Newtonian drop impact with a solid surface. *AIChE Journal*, 41(6):1357–1367, 1995.

Orest Shardt, JJ Derksen, and Sushanta K Mitra. Simulations of droplet coalescence in simple shear flow. *Langmuir*, 29(21):6201–6212, 2013.

JD Sherwood. Breakup of fluid droplets in electric and magnetic fields. *Journal of Fluid Mechanics*, 188:133–146, 1988.

Xu Shi, Chun-Hong Chen, Weimin Gao, Shih-hui Chao, and Deirdre R Meldrum. Parallel rna extraction using magnetic beads and a droplet array. *Lab on a Chip*, 15(4): 1059–1065, 2015a.

Ho Cheung Shum, Jin-Woong Kim, and David A Weitz. Microfluidic fabrication of monodisperse biocompatible and biodegradable polymersomes with controlled permeability. *Journal of the American Chemical Society*, 130(29):9543–9549, 2008.

Vincenzo Sibillo, Gilberto Pasquariello, Marino Simeone, Vittorio Cristini, and Stefano Guido. Drop deformation in microconfined shear flow. *Phys. Rev. Lett.*, 97(5): 054502, 2006.

Younggon Son. Development of a novel microcompounder for polymer blends and nanocomposite. *Journal of applied polymer science*, 112(2):609–619, 2009.

Howard A Stone. Dynamics of drop deformation and breakup in viscous fluids. *Annual Review of Fluid Mechanics*, 26(1):65–102, 1994.

Kai Sun, Ming Jia, and Tianyou Wang. Numerical investigation of head-on droplet collision with lattice boltzmann method. *International Journal of Heat and Mass Transfer*, 58(1-2):260–275, 2013.

Graeme Supeene, Charles R Koch, and Subir Bhattacharjee. Deformation of a droplet in an electric field: nonlinear transient response in perfect and leaky dielectric media. *Journal of colloid and interface science*, 318(2):463–476, 2008.

Geoffrey Ingram Taylor. The viscosity of a fluid containing small drops of another fluid. *Proceedings of the Royal Society of London. Series A, Containing Papers of a Mathematical and Physical Character*, 138(834):41–48, 1932.

Geoffrey Ingram Taylor. The formation of emulsions in definable fields of flow. *Proceedings of the Royal Society of London. Series A, containing papers of a mathematical and physical character*, 146(858):501–523, 1934.

Emine Tekin, Patrick J Smith, and Ulrich S Schubert. Inkjet printing as a deposition and patterning tool for polymers and inorganic particles. *Soft Matter*, 4(4):703–713, 2008.

Achim Wixforth, Christoph Strobl, Ch Gauer, A Toegl, Jürgen Scriba, and Z v Guttenberg. Acoustic manipulation of small droplets. *Analytical and bioanalytical chemistry*, 379(7-8):982–991, 2004.

Haowen Xi and Comer Duncan. Lattice boltzmann simulations of three-dimensional single droplet deformation and breakup under simple shear flow. *Phys. Rev. E*, 59(3):3022, 1999.

Hong Yang, C Charles Park, Y Thomas Hu, and L Gary Leal. The coalescence of two equal-sized drops in a two-dimensional linear flow. *Physics of Fluids*, 13(5):1087–1106, 2001.

Yukihiro Yonemoto and Tomoaki Kunugi. Analytical consideration of liquid droplet impingement on solid surfaces. *Scientific reports*, 7(1):1–11, 2017.

Pengtao Yue, James J Feng, Chun Liu, and Jie Shen. Diffuse-interface simulations of drop coalescence and retraction in viscoelastic fluids. *Journal of Non-Newtonian Fluid Mechanics*, 129(3):163–176, 2005.

Arthur Zakinyan, Elena Tkacheva, and Yury Dikansky. Dynamics of a dielectric droplet suspended in a magnetic fluid in electric and magnetic fields. *Journal of Electrostatics*, 70(2):225–232, 2012.

VITA

Rifat Hassan was born in Dinajpur, Bangladesh. He received his Bachelor of Science in Mechanical Engineering in April 2016 from Bangladesh University of Engineering and Technology, Dhaka, Bangladesh. In December 2021, he received his Doctor of Philosophy degree in Mechanical Engineering from Missouri University of Science and Technology, Rolla, Missouri. His research interests included fluid dynamics, droplet microfluidics, emulsion microfluidics, multiphase flows, magnetic fields, lab-on-a-chip, micro/nano technology, inkjet printing, and biomedical applications.

During his Ph.D. study, he was awarded the most prestigious College of Engineering and Computing Dean's Outstanding Ph.D. scholar award as well as Graduate Student Leadership award in 2021 for his scholarship excellence, academic and research excellence, and service contributions to the Missouri S&T community under the supervision of Dr. Cheng Wang. Moreover, he was nominated for Distinguished Research and Innovation Excellence Award by the College of Graduate Studies at Missouri S&T in 2021. He advised and assisted 8 undergraduate and graduate students on fabricating microfluidic channels and experimental setup. Additionally, he was the lab instructor of ME 4842 Mechanical Engineering Systems and ME 3131 Thermofluid Mechanics for three and half years.

During his Ph.D. study, he not only focused on his personal research projects, but also participated in collaborative works with other research groups from Civil Engineering, Mathematics, Biology, and Electrical Engineering. In total, he authored and co-authored 12 journal articles and 9 conference abstracts/papers/presentations in 4 years.